



City Research Online

City, University of London Institutional Repository

Citation: Chatterjee, S. (2018). Monte Carlo investigation of light-tissue interaction in photoplethysmography. (Unpublished Doctoral thesis, City, University of London)

This is the accepted version of the paper.

This version of the publication may differ from the final published version.

Permanent repository link: <https://openaccess.city.ac.uk/id/eprint/21266/>

Link to published version:

Copyright: City Research Online aims to make research outputs of City, University of London available to a wider audience. Copyright and Moral Rights remain with the author(s) and/or copyright holders. URLs from City Research Online may be freely distributed and linked to.

Reuse: Copies of full items can be used for personal research or study, educational, or not-for-profit purposes without prior permission or charge. Provided that the authors, title and full bibliographic details are credited, a hyperlink and/or URL is given for the original metadata page and the content is not changed in any way.

MONTE CARLO INVESTIGATION OF
LIGHT-TISSUE INTERACTION IN
PHOTOPLETHYSMOGRAPHY

By

SUBHASRI CHATTERJEE

A thesis submitted for the degree of DOCTOR OF PHILOSOPHY



School of Mathematics, Computer Science and Engineering

CITY, UNIVERSITY OF LONDON

2018

DECLARATION

I solemnly and sincerely declare that I am the sole author of the dissertation and the work presented here was carried out in accordance with the requirements of the regulations by City, University of London. Any use of any textbooks, theses and published works in which copyrights exist are cited, and title of the work and the authors have been carefully acknowledged. For any work done in collaboration, the credits have been given to the collaborator. The contents of the dissertation are original and have not been submitted in whole or in part for consideration for any academic or professional degree or award.

I grant the powers of discretion to the Librarian at City, University of London to allow the thesis to be copied partially or entirely without further reference to the author. This permission covers only single copies made for study purposes, subject to a normal condition of acknowledgement.

SIGNED: Subhasri Chatterjee

I dedicate this thesis to my mother.

ACKNOWLEDGEMENTS

First of all, I want to convey my profound gratitude to my supervisor Prof. Panicos Kyriacou, who always motivated and encouraged me, and has been immensely supportive whenever I was in any kind of professional and personal trouble. His guidance has helped me to grow as a researcher and boost up my confidence level. I am really grateful to have him as my supervisor.

I extend my gratitude to my co-supervisor Dr. Justin Phillips. The invaluable suggestions I received from him through our many formal and informal conversations helped me to channelise my research problem.

I wholeheartedly thank all my colleagues and alumni from the Research Centre for Biomedical Engineering, City, University of London. In particular, I want to thank Dr. Karthik Budidha, Dr. Tomas Ysehak Abay, Dr. Meha Qassem and Dr. James May for their support and help at different points of time.

I would like to acknowledge the Erasmus Mundus INTACT scholarship from European Commission for the financial assistance, and the School of Mathematics, Computer Science and Engineering of City, University of London, UK for providing me the facilities for pursuing my research.

I want to express my heartfelt gratitude to all the teachers from my university, college and school who built my vision for research. I am especially thankful to Dr. Nirmalya Ghosh for giving me the opportunity to work with him during my National Photonics Fellowship program (2012).

Finally and most importantly, I wish to thank my family for standing beside me in all circumstances. The thesis would never have been possible without the support and encouragement of my beloved parents, my brother Satyaban, and my husband Souvik.

ABSTRACT

Photoplethysmography (PPG) is a non-invasive photometric technique which measures changes in the volume of blood in the biological tissue. PPG is well-known for its application in pulse oximetry used for the continuous monitoring of arterial blood oxygen saturation (SpO_2). Over the past decade, there has been a plethora of research in the field of PPG, with potential applications beyond pulse oximetry and heart rate monitoring. Such applications explore the utilisation of PPG for the assessment of various bio-markers relating to vascular mechanics, haemodynamics and many others. With the growing research interest in the field of PPG, a comprehensive understanding of the light-tissue interaction-based working principle underlying the technique is essential. This thesis is focussed on the investigation of the fundamental light-tissue interactions in PPG using the Monte Carlo method. Tissue models have been developed in this thesis which were characterised by the optical properties (e.g., wavelength- dependent coefficients of scattering and absorption etc.), the anatomical features (e.g., stratification and dimension of tissue layers and sublayers etc.), and the physiological parameters (water and blood content in tissue layers etc.). The Monte Carlo strategy was verified, and was initially implemented to model the light propagation through a monolayer perfused dermal tissue volume in a reflective mode PPG at the red and near-infrared wavelengths, usually used in pulse oximetry. Results illustrated the distribution of the scattering-absorption interaction events, and quantified the optical pathlength, penetration depth and detected reflectance with the variable sensor geometry (i.e., source-detector separation) and physiological states (i.e., the volume of blood and oxygen saturation) of the tissue. The monolayer model was also employed to produce the plot resembling the ‘calibration curve’ used in pulse oximetry. With the knowledge gained from the monolayer-model study, a similar investigation was performed on a heterogeneous tissue structure of a human finger which was executed in both reflective and transmissive geometrical settings. The calibration curves produced from the detected reflectance and transmittance exhibited a high correlation. The absorbances of red and near-infrared light by individual layers of the finger were quantified at systole and diastole. To the relative absorbance, the contributions of dermis and bone were the maximum and the minimum, respectively. The dependence of the optical pathlength on the source-detector separation and the operating wavelength was quantified by the Differential Pathlength Factor (DPF), which was assessed for the reflective mode PPG by simulating light propagation through a human forearm tissue volume. The DPF values were used in experimentally obtained PPG signal in order to determine the time-change in the concentration of oxyhaemoglobin and deoxyhaemoglobin. Cross-talk and absolute errors were calculated between the simulated and approximated DPFs. The results presented in the thesis contribute greatly to the understanding on PPG light-tissue interaction. Such knowledge could also greatly contribute to the development of the new generation PPG sensors for various applications.

TABLE OF CONTENTS

	Page
List of Symbols and Acronyms	ix
List of Tables	xi
List of Figures	xii
List of publications	xv
1 INTRODUCTION	1
2 BACKGROUND PHYSIOLOGY	6
2.1 Introduction	6
2.2 Circulatory system	6
2.2.1 Heart	8
2.2.2 Arteries, Veins and Capillaries	9
2.2.3 Blood	10
2.2.4 Transport of Oxygen	11
2.2.5 Oxyhaemoglobin dissociation curve	11
2.2.6 Transport of Carbon dioxide	13
2.2.7 Oxygen Saturation of Blood	14
2.3 Respiratory system	16
2.3.1 Exchange of gases	17
2.4 Summary	17
3 BASICS OF TISSUE OPTICS	19
3.1 Introduction	19
3.2 Mechanism of light propagation through tissue	20
3.2.1 Scattering	20
3.2.2 Absorption	26
3.2.3 Interaction in the boundary	27
3.3 Tissue optical properties	28
3.4 Beer-Lambert-Bouguer law	30
3.4.1 Transmittance, Absorbance and Optical Depth	31

3.4.2	Derivation of the law: classical approach	31
3.4.3	Derivation of the combined Beer-Lambert law: modern approach	32
3.4.4	Modification in Beer-Lambert law for scattering	35
3.4.5	Beer-Lambert law in inhomogeneous medium	36
3.5	Radiative Transfer formalism	37
3.6	Summary	38
4	REVIEW ON MODELLING LIGHT-TISSUE INTERACTION IN PHOTO- PLETHYSMOGRAPHY	40
4.1	Introduction	40
4.2	Overview on modelling approaches for light-tissue interaction	40
4.3	Monte Carlo method - developments and advantages	44
4.4	Current state of the art in modelling Photoplethysmography and Pulse Oximetry	46
4.5	Summary	47
5	PHOTOPLETHYSMOGRAPHY AND PULSE OXIMETRY	49
5.1	Introduction	49
5.2	Working principle of Photoplethysmography	50
5.2.1	Components of PPG waveform	51
5.2.2	Beer-Lambert law in PPG	52
5.2.3	PPG measurement technique	53
5.3	PPG in Pulse Oximetry	54
5.3.1	Working principle of Pulse Oximetry	55
5.3.2	Calibrating Pulse Oximeter	58
5.3.3	Pulse Oximetry technique	61
5.4	Requirements for a modelling approach	62
5.5	Summary	63
6	MONTE CARLO MODELLING METHODOLOGY	65
6.1	Introduction	65
6.2	Development of the model	65
6.2.1	Concept and considerations	65
6.2.2	Geometrical representation and co-ordinate system	67
6.2.3	Transformation between co-ordinate systems	69
6.2.4	Calculation for the scattering angle	71
6.2.5	Sampling of random variables	72
6.2.6	Simulation procedure	75
6.3	Implementation strategy	88
6.3.1	Input and output	88
6.3.2	Monolayer and multilayer model	90
6.3.3	Execution of the model	90

6.4	Summary	92
7	CHARACTERISATION AND EVALUATION OF THE MONTE CARLO MODEL	93
7.1	Introduction	93
7.2	Characterisation of the model	93
7.3	Evaluation of the model	98
7.4	Correlating the optical parameters in the model	101
7.5	Summary	105
8	INVESTIGATING LIGHT-TISSUE INTERACTIONS IN REFLECTANCE PHOTOPLETHYSMOGRAPHY USING MONOLAYER PERFUSED SKIN MODEL	106
8.1	Introduction	106
8.2	Background	106
8.3	Model description	108
8.3.1	Monolayer model with static perfusion	108
8.3.2	Monolayer model with pulsatility	112
8.4	Distribution of scattering events	113
8.5	Mean optical path and reflectance as function of blood volume	115
8.6	Mean optical path and reflectance as function of blood oxygen saturation	116
8.7	Differential red and infrared mean optical path, mean penetration depth and reflectance	117
8.8	Reflectance and 'ratio of ratios' as function of oxygen saturation	125
8.9	Summary	126
9	INVESTIGATING LIGHT-TISSUE INTERACTIONS IN REFLECTANCE AND TRANSMITTANCE FINGER PHOTOPLETHYSMOGRAPHY	128
9.1	Introduction	128
9.2	Background	128
9.3	Description of the finger tissue model	129
9.4	Method of execution	133
9.5	Simulated results of the interaction events	134
9.6	Reflectance, Transmittance and Ratio of ratios	139
9.7	Mean optical path and mean depth of penetration	141
9.8	Normalised absorbances and modulation ratio	145
9.9	Summary	148
10	DIFFERENTIAL PATHLENGTH FACTOR ESTIMATION AND PERFUSION ASSESSMENT BY PHOTOPLETHYSMOGRAPHY	149
10.1	Introduction	149
10.2	Background	150

10.3 Methodology	153
10.3.1 Description of multilayer tissue model	154
10.3.2 Execution strategy	157
10.3.3 Experimental setting and data analysis	159
10.4 DPF in monolayer perfused skin tissue	161
10.5 Light-tissue interaction and DPF estimation in multilayer forearm tissue	164
10.6 Experimental data analysis and error calculation	170
10.7 Summary	173
11 DISCUSSION AND CONCLUSION	174
Appendices	
A Other applications of Monte Carlo model	183
B Computational program	190
Bibliography	201

LIST OF SYMBOLS AND ACRONYMS

θ	Angle of scatter or deflection
ϕ	Azimuthal angle
λ	Wavelength
S_aO_2	Arterial blood oxygen saturation
S_vO_2	Venous blood oxygen saturation
S_tO_2	Total blood oxygen saturation
S_pO_2	Oxygen saturation measured by Pulse Oximeter
V_a	Arterial blood volume
V_v	Venous blood volume
μ_a	Absorption coefficient
μ_s	Scattering coefficient
μ'_s	Reduced scattering coefficient
μ_t	Total interaction coefficient
μ_x, μ_y, μ_z	Direction cosines
g	Anisotropy factor
d	Source-detector separation
t	Thickness of tissue layer

w	Photon weight
l	Differential (or physical) optical pathlength
N	Number of scattering-absorption interaction events
n_i	Refractive index of internal medium
n_t	Refractive index of external medium
sr	Steradian
nm	Nanometres
mM	Millimolar
PPG	Photoplethysmography
PO	Pulse Oximeter
DPF	Differential pathlength factor
R	Ratio of ratios
MOP	Mean optical path
MW	Mean detected weight of photon
MD	Mean depth of penetration

LIST OF TABLES

TABLE	Page
7.1 Simulated results of diffuse reflectance (R_d) compared with pre-validated results.	99
7.2 Comparison of MC simulated total reflectance and transmittance with the analytical results for an anisotropic scattering tissue having matched boundary.	99
7.3 Comparison of developed Monte Carlo (MC) reflectance and transmittance simulations for an isotropic scattering slab	100
7.4 Comparison of developed Monte Carlo (MC) reflectance and transmittance simulations for an anisotropic scattering slab	101
8.1 Optical properties of tissue constituents (in unit of mm^{-1})	109
8.2 Percentage change in mean optical path ΔMOP , reflectance ΔW and mean penetration depth ΔMD with blood volume V and total blood oxygen saturation S_tO_2 for a certain source-detector separation of 6 mm.	124
9.1 Stratification of dermal sublayers.	131
9.2 Optical properties of tissue layer in finger tissue model.	132
9.3 Simulated distribution of relative absorbances and modulation ratio in tissue layers	147
10.1 Stratification order and properties of the tissue layers used for modelling the forearm. The thicknesses are presented with the volume distribution of blood and water in each layer.	156
10.2 Differential Pathlength Factor (DPF) at both red and infrared wavelengths for different source-detector separation distances d . The values are derived from the MC simulations of light transport through human forearm. The mean optical pathlength l can be calculated as $l = d \times DPF$	169
10.3 Cross talk between haemoglobin species calculated for the three conditions investigated. $CT_{Hb \rightarrow HbO_2}$ is the cross talk of deoxyhaemoglobin into oxyhaemoglobin, whereas $CT_{HbO_2 \rightarrow Hb}$ represents the cross talk of oxyhaemoglobin into deoxyhaemoglobin.	172

LIST OF FIGURES

FIGURE	Page
2.1 Human Circulatory System	7
2.2 Anatomy of human heart	8
2.3 Artery, Vein and Capillary	9
2.4 Oxygen-Haemoglobin dissociation curve	12
2.5 Human Respiratory System	16
3.1 Schematic of scattering event	21
3.2 Scattering anisotropy	23
3.3 Phase function with anisotropy factor	24
3.4 Mean free pathlength	25
3.5 Reflection and Refraction	27
3.6 Tissue absorption spectra	29
3.7 Tissue scattering spectra	30
3.8 Derivation of Veer-Lambert's law	33
3.9 Expression of Modified Beer-lambert's law	35
4.1 A sense of distribution of scaling	42
5.1 Typical PPG wave	50
5.2 The components in PPG waveform	51
5.3 The schematic of PPG system modalities	54
5.4 The correlation between SaO_2 and SpO_2 presented that has been adapted from [Moyle, 2002].	58
5.5 The comparative calibration curves obtained using the empirical calibration method, Beer-Lambert law and the Linear equation for commercial pulse oximetry calibration	60
5.6 The schematic diagram of the reflective and the transmissive mode of pulse oximetry in finger	62
6.1 Schematic diagram of model geometry	68
6.2 Relationship between co-ordinate systems	69
6.3 Random sampling of variables in Monte Carlo	74

6.4	Monte Carlo algorithm flowchart	76
6.5	Schematic of interactions to be simulated	77
6.6	Incidence of Gaussian beam to the tissue surface	80
6.7	Incidence of the photon cluster from source fibre	82
6.8	Correction in boundary in the model	86
6.9	Implementation of Monte Carlo model	89
7.1	Illustration of variables in Monte Carlo model	94
7.2	Scattering plot of Monte Carlo simulated photon path	95
7.3	Scattering density-plot of Monte Carlo simulated photon path	96
7.4	Scattering density-plot of Monte Carlo simulated path of all photons	98
7.5	Monte Carlo model with varying absorption coefficient	102
7.6	Monte Carlo model with varying scattering coefficient	103
7.7	Monte Carlo model with varying scattering anisotropy	104
8.1	Distribution of photon scatter in monolayer Monte Carlo model of photon scatter	114
8.2	Histogram plot for the scatter distribution in monolayer Monte Carlo model of perfused skin	115
8.3	Mean optical path and reflectance as function of blood volume in the perfused tissue	116
8.4	Mean optical path and reflectance as function of blood oxygen saturation in the perfused tissue	117
8.5	Red-infrared differential mean optical path at different blood volume and oxygen saturation	119
8.6	Percentage change of red-infrared differential mean optical path at different blood volume and oxygen saturation	120
8.7	Red-infrared differential mean penetration depth at different blood volume and oxygen saturation	121
8.8	Red-infrared differential reflectance at different blood volume and oxygen saturation	123
8.9	Reflectance and 'ratio of ratios' in a monolayer pulsatile model	126
9.1	Description of the multilayer finger tissue model	130
9.2	Distribution of light-tissue interaction in reflective and transmissive finger PPG	136
9.3	Histogram plots for the optical path and depth of penetration in reflectance mode finger pulse oximetry model	137
9.4	Histogram plots for the optical path and depth of penetration in transmittance mode finger PPG	138
9.5	Reflectance, transmittance and ratio of ratios in finger model pulse oximetry	140
9.6	Mean optical path and mean depth of penetration in reflectance finger pulse oximetry	143

9.7	Mean optical path and mean depth of penetration in reflectance finger pulse oximetry	144
9.8	Distribution of normalised absorbances in different tissue layers	146
10.1	Sensr location and anatomy of forearm	155
10.2	Multilayer model of human forearm	157
10.3	Experimental setting for acquiring PPG signal from volunteer	160
10.4	Differential Pathlength Factor in monolayer perfused skin dermis	163
10.5	Differential Pathlength Factor in monolayer perfused skin dermis	164
10.6	Differential Pathlength Factor in monolayer perfused skin dermis at a fixed $S_tO_2 = 90\%$	165
10.7	Scatter density plot at source-detector separation 5 mm in human forearm	166
10.8	Scatter density plot at source-detector at NIRS region in human forearm	167
10.9	Optical path and Differential Pathlength Function in human forearm at 660 nm and 880 nm	168
10.10	Cross-talk assesment between the time-change in concentration of oxy and deoxyhaemoglobin using simulated and approximated DPF	171
10.11	Boxplots of the normalised percentage errors of ΔC_{Hb} and ΔC_{HbO_2} in the three conditions (A, B, and C)	172
A.1	Differential pathlength factor of monolayer brain-like tissue	184
A.2	Differential pathlength factor of monolayer blood and muscle-like tissues	185
A.3	Blood cylinder in muscle slab	186
A.4	Multiple detectors on monolayer tissue	187
A.5	Depth and reflectance distribution at multiple detectors on monolayer tissue	188
A.6	Depth and reflectance distribution at multiple detectors on monolayer tissue	189

LIST OF PUBLICATIONS

- **Journal publications**

- S. Chatterjee, P. A. Kyriacou; "Opto-anatomical modelling of finger photoplethysmography", *Computers in Biology and Medicine* (submitted).
- S. Chatterjee, T. Y. Abay, J. P. Phillips, P. A. Kyriacou; "Investigating Optical Path and Differential Pathlength Factor to assess Tissue Perfusion from Reflectance Photoplethysmography", *Journal of Biomedical Optics*, 23(07):1, 2018.
- S. Chatterjee, J. P. Phillips, P. A. Kyriacou; "Monte Carlo investigation of the effect of blood volume and oxygen saturation on optical path in reflectance pulse oximetry", *Biomedical Physics and Engineering Express*, 2(6):065018, 2016.

- **Conference proceedings**

- S. Chatterjee, and P. A. Kyriacou; "Monte Carlo model for reflectance Pulse Oximetry using pulsatile monolayer perfused skin tissue", *Journal of Physics Conference series*, Newton Researcher Links Workshop: Bio-Photonics for Medical Technologies, Malaysia, 2018 (in press).
- S. Chatterjee, J. P. Phillips, P. A. Kyriacou; "Pulsatile Monte Carlo model for Reflectance Pulse Oximetry", *Proceedings of the MEIBioeng/MPEC2017 of the Institute of Physics and Engineering in Medicine (IPEM) Surrey UK*, no. 13, 2017 (Abstract).
- S. Chatterjee, J. P. Phillips, P. A. Kyriacou; "Investigating optical path in reflectance pulse oximetry using a multilayer Monte Carlo model", *SPIE-OSA Proceedings of the European Conferences on Biomedical Optics (ECBO) Munich, Germany*, 10411 1041106-1, 2017.
- S. Chatterjee, J. P. Phillips, P. A. Kyriacou; "Differential pathlength factor estimation for brain-like tissue from a single-layer Monte Carlo model", *Proceedings of 37th Annual International Conference of the IEEE Engineering in Medicine and Biology Society (IEEE EMBC) Milan Italy*, 3279-3282, 2015.

INTRODUCTION

Presently, optical methods have a significant impact on medical diagnostics and monitoring in clinical practice [Mudry *et al.*, 2003]. Such bio-optical methods encompass a range of modalities, which rely on detecting and analysing the optical radiation changes due to interaction with biological tissues [Yun and Kwok, 2017; Li and Harrington, 1998; Shen and van Wijk, 2006]. Commercial and experimental optical technologies have been significantly improved with the new developments in fibre optics, Light Emitting Diodes (LED), laser, Charge Coupled Device (CCD), photodetectors, photomultipliers etc., and therefore become available for various medical and biological applications [Vigneshvar *et al.*, 2016; Righini *et al.*, 2009]. These advancements led to modern research trends focussed on making medical diagnostics smaller, less expensive, faster and consequently more productive. Besides the advancement of the hardware and instrumentation, computational technology has also crossed an incredibly long path along the way of development [Doronin and Meglinski, 2011]. Fast and flexible computational processes and algorithms can be immensely helpful in conceptual design, optimisation, and modification of a particular experimental bio-optical system. In order to recreate, or ‘model’, a bio-optic experimental environment using a computational tool, and to rely on the results generated by the model for prediction or optimisation of the system, a very careful assessment of the modelling method is necessary [Wang and Tuchin, 2013; Prasad, 2004; Tuchin, 1993].

Monte Carlo method is a computational tool to model the propagation of light through

biological media [Prahl, 1988]. This method has been adopted by many researchers for solving critical problems related to light-tissue interaction which are very complicated to solve theoretically [Zhu and Liu, 2013; Tuchin, 1997; Wang and Tuchin, 2013]. The advantages of Monte Carlo over other available light-tissue interaction modelling approaches (such as diffusion approximation, random walk theory, adding-doubling etc.) are well-documented [Meglinski and Matcher, 2002; Tuchin, 1993; Zhu and Liu, 2013; Periyasamy and Pramanik, 2014], which makes this method the most acceptable tool for simulating light-tissue interaction.

Photoplethysmography (PPG) is a non-invasive bio-optical technique for measuring the volumetric changes in blood associated with the cardiac cycle in the vascular tissue beds [Allen, 2007]. In PPG, a volume of tissue is illuminated by an optical radiation that undergoes multiple interaction events as it traverses through different tissue-layers and finally transmits through the tissue [Kamshilin *et al.*, 2015]. Depending on the geometrical positioning of the optical source and detector of the PPG sensor, the signal can be recorded either in (a) a reflective mode, where the optical source and the detector are placed on the same side of the tissue site so that the reflected and backscattered light from the tissue is detected, or in (b) a transmissive mode, where the source and the detector are placed on the two opposite sides of the tissue site (e.g., finger) so that the refracted or transmitted light is detected. A PPG signal is divided into two components: an alternating component (AC PPG), which is synchronised with the cardiac cycle and is generated due to the absorption of light in the pulsatile tissue part (i.e., arterial blood), and a very slowly varying component (DC PPG) that is originated due to the light absorption in the non-pulsatile tissue part (i.e., venous blood, bloodless tissue etc.).

The PPG signal is widely utilised in the technique of Pulse Oximetry (PO) for the estimation of arterial oxygen saturation [Moyle, 2002]. In pulse oximetry, the PPG signals recorded at the red and near-infrared optical wavelengths, and the arterial oxygen saturation is derived from the ratio of the relative amplitudes of the detected signals. The pulse oximeter is frequently used in the clinical setting for the continuous monitoring of blood oxygenation. Recently, there has been a plethora of interest in extending the application of PPG beyond PO, for example, usage of PPG in the assessment of tissue perfusion, vascular mechanics, blood pressure, blood viscosity, pulse transit time estimation, pulse

rate variability etc. [Njoum and Kyriacou, 2017; Abay and Kyriacou, 2015; Budidha *et al.*, 2018; Reisner *et al.*, 2008].

A large volume of work has been carried out focussing on the technical improvement of Photoplethysmography and pulse oximetry, for example, reducing the noise and improving signal quality, eliminating the motion artefact, dealing with low tissue perfusion, acquiring signals from different tissue sites and so on [Allen, 2007; Budidha and Kyriacou, 2018; Hickey *et al.*, 2010; Patel *et al.*, 2018]. However, the field of research on the light-tissue interaction underlying the PPG technique has been minimally explored yet. Such a study is of utmost importance for a comprehensive understanding of the fundamental PPG principle and for widening the domain of PPG application. In order to grow the core understanding in this field, the present thesis aims to investigate the precise nature of the light-tissue interaction in PPG and pulse oximetry using the Monte Carlo modelling strategy.

The main objective of the thesis was to develop a robust and flexible opto-anatomical model illustrating a full three-dimensional distribution of light-tissue interactions in Photoplethysmography. In this process, a single layer of perfused skin tissue was simulated rigorously to analyse the behaviour of light through the skin at different states of perfusion and oxygen saturation at a reflective geometry. This initial study was followed by a further detailed analysis with a specific region of interest, i.e., a heterogeneous volume of finger tissue. A range of variables was recorded that described the light-tissue interaction pertinent to PPG and pulse oximetry. With the inspiration from the findings obtained from these studies, the Monte Carlo model was executed to assess the Differential Pathlength Factor (DPF) for a tissue-volume of human forearm in a reflective geometrical setting of PPG. The simulated DPF values were further utilised to determine the time-change in the concentration of oxyhaemoglobin and deoxyhaemoglobin from experimentally obtained PPG signal from the forearm.

A brief summary of the chapters of the thesis are discussed below:

- **Chapter 2:** This chapter describes the basics of human physiology pertinent to the subject Photoplethysmography. It presents an overview of the respiratory and circulatory system of the human body and the functions responsible for tissue

perfusion and oxygenation.

- **Chapter 3:** This chapter presents a theoretical overview of light-tissue interaction. It discusses the basic mechanism of light propagation through tissue by the steps of scattering, absorption, reflection etc. This section also describes the laws of tissue optics which are crucial for understanding the migration of photons through a biological media, namely, the Beer-Lambert law and Radiative Transfer formalism.
- **Chapter 4:** This chapter presents the current state of the art of modelling Photoplethysmography. It presents a brief overview of the light-tissue interaction modelling methods. Further, this chapter reviews the existing research related to modelling Photoplethysmography and establishes the importance of the Monte Carlo modelling.
- **Chapter 5:** In this chapter, the methodologies of Photoplethysmography and pulse oximetry are discussed. The working principle of the techniques, especially the Beer-Lambert law-based calculations are explicitly described and derived. This chapter states the basic requirements for an adequate modelling strategy for PPG.
- **Chapter 6:** This chapter presents the detailed steps and shows the necessary derivations for the basic Monte Carlo model. Additionally, this chapter discusses the strategy of how the Monte Carlo model is executed in the present work. It also introduces the two sections of the implementation strategy: monolayer and multilayer modelling, stating the importance of the individual sections.
- **Chapter 7:** In this chapter, the basic Monte Carlo model is verified, and the input and output parameters are characterised. These descriptions clarify the terminologies and annotations which have been defined in earlier chapters and will be used in the next chapters.
- **Chapter 8:** This chapter explores the Monte Carlo model for investigating the light-tissue interaction in a perfused dermal layer. Variables such as optical pathlength, penetration depth, and detected reflectance are investigated for different blood volume and oxygen saturation through a range of optical source-detector separation.

This chapter also finds the effect of pulsatility on the monolayer model and generates a plot resembling the typical calibration curve for a pulse oximeter.

- **Chapter 9:** This chapter executes the Monte Carlo model for estimating the light-tissue interaction in a volume of multilayer finger tissue. Different variables are studied in controlled environments. Comparative studies between the reflectance and transmittance modes are also explored.
- **Chapter 10:** This chapter explores the Monte Carlo model to find the DPF in the monolayer perfused dermis model and the multilayer model of the human forearm. The comparative values of DPFs in red and infrared wavelengths are plotted and tabulated for shorter and longer source-detector separations. The measured DPF values are applied to calculate the concentration-change of oxy and deoxy-haemoglobin from the experimentally obtained PPG signals. The cross-talk and absolute errors were assessed from between the simulated and approximated DPFs.
- **Chapter 11:** This chapter discusses the overall features of the models, results from the entire thesis, and provides recommendations for future works.

BACKGROUND PHYSIOLOGY

2.1 Introduction

Oxygen is required by tissue for its survival. Inadequate oxygen supply to cells leads to poor metabolism, and eventually cell death. In the human body, the oxygen is received, transported and released by the respiratory system. The carrier of oxygen is blood which circulates through the body as a part of the circulatory system. In the framework of this thesis, it is important to build an understanding of the physiological processes, namely cardiac cycle, oxygen saturation, gas exchange etc. This chapter, therefore, introduces the basic human physiology of blood circulation and gaseous transport which are parts of the circulatory and respiratory systems.

2.2 Circulatory system

The part of the circulatory system that carries oxygenated blood from the heart to the body parts and deoxygenated blood from the organs to the heart is known as systemic circulation. On the other hand, the part of the circulatory system that carries deoxygenated blood from heart to lungs and oxygenated blood from lungs to heart is called pulmonary circulation [Tortora and Derrickson, 2008]. The driving organ of this system is the Heart and the medium of transport is the Blood. Other main parts of the system

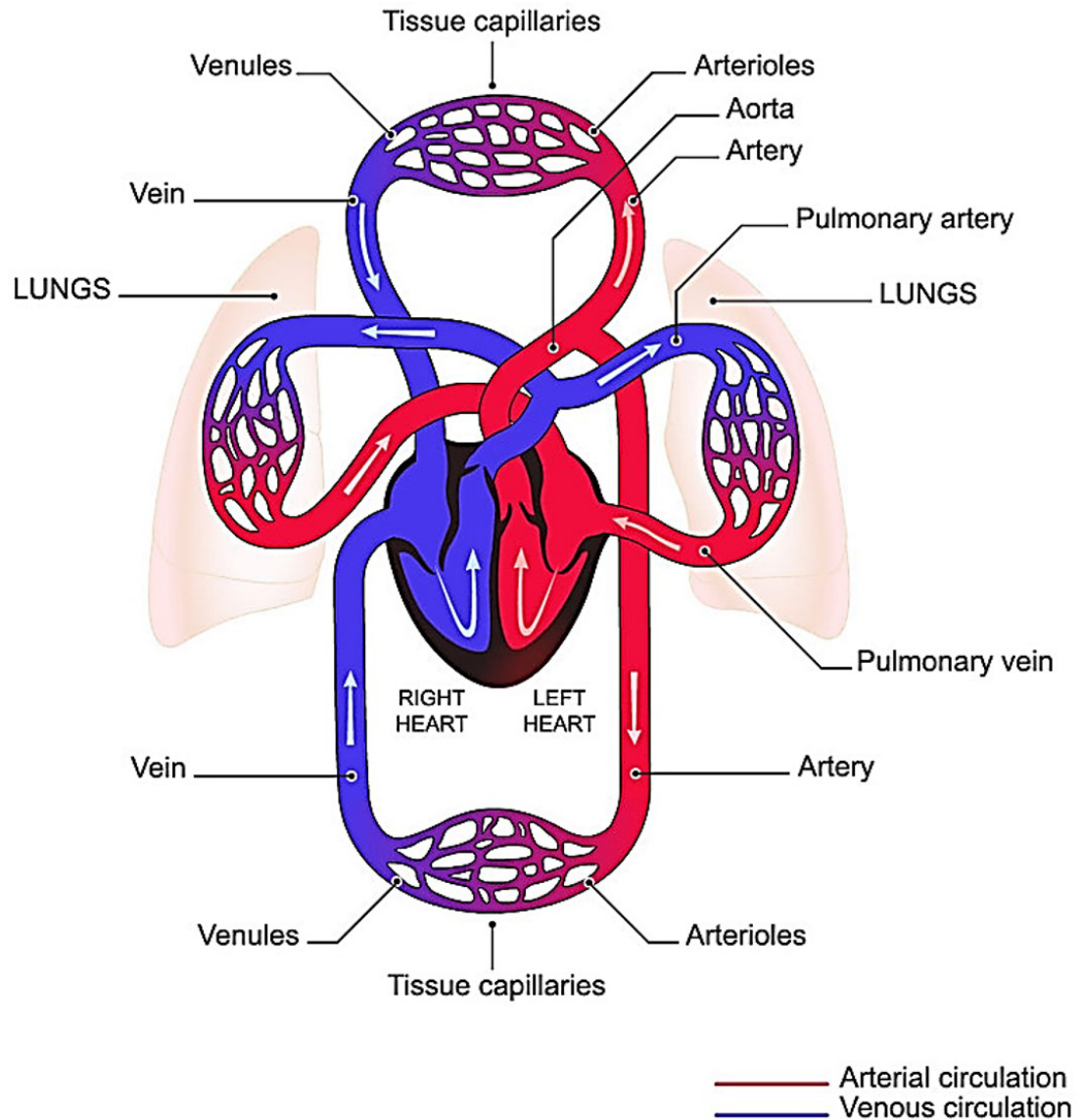


Figure 2.1: Schematic of the human circulatory system [Williams *et al.*, 1989]

include Arteries, Arterioles, Capillaries, Venules, and Veins. A schematic of the circulatory system is presented in Figure 2.1. The arterial circulation carries blood with Oxygen (O_2) from heart to the upper (head and neck) and lower (rest of the body) parts of the body, and the venous circulation carries the blood with carbon dioxide (CO_2) from different corners of the body to the heart. The pulmonary vein and artery connect the circulatory system to the Lungs for the pulmonary circulation, which is also a part of the Respiratory system.

2.2.1 Heart

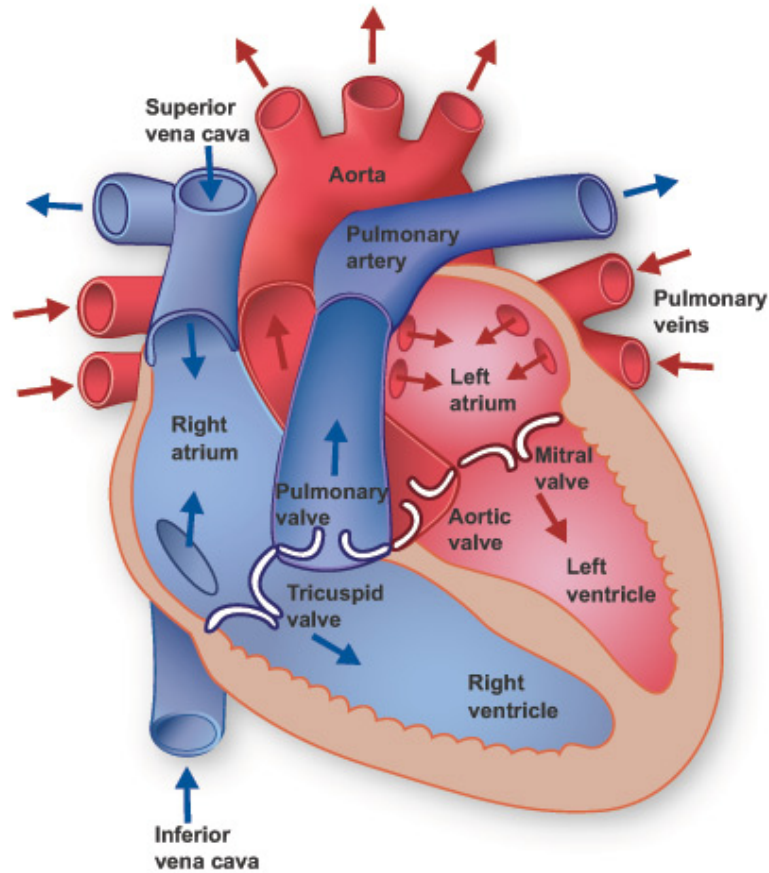


Figure 2.2: An anatomical view of the Human Heart [Williams *et al.*, 1989]

The heart is the main organ of the Systemic circulation [Tortora and Derrickson, 2008]. A muscle wall, known as the septum, divides the heart into left and right parts, each of which again is divided into two chambers. The upper and lower chambers of each part of the heart are known as the atrium and ventricle, respectively. The right atrium receives deoxygenated blood returning from the whole body through superior and inferior vena cava, and the right ventricle pumps out that blood to lungs via pulmonary arteries. The left atrium receives the oxygenated blood returning from the lungs through pulmonary veins and the left ventricle then pumps this blood around the body through the aorta. There are four valves (namely, two semilunar (SL) valves and two atrioventricular (AV) valves) in the heart that control the flow of blood coming in and going out from the heart. All these four valves open in only one direction, preventing any backward flow of blood. The sound of the heartbeat, often known as ‘lub-dub’ sound, is originated from

the movements of these heart valves. The AV valves allow blood to move from atria to ventricles, right after which those snap shut, causing the first heart sound or 'lub'. The second heart sound or 'dub' is generated when the SL valves shut following the blood flow from the ventricles to the arteries. The anatomical features of the heart chambers, valves, arteries and veins are presented in Figure 2.2.

A cardiac cycle consists of a series of 'Systole' and 'Diastole' conditions of the heart, which are caused due to the contraction and relaxation of the cardiac muscles. The entire process is repeated through the cycles of atrial diastole, atrial systole, ventricular systole and ventricular diastole.

2.2.2 Arteries, Veins and Capillaries

Arteries carry blood away from the heart and veins carry blood back to the heart, only except pulmonary circulation, where the reverse case happens. An artery, when it reaches an organ, branches out into narrower arterioles, which branch into even narrower capillaries. The exchanges of food substances, gases etc. take place in capillaries. The capillaries then combine into venules, which further combine and connect to veins.

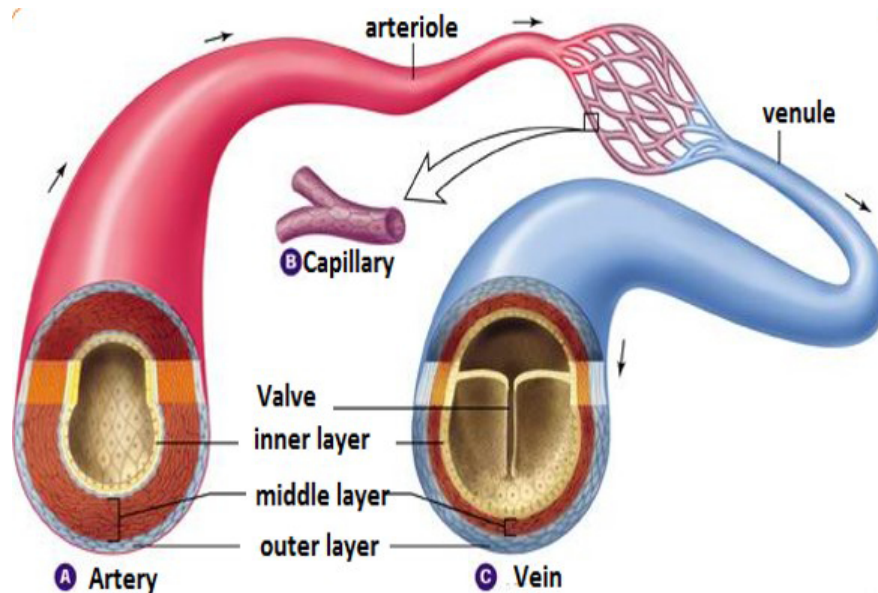


Figure 2.3: The anatomy of Artery (A), Capillary (B), and Vein (C) [Williams *et al.*, 1989]

Arteries and arterioles have thicker walls than veins and venules because they are closer to the heart and receive blood that is surging at a far greater pressure [Tortora

and Derrickson, 2008]. By the time blood has passed through capillaries and entered venules, the pressure initially exerted upon it by heart contractions has diminished. The venule and vein walls are considerably thinner allowing more blood to flow with less vessel resistance [Tortora and Derrickson, 2008]. Capillary is the junction where the arterial and venous circulations meet. The capillaries supply blood to the corresponding organ and tissues and help in 'tissue perfusion'. Exchange of gases and other substances occurs in the capillaries between the blood and the surrounding cells and their tissue fluid. The diameter of a capillary is much smaller than those of arterioles and venules. Blood flow through capillaries is often described as 'microcirculation' [Williams *et al.*, 1989]. The muscle fibre present in the vessels, especially in arteries, contracts and dilates periodically, which are commonly known as 'vasocontraction' and 'vasodilation'. These two phenomena result in changes in the pressure in the vessel, and thus control the blood flow.

2.2.3 Blood

Blood accounts for 7% of the total human bodyweight [Elert, 2014]. The average adult blood volume is roughly 5 litres. The mean temperature of blood is 38 ° C and pH is 7.35-7.45. Blood consists of several types of cells (i.e, Erythrocytes, Leukocytes and Thrombocytes) and liquid Plasma.

Normal blood plasma contains 90-92% of water. Plasma consists of dissolved substances including electrolytes (e.g. sodium, chlorine, potassium, manganese, and calcium ions); blood plasma proteins (e.g. albumin, globulin, fibrinogen); and Hormones. The cellular structures of blood are embedded in the plasma.

The Erythrocytes, also known as Red Blood Cells (RBC), are one of the main components of blood, which are as numerous as 4.7 – 6.1 million for male and 4.2 – 5.4 million for female per μL of blood, making up about 25% of the total cells in the body. Erythrocytes contain Haemoglobins and take the most essential part in transport of gases all around the body.

The Leukocyte, commonly known as White Blood Cell (WBC), is a major component of the body 's immunity system. Leukocytes are less numerous than erythrocytes: typically 5000 to 10,000 per μL of blood. The main function of leukocytes is to protect the body

against invading micro-organisms and body cells with mutated DNA, and cleaning up the debris.

The Thrombocyte, also known as Platelet is an important component of blood that helps blood to clot. Platelets are typically 150,000 – 160,000 in number per μL of blood. Platelets are mainly responsible for Hemostasis, i.e., the process by which the body seals a ruptured blood vessel and prevents further loss of blood.

2.2.4 Transport of Oxygen

A small amount of oxygen (about 1.5% of the total blood) is dissolved in the blood plasma and transported. The major part of the gases form chemical bonding with blood constituent and transported as some compounds.

Oxygen transport relies mainly on erythrocytes. Erythrocyte contains Haemoglobin (Hb). Haem is the portion of haemoglobin that contains iron and is capable of binding oxygen. Each Hb molecule contains four subunits, allowing maximum four oxygen molecules to bind with [Williams *et al.*, 1989]. The following reversible reaction between Hb and O_2 forms the final product, Oxyhaemoglobin (HbO_2):



Binding of the first oxygen molecule causes a conformational change in haemoglobin that allows the second molecule of oxygen to bind more readily. As each molecule of oxygen is bound, it further facilitates the binding of the next molecule, until all four haem sites are occupied by oxygen [Tortora and Derrickson, 2008]. The haemoglobin becomes saturated when all four oxygen molecules are attached. Thus, considering whole blood, haemoglobin saturation refers to the percentage of the haem that is bound with oxygen at that instant, which is 95-99% for a normal adult human [Williams *et al.*, 1989].

2.2.5 Oxyhaemoglobin dissociation curve

An important aspect of the binding of oxygen to and disassociating from haem is the partial pressure. In a gas mixture, the pressure exerted by an individual gas is known as the partial pressure of that gas. Gases have the tendency to diffuse from an area of higher partial pressure to an area of lower partial pressure.

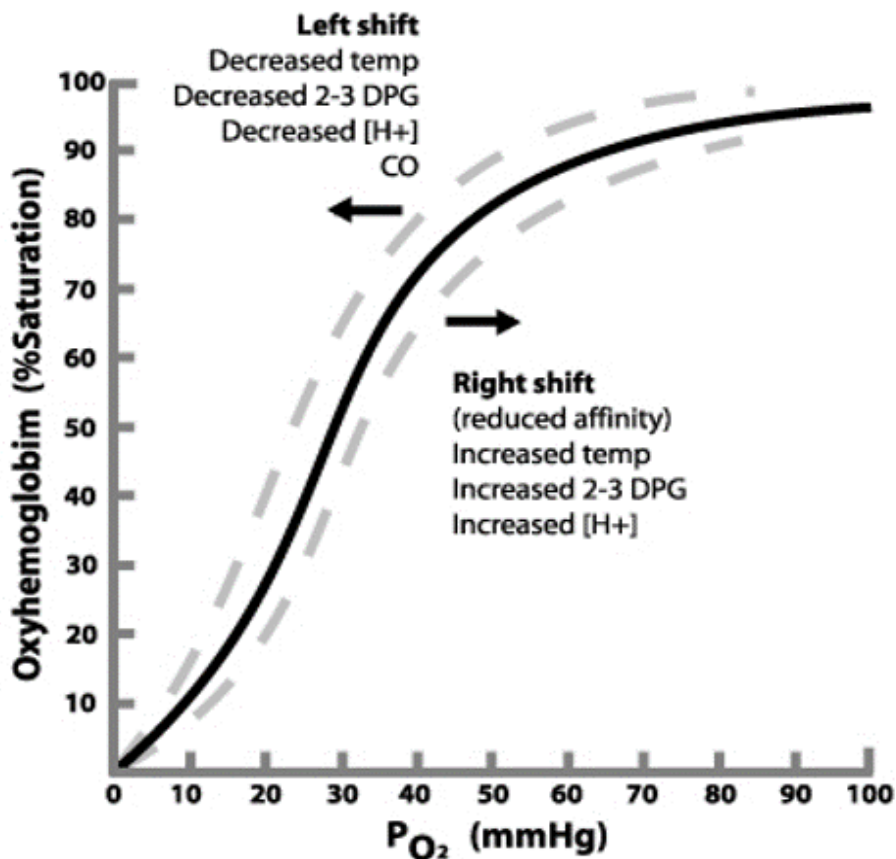


Figure 2.4: Oxygen - Haemoglobin dissociation curve [Moyle, 2002]

The relationship between the partial pressure of oxygen P_{O_2} and the ability how readily oxygen binds to or dissociates from haemoglobin is represented by the oxygen-haemoglobin dissociation curve. The curve possesses a sigmoid shape, as shown in Figure 2.4. It describes the nature of the interaction between the haemoglobin and oxygen. Haemoglobin's affinity to bind oxygen increases gradually with the gradual increase of the partial pressure of oxygen, until it reaches a maximum value, typically 60 mmHg. After this point, oxygen saturation very slightly increases despite a rapid increase in partial pressure. Then it appears as the haemoglobin is saturated with oxygen. Beyond this point, an urgent requirement of increased oxygenation for a patient would need either external blood supply (blood transfusion) for increasing the haemoglobin count or supplemental oxygen supply for dissolving in the blood plasma.

The partial pressure of oxygen in the blood at which the haemoglobin is 50% saturated is typically about 26.6 mmHg for a healthy person. This point is known as the P_{50} . The

P_{50} is a conventional measure of haemoglobin affinity for oxygen. In abnormal conditions, the haemoglobin's oxygen affinity is altered resulting in shifting the curve to the right or left, and alteration in the P_{50} value. An increased P_{50} indicates a right shift of the standard curve, which means that a larger partial pressure is necessary to maintain a 50% oxygen saturation. This indicates a decreased affinity. Conversely, a lower P_{50} indicates a left shift and a higher affinity. The right or left shift of the curve depend on several factors, such as blood pH, temperature, presence of hydrogen ion due to presence of carbon dioxide or other acidic byproducts (which influences the pH of blood), presence of the byproduct called 2,3-diphosphoglyceric acid (2,3-DPG) etc., as illustrated in Figure 2.4 [Tortora and Derrickson, 2008]. This shift is known Bohr shift. In this context, the physiological significance of the Bohr effect should be discussed. The Bohr effect enables the body to adapt to changing conditions and makes it possible to supply extra oxygen to tissues that need it the most. For example, when muscles are undergoing strenuous activity, they require large amounts of oxygen to conduct cellular respiration, which generates CO_2 (and therefore HCO_3^- and H^+) as byproducts. These waste products lower the pH of the blood, which increases oxygen delivery to the active muscles. Carbon dioxide is not the only molecule that can trigger the Bohr effect. If muscle cells are not receiving enough oxygen for cellular respiration, they resort to lactic acid fermentation, which releases lactic acid as a byproduct. This increases the acidity of the blood far more than CO_2 alone, which reflects the cells' even greater need for oxygen. In fact, under anaerobic conditions, muscles generate lactic acid so quickly that pH of the blood passing through the muscles will drop to around 7.2, which causes haemoglobin to begin releasing roughly 10% more oxygen.

2.2.6 Transport of Carbon dioxide

A certain fraction of carbon dioxide (7-10%) dissolves in the blood plasma and gets transported. Most of the carbon dioxide is transported to the lungs as bicarbonate. Carbonic anhydrase (CA) causes carbon dioxide and water to form carbonic acid (H_2CO_3), which dissociates into two ions: bicarbonate (HCO_3^-) and hydrogen (H^+). The following formula

depicts this reaction:



Bicarbonate tends to build up in the erythrocytes so that there is a greater concentration of bicarbonate in the erythrocytes than in the surrounding blood plasma. Some of the bicarbonates leave the erythrocytes and move down its concentration gradient into the plasma in exchange for chloride (Cl^-) ions, a phenomenon known as the chloride shift.

About 20% of carbon dioxide is bound with haemoglobin and is transported to the lungs. Carbon dioxide does not bind to iron as oxygen does; instead, carbon dioxide binds amino acid on the globin portions of haemoglobin to form carbaminohaemoglobin following the equation below:



When haemoglobin is not transporting oxygen, it tends to have a bluish-purple tone to it, creating the darker maroon colour typical of deoxygenated blood. Similar to oxygen transport, carbon dioxide transport also is governed by the partial pressure of the gas. Since CO_2 is released in lungs, blood transported from lungs to the tissues contain lower P_{CO_2} , resulting in diffusion of CO_2 in the tissue capillaries to the bloodstream. This is then brought to lungs alveoli where blood with higher P_{CO_2} releases the gas. In addition to P_{CO_2} , the oxygen saturation and P_{O_2} in the blood also influence the affinity of haemoglobin for carbon dioxide. When oxygen is not bound to haem, and also the P_{CO_2} is low, then only haemoglobin readily binds to carbon dioxide [OpenStax, 2013].

2.2.7 Oxygen Saturation of Blood

Oxygen saturation of blood is an expression of the amount of oxygen carried by the blood. Arterial blood oxygen saturation (SaO_2) is measured as the ratio of oxygenated haemoglobin to the total haemoglobin present in the arterial blood [Moyle, 2002], that can be written in a percentage form as:

$$SaO_2 = \frac{[HbO_2]}{[Hb] + [HbO_2]} \times 100\% \quad (2.4)$$

where $[Hb]$ and $[HbO_2]$ are the concentrations of deoxyhaemoglobin and oxyhaemoglobin respectively. Arterial blood oxygen saturation measured by Pulse Oximeters (PO) is known

as SpO_2 . PO specifically measures the peripheral blood oxygen saturation. Although SpO_2 is not exactly the same as to SaO_2 , the two have been shown to correlate well [Moyle, 2002; Volgyesi *et al.*, 1990]. PO is used for the continuous non-invasive monitoring of SaO_2 , whereas for a more specific measurement, Arterial Blood Gas (ABG) analysis is performed on the blood sample collected from the artery through invasive procedure. An arterial oxygen saturation $SaO_2 = 95 - 100\%$ is considered to be a normal value, and $SaO_2 < 90\%$ is considered low. Low blood oxygen saturation reading indicates the inadequacy of oxygen in the blood (hypoxaemia) which results in shortness of breath, an increased rate of breathing and pursed lip breathing. A serious hypoxaemia leads to respiratory failure [Colledge *et al.*, 2010].

Measurement of oxygen saturation from venous blood (SvO_2) also offers clinical importance, reflecting the average amount of oxygen remaining in the blood after all tissues in the body have removed oxygen from the haemoglobin [Ladakis *et al.*, 2001]. Mixed venous oxygen saturation is measured from a true mixed venous blood sample drawn from the tip of the pulmonary artery catheter, which includes all of the venous blood returning from the head and arms (via superior vena cava), the gut and lower extremities (via the inferior vena cava) and the coronary veins (via the coronary sinus). However, the use of a pulmonary catheter has been declined in medical practice due to potential risk factors associated with it. Thus as an alternative, the venous oxygen saturation is derived in a less invasive manner from the blood drawn from the internal jugular or subclavian catheters (central line) and known as central venous oxygen saturation, which is found to closely correlate to the mixed venous oxygen saturation [Ladakis *et al.*, 2001]. The normal value of SvO_2 of mixed blood is around 70%, however that measured from peripheral blood is found to be slightly higher [Nitzan and Taitelbaum, 2008]. The values of SvO_2 are found to be about 10% lower than SaO_2 [Nitzan *et al.*, 2000].

Total tissue oxygen saturation (StO_2) is also measured sometimes which gives an idea of the oxygenation of tissue in different conditions, and Near Infrared Spectroscopy method is normally used for StO_2 monitoring, especially from muscle and brain [Nitzan and Taitelbaum, 2008; Scheeren *et al.*, 2012; Epstein and Haghenbeck, 2014].

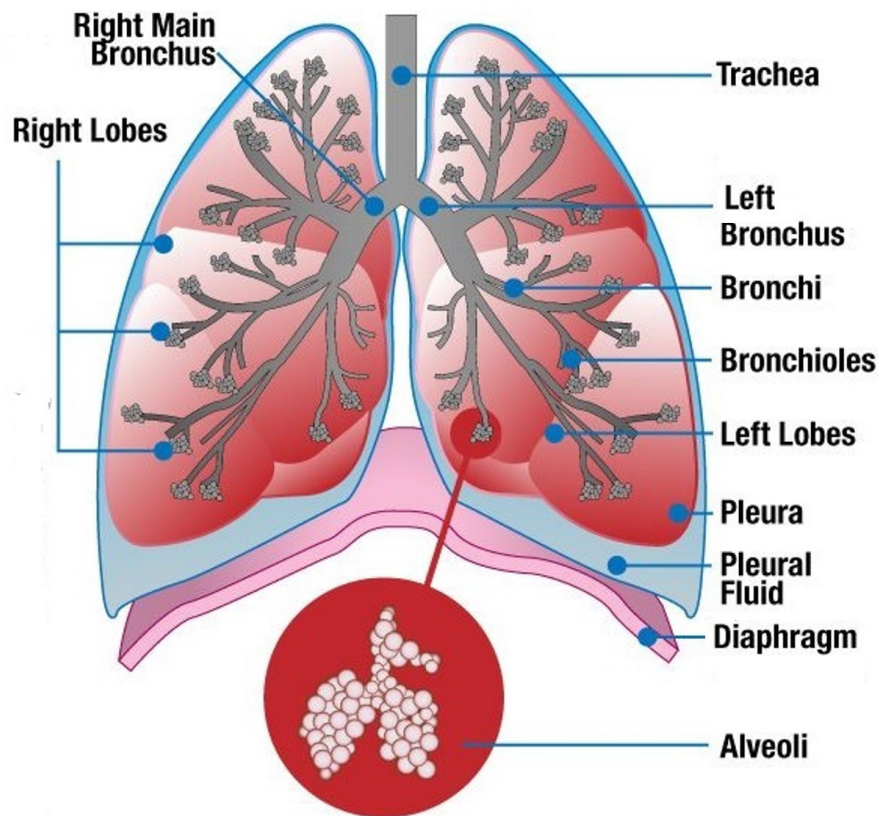


Figure 2.5: The Respiratory structure in human body [Scanlon and Sanders, 2014]

2.3 Respiratory system

Respiratory system comprises specific organs and structures responsible for inhaling oxygen and expelling carbon dioxide from the human body. A schematic of the human respiratory system is presented in Figure 2.5. The oxygen-rich air is carried to the lungs and carbon dioxide is carried out from the lungs through the airways. The airways include nose and linked air passages (nasal cavities), mouth, larynx (voice box), trachea (windpipe), bronchial tubes or bronchi, and their branches [Tortora and Derrickson, 2008]. The lungs lie on either side of the breastbone, within the chest cavity of the human body. Pleura is the cavity that attaches the lungs with the thoracic cavity which normally contains a little amount of fluid. The lungs are divided into five main sections called lobes. Within the lungs, the bronchi branch into thousands of smaller, thinner tubes called bronchioles. These tubes end in bunches of tiny round air sacs called alveoli. Each of these air sacs is covered with capillaries that connect with the circulatory system of the body. Diaphragm is the membrane that separates lungs and thorax from the abdominal cavity

[Tortora and Derrickson, 2008].

The pulmonary artery and its branches deliver blood rich in carbon dioxide, and lacking in oxygen, to the capillaries that surround the alveoli. The alveolar walls are extremely thin (about $0.2 \mu\text{m}$). These walls are composed of single layers of tissues called epithelial cells, which are very thin and take part in gas exchange.

2.3.1 Exchange of gases

The exchange of gases (oxygen and carbon dioxide) depends on the mechanism of diffusion. In the current context, diffusion refers to the process of movement of gases from a higher to a lower concentration area. This process does not require any energy. Instead, it depends on the partial pressure gradient. The exchange takes place at two sites in the body: in the alveoli of the lungs, where oxygen is picked up and carbon dioxide is released at the respiratory membrane (external exchange), and at the capillary beds of the tissues, where oxygen is released and carbon dioxide is picked up (internal exchange). In the alveolar air, P_{O_2} is about 100 mm Hg, whereas in the pulmonary capillary blood P_{O_2} is 40 mm Hg, causing a strong pressure gradient resulting in oxygen to diffuse through the respiratory membrane to the pulmonary capillary blood. On the other hand, P_{CO_2} in the pulmonary capillary blood is about 46 mm Hg, whereas that in the alveolar air is 40 mm Hg, causing a release of CO_2 . Therefore, the blood coming out from the lungs is rich in oxygen and lack carbon dioxide. In the tissue capillaries, where P_{O_2} and P_{CO_2} are respectively 40 mm Hg and 46 mm Hg, the created pressure gradient causes oxygen to dissociate from haemoglobin, diffuse out of the blood, cross the interstitial space, and enter the tissue. In a reverse manner, carbon dioxide released into the tissues diffuse into the blood and is carried to the heart and lungs again.

2.4 Summary

The basic principles of physiology and anatomy in relevance to the present thesis have been demonstrated in this chapter. The physiological processes such as perfusion, oxygen saturation, transport and exchange of gases, cardiac cycle etc. have been introduced in this chapter, which is crucial for understanding the in-depth studies presented later in the

thesis. The physiological process of oxygen affinity of haemoglobin has been introduced in this chapter. The biochemical processes taking place during the transport of oxygen and carbon di-oxide has been described and the the Bohr shift in the oxygen dissociation curve in relationship with the gaseous transport have been described. The definitions and descriptions demonstrated in this chapter, therefore, set the necessary background for the following chapters, where the light-tissue interactions in Photoplethysmography and Pulse Oximetry will be discussed.

BASICS OF TISSUE OPTICS

3.1 Introduction

The interactions between light and the medium it is propagating through largely depend on the two main factors: *homogeneity* and *isotropy* of the medium. Homogeneity and isotropy refer to the spatial change and the angular symmetry of the optical properties in the medium, respectively [Jacques and Prahl, 2007]. Biological tissue, due to its complex non-uniform architecture, exhibits high levels of inhomogeneity and anisotropy. In order to model the propagation of light through a complex biological tissue medium, it is important to understand all the physical processes behind it. The main mechanisms of interaction between light and biological tissues are ‘scattering’ and ‘absorption’. Also, in a finite medium, when light interacts with the boundary, there are the events of ‘reflection and refraction’. The present chapter is dedicated to the theories and concepts behind modelling the migration of photons through a biological tissue medium [Wang and Tuchin, 2013; Tuchin, 2007; Prasad, 2004].

3.2 Mechanism of light propagation through tissue

3.2.1 Scattering

The scattering of light may be defined as the redirection of light that takes place when an incident light ray encounters an obstacle, or in this case, the scattering particle. Depending on the size of the scatterer relative to the optical wavelength, the scattering is divided into two main categories, namely, Rayleigh scattering and Mie scattering [Bohren and Huffman, 2008]. When the radius of the scattering particle is much smaller than the wavelength of the incident light, Rayleigh scattering occurs. When the dimension of the scattering particle is bigger than or in the order of the incident radiation, Mie scattering dominates. When a photon interacts with a particle, it may undergo the ‘elastic’ type of scattering where the direction of scattered photons change but no change in energy takes place between the exciting photon and scattered photon. There is also a form of *inelastic scattering* where the light is scattered with an energy different from the incident radiation, for example, Raman scattering. For a simpler understanding on the general scattering theory, the *elastic* scattering type will be discussed in this chapter where the energy remains constant and no particle is annihilated or created.

Figure 3.1 represents a typical scattering interaction where a photon redirects from its initial direction \mathbf{s} to a new direction \mathbf{s}' through a zenith angle θ and an azimuth ϕ respectively, as shown in Figure 3.1. Generally, all new possible directions do not occur with equal probability, but depend on the type of the scatterer and the possible structure of the scattering medium [Bohren and Huffman, 2008]. The change in direction due to scattering, in general, shows a distinct distribution. The distribution, which represents the likelihood that a photon with an initial direction \mathbf{s} will be scattered into a direction \mathbf{s}' , is expressed by the factor ‘differential scattering cross-section’ ($\frac{dC_s}{d\Omega}$) where $d\Omega$ is the differential solid angle, i.e., $d\Omega = \sin\theta d\theta d\phi$.

The ability of the particle to scatter light in all directions is expressed as an effective surface area and called *total scattering cross-section*, C_s which is obtained by integrating the differential cross-section over all angles [Träger, 2012]:

$$C_s = \int_{4\pi} \frac{dC_s}{d\Omega} d\Omega \quad (3.1)$$

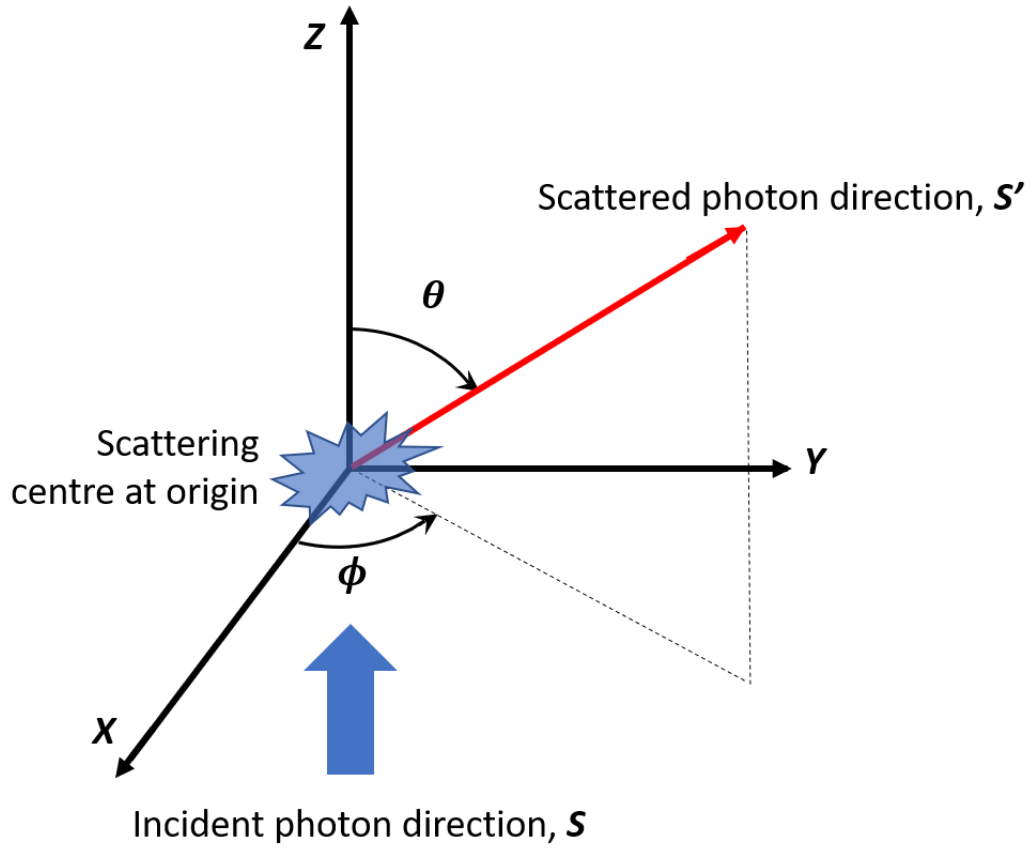


Figure 3.1: A typical scattering event of a photon in a conventional 3-D Cartesian coordinate system is shown. The photon is incident from a direction \mathbf{S} along z-axis (shown by the blue solid arrow) and interacts with the scatterer positioned at the origin, i.e., scattering centre (shown by blue shaded region). The interaction results in a deviation of from the initial direction to a new direction \mathbf{S}' (shown by red line) through a zenith angle θ and an azimuth ϕ .

The *scattering coefficient* μ_s for a scattering medium with particle density ρ is defined as the product of the scattering cross-section and the density of the scatterers:

$$\mu_s = \rho \cdot C_s \quad (3.2)$$

This is the likelihood that the photon will be scattered while travelling through the medium.

The probability that a photon propagating through a medium with a scattering coefficient μ_s does not scatter over a distance x is equal to $e^{-\mu_s x}$. Therefore, the probability that the photon scatters between the distances l' and $l' + dl'$ is:

$$p(l') = \mu_s e^{-\mu_s l'} dl'. \quad (3.3)$$

This leads to the following expression for the average scattering length l for light through the medium with a scattering coefficient μ_s :

$$\begin{aligned} l &= \int_{l'=0}^{\infty} l' \mu_s e^{-\mu_s l'} dl' \\ &= \frac{1}{\mu_s} \end{aligned} \quad (3.4)$$

Therefore, the scattering coefficient of a medium is the inverse of the free path length (i.e., the distance between two scattering interactions) of the photon travelling through the medium, and is expressed in the unit of $length^{-1}$.

3.2.1.1 Phase function and Scattering anisotropy

The cumulative effect of all scattering events throughout the entire volume of the medium results in a scattering profile. The scattering profile is a representation of all possible angles of scattering and the likelihood of each scattering direction. This profile is known as the ‘Scattering phase function’. The name ‘phase function’ does not have any correlation with the phase of the electromagnetic wave [Splinter and Hooper, 2006].

The phase function $p(s, s')$ (expressed in sr^{-1}) represents the probability of a photon to redirect from the incident direction \mathbf{s} to the scattered direction \mathbf{s}' [Bohren and Huffman, 2008; Tuchin, 2007]. Generally, phase functions are different for different scatterers. For light propagation in medium, an average phase function is often considered. Usually, the average phase function assumes that the scattering event is symmetric about the direction of the incident light, i.e., to z-direction (Fig. 3.1). Therefore, the phase function is independent of ϕ and a function of the scattering angle θ only. The scattering angle ranges from 0° to 180° , with $\theta = 0^\circ$ and $\theta = 180^\circ$ corresponding to the forward and backward scattering, respectively. The assumption of the scattering symmetry about the angle ϕ leads to the identity:

$$p(s, s') \equiv p(\theta). \quad (3.5)$$

It should be noted that $\cos(\theta)$ has a one-to-one relationship with the angle θ within the range $[0^\circ, 180^\circ]$. So the average phase function can also be expressed as a function of $\cos(\theta)$, i.e., $p(\cos(\theta))$, which additionally implies that each interaction takes place in same plane during light-tissue interaction [Splinter and Hooper, 2006].

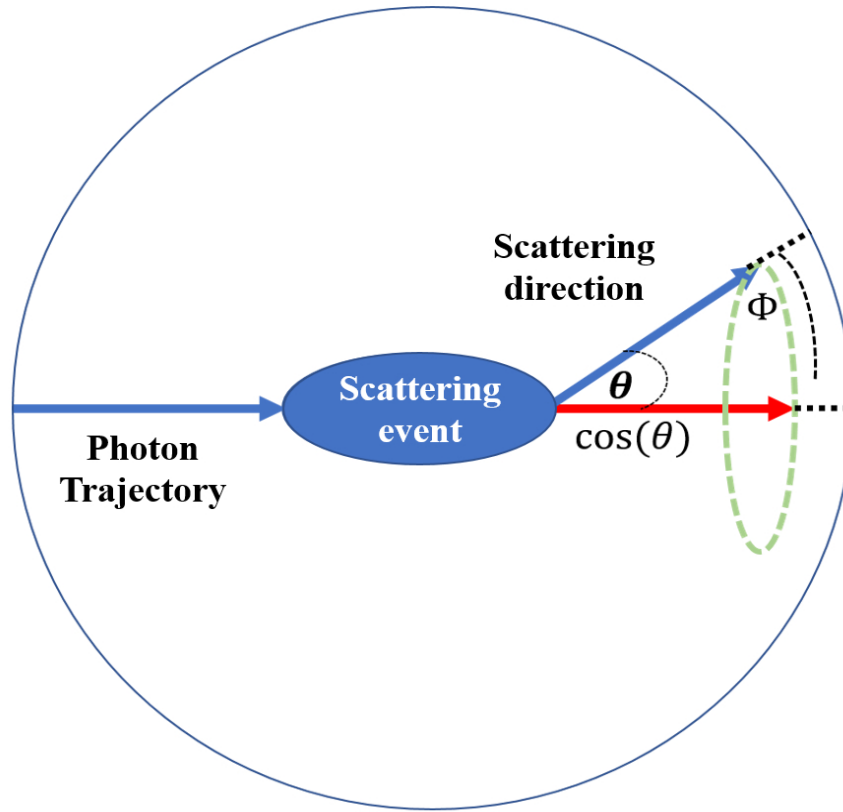


Figure 3.2: A demonstration of the anisotropy factor is presented. Scattering event causes a photon angle to deviate at any scattering angle θ and azimuth ϕ . The mean of cosine of the scattering angles produce the net scattered amount in the forward direction.

Phase function is a probability distribution, thus the condition of normalisation will require that the integral of the phase function over all angles equals to unity:

$$\int_0^{4\pi} p(s, s') d\Omega = 1 \quad (3.6)$$

Comparing the above equation with Eq. 3.2, the differential scattering cross-section in its normalised form can be replaced by the scattering phase function.

An isotropic phase function can be expressed from the above equation as:

$$p(s, s') = \frac{1}{4\pi} \quad (3.7)$$

which entails that scattering in every 4π solid angle has equal probability, and is referred to the isotropic scattering.

In the complex medium such as biological tissue, introduction of potentially different probabilities for scattering over the various quadrants of space is required. The anisotropic

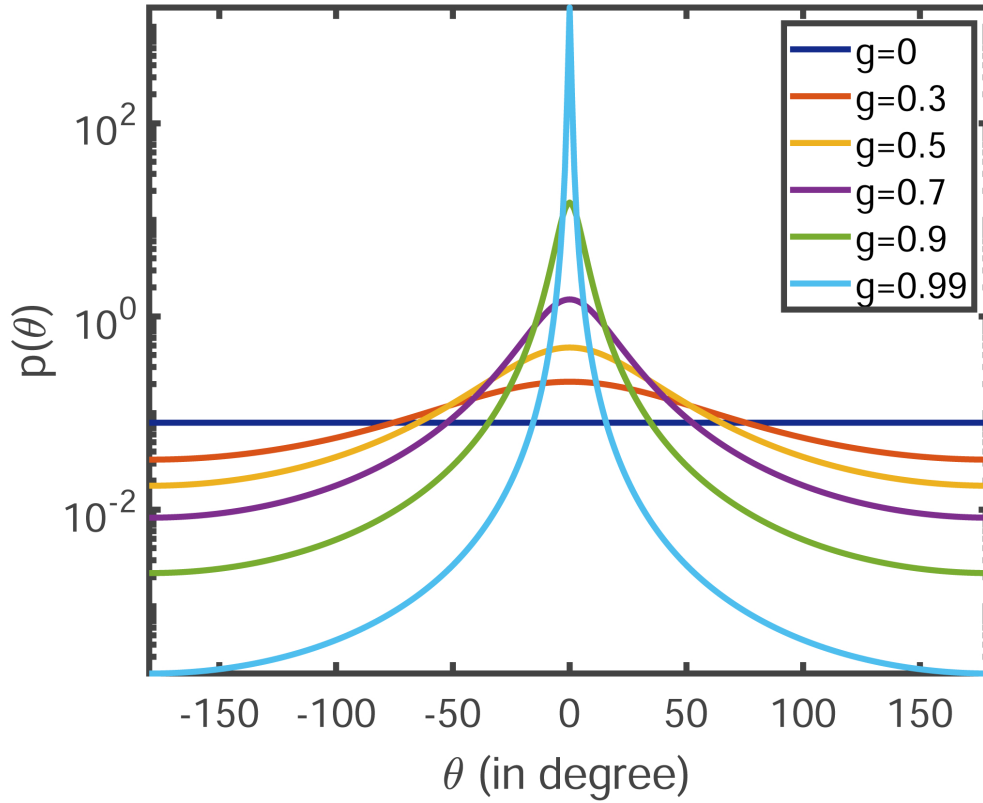


Figure 3.3: The relationship of the Henyey-Greenstein phase function $p(\theta)$ with the scattering angle θ for different anisotropy factor (with $g=0,0.3,0.5,0.7,0.9$ and 0.99) is presented. For $g = 0$, i.e., for isotropic scattering the phase function is a straight line, and for higher values of g it tends toward a sharp peak at the scattering angle 0° .

behaviour of the scattering angle relative to the incident direction is best characterised by the Henyey-Greenstein (HG) phase function [Henyey and Greenstein, 1941]. This phase function was originally derived to explain the scattering phenomena in interstellar gas clouds, and has been successfully implemented for explaining the scattering of light in tissue [Splinter and Hooper, 2006; Calabro and Bigio, 2014]. The mathematical expression for HG phase function in its three-dimensional form is given by:

$$p_{HG}(\theta) = \frac{1}{4\pi} \frac{1 - g^2}{(1 - 2g \cos(\theta) + g^2)^{3/2}} \quad (3.8)$$

where g is known as the anisotropy factor [Bohren and Huffman, 2008; Henyey and Greenstein, 1941; Tuchin, 2007]. g is a dimensionless quantity, expressed as the average cosines of the scattering angles, i.e., the component along the forward scattering direction: $g = \langle \cos(\theta) \rangle$. In common practice, HG phase function is described as the probability of

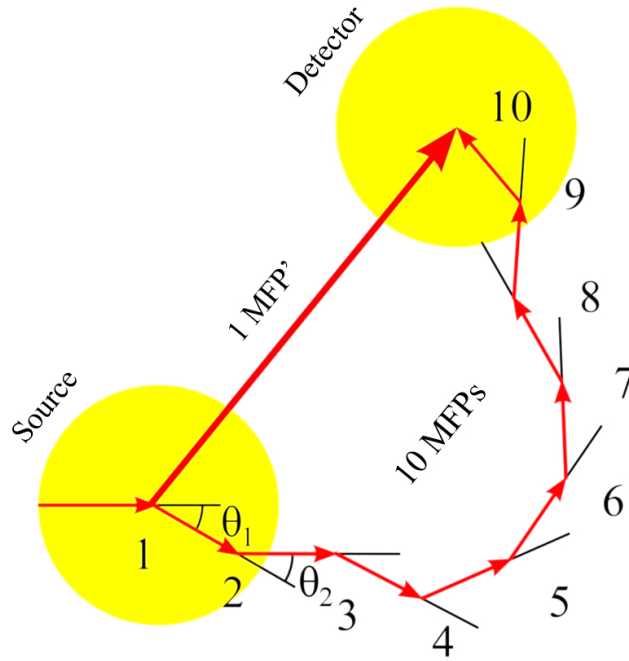


Figure 3.4: An example of the typical relationship between the mean free path (MFP) and reduced mean free path (MFP') from a source to a detector that are marked yellow is shown [Tuchin, 1993]. In this case, one MFP' is equivalent to ten MFPs, creating random small deflection angles $\theta_1, \theta_2, \dots, \theta_{10}$. The free pathlengths between two consecutive photon interactions are random and not equal.

$\cos\theta$:

$$p_{HG}(\cos(\theta)) = \frac{1}{2} \frac{1 - g^2}{(1 - 2g \cos(\theta) + g^2)^{3/2}} \quad (3.9)$$

The physical explanation of the anisotropy factor is illustrated in Figure 3.2. All photons deviated through any scattering angle θ will have components along the forward direction, i.e., $\cos(\theta)$. Therefore, the average of these components gives the measure of net scattering in the forward direction. The value of g varies in the range from -1 to 1 ; $g = 0$ corresponds to isotropic (Rayleigh) scattering, $g = 1$ to total forward scattering (Mie scattering at large particles), and $g = -1$ to total backward scattering. In tissue medium, the value of g is close to 1 which implies that forward scattering dominates there. Consequently, the mean scattering angle $\cos^{-1} g$ is very small, i.e., small angles of scattering is favoured in tissue medium. The relationship between the phase function and the anisotropy factor g is given in Figure 3.3.

The reduced scattering coefficient is a lumped property incorporating the scattering coefficient μ_s and the anisotropy g :

$$\mu'_s = \mu_s(1 - g). \quad (3.10)$$

The purpose of μ'_s is to describe the diffusion of photons in a random walk of step size of $1/\mu'_s$ where each step involves isotropic scattering. Such a description is equivalent to describing the photon movement using many small steps $1/\mu_s$ that each involves only a partial deflection angle θ if there are many scattering events before an absorption event. This situation of scattering-dominated light transport is called the diffusion regime.

Figure 3.4 shows the equivalence of taking ten smaller steps of mean free path ($MFP = \frac{1}{\mu_s}$) with anisotropic deflection angles, and one big step with a reduced mean free path ($MFP' = \frac{1}{\mu'_s}$).

3.2.2 Absorption

In general, absorption quantifies the conversion of light energy into other forms of energy. A molecule, when interacts with a photon, might rise to an excited state. There is a number of mechanisms which it might follow to come back to the lower ground state. It might lead to fluorescence or phosphorescence where the excited molecules decay back to the ground state by emitting light of higher wavelength than the exciting light, with a delay governing by the life time of the system. However, in most cases the molecule returns to its ground state via a radiation-less decay and the absorbed energy gets converted into thermal energy through inter-molecular de-excitation processes like molecular vibrations and rotations, and extra-molecular de-excitation processes like collisions and general molecular motion [Splinter and Hooper, 2006]. There are several expressions to quantify the absorption of light, namely, extinction coefficient, absorption coefficient, molar attenuation coefficient etc. These expressions are not quantitatively similar to each other and have different applications. The coefficients of absorbance is discussed in details later in this chapter (in the Section 3.4).

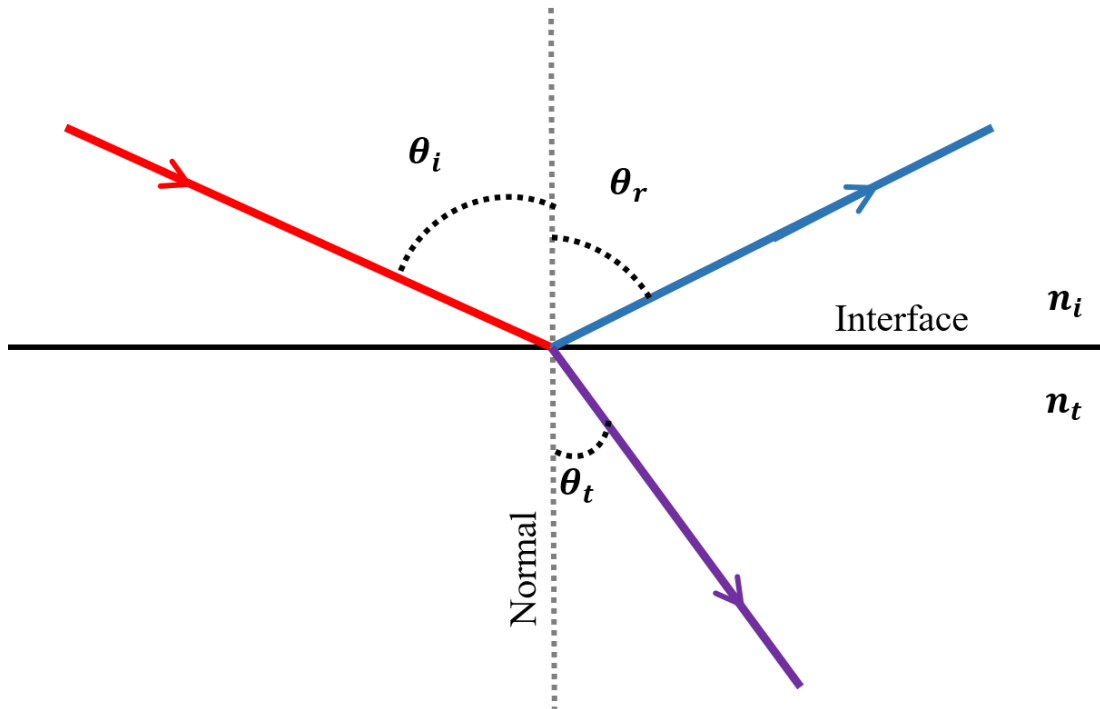


Figure 3.5: A schematic diagram of reflection and refraction is presented. Red, blue and violet lines are respectively the incident, reflected and refracted beam directions. $\theta_i, \theta_r, \theta_t$ are the angles of incidence, reflection and transmission (refraction), respectively. n_i and n_t are the refractive indices of the two different media, separated by the interface.

3.2.3 Interaction in the boundary

During propagating through a medium, when light hits the boundary, i.e., either at the interface of the tissue layer and the external medium or at the interface between two consecutive different tissue layers, a fraction of light is reflected back into the medium and the rest of the light is refracted or transmitted to the other medium. As shown in Figure 3.5, if a light beam is incident on the interface between two media having two different indices of refraction (n_i and n_t), the beam is partially reflected at an angle equal to the angle of incidence ($\theta_i = \theta_r$). The rest of the beam is refracted or transmitted to the other medium at an angle θ_t , which is different from θ_i . The angle of refraction is determined by Snell's law [Ganesan and Hecht, 2008]:

$$n_i \sin \theta_i = n_t \sin \theta_t \quad (3.11)$$

The reflectance R , i.e., the intensity of reflected beam is determined by Fresnel

equation [Ganesan and Hecht, 2008]:

$$R = \frac{1}{2} \left[\frac{\sin^2(\theta_i - \theta_t)}{\sin^2(\theta_i + \theta_t)} + \frac{\tan^2(\theta_i - \theta_t)}{\tan^2(\theta_i + \theta_t)} \right] \quad (3.12)$$

For normal incidence, the direction of incidence and reflection is the same, i.e., along the normal to the surface ($\theta_i = \theta_r = 0$). In that condition, the reflectance value reduces to:

$$R = \left(\frac{n_i - n_t}{n_i + n_t} \right)^2 \quad (3.13)$$

The sum of the reflectance (i.e., reflected intensity R) and the transmittance (i.e., transmitted intensity T) equals to the total intensity of the light (considering the total intensity of light is unity, i.e., $I = 1$) [Ganesan and Hecht, 2008] (in an non-absorbing medium):

$$R + T = 1 \quad (3.14)$$

3.3 Tissue optical properties

Specifying the optical properties of tissue is the first step for light-tissue interaction modelling [Jacques, 2013]. The main optical properties of tissue are [Splinter and Hooper, 2006]:

1. absorption coefficient μ_a ;
2. scattering coefficient μ_s ;
3. anisotropy factor g .

Different tissue species exhibit different optical properties, i.e., the capacity of absorbing and scattering light is different for different tissue components. Also, the optical properties vary with wavelengths. To illustrate the variability of the optical properties, the absorption spectra for some of the common absorbers present in the tissue, e.g., oxyhaemoglobin, deoxyhaemoglobin and water are shown in Figure 3.6. As shown, the three absorbers exhibit different natures of absorption. For example, around 650 nm optical wavelength, oxy and deoxyhaemoglobin absorb much higher amount of light than the water. Again, around 1200 nm, absorption by water is much higher compared to oxy and deoxyhaemoglobin.

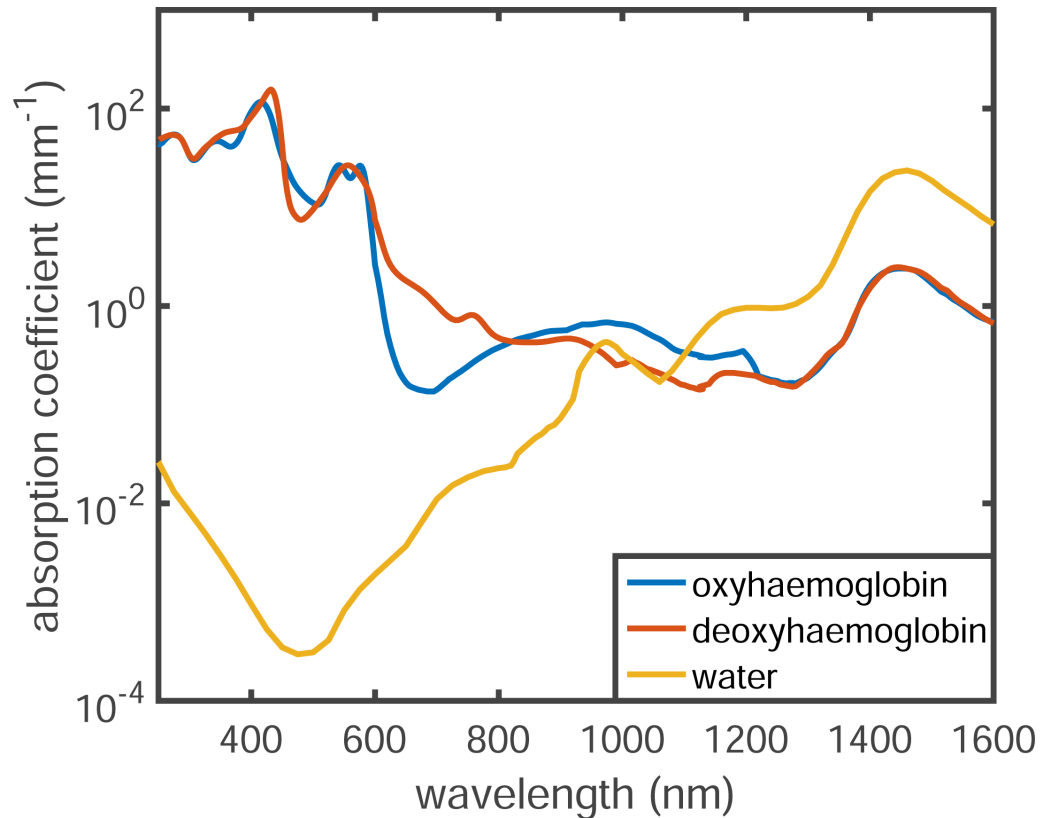


Figure 3.6: Absorption spectra for deoxyhaemoglobin, oxyhaemoglobin and water are presented. The absorption coefficient and the wavelength are expressed in the units of mm^{-1} and nm respectively. Y-axis is presented in logarithmic scale for clear visibility. The graph is produced using the data from Bosschaart *et al.* [2014]; Hale and Querry [1973].

The scattering coefficient and anisotropy factor also exhibit different values for different tissue specimen and vary with wavelength. An example of the variability in the reduced scattering coefficient (which is a combination of the scattering coefficient and the anisotropy factor as defined earlier) for human dermis, subdermal fat and muscle tissues is illustrated in Figure 3.7. The dermis is found to exhibit stronger scattering properties compared to muscle and fat, and also the values vary with wavelengths.

Determination of the optical properties of tissues is a complex method which includes sophisticated experiments with the tissue-region of interest, followed by theoretical analysis [Jacques, 2013; Tuchin, 1997; Wang and Tuchin, 2013]. The absorption and scattering data presented in this section are collected from published literature [Bosschaart *et al.*, 2014; Hale and Querry, 1973; Simpson *et al.*, 1998; Laufer *et al.*, 1998]. In the model

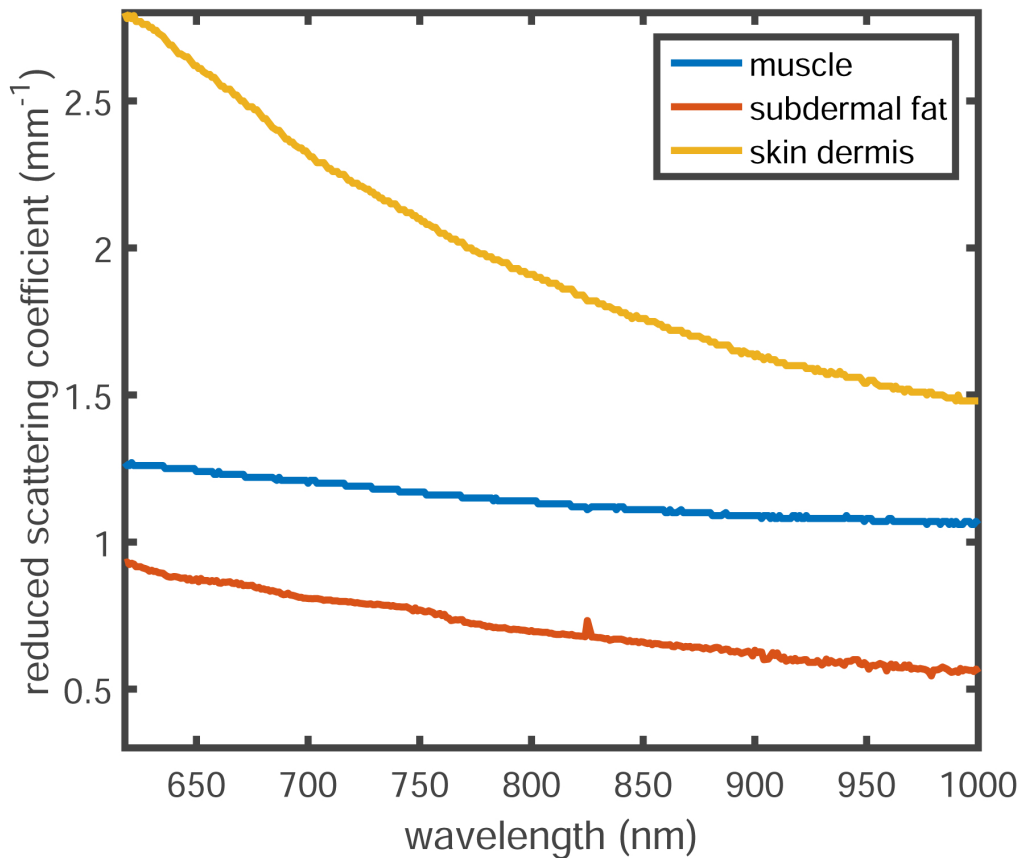


Figure 3.7: Scattering spectra for dermal tissue, subdermal fat and muscle tissue are presented. The scattering coefficient and the wavelength are presented in the units of mm^{-1} and nm respectively. The graph is produced using the data from [Simpson *et al.*, 1998; Laufer *et al.*, 1998]

presented in this thesis, the tissue volume will be characterised using the data collected or derived from literature and text books, and will be discussed in the next chapters.

3.4 Beer-Lambert-Bouguer law

Attenuation of light through a material sample is often described by the Beer-Lambert-Bouguer law, also known as Beer-Lambert law, Beer's law or Lambert-Beer law. The law was first discovered by Pierre Bouguer before 1729, which was cited by Johann Heinrich Lambert in 1760 [Bouguer, 1729; Lambert, 1892]. This law stated the relationship between the optical path through the sample material and the attenuation of light. Much later, August Beer discovered another attenuation relation in 1852, stating the relation-

ship between the light absorbance through the sample material and the concentration of the sample [Beer, 1852]. This law has an extensive application in various fields including chemical analysis and physical optics [Splinter and Hooper, 2006]. The foundation of Photoplethysmography and pulse oximetry also relies on the Beer-Lambert law [Webster, 1997]. For a clear view on this fundamental law, different aspects of expressions and derivations are described in details in this section.

3.4.1 Transmittance, Absorbance and Optical Depth

Prior to the derivation of Beer-Lambert law, it is important to define the basic factors. The amount of absorbed light in the medium is termed as ‘absorbance’ A . Transmittance represents the unabsorbed amount of light, transmitting through the medium. Considering I_0 and I_t represent respectively the incident and transmitted intensity, the absorbance can be related to the transmittance ($T = \frac{I_t}{I_0}$) by a negative logarithmic (with base 10) relationship as shown below:

$$A = -\log_{10}(T) = -\log_{10}\left(\frac{I_t}{I_0}\right). \quad (3.15)$$

For convenience, the above relationship also can be presented in its natural logarithmic form, and the attenuation then is termed as Optical Depth (OD), which is given by,

$$OD = -\ln\left(\frac{I_t}{I_0}\right) = A \times \ln(10). \quad (3.16)$$

In some cases, the absorbance is also termed as **Optical Density** [Matcher *et al.*, 1994], however, this use is discouraged scientifically [Nic *et al.*, 2005].

3.4.2 Derivation of the law: classical approach

According to Lambert’s law, the rate of decrease in the intensity of light with thickness (x) of the medium is proportional to the intensity of the incident light I . When expressed mathematically,

$$\begin{aligned} -\frac{dI}{dx} &\propto I \\ -\frac{dI}{dx} &= k_1 I \end{aligned} \quad (3.17)$$

where k_1 is the proportionality constant. Integrating the left side between the minimum and maximum intensity values ($I = I_0$ and $I = I_t$), and the right side between the minimum and maximum pathlength covered by light ($x = 0$ to $x = d$), the above equation reduces to:

$$\begin{aligned} -\frac{dI}{I} &= k_1 dx \\ \Rightarrow \int_{I_0}^{I_t} \frac{dI}{I} &= k_1 \int_0^d dx \\ \Rightarrow \ln\left(\frac{I_t}{I_0}\right) &= -k_1 d \end{aligned} \quad (3.18)$$

For convenience, the above equation in natural logarithm sometimes is converted into the logarithm with base 10 as:

$$\log_{10}\left(\frac{I_t}{I_0}\right) = \frac{-k_1 d}{\ln(10)} \quad (3.19)$$

Therefore, from Lambert's law, a relationship between the attenuation and the pathlength traversed by light in the medium are expressed as:

$$A = \frac{-k_1 d}{\ln(10)} \quad (3.20)$$

On the other hand, Beer's law presents the relationship between the attenuation A and the concentration C of the absorber in the medium. Following the similar algebraic steps as above, the Beer's law presents:

$$A = \frac{-k_2 C}{\ln(10)} \quad (3.21)$$

where k_2 is the proportionality constant.

Combination of Lambert's and Beer's law presents the linear relationship of A with both d and C :

$$A = K C d \quad (3.22)$$

where K is the proportionality constant.

3.4.3 Derivation of the combined Beer-Lambert law: modern approach

Let us Consider a beam of parallel monochromatic light with intensity I_0 striking the sample at the surface of the sample (medium) as shown in Figure 3.8. After passing through the path length d of the sample, which contains N molecules/cm³, the intensity of the light reduces to I_t .

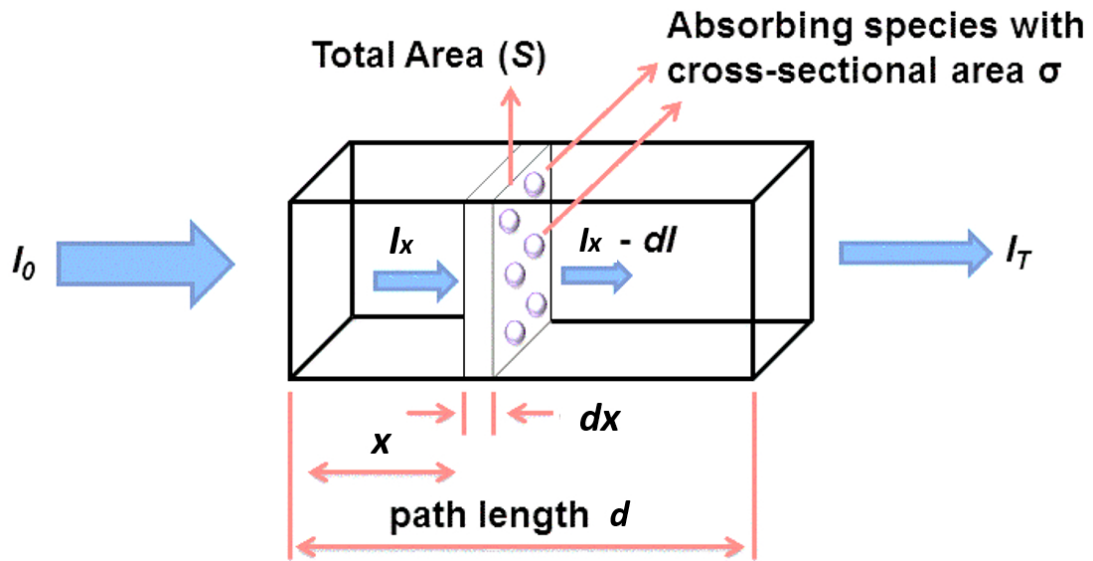


Figure 3.8: A schematic to demonstrate Beer-Lambert law is presented. I_x is the propagating light beam towards the x -axis through the medium with the incident and transmitted intensity I_0 and I_t respectively. There is a small slab of cross-section with an area S and infinitesimal thickness dx within the medium that absorbs dI amount of light intensity. The total thickness of the medium, i.e., the total pathlength traversed by light through the medium is d .

Now, let us consider a cross-section of the block having an area S and an infinitesimal thickness dx placed at a distance x from the surface. Clearly, the number of molecules present in the infinitesimal block would be $= N \times S \times dx$. If each molecule has a cross-sectional area σ where photons of light get absorbed, then the fraction of the total area where light gets absorbed due to each molecule would be $= \frac{\sigma}{S}$.

Therefore, the total fractional area for all molecules in the block where light gets absorbed would therefore be $= (\text{number of molecules}) \times (\text{fractional area for each molecule}) = (N \times S \times dx) \times \frac{\sigma}{S} = \sigma \times N \times dx$.

If I_x is the light entering the infinitesimal block, and the light absorbed due to the absorbing particles is dI , the light exiting the slab would be $= I_x - dI$. Thus, the fraction of light absorbed would be $\frac{dI}{I_x}$.

Now, since the fractional area is the probability of light striking a molecule, the fraction of light absorbed in the block $=$ fractional area occupied by all the molecules in the slab. i.e., $\frac{dI}{I_x} = -\sigma \times N \times dx$, the negative sign is to denote the intensity loss due to absorption.

Integrating this infinitesimal block over the whole sample of thickness from $x = 0$ to $x = d$, where d is the path length of the entire sample, followed by few algebraic steps, we get:

$$\ln\left(\frac{I_t}{I_0}\right) = -\sigma \times N \times d. \quad (3.23)$$

Let us consider C is the concentration of the absorbers in moles/litre. As N is the number of molecules/ cm^3 , the number of molecules in $1L = 1000cm^3$ volume is $N \times 1000$. Also, (6.023×10^{23}) is the Avagadro number (number of molecules per 1 mole of the sample). Using these values, the number of molecules/ cm^3 of the sample can be correlated to the concentration of the sample C in moles/litre using the relationship:

$$\begin{aligned} C &= N \times \frac{1000}{6.023 \times 10^{23}} \\ \Rightarrow N &= 6.023 \times 10^{20} \times C. \end{aligned} \quad (3.24)$$

Putting above value of N in the Eq. 3.23,

$$\ln\left(\frac{I_t}{I_0}\right) = -\sigma \times 6.023 \times 10^{20} \times C \times d. \quad (3.25)$$

For a convenient notation, the above natural logarithmic relationship can be converted into a 10-based logarithmic relationship:

$$\log_{10}\left(\frac{I_0}{I_t}\right) = \frac{\sigma \times 6.023 \times 10^{20}}{\ln(10)} \times C \times d \quad (3.26)$$

The left hand side of the above equation stands for the absorbance A . Replacing the fraction in the right hand side by a constant $\epsilon = \frac{\sigma \times 6.023 \times 10^{20}}{\ln(10)}$, the above equation reduces to the simplistic format:

$$A = \epsilon C d \quad (3.27)$$

A is unitless. ϵ is known as **molar absorptivity** or **extinction coefficient** of the sample material, which is expressed in the unit of $M^{-1}cm^{-1}$. The molar concentration C and pathlength d are expressed in the units of M and cm respectively.

Considering $\mu_a = \ln(10) \times \epsilon \times c$, Eq. 3.25 reduces to

$$\begin{aligned} \ln\left(\frac{I_t}{I_0}\right) &= -\mu_a \times C \times d \\ I_t &= I_0 e^{-\mu_a C d}. \end{aligned} \quad (3.28)$$

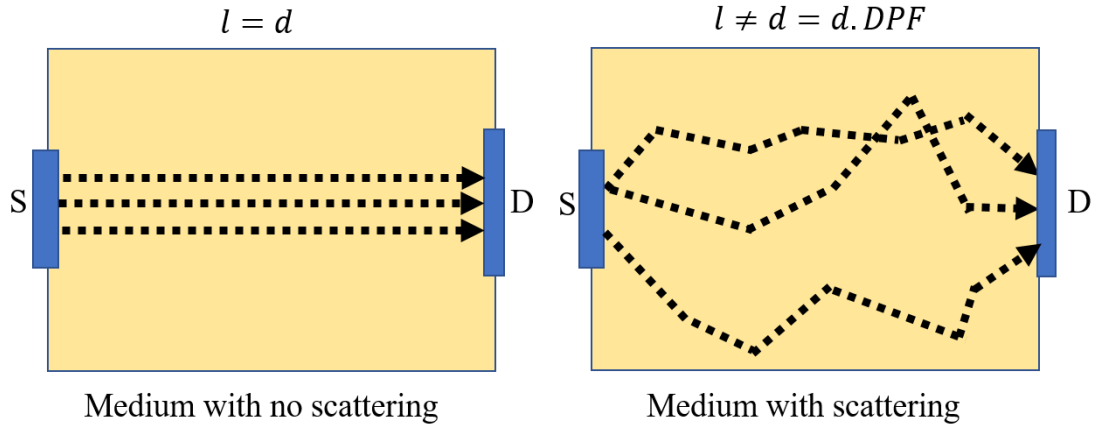


Figure 3.9: Schematic diagram of the optical paths (l) between the source (S) and a detector (D) through a scattering and a non-scattering medium are shown. The paths of the photon are denoted by black dotted lines [Budidha, 2016]. The distance between source and detector is d . The optical path and the source-detector separation are the same in a non-scattering medium. In a scattering medium, light takes a random path between source and detector, resulting in the optical path to be DPF-times higher than the source-detector separation.

μ_a is termed as Napierian absorption coefficient or just the **absorption coefficient**, expressed in the units of cm^{-1} .

If expressed in the 10-based logarithmic form, μ_a is replaced by the Decadic absorption coefficient $\mu_{10} = \frac{\mu_a}{\ln(10)}$, leading to another representation of the law from Eq. 3.26:

$$I_t = I_0 10^{-\mu_{10} C d} \quad (3.29)$$

In conventional use, however, μ_a is expressed as the (Decadic) absorption coefficient so that

$$A = \epsilon \cdot c \cdot d = \mu_a \cdot d. \quad (3.30)$$

3.4.4 Modification in Beer-Lambert law for scattering

Attenuation of light through a highly inhomogeneous medium such as biological tissue attributes to both strong absorption and multiple scattering. However, Beer-Lambert law in its generic form does not account for the effects of scattering. Thus, in order to describe the propagation of light through biological media, hence to incorporate the effect of scattering, the law is modified and known as the **Modified Beer-Lambert law (MBLL)**, as given by Eq. 3.31 and 3.34:

$$A = \epsilon c l + G. \quad (3.31)$$

where l is the physical pathlength of the photon. Expressing with the Decadic absorption coefficient $\mu_a = \epsilon \cdot c$, above expression can be written as

$$A = \mu_a \cdot l + G. \quad (3.32)$$

The pathlength l can be expressed as the differential of absorbance with respect to the absorption coefficient as:

$$l = \frac{\delta A}{\delta \mu_a}. \quad (3.33)$$

Therefore, the physical pathlength l is also termed as ‘differential pathlength’. It is found that for a scattering-absorbing medium, the physical optical pathlength is greater than the geometrical optical pathlength, i.e., the source-detector separation ($l > d$). This relationship is quantified by the parameter Differential Pathlength Factor (DPF). DPF is unitless, and defined as the ratio of the physical or differential pathlength to the geometrical pathlength:

$$l = d \times DPF \quad (3.34)$$

A value of the DPF equal to 1 reduces the above equation to $l = d$, which is the original Beer-Lambert law for an absorption-only medium. For a highly scattering medium such as biological tissue, $DPF > 1$, resulting in $l > d$. Scattering causes random optical paths within the medium, resulting in the physical optical path to be higher than the geometrical optical path [Delpy *et al.*, 1988]. This scenario is shown in Figure 3.9. There is another new term in the MBLL presented as G in Eq. 3.31 which is a function of the geometry of the experimental setting associated with the measurement procedure [Delpy *et al.*, 1988].

3.4.5 Beer-Lambert law in inhomogeneous medium

Beer-Lambert law is found to work accurately in inhomogeneous medium, i.e., a medium where the distribution of the absorbers are not the same and the absorption properties change spatially [Zijlstra *et al.*, 2000]. If light travels a pathlength l through a medium having n absorbers with different extinction coefficients (e.g., $\epsilon_1, \epsilon_2, \dots, \epsilon_n$), and the concentrations of the absorber also change accordingly, the overall absorption in that medium

will be:

$$\begin{aligned}
 A &= (\epsilon_1 \cdot c_1 + \epsilon_2 \cdot c_2 + \dots + \epsilon_n \cdot c_n) \cdot l \\
 &= l \sum_{i=1}^{i=n} \epsilon_i \cdot c_i
 \end{aligned} \tag{3.35}$$

Expressing with the Decadic absorption coefficient $\mu_a = \epsilon \cdot c$, above expression can be written as

$$A = l \cdot \sum_{i=1}^{i=n} \mu_{a_i}. \tag{3.36}$$

3.5 Radiative Transfer formalism

Radiative Transfer Theory (RTT), also known as Transport theory, describes the transportation of any radiation through a medium. In general, the foundation of RTT is the assumption of migrating particles that do not interact with each other, and conservation of energy applies [Splinter and Hooper, 2006].

In tissue optics, the particles are photons, which are probability electromagnetic wave packets, interacting with atomic structure and with optical geometries. In order for the transport theory to be applicable, the photon's localisation in space needs to be small with respect to the dimensions of the medium it interacts with, and the spread of momentum needs to be small as well. Under these conditions, photons will not interact with each other. Even if the optical radiation is incident from a coherent source like laser, the coherence is lost immediately after it interacts with the medium due to many scattering events taking place. Since the photon is small and likely to undergo numerous scattering events in its lifetime, the chances of interference is very low [Splinter and Hooper, 2006].

Radiative Transfer Equation (RTE), which is basically the equation of conservation of energy, is expressed as an integro-differential equation of the **Radiance** (Specific Intensity, or often termed as just 'Intensity'), $I(\mathbf{r}, \mathbf{s}, t)$. The position of the specific intensity is denoted by the vector \mathbf{r} , and the direction of the radiance is along \mathbf{s} . The energy balance results in a description of the dissemination of the light, which is expressed as:

$$\begin{aligned}
 \frac{1}{v} \frac{\partial I(\mathbf{r}, \mathbf{s}, t)}{\partial t} &= -\mathbf{s} \cdot \nabla I(\mathbf{r}, \mathbf{s}, t) - [\mu_a(\mathbf{r}) + \mu_s(\mathbf{r})] I(\mathbf{r}, \mathbf{s}, t) + \mu_s(\mathbf{r}) \int_{4\pi} p(\mathbf{s}, \mathbf{s}') I(\mathbf{r}, \mathbf{s}', t) d\Omega' \\
 &\quad + Q(\mathbf{r}, \mathbf{s}', t) \tag{3.37}
 \end{aligned}$$

The terms of the equation are described as follows [Splinter and Hooper, 2006; Wang and Tuchin, 2013; Chandrasekhar, 2013]:

1. The term in left hand side is the change in radiance per unit volume:

$$\frac{1}{v} \frac{\partial I(\mathbf{r}, \mathbf{s}, t)}{\partial t} \quad (3.38)$$

2. The first term on right hand side of equation represents the radiance lost through the boundaries of the volume:

$$-\mathbf{s} \cdot \nabla I(\mathbf{r}, \mathbf{s}, t) \quad (3.39)$$

3. The second term indicates the loss due to absorption and scattering of a photon from direction \mathbf{s} into different directions:

$$-[\mu_a(\mathbf{r}) + \mu_s(\mathbf{r})] I(\mathbf{r}, \mathbf{s}, t) \quad (3.40)$$

4. The subsequent term identifies the recovery of radiance into the original direction as a result of scattering from direction \mathbf{s}' into the initial direction \mathbf{s} .

$$+ \mu_s(\mathbf{r}) \int_{4\pi} p(\mathbf{s}, \mathbf{s}') I(\mathbf{r}, \mathbf{s}', t) d\Omega' \quad (3.41)$$

The amount of light that will be scattered back from the direction \mathbf{s}' to \mathbf{s} is decided by the phase function of the system $p(\mathbf{s}, \mathbf{s}')$. Since light can scatter back from any direction to the initial direction \mathbf{s} , to account for the overall effect the solid angle $d\Omega'$ is integrated over all angles, i.e. 4π .

5. The last term of the equation is a source term:

$$Q(\mathbf{r}, \mathbf{s}', t) \quad (3.42)$$

It depends on the position and property of the light source, like the light is incident on the surface or within the medium; or even fluorescence.

3.6 Summary

In this chapter, the basic laws and theorems of tissue optics have been discussed. The interaction events (scattering, absorption and reflection/ refraction) responsible for of

light propagation through tissue have been introduced and the laws governing those interactions, namely, the Beer-Lambert law, Fresnel equations, and the Radiative Transfer formulations have been discussed. The optical properties of tissue (e.g., absorption and scattering coefficients, anisotropy factor etc.) have been introduced which play very important in the tissue-optics modelling. The basic concept, definitions and descriptions related to photon transport through biological tissue medium narrated in this chapter make a base of the following studies focused on the development and implementation of the light-tissue interaction model of Photoplethysmography.

REVIEW ON MODELLING LIGHT-TISSUE INTERACTION IN PHOTOPLETHYSMOGRAPHY

4.1 Introduction

It is needless to state that biological tissues exhibit a complex and inhomogeneous structure, consisting of multiple layers and at a microscopic scale, composed of individual cells entrapped in a network of fibres filled with extracellular fluid [Williams *et al.*, 1989]. The propagation of light through a biological matter is a complicated process with many peculiarities. An adequate and accurate description of the propagation of the optical radiation through biological tissue is one of the key priorities to biomedical optics community. This chapter will present an overview on the approaches that can predict and explain the behaviour of photons in a tissue medium. Additionally, this chapter will address the research works carried out in order to understand the light-tissue interaction in Photoplethysmography.

4.2 Overview on modelling approaches for light-tissue interaction

An example of the interaction of different biological species of different length scales with the range of electromagnetic radiation is illustrated in Fig. 4.1. As shown, light interacts

with the tissue in different length scales, from several microns to sub-micron level [Prasad, 2004]. The biological matter light interacts with can be of a dimension much smaller or much larger than the operating optical wavelength ($\sim nm$) [Prasad, 2004]. In different length scales, biological tissues exhibit distinct features of architectural complexities [Wang and Tuchin, 2013; Prasad, 2004]. Factors related to tissue morphology, such as absorption and scattering coefficients, anisotropy and heterogeneity, refractive indices etc. are responsible for the nature of the interaction between light and tissue. Further, the quantitative and qualitative features of the outcome of the light-tissue interaction based technology depend on the external factors such as size and position of the incident optical radiation, the distance between the optical source and detector, numerical aperture, incident intensity or exposure time and so on [Wang and Tuchin, 2013]. Therefore, for an accurate prediction and interpretation of the light-tissue interaction, a feasible and flexible modelling approach is necessary. The choice of the best modelling approach for a particular tissue-optics related problem is strongly correlated with the optical properties of the tissue site and the geometrical description of the system.

Theoretical formalisms based on electromagnetic theory and Mie scattering theory have been shown to provide unsolvable equations for the cases of practical biomedical optics applications [Doronin, 2014; Wang and Tuchin, 2013]. **Radiative Transfer** formalism, on the other hand, originates from energy conservation and serves as a basis of photometry [Tuchin, 2002]. The Radiative Transfer Equation (RTE) is already introduced in Chapter 3. In RTE, the wave nature of the light and phase relations are ignored, and the particle nature of photon is considered. The theory has been extensively used in a number of studies including atmospheric and ocean radiative transfer, astrophysics, geophysics, the optics of photographic layers and others [Ishimaru, 1978; Pomraning, 1973; Tuchin, 2002]. RTE has found its adaptability in biomedical optics since it satisfies all the required criteria for a model, and also fairly correlates with electromagnetic theory-based solutions but offers much lesser complexities than the analytical solutions [Ishimaru, 1978; Splinter and Hooper, 2006; Wang and Tuchin, 2013]. There are numbers of approaches to solving RTE, a comprehensive description of which can be found in textbooks [Case and Zweifel, 1967; Wing, 1962; Mitra and Kumar, 1999; Patterson *et al.*, 1991; Splinter and Hooper, 2006]. The RTE can be solved deterministically and stochastically.

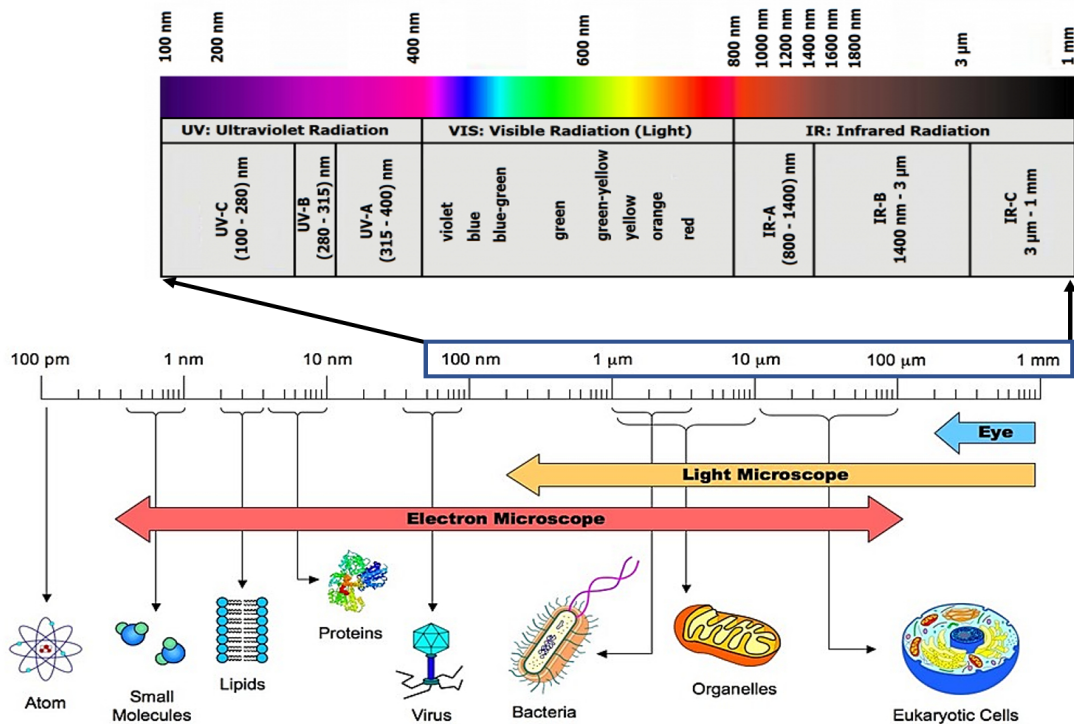


Figure 4.1: A sense of scaling distribution of biological components with respect to the wavelengths of the electromagnetic radiations is presented. The optical wavelength region is illustrated separately to present the more detailed wavelength range divisions. Images are reproduced from the work by Alberts [Alberts, 2017]

One of the main approaches to solve RTE which particularly has been used for modelling propagation of light through biological media for different applications related to clinical treatment, diagnosis and monitoring is the **Diffusion Approximation** [Tuchin, 2002; Durduran *et al.*, 1997; Patterson *et al.*, 1989; Schmitt, 1991; Marble *et al.*, 1994; Gate, 1972; De Mul *et al.*, 2007]. Diffusion approximation is only valid for a medium having predominant scattering. In this approach, it is approximated that the number of scattering events in the medium is much higher compared to the number of absorption events, i.e., after numerous scattering events, few absorption events will occur and the radiance will become nearly isotropic. Diffusion approximation, however, has some critical limitations to present proper solutions to RTE in cases such as varying sizes of the radiation source and detector, numerical aperture, low-order scattering photons etc. [Yoo *et al.*, 1990; Chen *et al.*, 2001; Durian and Rudnick, 1997]. The main limitations are enlisted below:

1. The distance between sources and detectors should be much greater than the mean transport length so that enough scattering events occur to generate a diffuse field (i.e., a region where scattering becomes isotropic). Thus the approach is not suitable for short source-detector separations.
2. The source and detector sizes must be small enough as compared to the distance of their separation. It compromises with the flexibility of the model.
3. The diffusion approximation is also not valid for photons with short arrival time to the detector.

Numerical methods to solve RTE include **flux theory** [Kubelka, 1948, 1954] and **adding-doubling method** [Prah, 1995]. Although the flux theory has been used extensively for solving the light-tissue interaction based problems, it imposes restrictions in the tissue properties and involves complexities. Adding-doubling method, on the other hand, provides a fast-processed accurate solution and can incorporate the inhomogeneity and anisotropy of the medium. However, this method has restrictions in term of tissue geometry and can measure only the reflectance and transmittance from the tissue but not the distribution of flux within the medium.

Apart from the above deterministic approaches, **Random walk theory** is one of the stochastic approaches to solve RTE. It describes the propagation of light through tissue as within a cube of lattice consisting of adjacent points. Within the lattice, photon progresses with a step size inversely proportional to the reduced scattering coefficient, and the photons' propagation is isotropic between the points of the lattice [Splinter and Hooper, 2006]. This approach is in good agreement with the Diffusion approximation and provides simple Reflectance values. However, this method imposes restrictions on the number of possible directions of photon migration and thus, makes multilayer modelling challenging [Bonner *et al.*, 1987; Gandjbakhche and Weiss, 1995].

Another statistical approach for modelling light propagation through tissue is **Monte Carlo** (MC) method. Monte Carlo is a probabilistic method that traces the path of photons through tissue by random sampling of the optical properties of the medium. This method has several considerable advantages in comparison with other methods, which are highlighted in the next subsection. According to many studies related to biomedical optics,

MC is considered to be the best choice for modelling light propagation in tissue [Splinter and Hooper, 2006; Wang and Tuchin, 2013; Meglinski and Matcher, 2003; Patwardhan *et al.*, 2005; Zhu and Liu, 2013]. The development and advantages of the Monte Carlo approach will be discussed in the next section.

4.3 Monte Carlo method - developments and advantages

The history of Monte Carlo can go back up to centuries. The earliest example of the implementation of MC technique was the evaluation of pi (π) [Ramaley, 1969] which happened in 1777. Starting from then, it underwent lots of discussions, mathematical verifications and modifications. In 1930s during the work on atom bomb in Manhattan Project, Von Neumann and Ulam were studying random diffusion and interaction in fissile materials. During this work, they needed a method that may take account for random sampling and eventually the method they found appropriate to use got introduced by the codename "Monte Carlo" after a casino because of the similarity of the process, which refers to "a game of chance" [Metropolis, 1987]. The finding was published in 1949 [Metropolis and Ulam, 1949]; meanwhile, MC method became popular. The first publicly available MC code for modelling photon scattering was developed to study the transport of monochromatic light through Earth's atmosphere [Collins and Wells, 1965]. This code has been modified and with the advancement of computer technologies, has been extensively used for a number of applications including in atmospheric, geological, astrophysical and medical sciences. MC was applied for the first time to tissue optics for calculating the absorption and flux distributions by Wilson and Adam in 1983 [Wilson and Adam, 1983]. Later on, Wang *et al.* developed a set of MC programs (MCML) in standard C language for a multilayered turbid medium with infinitely narrow beam [Wang *et al.*, 1995]. They published it as an open-source code which has been used widely and successfully in different applications [Nicolai *et al.*, 2007; Evans *et al.*, 2005; Rice *et al.*, 2001; Zhu and Liu, 2013]. Considering the advantages of Monte Carlo for light-tissue interaction related problems, many works have been carried out to overcome the only drawback of the method, i.e., the high computational cost [Preis *et al.*, 2009; Lee *et al.*, 2010; Doronin and Meglinski, 2011]. With all these modifications in the programming language and

advancements in hardware, Monte Carlo presently is the most convenient and reliable tool for modelling light-tissue interactions.

There are certain advantages of MC technique which make it the most justified choice for modelling light-tissue interaction. The main advantages of the method over other approaches can be stated as:

1. **Absorption and Scattering:** Almost in all kinds of biological tissue, the scattering coefficient is much larger than the absorption coefficient especially in the visible and near infrared region, i.e. in the region of clinical importance. Also, tissue-medium is a multiple-scattering medium, and the scattering in tissue is anisotropic. The rest of the modelling approaches are unable to consider all these properties at a time. However, MC considers all these specific optical properties of the medium and brings the model close to the real phenomena.
2. **Geometry:** MC allows full three-dimensional description of the light-tissue model. It gives the freedom to consider any shape and size of the tissue medium. It is also compatible with any possible shape and position of the source and detector. Especially, some of the other approaches such as diffusion approximation fails to produce accurate results for problems with smaller source-detector separations, whereas Monte Carlo works correctly in all source-detector separations. Additionally, MC is flexible enough to alter these geometries any time very easily.
3. **Inhomogeneity:** Practically tissue is a highly inhomogeneous medium. MC allows the inclusion of any number of layers having different optical properties easily, where other models fail. It makes the model more realistic and useful.
4. **Boundary effect:** The problem that occurs near the boundary between the tissue and the outside medium (e.g. air) or between two consecutive tissue-layers is a difficult question to solve where many modelling theorems (e.g., diffusion approximation) fail. But MC can take into account both diffuse reflection at the tissue-air boundary or Fresnel reflection/ refraction at the boundary between two consecutive layers, and thus makes a more realistic model.

5. **Flexible output:** A wide range of output data can be scored from the MC model. Depending on the interest, one can record the values of outgoing intensity of light, number of photons detected, number of photons absorbed in tissue, rate of absorption within tissue, number of scattering events, time taken by photons of travel the path, photon path length within tissue, reflected and transmitted intensities at boundaries, amount of attenuated intensity of light in tissue and so on. The variation of the recorded data with the variation of the geometry can also be measured easily.
6. **Accuracy:** Based on the single photon physics and the theory of randomness of scattering, MC gives an exact accurate result.

4.4 Current state of the art in modelling

Photoplethysmography and Pulse Oximetry

There have been a significant technological advancements in the field of pulse oximetry, i.e., the well-known application of PPG, in the recent years [Allen, 2007; Budidha and Kyriacou, 2018; Kyriacou, 2013; Phillips *et al.*, 2011; Hickey *et al.*, 2010; Patel *et al.*, 2017]. Still the aspect of fundamental modelling has been neglected in this field. Very few research works are available in the field of modelling light-tissue interaction in PPG and PO.

The first ever published study for modelling light-tissue interaction in a transmission mode pulse-oximetry is found by [Marble and Cheung, 1988]. It presented a simplistic model based on one-dimensional photon diffusion theory. The second study in this field by [Schmitt, 1991] presented a photon diffusion analysis for both reflectance and transmittance pulse-oximetry. This study was rigorous, the detailed description of the derivation of optical properties was presented, and the detailed calculations for the PPG parameters (e.g. AC and DC signal, and ratio-of-ratios) were discussed. This work created the platform for future researches on modelling light-tissue interaction in PPG. However, these models are restricted by the well-known limitations of diffusion approximation.

Later on, valuable works have been carried out by P. D. Mannheimer [Mannheimer

et al., 1997, 2004; Mannheimer, 2007], where computational and mathematical models (using Photon Random Walk theory and homogeneous Monte Carlo model) were used to explain the basic questions, such as, influence of absorption and scattering in pulse-oximetry, wavelength selectivity for pulse oximetry, influence of larger artery in pulse-oximetry readings etc. The studies were comprehensive and detailed, and presented a picture of an overall understanding. However, the model description was not accurate enough to be compared with any practical scenario.

The most recent, and the most detailed models were presented by [Reuss and Siker, 2004], which was followed by another publication by [Reuss, 2005], in which heterogeneous Monte Carlo model of the human skin was executed to study the functionalities of reflectance pulse oximetry. The optical properties and dimensions of the tissue components used in the simulation were very close to the real situation. The model was executed for different oxygen saturation and for a range of source-detector separations, for both systolic and diastolic cases. However, some limitations still remained. Even though the model was detailed and in line with other similar modelling-based works on skin tissue [Tuchin *et al.*, 2011; Meglinski and Matcher, 2003; Wang and Tuchin, 2013], it was just a skin model, and no particular ROI (region of interest) was mentioned, whereas it is known that the dimension of the tissue layers and the vascular distribution are very different at different ROIs [Williams *et al.*, 1989].

4.5 Summary

In this chapter, different aspects of modelling light-tissue interaction in biological tissue have been discussed. Monte Carlo method has been introduced as a probabilistic method to solve radiative transfer formalism, amongst other methods. The limitations of different approaches (e.g., flux theory, adding-doubling method, random walk theory, and diffusion approximation), and the advantages of the Monte Carlo modelling approach over others to simulate light-tissue interaction have been addressed further. Finally, the current state of the art of the modelling approaches in Photoplethysmography has been discussed. The overview of the available studies on PPG light-tissue interaction-based modelling, irrespective of any particular approach, has been found to be very few in

number. Available models also do not provide adequate and precise information on PPG and PO such as optical pathlength, depth of penetration, distribution of scattering, the effect of physiological factors etc. This chapter has concluded with the feasibility and importance of using Monte Carlo method as a reliable tool for computing light-tissue interactions in PPG. The following chapter will concentrate on the further details on the theoretical aspects of Photoplethysmography, focussing on the requirements of a model of PPG light-tissue interactions.

PHOTOPLETHYSMOGRAPHY AND PULSE OXIMETRY

5.1 Introduction

Plethysmography is the method to measure the volumetric changes within an organ or the whole body, usually achieved by analysing the change in volume of blood or air contained in that part of the body [Criée *et al.*, 2011]. The method to obtain the plethysmogram optically is known as Photoplethysmography (PPG). PPG has a wide range of applications in clinical practices and biomedical researches, for example, perfusion indication, respiratory rate monitoring, heart rate monitoring, blood pressure monitoring, cardiovascular assessment, arterial and venous blood oxygen saturation measurement etc. [Alian and Shelley, 2014; Nilsson *et al.*, 2007; Nitzan *et al.*, 2000; Allen and Murray, 2002; Lima *et al.*, 2002; Njoun and Kyriacou, 2017; Abay and Kyriacou, 2015]. PPG is mostly recognised for its application in studying and monitoring the pulsations associated with the changes in blood volume in the peripheral vascular tissue bed, a clinical method known as Pulse Oximetry (PO) [Allen, 2007; Moyle, 2002]. Pulse oximeters monitor arterial oxygen saturation continuously, which is the primary indicator of hypoxic events occurring in patients in anaesthesia, critical care and neonatal care units [Severinghaus, 1993]. In this chapter, the theoretical concept of Photoplethysmography and Pulse Oximetry will be discussed in detail. In addition, the requirement for a modelling approach will also be discussed.

5.2 Working principle of Photoplethysmography

Photoplethysmography utilises the absorptivity of light to detect the fluctuations of blood volume in vascular tissue bed during the cardiac cycle.

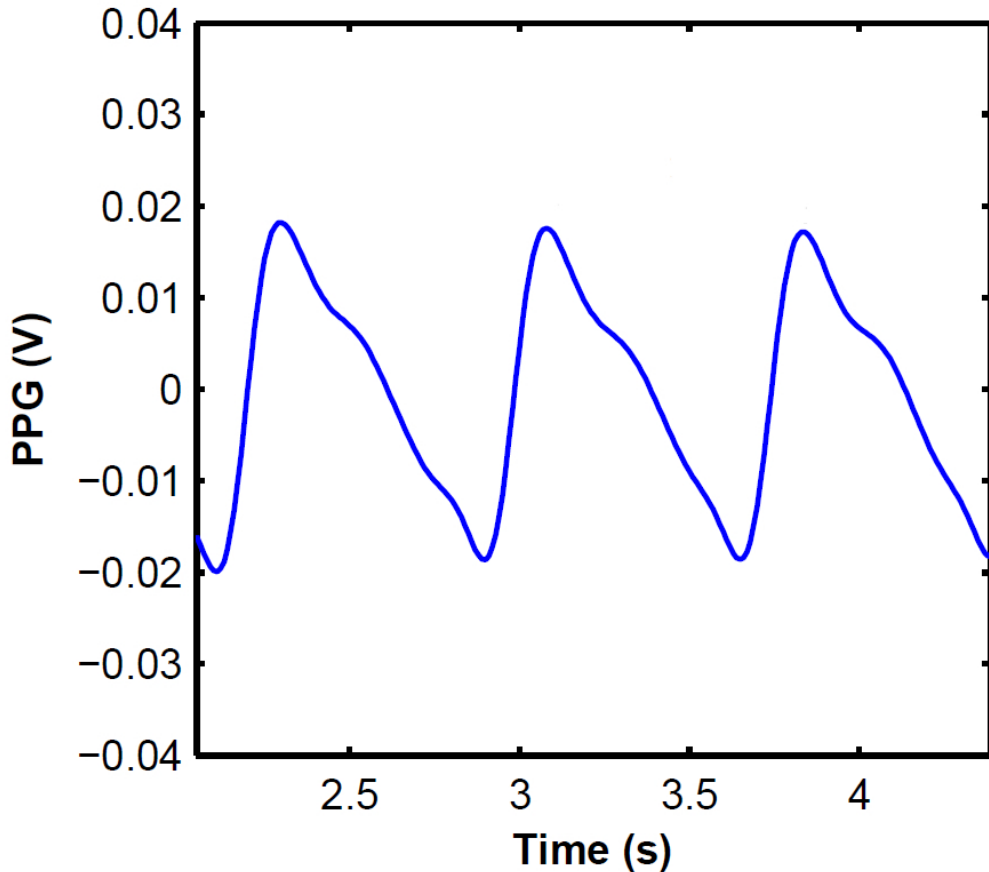


Figure 5.1: A typical Photoplethysmogram is shown as a function of time. The plot is adapted from [Abay, 2016].

A cardiac cycle, as already discussed in Chapter 2, consists of two stages: systole and diastole. During systole, blood pumped out of the heart rushes throughout the body, including peripheral tissue sites. This systolic increase in blood volume results in increased absorbance of light in tissue compared to the diastolic state. This relative change in light absorbance gives rise to the PPG waveform. In order to obtain a PPG signal, the tissue site is irradiated by an optical illumination, of which a certain amount of light is absorbed and the unabsorbed light is reflected or transmitted, depending on the measurement modality being used. A typical PPG waveform is shown in Fig. 5.1.

5.2.1 Components of PPG waveform

The PPG waveform is the amount of unabsorbed light intensity detected by the sensor detector. Clearly, the higher is the absorbance (A), the lower is the detected PPG intensity (I). As shown in Fig. 5.2, the recorded PPG waveform has an inverse relationship with the absorbed light within the tissue. Corresponding to the effect of light absorbance in the pulsatile and non-pulsatile compartments of tissue, the PPG intensity can be divided into two parts as stated below.

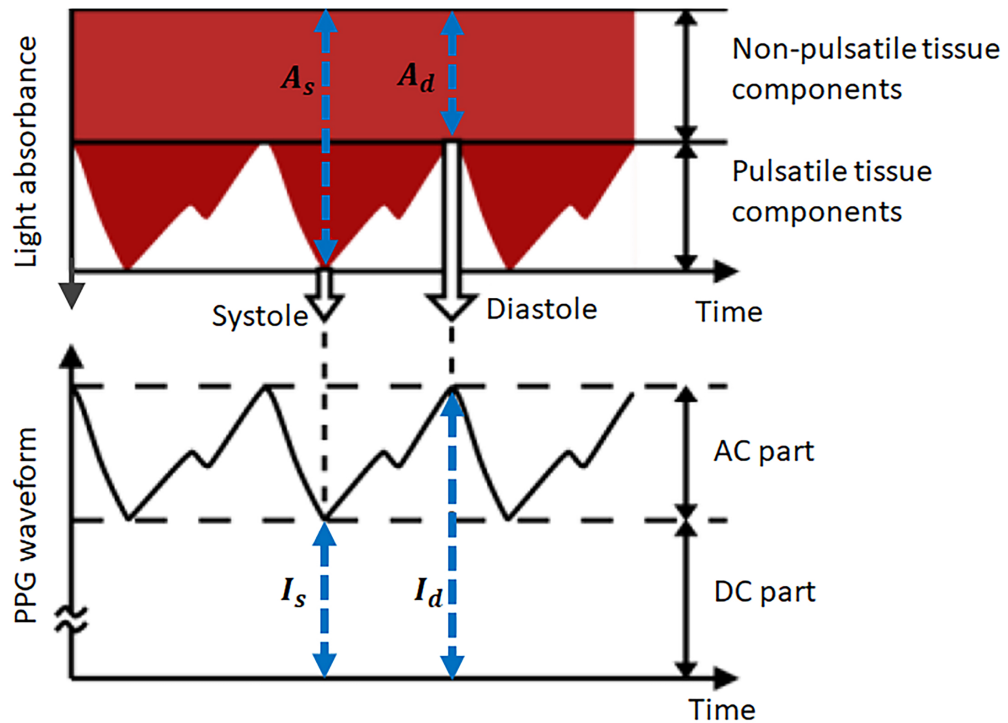


Figure 5.2: The schematic of PPG waveform produced due to the absorbance of light in tissue, as a function of time. Light absorbance in the pulsatile tissue component produces the pulsatile AC part in the PPG waveform. Absorbance in the non-pulsatile tissue components contributes to the slowly varying DC part of the PPG waveform. The absorbances in the systolic and diastolic parts are denoted as A_s and A_d respectively. The PPG intensity during systolic and diastolic parts are denoted as I_s and I_d respectively [Tamura *et al.*, 2014]. It should be noted that in this figure, only a qualitative correspondence between A and I are shown, however, numerically these variables have a non-linear relationship.

1. The non-pulsatile, relatively continuous DC (direct current) component generates due to the absorption of light in the non-pulsating tissue parts (e.g., bloodless tissue,

muscle, bone etc.). The slow variation in the DC wave is attributed to respiration, the sympathetic nervous system, and the thermoregulation [Webster, 1997].

2. The pulsating AC (alternating current) component originates from the absorption of light in the pulsatile arterial blood and varies synchronously with the heart rate [Webster, 1997]. The AC PPG is divided into two phases: the rising edge of the pulse or anacrotic phase that is primarily concerned with systole, and the falling edge of the pulse catacrotic phase which is associated with the diastole. A dicrotic notch is usually seen in the second phase of the PPG wave recorded from a healthy subject [Marcinkevics *et al.*, 2009].

5.2.2 Beer-Lambert law in PPG

The Beer-Lambert law has been stated in Chapter 2. Recalling and combining Eq. 3.15 and Eq. 3.31, the absorbance (A) of light in the tissue medium having the extinction coefficient ϵ and concentration c can be expressed in terms of the logarithmic ratio of the incident light intensity I_0 and the detected (i.e, reflected or transmitted) light intensity I_t , as shown below:

$$A = \log\left(\frac{I_0}{I_t}\right) = \epsilon c l + G \quad (5.1)$$

where the optical pathlength is l and the scattering dependent term is G . Considering the same amount of light to be incident to the tissue throughout the entire cardiac cycle, above equation can be manipulated for diastolic and systolic states as:

$$A_d = \log\left(\frac{I_0}{I_d}\right) = \epsilon l_d C_d + G \quad (5.2)$$

$$A_s = \log\left(\frac{I_0}{I_s}\right) = \epsilon l_s C_s + G \quad (5.3)$$

where the terms with suffices d and s present the corresponding factors in diastolic and systolic states respectively. As shown in Fig. 5.2, due to higher amount of pulsatile blood in tissue during systole compared to diastole, the light absorbance will be higher and the transmitted intensity will be lower in systole compared to diastole, i.e.,

$$A_s > A_d \quad (5.4)$$

$$I_s < I_d$$

It is considered that $l_s \approx l_d = l$ (this assumption will be validated later on in the thesis). If the change in the concentration of the absorbers in blood due to its increased volume is expressed as $\Delta C = C_s - C_d$, the change in absorbance from diastole to systole can be written as:

$$\Delta A = A_s - A_d = \epsilon l \Delta C. \quad (5.5)$$

Therefore, the change in absorbance in PPG between diastole to systole also can be expressed as

$$\begin{aligned} \Delta A &= \epsilon l \Delta C \\ &= \log\left(\frac{I_0}{I_s}\right) - \log\left(\frac{I_0}{I_d}\right) \\ &= \log\left(\frac{I_0}{I_s} / \frac{I_0}{I_d}\right) \\ &= \log\left(\frac{I_d}{I_s}\right). \end{aligned} \quad (5.6)$$

5.2.3 PPG measurement technique

In order to record PPG from a tissue site, a system with an optical source and detector is required. Often LED and photodetectors are chosen for size, cost and availability in a wide range of wavelengths [Allen, 2007]. There are PPG systems utilising optical fibre probes as the source and detector which have mainly been used for research purposes [Hickey *et al.*, 2010; Phillips *et al.*, 2006; Chen *et al.*, 2013; Morley *et al.*, 2017]. Depending on the positioning of the optical source and detector, the PPG wave can be recorded in two different modalities, namely, transmittance mode and reflective mode. A comparative view of the two modes of PPG measurement system is presented in Fig. 5.3.

In the transmittance mode measurement system, the tissue site is placed between the source and detector. The tissue site is illuminated by the optical wavelength emitted from the source. A certain amount of light is absorbed within the tissue and the rest is transmitted. The detector detects the amount of light that is captured within its area. In the reflective mode, light is emitted from the source, and the unabsorbed light that reaches the area of the detector is detected. The journey of the photons from the source to the detector is governed by the interactions between light and tissue, e.g., scattering, reflection, refraction etc. [Mannheimer, 2007].

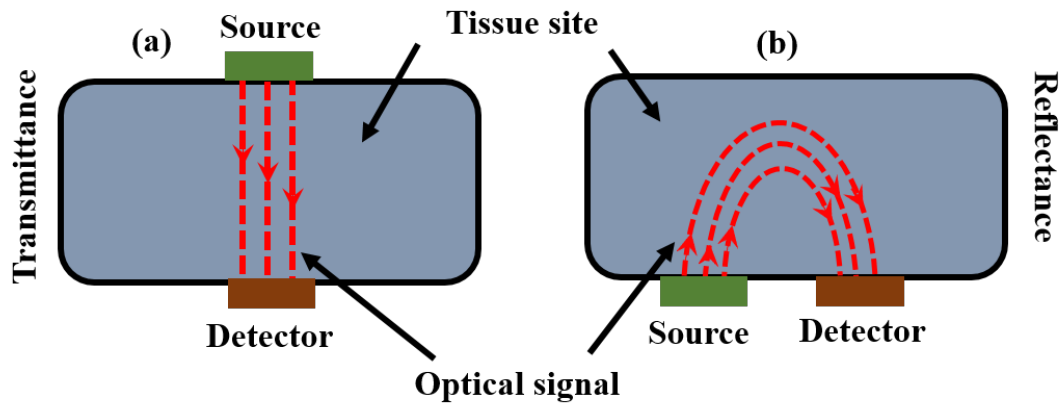


Figure 5.3: The schematic of PPG system modalities, i.e., Transmittance (a) and Reflectance (b) are shown. In transmittance mode, the optical source and detector are placed at two opposite sides of the tissue site, whereas in reflective mode, the source and detector are placed in the same side of the tissue site. The red dotted lines present the direction of the light propagation from the source to the detector through the tissue site. It should be noted that the typical photon trajectory only of the detected photons are shown in the schematic.

The mode of measurement is chosen depending on the site of application. The configuration of the transmissive mode system allows it to be used at the small extremities, e.g., toe, finger or earlobe, whereas the reflective mode system can be used almost any part of body [Allen, 2007]. Usually, PPG signals are recorded from the peripheral tissue sites where the pulses can be detected easily [Stern, 1974; Sherebrin and Sherebrin, 1990; Budidha and Kyriacou, 2018; Middleton *et al.*, 2011]. However, applications of PPG also are found at tissue sites such as the oesophagus, large intestine, supra-orbital artery, arm, chest and abdominal organs [Kyriacou *et al.*, 2001; Patel *et al.*, 2017; Barnes *et al.*, 1977; Abay and Kyriacou, 2015].

5.3 PPG in Pulse Oximetry

As mentioned earlier, the most common application of PPG is Pulse Oximetry (PO) that is used very frequently in the clinical setting for continuous measurement of arterial blood oxygen saturation SaO_2 . Pulse oximeters measure SpO_2 (i.e., the peripheral SaO_2 measured by PO) using PPG signals obtained at different wavelengths in living tissue [Hertzman, 1937]. The wavelength selection is the most important criteria for PO to function properly [Mannheimer *et al.*, 1997]. PO exploits the relative absorbance at

minimum two (or more) wavelengths of light by the main two absorbers present in blood, i.e., oxyhaemoglobin and deoxyhaemoglobin (from now on, these will be denoted by HbO_2 and Hb respectively) [Moyle, 2002]. PPG signals are recorded in the red and near-infrared wavelength regions (typically at 660 nm and 940 nm) as the relative differences between the absorbance by HbO_2 and Hb are the maximum at these wavelengths (the absorbance by these haemoglobin species at different wavelengths have been illustrated in Chapter 3). In these two wavelengths, absorption of light both during diastolic state (i.e., the absorption within the non-pulsatile tissue component) and systolic state (i.e., the absorption within the pulsatile tissue component) possess different values, resulting in different amplitudes of the red and infrared AC and DC PPG signals. Again, the absorption property of blood is related to the arterial oxygen saturation (described later in this chapter). Thus, from the normalised amplitudes of the absorbance of light in pulsatile blood at the red and infrared wavelengths, the SpO_2 values are determined.

5.3.1 Working principle of Pulse Oximetry

The formulations and equations used in order to explain the PO working principle are straightforward, however, the explanations and derivations are presented differently in various books and articles which are sometimes unclear, disconnected or approximated [Webster, 1997; Nitzan and Taitelbaum, 2008; Chan *et al.*, 2013; Mannheimer *et al.*, 1997; Mannheimer, 2007]. In this section, a detailed yet simplistic derivation is demonstrated which links the fundamental laws with the practical quantifications globally used to describe PO.

Application of Beer-Lambert law in PPG can be further extended to explain the PO working principle. As shown earlier in Eq. 5.6, at any particular wavelength λ , the change in absorbance between diastole and systole can be expressed as the logarithmic ratio of the diastolic and systolic intensity:

$$\Delta A(\lambda) = \log \left(\frac{I_d(\lambda)}{I_s(\lambda)} \right) \quad (5.7)$$

Manipulating $\Delta A(\lambda)$ algebraically (e.g., changing the base 10 equation to the natural base, and inverting the fraction), and considering the change in intensity between systole

and diastole to be $\Delta I = I_d - I_s$, few steps of equations can be written as follows:

$$\begin{aligned}
 \Delta A(\lambda) &= -\ln\left(\frac{I_s(\lambda)}{I_d(\lambda)}\right) / \ln(10) \\
 &= -\ln\left(\frac{I_d(\lambda) - \Delta I(\lambda)}{I_d(\lambda)}\right) / \ln(10) \\
 &= -\ln\left(1 - \frac{\Delta I(\lambda)}{I_d(\lambda)}\right) / \ln(10) \\
 &\approx -\left(-\frac{\Delta I(\lambda)}{I_d(\lambda)}\right) / \ln(10) \\
 &= \frac{\Delta I(\lambda)}{I_d(\lambda)} / \ln(10)
 \end{aligned} \tag{5.8}$$

where $\frac{\Delta I(\lambda)}{I_d(\lambda)} \ll 1$, so the higher order terms could be ignored in the logarithmic series (this assumption will be validated later on in the thesis) [Nitzan *et al.*, 2000].

The ratio of the wavelength-dependent change in absorbance is termed as the "**ratio of ratios**" R :

$$R = \frac{\Delta A(\lambda_1)}{\Delta A(\lambda_2)} \tag{5.9}$$

Using the absorbance values for red and infrared wavelengths (i.e., $\lambda_1 = r$ and $\lambda_2 = ir$) from the above equations, R can be written in the form as shown below:

$$R = \frac{\Delta I(r) / I_d(r)}{\Delta I(ir) / I_d(ir)} \tag{5.10}$$

By definition, the change in the light intensity from systole to diastole is known as AC signal and the intensity absorbed in the non-pulsatile part of tissue is known as the DC signal, i.e., $\Delta I = AC$ and $I_d = DC$. Replacing ΔI and I_d by AC and DC, R is reduced to the a well-known equation to quantify pulse oximetric measurement [Moyle, 2002; Kyriacou *et al.*, 2001; Nitzan and Taitelbaum, 2008; Mannheimer, 2007]:

$$R = \frac{AC(r)/DC(r)}{AC(ir)/DC(ir)}. \tag{5.11}$$

For deriving SaO_2 from PO, it is considered that only the change in absorption by blood from diastole to systole (of concentration ΔC) contributes to the arterial pulsation, and the absorption in non-pulsatile tissue-bed cancels out while taking the ratio between the diastole and systole. The main two absorbers present in blood are considered to be deoxyhaemoglobin and oxyhaemoglobin. Now, recalling Eq. 3.35 to describe the Beer-Lambert law in a medium having mixture of absorbers, and using Eq. 5.6, the change in

absorbance by blood at any wavelength expressed as shown below:

$$\Delta A(\lambda) = (\epsilon_{HbO_2}(\lambda) \cdot [HbO_2] + \epsilon_{Hb}(\lambda) \cdot [Hb]) l(\lambda) \quad (5.12)$$

where ϵ_{Hb} and ϵ_{HbO_2} are the extinction coefficients, and $[Hb]$ and $[HbO_2]$ are the change in concentrations of deoxy and oxyhaemoglobin respectively.

Now, recalling the definition of arterial oxygen saturation (Eq. 2.4),

$$\begin{aligned} SaO_2 &= \frac{[HbO_2]}{[Hb] + [HbO_2]} \\ \Rightarrow [HbO_2] &= SaO_2 \cdot ([Hb] + [HbO_2]); \\ [Hb] &= (1 - SaO_2) \cdot ([Hb] + [HbO_2]) \end{aligned} \quad (5.13)$$

Putting the values of $[Hb]$ and $[HbO_2]$ in Eq. 5.12,

$$\Delta A(\lambda) = (\epsilon_{HbO_2}(\lambda) \cdot SaO_2 + \epsilon_{Hb}(\lambda) \cdot (1 - SaO_2)) \cdot ([Hb] + [HbO_2]) \cdot l(\lambda) \quad (5.14)$$

Replacing the values of $\Delta A(\lambda)$ for red and infrared wavelength in Eq. 5.9,

$$\begin{aligned} R &= \frac{\Delta A(r)}{\Delta A(ir)} \\ &= \frac{\epsilon_{HbO_2}(r) \cdot SaO_2 + \epsilon_{Hb}(r) \cdot (1 - SaO_2) \cdot l(r)}{\epsilon_{HbO_2}(ir) \cdot SaO_2 + \epsilon_{Hb}(ir) \cdot (1 - SaO_2) \cdot l(ir)}. \end{aligned} \quad (5.15)$$

Through several simple algebraic steps, SaO_2 can be expressed by a relationship with R as follows:

$$SaO_2 = \frac{R \cdot l(ir) \cdot \epsilon_{Hb}(ir) - l(r) \cdot \epsilon_{Hb}(r)}{R \cdot l(ir) \cdot [\epsilon_{Hb}(ir) - \epsilon_{HbO_2}(ir)] + l_r \cdot [\epsilon_{HbO_2}(r) - \epsilon_{Hb}(r)]}. \quad (5.16)$$

In general approximation, the optical pathlength at red and infrared wavelengths are considered to be identical, i.e. $l(r) = l(ir)$ (the validity of this approximation will be analysed later in this thesis) [Webster, 1997; Moyle, 2002]. Using this approximation in the above equation, SpO_2 (peripheral arterial oxygen saturation measured by PO, as already discussed earlier) is expressed as a function of R and the extinction coefficients of the oxy and deoxyhaemoglobin. The SpO_2 value is normally presented in the percentage form, which is given by:

$$SpO_2 = \frac{R \cdot \epsilon_{Hb}(ir) - \epsilon_{Hb}(r)}{R \cdot [\epsilon_{Hb}(ir) - \epsilon_{HbO_2}(ir)] + \epsilon_{HbO_2}(r) - \epsilon_{Hb}(r)} \times 100\% \quad (5.17)$$

Actual arterial SaO_2 and the SpO_2 measure by PO are not exactly the same, however, those exhibit excellent correlation as shown in 5.4.

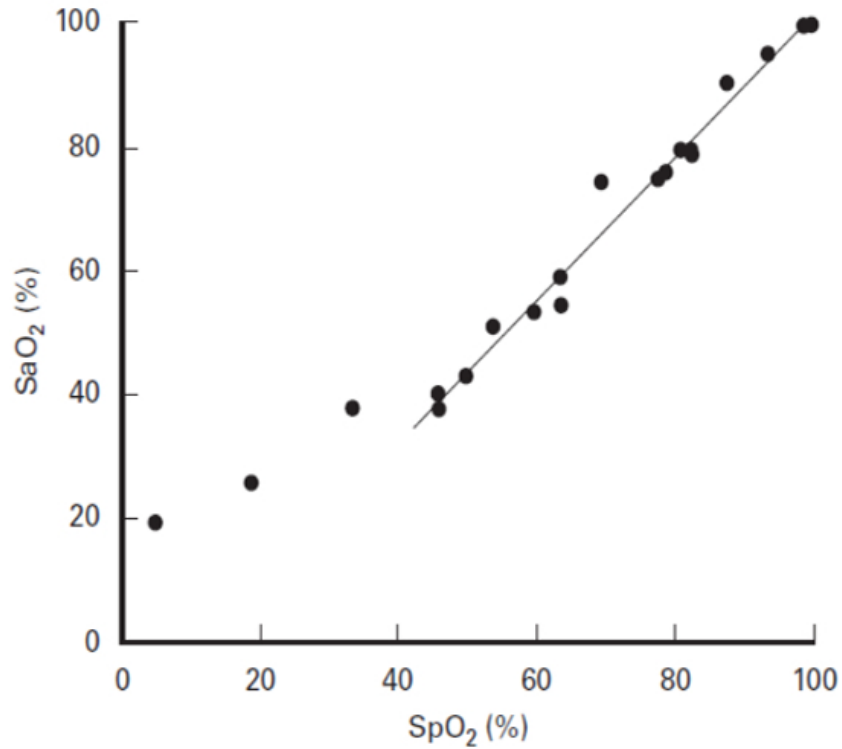


Figure 5.4: The correlation between SaO_2 and SpO_2 presented that has been adapted from [Moyle, 2002].

5.3.2 Calibrating Pulse Oximeter

To relate the measured values of the ratio R to the reading of the pulse oximeter, the equation based on Beer's law can be modified [Webster, 1997]. SpO_2 can be calculated from the Eq. 5.17 directly, if the extinction coefficients of oxy and deoxyhaemoglobin are known. Using the values of the extinction coefficients from textbook [Zijlstra *et al.*, 2000], e.g., $\epsilon_{Hb}(r) = 0.814$, $\epsilon_{HbO_2}(r) = 0.080$, $\epsilon_{Hb}(ir) = 0.183$, $\epsilon_{HbO_2}(ir) = 0.294$, all values having the units of $L^{-1}mM^{-1}cm^{-1}$, Eq. 5.17 can be re-written as:

$$SpO_2 = \frac{R \times 0.183 - 0.814}{R(0.183 - 0.294) + 0.08 - 0.814} \times 100\% \quad (5.18)$$

The above expression can be represented in the following format (denoting the multiplication by 100 by the percentage sign):

$$SpO_2 = \frac{814 - 183R}{734 + 111R} \times 100\% \quad (5.19)$$

Replacing the coefficients the constants and coefficients by the terms k_1, k_2, k_3, k_4 respectively, it is obtained as (when SpO_2 obtained in its percentage form):

$$SpO_2 = \frac{k_1 - k_2R}{k_3 - k_4R} \quad (5.20)$$

Eq. 5.20 is one of the form of the equation for calibration as described by [Mendelson and Kent, 1989].

By the use of algebraic series expansion and ignoring the higher order terms, Eq. 5.19 also can be represented in a quadratic form as described below through the following steps:

$$\begin{aligned} SpO_2 &= \frac{814(1 - 0.22R)}{734(1 + 0.15R)} \times 100\% \\ &= 1.11(1 - 0.22R)(1 + 0.15R)^{-1} \times 100\% \\ &\Rightarrow [1.11(1 - 0.22R)(1 - 0.15R)] \times 100\% \\ &= [1.11(0.033R^2 - 0.37R + 1)] \times 100\% \\ &= [0.037R^2 - 0.41R + 1.11] \times 100\% \end{aligned} \quad (5.21)$$

To generalize the above equation, putting k_1, k_2, k_3 as the coefficients in the polynomial, it is obtained in the percentage form as:

$$SpO_2 = k_1R^2 + k_2R + k_3 \quad (5.22)$$

which is another form of the equation for pulse oximetry calibration stated by [Fine and Weinreb, 1995].

In the final quadratic equation in Eq. 5.21, considering the fractional value of R gives a lesser value when squared, it may be ignored which reduces the equation to a liner form:

$$SpO_2 = (1.11 - 0.41R) \times 100\% \quad (5.23)$$

which leads to a generic form of calibration equation for pulse oximeters, considering the saturation is expressed in percentage:

$$SpO_2 = 111 - 41 \times R \quad (5.24)$$

In practice, however, SpO_2 is determined empirically. Pulse oximeters are calibrated by collecting a huge dataset from healthy volunteers and lookup table is formed for SpO_2

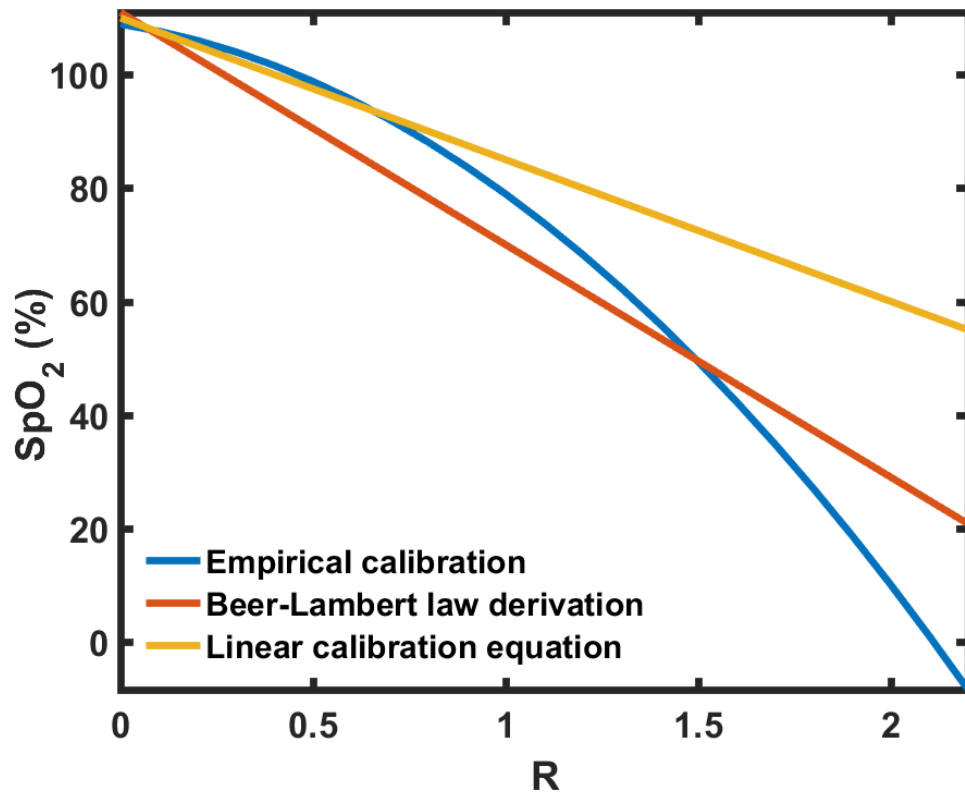


Figure 5.5: The comparative calibration curves obtained using the empirical calibration method, Beer-Lambert law (according to Eq. 5.24) and the Linear equation for commercial pulse oximetry calibration (according to Eq. 5.25) are presented by the blue, red and yellow lines respectively.

values corresponding to R . An accurately computed empirical calibration formulation, which is generally used by them who have an experience with pulse oximetry technology is given by the linear standard equation [Shafique and Kyriacou, 2012; Kyriacou *et al.*, 2002; Abay and Kyriacou, 2015; Oak and Aroul, 2015; Budidha and Kyriacou, 2018]:

$$SpO_2 = 110 - 25 \times R \quad (5.25)$$

However, most of the modern manufacturers build their own calibration curves instead of relying on the available theoretical formulations given by Eq. 5.24 or Eq. 5.25. One of such equation for a pulse-oximetric system, given by [Budidha *et al.*, 2018]:

$$SpO_2 = -19.49.R^2 - 10.47.R + 108.9. \quad (5.26)$$

The calibration curve obtained using Eq. 5.24, Eq. 5.25 and Eq. 5.26 are presented in Fig. 5.5 showing the correlation among the three datasets.

In the empirical calibration, it involves the comparison of the oximeter R value to the oxygen saturation ratio obtained from *in vivo* samples using human test subjects. Although this method requires a variety of laboratory instrumentation and is typically done in a hospital setting, this collection process is only required during the design and development of the device [Webster, 1997]. This calibration procedure needs the use of a system named CO-oximeter [Rees *et al.*, 1980] that can measure the concentration of all species of haemoglobin in blood, namely oxyhaemoglobin, deoxyhaemoglobin, carboxyhaemoglobin (COHb) and methaemoglobin (MetHb) etc. The last two haemoglobin species normally exist in a very small quantity in blood, abundance in which is resulted by an exposure or a disease. During the calibration procedure, the percentages of COHb and MetHB are checked by the CO-oximeter. Once a low level of these two species is confirmed, the test begins by first ensuring that the subject is at the 100% oxygen saturation level and then the saturation is dropped incrementally by manipulating the oxygen-nitrogen gas mixture inhaled by the subjects. At each level where the pulse oximeter indicates a stable reading, an arterial blood sample is immediately taken and corresponding readings are recorded from the CO-oximeter. The data are plotted with oxygen saturation percentage (as determined by the CO-oximeter) on the y-axis and R ratio (as determined by the pulse oximeter under test) on the x-axis yielding a traditional calibration curve. Usually, the test for calibration is carried out on a very large number of healthy subjects.

5.3.3 Pulse Oximetry technique

Continuing from the PPG modalities mentioned in Sec. 5.2.3, PO operates in both reflective and transmissive modes. The most common application site of the pulse oximeter is a human finger. A schematic of finger pulse oximeter is shown in Fig. 5.6. Red and infrared light are emitted from LED to the surface of the finger, and the light traversed through the vascular tissue beds of the finger is recorded by a photodetector placed either on the opposite surface or in the same surface of the finger, depending the mode of the system (transmissive and reflective mode, respectively).

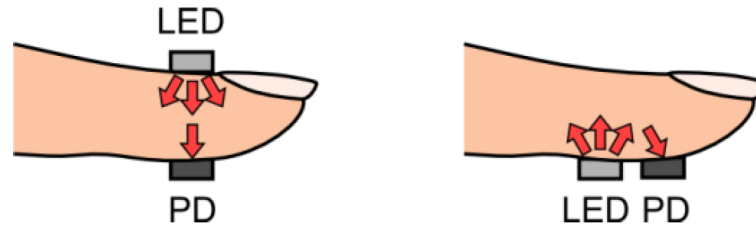


Figure 5.6: The schematic diagram of a reflective and a transmissive mode of pulse oximetry in the finger is shown. The figure is reproduced from [Tamura *et al.*, 2014].

Transmissive mode pulse oximeters are found to be used in the clinical setting often for continuous measurement of arterial oxygen saturation. However, transmissive probes have their limitations with respect to the site of application, and cannot be used in any places other than fingertip, earlobe or toe. The reflective probe, on the other hand, does not have any such limitations regarding the probe positioning and can be used almost at any part of the body. The most used application of the reflective probe is forehead and temple. The distance between the source and the detector of the sensor is a vital parameter in order to obtain good PPG from reflective PO. It has been found that a source-detector separation anywhere between 3 mm and 6 mm is a good choice for achieving good quality signals [Hickey and Kyriacou, 2007].

5.4 Requirements for a modelling approach

Photoplethysmography, with its application in pulse oximetry, plays an important role in critical patient monitoring and physiological measurements. The fundamental theory of PPG bases on a straightforward derivation from the standard Beer-Lambert law. It is already known that Beer-Lambert law needs modifications to be used in the highly scattering medium like biological tissue (Chapter 3). The theoretical explanation, as presented in this chapter, depends on some assumptions which have never been verified for PPG, for example, the consideration of wavelength-independence of the optical pathlength. Besides, the Beer-Lambert law considers the absorption of light by oxyhaemoglobin and deoxyhaemoglobin only. This consideration may be sufficient for pulse oximetry as the only interest there is to measure the change in absorbance due to the pulse, i.e., the change in blood volume during the cardiac cycle. However, for a larger picture, i.e., to

understand the entire PPG process, the absorbance due to the blood less tissue layers, other chromophores present in tissue such as water and melanin etc. should also be considered. Beer-Lambert law based theory also does not provide any information on the penetration depth, which is important to predict the origin of the signal within the tissue.

In the recent age of an ongoing research interest in PPG beyond its application in pulse oximetry, an intimate investigation with a detailed opto-anatomical model is necessary. An opto-anatomical model of photoplethysmography must consider the following features.

1. Tissue is a highly scattering medium. Any model, therefore, has to be able to deal with the effects of multiple scattering.
2. For most tissues, over the wavelength range of interest (500-1000 nm), the scattering coefficient is considerably larger than the absorption coefficient.
3. Scattering of light in biological tissue is highly anisotropic.
4. On a macroscopic scale, tissues are not homogeneous. Ideally, a model should be able to take into account multiple layers or sections within the tissue each with different absorption and scattering coefficients.
5. Not all tissue-structures can be accurately described by a simple slab or sphere geometry. Thus the model must be able to deal with complex tissue geometries.
6. The computation time necessary to obtain the required results should not be excessive.
7. The model must be able to incorporate any geometrical setting between the optical source and detector, i.e., variable separation distance, different beam profiles, different spatial and angular dimensions of the source and detector etc.

5.5 Summary

This chapter has explained the basic principle in PPG and PO, with the detailed Beer-Lambert law-based derivations. Additionally, this chapter has elucidated the requirements for a comprehensive light-tissue interaction based model for PPG. The basic criteria for

the modelling approach have been discussed. Previously, the advantages of Monte Carlo as a tool for tissue-optical modelling have been discussed in Chapter 4. From the outlook of the requirements stated in this chapter, it is apparent that the Monte Carlo method is the most suitable approach for modelling photoplethysmography. Henceforth, the following chapters in the thesis will be focussed on the development and execution of the Monte Carlo method to modelling photoplethysmography and pulse oximetry.

MONTE CARLO MODELLING METHODOLOGY

6.1 Introduction

This chapter will concentrate on the developmental stages of the Monte Carlo model which will be used in this thesis. The algorithm and the fundamental steps of the simulation will be discussed which will follow the light-tissue interaction theory presented in Chapter 3. This chapter will also discuss the implementation strategy of the model for different applications in the thesis.

6.2 Development of the model

6.2.1 Concept and considerations

In the Monte Carlo (MC) model, the paths of virtual ‘photons’ were traced through the optically characterised ‘biological tissue’. The optical properties of the tissue were described by the wavelength-dependent parameters μ_a , μ_s , g , and n which have been introduced in Chapter 2. Once the optical parameters of the tissue had been defined, the photon transport through the medium was simulated. Prior to describing the simulation algorithm, the features and considerations for the model are furnished below.

1. **Three-dimensional model geometry:** The model provided a full three-dimensional simulation of light transport. The three-dimensional feature gave the freedom to

include any structure model, e.g., slab, sphere, cylinder etc. A three-dimensional feature of the model was also important for illustrating the distribution of light in all probable directions in tissue.

2. **Homogeneity and heterogeneity in tissue model:** The tissue was not composed of discrete scattering and absorption centres distributed in a non-scattering, non-absorbing medium [Prah], 1988]. Instead, it showed the volumetric distribution of the scattering and absorption properties. In other words, the macroscopic tissue-optical properties were considered in the model rather than the micro-cellular structural inhomogeneities [Wang *et al.*, 1995]. Therefore, a certain type of tissue (e.g., dermis, muscle, fat etc.) could be individually presented as homogeneous layers, and the heterogeneity in the model could be incorporated by addition of more layers and sublayers with different optical properties.
3. **Refraction and polarisation:** The index of refraction was assumed to be uniform in a single tissue layer so that light did not deviate from the straight line direction until it was scattered. Also, the boundaries of the tissue layers were considered smooth so that light went through specular reflection only according to Fresnel's law. Polarisation effect was not considered in the present model as it is expected that even if a polarised light beam is incident on the tissue, due to the random scattering the photon will lose its polarisation information [Van der Zee, 1992].
4. **Scattering anisotropy:** Scattering was considered symmetric about the direction of incidence, i.e., was independent of the azimuth (ϕ), indicating, on an average, no preferred direction or orientation of the scatterers present in tissue.

In the execution of the model, the 'implicit capture' approach was used to reduce the variance in the method [Witt, 1977] where the simulation of a 'photon cluster' was considered instead of a single photon. Therefore, from now on in this thesis, the term 'photon' will directly refer to a 'photon cluster'. The concept about the inputs and outputs in this model are described below.

- **Tissue properties:** The input parameters to define the optical properties of tissue at the operating wavelength λ were: μ_a , μ_s , g , n ; and the parameters to define the

anatomical properties of the tissue were the shape(s) and thickness(es) of tissue layer(s).

- **Incident photon:** The input parameters to define the ‘incident photon’ were: (1) ‘weight’ of the photons, which was assigned to the photon cluster which equals to unity, i.e., $w = 1$; and (2) the direction and position co-ordinates.
- **Recorded quantities:** There was a range of variables that were recorded throughout the simulation process which included: (1) absorbed, reflected, transmitted and detected weight of photon, (2) number of scattering within tissue, (3) depth of penetration, and (4) mean and total optical path of photons through tissue.

The aforementioned conditions were fundamental for the developed MC model which will be maintained throughout all the simulations in this thesis.

6.2.2 Geometrical representation and co-ordinate system

A ‘slab’ geometry was chosen for the basic tissue-model which was presented in a three-dimensional Cartesian co-ordinate system. Focussing on the pulse oximetry applications, the MC model was executed in the reflective and transmissive geometries. The geometrical representations of the tissue slab with a finite thickness t are illustrated in Figure 6.1(a) and Fig. 6.1(b). In the Cartesian co-ordinate system (x,y,z) , the top surface of the tissue was presented by the plane $z = 0$, and the negative z -direction presented the depth within the tissue. The virtual photon clusters were incident on the tissue surface from an optical ‘source’ (S), placed at the origin $(0,0,0)$ of the co-ordinate system. From there, the photons propagated through the tissue medium through the ‘step sizes’ generated by MC simulation. While traversing through tissue, a photon satisfying the ‘detection criteria’ was captured by a ‘detector’ (D). As shown in Figure 6.1 (a), the detector was placed at a certain distance d from the source at the adjacent side of the tissue (on $z = 0$) in reflective mode, i.e., the position co-ordinate of the detector was $(d,0,0)$. In the transmissive geometry as shown in Figure 6.1 (b), the detector was at the bottom surface ($z = t$) with the position co-ordinate $(0,0,t)$.

In addition to the main Cartesian co-ordinate system, a spherical polar co-ordinate system was also required to describe the photon movements [Wang and Tuchin, 2013].

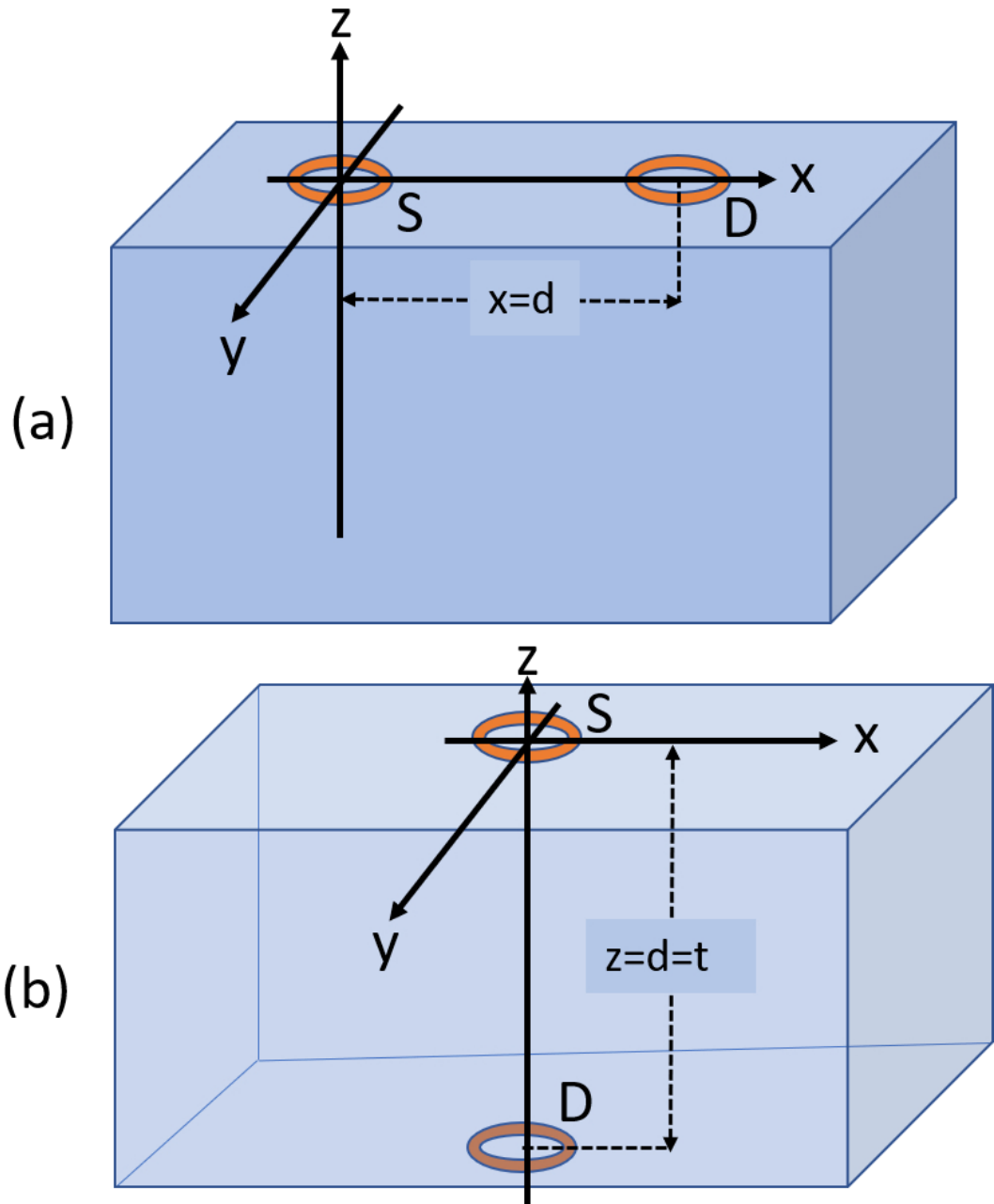


Figure 6.1: Schematics of the slab of tissue in the (a) reflectance and (b) transmittance geometries of the model are presented in 3D Cartesian co-ordinate system xyz . The centre of the source is assumed to be placed at the origin of the co-ordinate system, i.e., at $(0,0,0)$. In the reflectance geometry, the source (S) and the detector (D) are placed at a distance d at the same side of the tissue, thus the centre of the detector is at $(d,0,0)$. In the transmittance geometry, they are placed at two opposite sides of the tissue separated by a distance equal to its thickness t , thus the co-ordinate of the centre of the detector is $(0,0,d)$ or $(0,0,t)$. The ring shape of the source and detector are arbitrarily chosen to explain the schematic.

A moving spherical polar co-ordinate system was associated with each photon, which had its z-axis always aligned with the direction of propagation of the photon. Each time the direction of photon was deviated due to the interaction with scatterers in tissue, the change in direction was first calculated in spherical co-ordinate, and then transformed into the main Cartesian co-ordinate system.

6.2.3 Transformation between co-ordinate systems

Let us consider \mathbf{R} is vector denoting the direction of a photon in an instant. The direction of photon is presented in the spherical polar co-ordinate system by the angle of deflection θ , and the azimuthal angle ϕ as shown in Figure 6.2. Again, with respect to the Cartesian co-ordinate system, the position vector \mathbf{R} makes angles α , β , γ respectively with x, y, and z-axis.

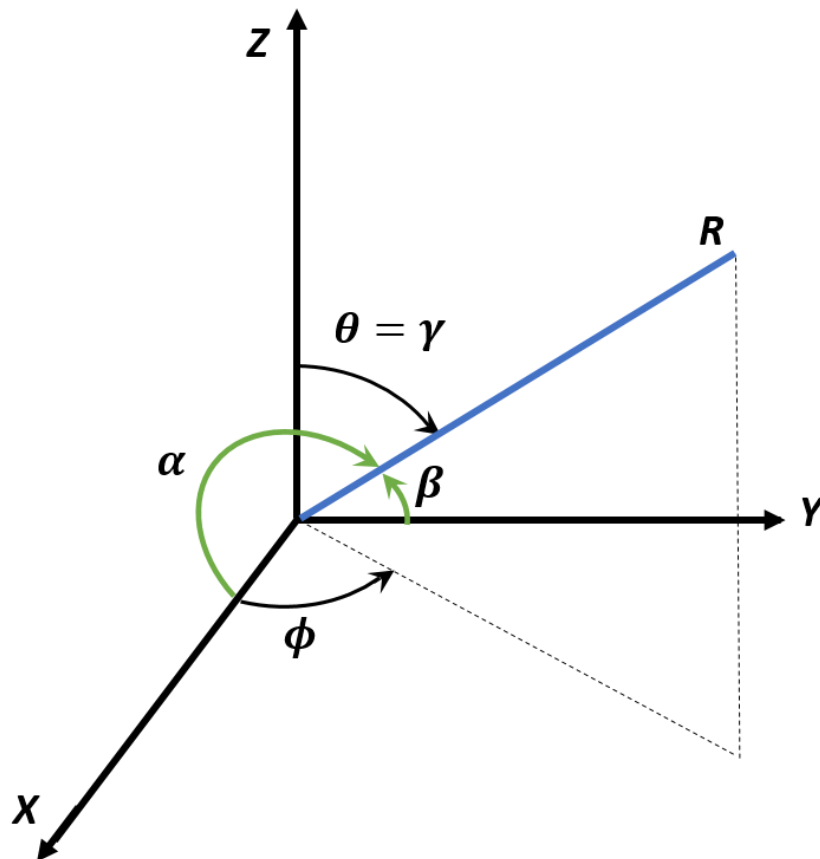


Figure 6.2: Relationship between the Cartesian co-ordinate and Spherical polar co-ordinate system is shown. The vector \mathbf{R} makes the angle of deflection and the azimuth, θ and ϕ respectively in the spherical polar co-ordinate. Again, \mathbf{R} makes the angles α, β, γ with the x, y and z-axes respectively in the Cartesian co-ordinate system.

In Cartesian co-ordinate system the position vector is defined by its direction cosines, namely, (μ_x, μ_y, μ_z) , which are the cosines of the angles made by the position vector with the unit vectors along x, y and z axes respectively:

$$\begin{aligned}\mu_x &= \cos \alpha; \\ \mu_y &= \cos \beta; \\ \mu_z &= \cos \gamma.\end{aligned}\tag{6.1}$$

According to Figure 6.2

$$\begin{aligned}\gamma &= \theta \\ \implies \cos \gamma &= \cos \theta.\end{aligned}\tag{6.2}$$

With respect to the Cartesian co-ordinate system, the components of \mathbf{R} along the three axes are:

$$\begin{aligned}R_x &= R \cos \alpha \\ R_y &= R \cos \beta \\ R_z &= R \cos \gamma\end{aligned}\tag{6.3}$$

Again, with respect to the spherical polar co-ordinates, the components can be written as $R \sin \theta \cos \phi$, $R \sin \theta \sin \phi$, and $R \cos \theta$. Thus, relating the expressions in both the co-ordinate system, it can be written as:

$$\begin{aligned}R_x &= R \cos \alpha = R \sin \theta \cos \phi \\ R_y &= R \cos \beta = R \sin \theta \sin \phi \\ R_z &= R \cos \gamma = R \cos \theta\end{aligned}\tag{6.4}$$

from which, the direction cosines can be related to the spherical polar co-ordinate as:

$$\begin{aligned}\mu_x &= \sin \theta \cos \phi \\ \mu_y &= \sin \theta \sin \phi \\ \mu_z &= \cos \theta.\end{aligned}\tag{6.5}$$

In the MC simulation, the deflection and azimuthal angles were randomly created and converted into the corresponding direction cosines using the above relationships and were updated in the main system.

6.2.4 Calculation for the scattering angle

The calculation of angle of scatter is important in order to simulate the deflection of photon each time it undergoes scattering event. The calculation for the angle is briefly described below.

Mathematically, any point (a,b) can be represented in a complex form as $a + ib$. If that point is rotated through an angle, say, α , the resultant position can be expressed according to Euler's formula [Arfken and Weber, 1999] as:

$$(a + ib)e^{i\alpha} = (a + ib)(\cos \alpha + i \sin \alpha) \quad (6.6)$$

This simple formula will be used twice to calculate the rotation of a point, say, (x,y,z), on a unit sphere, ie., first through the angle γ' about y-axis and then through an angle ϕ' about z-axis [Cashwell and Everett, 1959]. Figure 6.2 can be considered for understanding the spherical polar co-ordinate system representing a unit sphere. First, the rotation of (x,y,z) to (x',y',z') about y-axis through γ' can be expressed according to Eq. 6.7:

$$\begin{aligned} z' + ix' &= (z + ix)(\cos \gamma' + i \sin \gamma'); \\ y' &= y \end{aligned} \quad (6.7)$$

Now the rotation of (x',y',z') to (x'',y'',z'') about z-axis through ϕ is expressed according to Eq. 6.8:

$$\begin{aligned} x'' + iy'' &= (x' + iy')(\cos \phi' + i \sin \phi') \\ z'' &= z' \end{aligned} \quad (6.8)$$

Now, separating the real and imaginary parts gives in above two equations and substituting the values of x',y' and z' in Eq. 6.8, the relationship between the initial and final position of the point is obtained as:

$$\begin{aligned} x'' &= x \cos \gamma' \cos \phi' + z \sin \gamma' \cos \phi' - y \sin \phi' \\ y'' &= y \cos \phi' + x \cos \gamma' \sin \phi' + z \sin \gamma' \sin \phi' \\ z'' &= z \cos \gamma' - x \sin \gamma' \end{aligned} \quad (6.9)$$

Let p be the distance from the origin in the unit sphere to the projection of the new position (x'',y'',z'') onto the xy-plane. Considering $\bar{x}, \bar{y}, \bar{z}$ are the projections of the vector in the respective axes, following relationships are obtained:

$$\begin{aligned}
 p &= \sin \gamma' \\
 \frac{\bar{x}}{p} &= \cos \phi' \\
 \frac{\bar{y}}{p} &= \sin \phi' \\
 z &= \sin \gamma'
 \end{aligned} \tag{6.10}$$

Since all derivations have been performed on a unit sphere, the vector having components $(\bar{x}, \bar{y}, \bar{z})$ is the same as the directional cosine vector $(\mu_x, \mu_y, \mu_z) = (\sin \theta \cos \phi, \sin \theta \sin \phi, \cos \theta)$, as seen from Eq. 6.5. Thus, several algebraic steps make the following relationships between new direction cosines (μ'_x, μ'_y, μ'_z) with old direction cosines (μ_x, μ_y, μ_z) [Cashwell and Everett, 1959]:

$$\begin{aligned}
 \mu'_x &= \frac{\sin \theta (\mu_x \mu_z \cos \phi - \mu_y \sin \phi)}{\sqrt{1 - \mu_z^2}} + \mu_x \cos \theta; \\
 \mu'_y &= \frac{\sin \theta (\mu_y \mu_z \cos \phi + \mu_x \sin \phi)}{\sqrt{1 - \mu_z^2}} + \mu_y \cos \theta; \\
 \mu'_z &= -\sin \theta \cos \phi \sqrt{1 - \mu_z^2} + \mu_z \cos \theta.
 \end{aligned} \tag{6.11}$$

Above relationships also can be derived by the matrix multiplication due to the two consecutive rotations of a vector having direction cosines (μ_x, μ_y, μ_z) through an angle θ about y-axis and an angle ϕ about z-axis, as detailed in several text books [Wang and Tuchin, 2013; Marchuk *et al.*, 2013].

6.2.5 Sampling of random variables

In order to simulate the random behaviour of the photons in tissue, several variables were needed to be generated randomly and repeatedly. Examples of those variables include free pathlength of photon between two consecutive interactions, and angle of photon scattering. These variables were randomly sampled from well-defined probability distribution functions. The mathematical explanation of the random sampling in Monte Carlo modelling can be found in several text books [Cashwell and Everett, 1959; Lux and Koblinger, 1991; Kalos and Whitlock, 2008].

Let us consider X is the random variable needed in the simulation. There is a probability density function that is defined by the distribution of X over an interval (a, b) . In its

normalised form, the probability density function (PDF) is written as:

$$\int_a^b p(X)dX = 1 \quad (6.12)$$

In order to choose the value for X randomly and repeatedly, a pseudo-random generator (inbuilt MATLAB function) was used. It should be noted that inbuilt random number generators in the computer are known to produce ‘pseudo-random’ numbers because those are not truly ‘random’ as per its mathematical definition, however, those numbers approximate the properties of the sequence of actual random numbers [Niederreiter, 1992].

The computer provides a random variable ξ , the value of which is uniformly distributed between 0 and 1. Let us consider F_ξ is the Cumulative distribution function (CDF) for ξ . CDF of a random variable at a certain input value is the probability that the variable is always less than or equal to the given input. By definition, CDF for the uniformly distributed random variable ξ at an input value ξ_1 is given by:

$$F_\xi(\xi_1) = \begin{cases} 0 & \text{if } \xi_1 \leq 0 \\ \xi_1 & \text{if } 0 < \xi_1 \leq 1 \\ 1 & \text{if } \xi_1 > 1. \end{cases} \quad (6.13)$$

Let us consider that there exists a function $X = f(\xi)$, which maps $\xi \in (0,1)$ to $X \in (a,b)$ [Kalos and Whitlock, 2008]. The variables X and ξ , hence, have a one-to-one mapping. This is described in the Figure 6.3. As shown in the Figures 6.3(a) and (b), the shaded area depicting the integral of $p(X)$ over $[0, X_1]$ is equated with the shaded area depicting the integral of $p(\xi)$ over $[0, \xi_1]$. According to the definition of the probability distribution functions, the areas under both the curves $p(X)$ and $p(\xi)$ equal to unity. The result is a one-to-one mapping between the upper boundaries ξ_1 and X_1 based on the equality of the shaded areas in the figure. Thus, according to Figures 6.3(a) and (b), the probability of finding X between a and X_1 equals to the probability of finding ξ between 0 and ξ_1 . This can be written as a probability equality equation:

$$P(a < X \leq X_1) = P(0 < \xi \leq \xi_1). \quad (6.14)$$

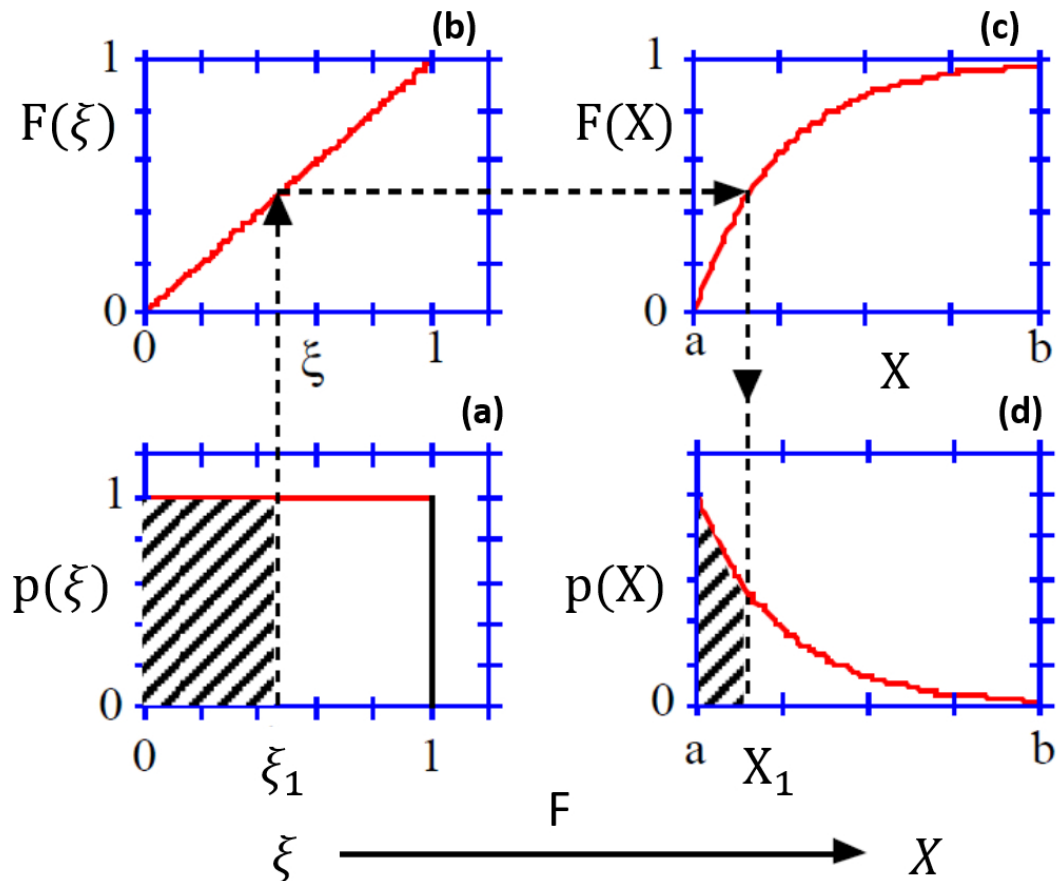


Figure 6.3: The steps of sampling a random variable, X , based on a uniformly distributed random variable, ξ are illustrated. The probability of the random number x_i , lying between 0 and 1, to have a value equals to x_{i1} is presented in (a), and the corresponding cumulative distribution function is presented in (b). Again, the probability that a random variable X , lying between a and b , to have a value equals to X_1 is presented in (d) and the corresponding cumulative distribution function is presented in (c). By definition, both the cumulative distribution functions $F(\xi)$ and $F(X)$ have values between 0 and 1, as shown in (b) and (c), respectively. The graphs are adapted from [Wang and Jacques, 1992].

According to the definition of CDF, above probability equation can be written in the form of two CDFs:

$$F_x(X_1) = F_\xi(\xi_1). \quad (6.15)$$

The CDFs are shown in Figures 6.3 (c) and (d) corresponding to the PDFs in (b) and (a) respectively. The transformation process $X_1 = f(\xi_1)$ is shown by the arrows. For each ξ_1 , a X_1 is chosen such that the cumulative distribution functions for ξ_1 and X_1 have the same value. Correspondingly, the hatched areas are equal.

Expanding the cumulative distribution function $F_\xi(\xi_1)$ in terms of the corresponding probability density function for the left-hand side of Eq.6.15 and employing Eq. 6.13 for the right-hand side, Eq. 6.15 is converted into:

$$\int_a^{X_1} p(X) dX = \xi_1 \text{ for } \xi_1 \in (0, 1). \quad (6.16)$$

Above equation is solved for X_1 to get the function $F(\xi_1)$. This above relationship will be often used in the next sections.

6.2.6 Simulation procedure

The algorithm for simulating a desired number of photon clusters through the tissue medium is presented in Figure 6.4. In the model, first, a number of photon clusters were selected to be simulated or detected. A photon cluster was ‘launched’ down the surface from the optical source places on it. After the correction for ‘specular reflection’, the photon started propagating through a randomly generated ‘step size’. After moving through each step size, it was checked whether the photon ‘hit the boundary’ of tissue. In case of an interaction with the boundary, a check was made for ‘reflection and transmission’. If the photon was ‘transmitted’ to the outside medium, another check was made if it was ‘detected’. In cases where the photon was transmitted without being detected, the photon cluster was ‘terminated’. If it was ‘reflected’ internally, the position and direction co-ordinates were updated and the photon continued to propagate through a new step size, repeating the same steps. In case of no collision with the boundary, the photon went to the interaction site where the ‘scattering and absorption’ events took place, and the photon weight, position and directions were updated in the system accordingly. The simulated photon had to ‘survive’ in order to propagate further through tissue. If the photon did not

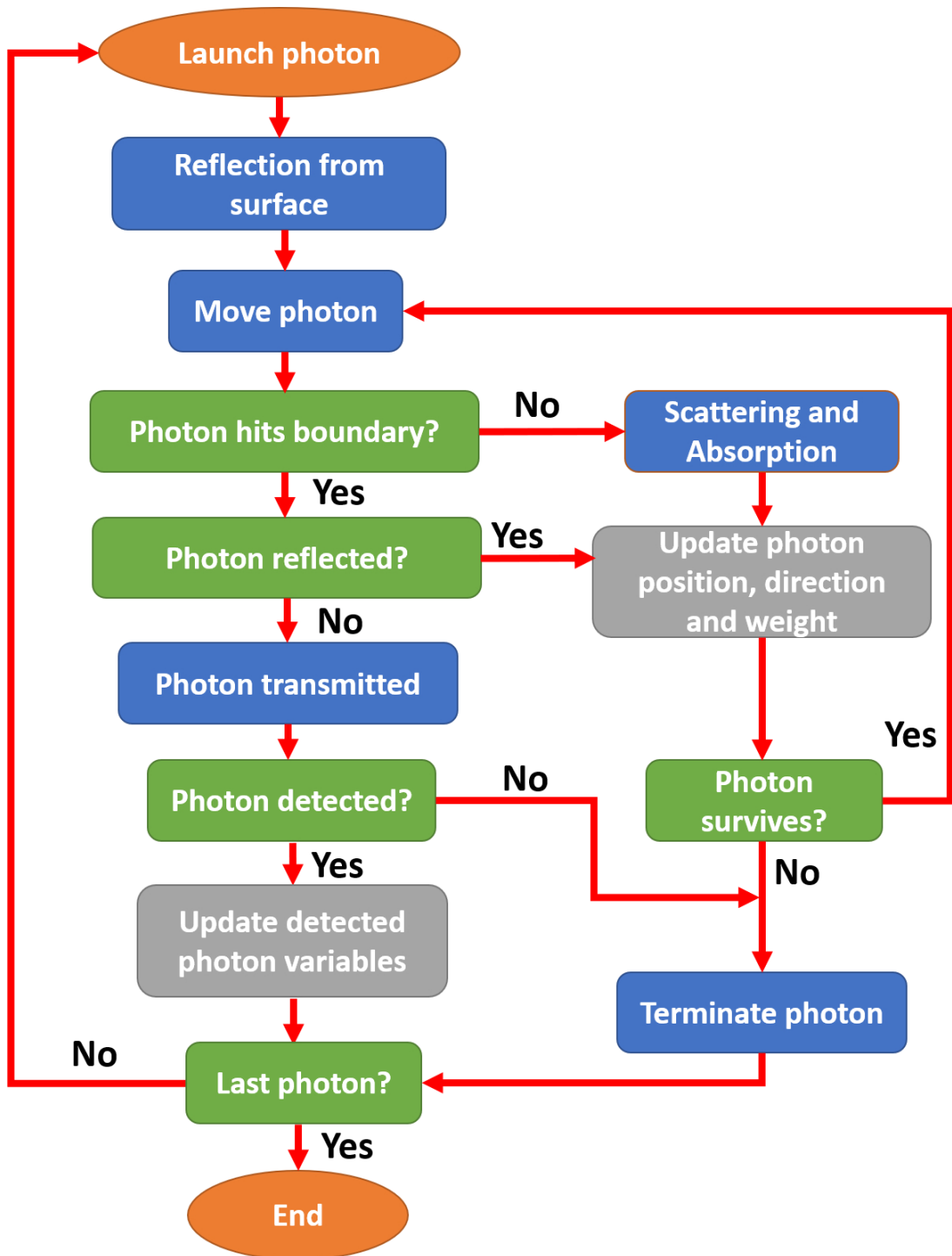


Figure 6.4: The flowchart for the algorithm of Monte Carlo modelling is presented.

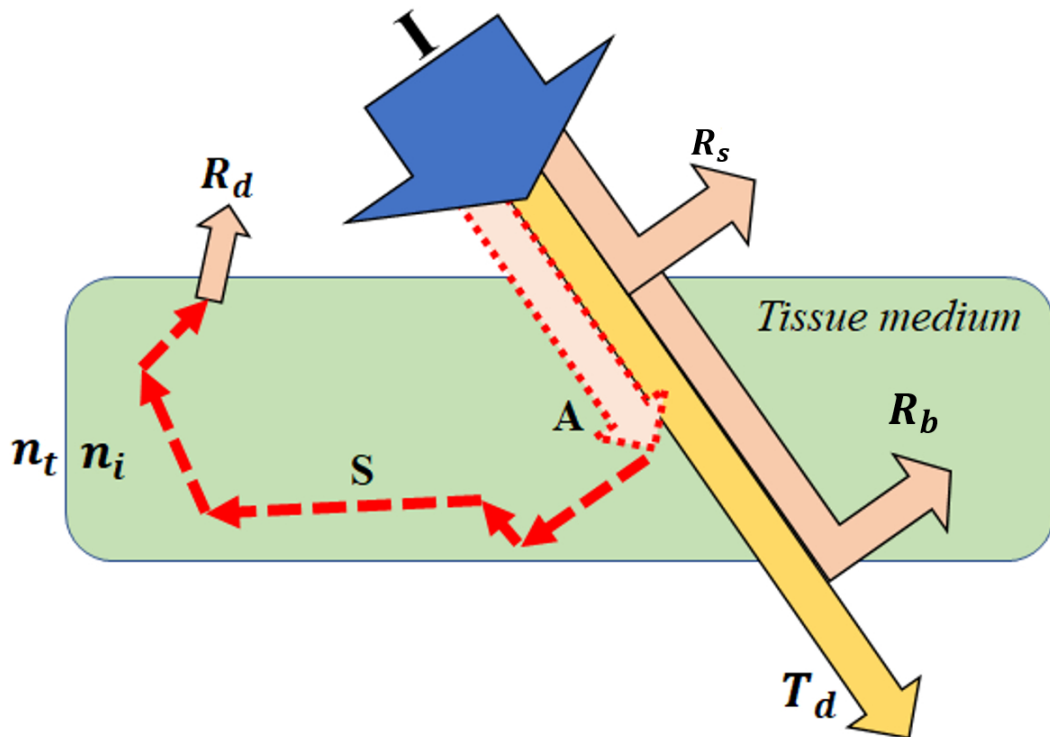


Figure 6.5: Schematic of light-tissue interactions to be simulated by the Monte Carlo model through a ‘slab’ of biological tissue is shown. The internal (tissue) medium and the transmitting (outside) medium have refractive indices n_i and n_t respectively. I is the total initial ‘weight’ of the photon incident cluster. A is the amount of light intensity absorbed in the medium, and S represents the scattering event of the remaining photon cluster. R_s and R_b respectively represent reflectance at the tissue surface (i.e., entrance of the photon cluster) and at any tissue boundary (reflectance at the bottom surface is shown in the diagram, however it can occur at the top surface also). R_d and T_d represent the weight of the photon cluster that exit from the top surface (i.e., diffuse reflectance) and the bottom surface (i.e., diffuse transmittance) respectively. The occurrences in the diagram follows the steps from the previous flowchart.

satisfy the criteria for the survival, termination of the photon propagation happened. For the photon surviving through the criteria, a new step size was made and the previous steps repeated. Iterations continued until the desired number of photon clusters were not simulated. Once the requirement was met, the program ended.

The physical theory of the light-tissue interactions behind the simulation has been discussed in Chapter 3. In the current section, the simulation steps following those physical theories will be discussed. The schematic Figure 6.5, that corresponds to the flowchart in Figure 6.4, summarises all the interactions between light and tissue occurred. The tissue medium represented by the green block, which (incident medium) has a refractive index n_i , whereas the outside (transmitting medium) refractive index is n_t . The incident weight of the photon cluster is (I). A part of the photon weight undergoes reflectance R_s on the medium surface, whereas some part of the weight undergoes reflectance R_b in the boundary of the medium. A part of the photon cluster is absorbed in the medium (A). The photon cluster with the remaining weight undergoes scattering event, i.e., shifts directions (S). It should be noted that scattering and absorption events take place simultaneously at each interaction site, i.e., each time the photon cluster interacts with a scattering centre (though in the schematic, the absorption is shown only once). The photon cluster might leave the tissue from the top surface, contributing to the diffuse reflectance R_d . It also can leave the tissue from its bottom surface to the transmitting medium resulting in the diffuse transmittance T_d . All the reflected, absorbed and transmitted photon weights always are summed up to give the incident photon weight:

$$R_d + R_s + A + T_d = I \quad (6.17)$$

6.2.6.1 Incidence of photon

The first step of the simulation was to introduce a photon cluster with an initial weight, and the initial position and direction. The initial position and direction of the photon depended on the characterisation of the photon ‘source’. In the MC model, there are provisions to incorporate different types of optical radiation, such as, collimated Gaussian beam, incidence from isotropic source, plain flat beam source, optical fibre source etc. [Jacques, 2011; Prahl, 1988; Phillips *et al.*, 2010; Reif *et al.*, 2007]. In this thesis, three

cases of photon incidence are considered for different applications which are described below.

- **Collimated beam from a point source:** Photons were launched perpendicular to the tissue (i.e, $\theta = 0$). The direction cosines were calculated using Eq. 6.5. The photons were incident exactly on the origin. Therefore, position co-ordinates and direction cosines of the incident photon are given below:

$$\begin{aligned}
 x &= 0, \\
 y &= 0, \\
 z &= 0; \\
 \mu_x &= 0, \\
 \mu_y &= 0, \\
 \mu_z &= 1.
 \end{aligned}
 \tag{6.18}$$

- **Collimated Gaussian beam:** Photons were launched as collimated Gaussian beam (e.g., laser). Here, the beam was considered to emerge from a ring shaped source placed on the tissue surface, as shown in Figure 6.1. Let us consider the Figure 6.6 representing the top view of the photon ‘launch’ down into tissue. A choice of the launch position was described by a radius r and an angle ψ . The co-ordinate system used for the incidence of the Gaussian beam was different from the other two systems used to define the tissue geometry and the photon movement. The origin of this present co-ordinate system coincided with that of the Cartesian co-ordinate system.

Gaussian beam has a probability distribution function which is given by (in normalised form) [Wang and Jacques, 1992]:

$$p(r) = \frac{e^{-\frac{r^2}{b^2}} 2\pi r}{\pi b^2}
 \tag{6.19}$$

where b is the $1/e^2$ radius (i.e., the radius where the intensity values fall to $1/e^2$ of its axial values). Integrating the probability function over the entire area of the annular ring, it is obtained as:

$$\int_0^\infty p(r)dr = 1.
 \tag{6.20}$$

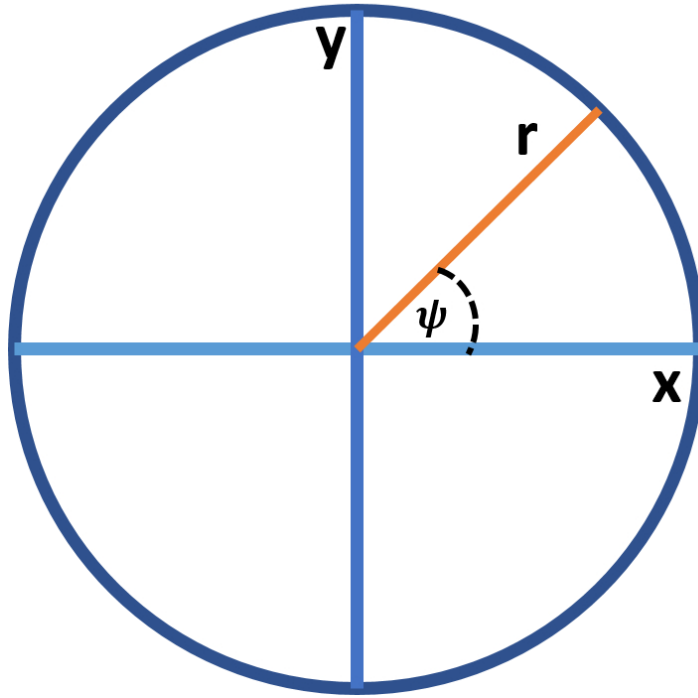


Figure 6.6: The diagram presents the top view of the incidence of a cylindrically symmetric Gaussian beam to the tissue surface. In the 2D polar co-ordinate system, the photon has a radial position r and an angle ψ with the x-axis.

Due to cylindrical symmetry, the radius and angle of the photon should be randomly generated within the circumference of the source. Recalling Eq. 6.16, the above probability can be expressed in the form of a random number $\xi \in (0, 1)$:

$$\begin{aligned}
 \int_0^{r_1} p(r) dr &= \xi \\
 \Rightarrow 1 - e^{-\frac{r_1^2}{b^2}} &= \xi \\
 \Rightarrow r_1 &= b \sqrt{-\ln(1 - \xi)} \\
 &= b \sqrt{-\ln(\xi)}
 \end{aligned} \tag{6.21}$$

which expresses the probability of finding the radial position within 0 and a certain value r_1 . $-\ln(1 - \xi)$ and $-\ln(\xi)$ are equivalent as ξ is uniformly distributed between 0 and 1.

Using this expression, the radial position r of the photon is generated randomly and repeatedly. Also, the radial angle ψ is chosen randomly between 0 and 2π :

$$\psi = 2\pi \cdot \xi \tag{6.22}$$

Utilizing the above two conditions, the x and y position co-ordinates of the photon on the tissue surface are determined. Considering the photon is incident on the tissue surface, the position co-ordinates are given below:

$$\begin{aligned}x &= r_1 \cdot \cos \psi \\y &= r_1 \cdot \sin \psi \\z &= 0.\end{aligned}\tag{6.23}$$

Due to normal incidence, the direction cosines are the same as the collimated beam from a point source described before: $\mu_x = 0$, $\mu_y = 0$, $\mu_z = 1$.

- **Incidence from optical fibre:** The source fibre had a circular emitter of radius r (mm). Thus the co-ordinates of the incident photon were constrained by the emitter diameter. The x and y-coordinates of the photon were described as:

$$\begin{aligned}x &= (2\xi - 1)r \\y &= (2\xi - 1)r\end{aligned}\tag{6.24}$$

so that

$$(x^2 + y^2) < r^2\tag{6.25}$$

where ξ is a randomly generated number between 0 and 1. Since photon is supposed to be launched on the tissue-surface, the initial value for the z-coordinate is $z = 0$.

The numerical aperture NA of an optical fibre is a dimensionless number that characterizes the range of angles over which the system can accept or emit light, i.e., the light fallen within the range of angles defined by the NA of an optical fibre will be entered and transmitted by the fibre. It is expressed as the *sin* of the ‘acceptance angle’ of the fibre. An acceptance angle is the maximum angle of a light beam (against the fibre axis) hitting the fibre core which allows the incident light to be guided by the core. Considering (θ) to be the acceptance angle of the optical fibre in this case, as depicted in Figure 6.7, the numerical aperture of the fibre is defined as:

$$NA = n \sin \theta \quad (6.26)$$

where n is the refractive index (r.i.) of the outside medium.

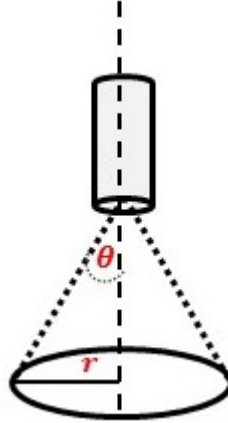


Figure 6.7: Incidence of the photon cluster from source fibre of radius r and numerical aperture $NA = n \sin \theta$, where θ is the half-acceptance angle of the fibre.

Considering the equal probability of angles about the axis of fibre, it is considered that the photon cluster can be incident at any angle within the acceptance cone of the optical fibre. Thus the zenith angle of the incident photon (considering outside medium to be air so that $n = 1$) can be written as:

$$\theta = \xi \sin^{-1}(NA) \quad (6.27)$$

The azimuthal angle of the photon can take any value between 0 and 2π and can be expressed in terms of a random number ξ as:

$$\phi = 2\xi\pi \quad (6.28)$$

Henceforth, an incident photon cluster was ready for propagation with its initial weight w , position co-ordinates (x, y, z) and the direction cosines (μ_x, μ_y, μ_z) .

6.2.6.2 Step size calculation and moving photon

In order to move the photon, a 'step size' l was calculated. A step size refers to the free path length of photon, i.e., the pathlength it traverses without being absorbed or

scattered, which is also the distance between two consecutive interaction (scattering and absorption) sites. As the photon took a path randomly within tissue, the step size was calculated by the random sampling of the probability of photon path through tissue. Let us define a suitable normalised probability distribution function for the free pathlength: $p(l)$, expressed as a function of the total interaction coefficient of tissue, $\mu_t = \mu_a + \mu_s$ [Wang and Jacques, 1992]:

$$p(l) = \mu_t e^{-\mu_t l} \quad (6.29)$$

so that

$$\int_0^{\infty} p(l) dl = 1 \quad (6.30)$$

Therefore, following the rule of random sampling of variable, the probability of photon free path taking a value between 0 and $l = l_1$ can be expressed as a random number $\xi \in (0, 1)$ according to Eq. 6.16:

$$\begin{aligned} \int_0^{l_1} p(l) dl &= \xi \\ \Rightarrow \int_0^{l_1} \frac{e^{-\mu_t l}}{\mu_t} dl &= \xi \\ \Rightarrow 1 - e^{-\mu_t l_1} &= \xi \\ \therefore l_1 &= \frac{-\ln(1 - \xi)}{\mu_t} = \frac{-\ln(\xi)}{\mu_t} \end{aligned} \quad (6.31)$$

For a highly scattering medium as tissue, $\mu_s \gg \mu_a$, thus, $\mu_t \simeq \mu_s$, expressing the pathlength as:

$$l_1 = \frac{-\ln(\xi)}{\mu_s}. \quad (6.32)$$

Once the pathlength, i.e., the ‘step size’ was determined using the above equation, the new position of the photon (x', y', z') was updated as [Wang *et al.*, 1995]:

$$\begin{aligned} x' &= x + \mu_x \cdot l_1 \\ y' &= y + \mu_y \cdot l_1 \\ z' &= z + \mu_z \cdot l_1. \end{aligned} \quad (6.33)$$

6.2.6.3 Absorption and scattering

Through the step size, the photon was moved to an interaction site and went through the absorption and scattering events. The absorbed fraction of photon weight is expressed by

an absorption factor $a = \frac{\mu_a}{\mu_t}$. Therefore, the absorbed weight Δw is given by

$$\Delta w = w.a = w \frac{\mu_a}{\mu_t}. \quad (6.34)$$

The unabsorbed amount of photon cluster, i.e. $w = w - \Delta w$ then was subjected to the scattering event.

Scattering of photon was achieved by deviating the photon direction by a deflection angle θ ($0 \leq \theta < \pi$), and simultaneously rotating through an azimuthal angle, ϕ ($0 \leq \phi < 2\pi$). The scattering angle was calculated by random sampling of its probability density function determined from the Henyey-Greenstein phase function, introduced in Chapter 3. Recalling Eq. 3.8, putting the value of $p(\cos\theta)$, the value of cosine of the deflection angle was obtained in the term of the random number ξ and anisotropy factor g as:

$$\cos\theta = \begin{cases} \frac{1}{2g} \left[1 + g^2 - \left(\frac{1-g^2}{1-g+2g\xi} \right)^2 \right] & \text{if } g \neq 0 \\ 2\xi - 1 & \text{if } g = 0. \end{cases} \quad (6.35)$$

Next, the azimuthal angle ϕ , uniformly distributed between 0 and 2π , was sampled as:

$$\phi = 2\pi\xi. \quad (6.36)$$

Once both the angles were calculated, the new directions of photon cluster were updated using the following relationships [Cashwell and Everett, 1959]:

$$\begin{aligned} \mu'_x &= \frac{\sin\theta(\mu_x\mu_z \cos\phi - \mu_y \sin\phi)}{\sqrt{1-\mu_z^2}} + \mu_x \cos\theta; \\ \mu'_y &= \frac{\sin\theta(\mu_y\mu_z \cos\phi + \mu_x \sin\phi)}{\sqrt{1-\mu_z^2}} + \mu_y \cos\theta; \\ \mu'_z &= -\sin\theta \cos\phi \sqrt{1-\mu_z^2} + \mu_z \cos\theta. \end{aligned} \quad (6.37)$$

If the photon was sufficiently close to the z-axis, then the following formulas should be used:

$$\begin{aligned} \mu'_x &= \sin\theta \cos\phi \\ \mu'_y &= \sin\theta \sin\phi \\ \mu'_z &= \text{SIGN}(\mu_z) \cos\theta \end{aligned} \quad (6.38)$$

where $\text{SIGN}(\mu_z)$ returns 1 when μ_z is positive, and returns -1 when it is negative.

6.2.6.4 Correction at the boundary

During travelling through tissue, each time the photon interacted with the boundary, the events of reflection and transmission took place. For these events to occur, the refractive index mismatch between both sides of the boundary line was necessary. In the model, the refractive index mismatch was found at the air-tissue interface only. Thus, the boundary correction was implemented in the following conditions:

1. **At surface:** When a photon cluster was incident from the source on the tissue term, reflection took place and a fraction of the photon weight was always lost. In all cases in the modelling, it was assumed that the photon clusters were normally incident from the source on the tissue surface. Therefore, the Fresnel's reflection equation for normal incidence ($\theta_i = 0^\circ$) was used for calculating the reflection factor at the surface, i.e., R_s [Born and Wolf, 2013; Ganesan and Hecht, 2008]:

$$R_s = \left(\frac{n_i - n_t}{n_i + n_t} \right)^2. \quad (6.39)$$

Upon incidence, the weight w of the photon was lost by $R_s \cdot w$, and the photon entered the medium with a weight $w = w - R_s \cdot w$.

2. **At boundary:** During travelling through the tissue medium, when the photon cluster reached the air-tissue boundary either at the top $z = 0$, or at the bottom $z = t$ (for a tissue volume of finite thickness t), reflection or transmission took place. In case of light travelling from an optically denser medium to an optically rarer medium, e.g., from tissue to air (i.e., $n_i > n_t$), for the angle of incidence θ_i larger than the critical angle θ_c , 'total internal reflection' takes place while in other cases, the reflection or transmission depended on the *reflectance* R . The conditions were defined as follows:

$$R = \begin{cases} \left(\frac{n_t - n_i}{n_i + n_t} \right)^2, & \text{if } \theta_i \approx 0 \\ \frac{1}{2} \left[\frac{\sin^2(\theta_i - \theta_t)}{\sin^2(\theta_i + \theta_t)} + \frac{\tan^2(\theta_i - \theta_t)}{\tan^2(\theta_i + \theta_t)} \right], & \text{if } 0 < \theta_i < \theta_c \\ 1, & \text{if } \theta_c \leq \theta_i < \pi/2. \end{cases} \quad (6.40)$$

If the photon hit boundary, a check was made to determine whether the photon was internally reflected or transmitted by comparing the reflection coefficient R with a

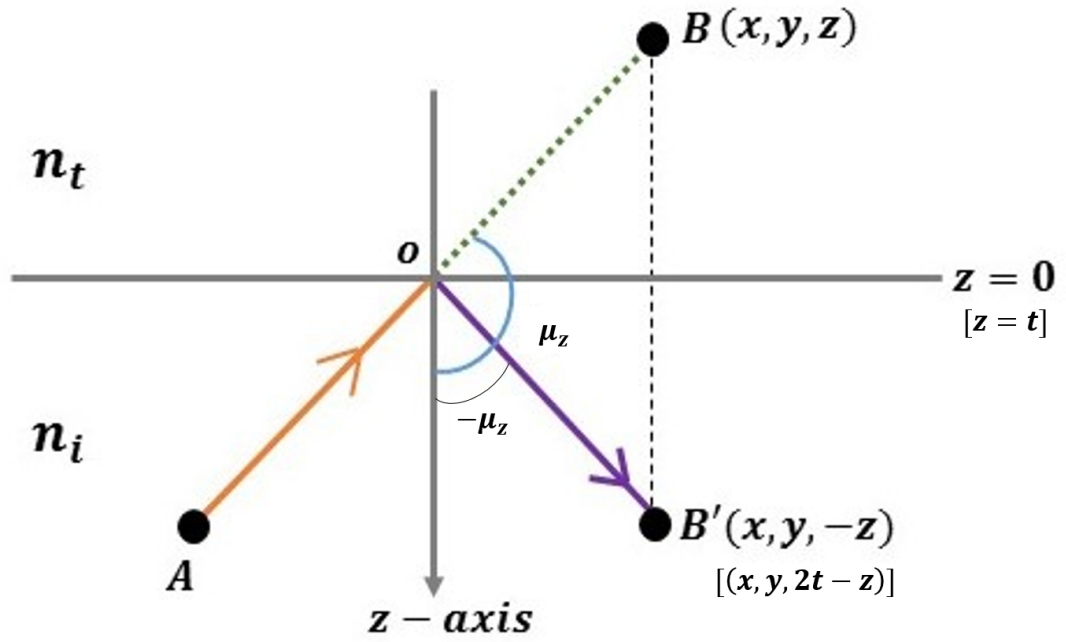


Figure 6.8: The correction for reflection at boundary in the model is shown. From the position A, a new step size of the photon cluster is generated such that the photon reaches B crossing the boundary. To make the correction at boundary, the photon position and direction cosines are reversed so that photon is traced at the position B'. The position is updated as $z = -z$ (if the photon hits the the top boundary $z = 0$) or $z = 2t - z$ (if photon hits the bottom boundary $z = t$, t being tissue thickness), and the direction is updated as $\mu_z = -\mu_z$. The alternative cases are written within brackets.

randomly generated number ξ . If $R > \xi$, the photon cluster would transmit, else it would reflect internally.

For a slab of thickness t , the coordinates of a reflected photon was achieved by updating its position and direction with respect to z -axis only. Thus, after reflection, the position and direction of the photon was updated as:

$$z = \begin{cases} -z, & \text{if } z < 0 \\ 2t - z & \text{if } z > t \end{cases} \quad (6.41)$$

$$\mu_z = -\mu_z.$$

The reflection and refraction process was depicted in the Figure 6.8.

6.2.6.5 Termination of photon propagation

The propagation of photon ended in two circumstances:

1. The photon was ‘detected’.
2. The photon did not ‘survive’.

Let us first discuss the detection part. Different Monte Carlo models define different detection criteria according to the requirement. In the present work, the photon clusters were detected if their position and direction co-ordinates fell within the area of a ring-shaped detector of a known radius, placed on the tissue surface (top or bottom, depending on the mode of application). Once the photon cluster was detected, its propagation in the medium was terminated. The detected ‘weight’ of photon is called ‘reflectance’ when the detector was placed at the same side of tissue adjacent to the source (in reflectance geometry), and ‘transmittance’ when the detector was placed at the opposite side to the source (in the transmittance geometry). Once the photon was detected, numbers of related variables were updated, such as the total transmittance or reflectance detected, optical pathlength and photon weight, number of scattering in medium, absorbed weight in tissue-layer, the distribution of the scattering centres in the medium, penetrated depth and so on.

The photon cluster, on the other hand, was discarded when it did not meet the criteria for ‘survival’. A fraction of photon weight was absorbed in the tissue at each interaction site. After each interaction event it was checked whether the photon weight has dropped below a certain threshold weight w_{th} . Usually, for the photon migration through biological tissue, the value was set to $w_{th} = 10^{-4}$. A photon cluster with weight w below the threshold (i.e., $w < w_{th}$) was unlikely to contribute to any information from the tissue. In other words, the weight of photon which is equivalent to the intensity of the beam became too feeble to be detected. Hence, the photon was terminated. However, the termination of a photon below a certain threshold might impose a bias to the termination technique. The biased termination of photons might compromise with the law of conservation of energy [Wang and Jacques, 1992; Prahl, 1995]. To deal with this problem, a probabilistic method was used for the photon termination which is known as Russian roulette. This paradigm gave a chance to one photon in, say, m number of photons to survive with an additional weight of mw . Usually, it was considered that $m = 10$. If the photon did not survive the Russian roulette, its weight was reduced to zero and its propagation was

ceased. Therefore, the rule of survival of a photon having a weight below the threshold ($w < w_{th}$) was expressed as:

$$w = \begin{cases} mw & \text{if } \xi \leq \frac{1}{m} \\ 0 & \text{if } \xi > \frac{1}{m}. \end{cases} \quad (6.42)$$

Once the photon was terminated, a new photon was launched and the loops continued until the desired number of photons were detected. Once the requirement was met, the program ended.

6.3 Implementation strategy

The MC model was designed in MATLAB (Mathworks, Inc., USA) version 2015b (licensed by City, University of London). A 64-bit Operating System with an installed memory of 24 GB and an Intel Xeon CPU (2.40 GHz, 2 processors) was dedicated for the simulation. The code was written using ‘parallel programming’ method utilising an inbuilt MATLAB function in 16 parallel threads. Figure 6.9 describes the detailed strategy to implement the Monte Carlo model for different applications in the frame of the thesis.

6.3.1 Input and output

Figures 6.9 (a) and (b) respectively present the model inputs and outputs. The input parameters to define the tissue volume were its optical properties (μ_a , μ_s , g , n) at the operating wavelength λ , and its anatomical properties (thickness of tissue, stratification of tissue layers, the concentration of absorbers present in the layers etc.). The input sensor geometry was defined by the shape, dimension and position of the optical source and detector. The model was provided with the information on the desired number of detected photon so that the program ends when this requirement is met. In the output, MC model provided the information on weight of detected photon, distribution of photon scattering events in tissue, optical pathlength, depth of penetration, number of scattering in tissue, absorbed photon weight in tissue layer(s), the record of lost photons (i.e., photons leave tissue without being detected or fall below the threshold weight), number of reflected and transmitted photon from boundary and time consumed for the interactions.

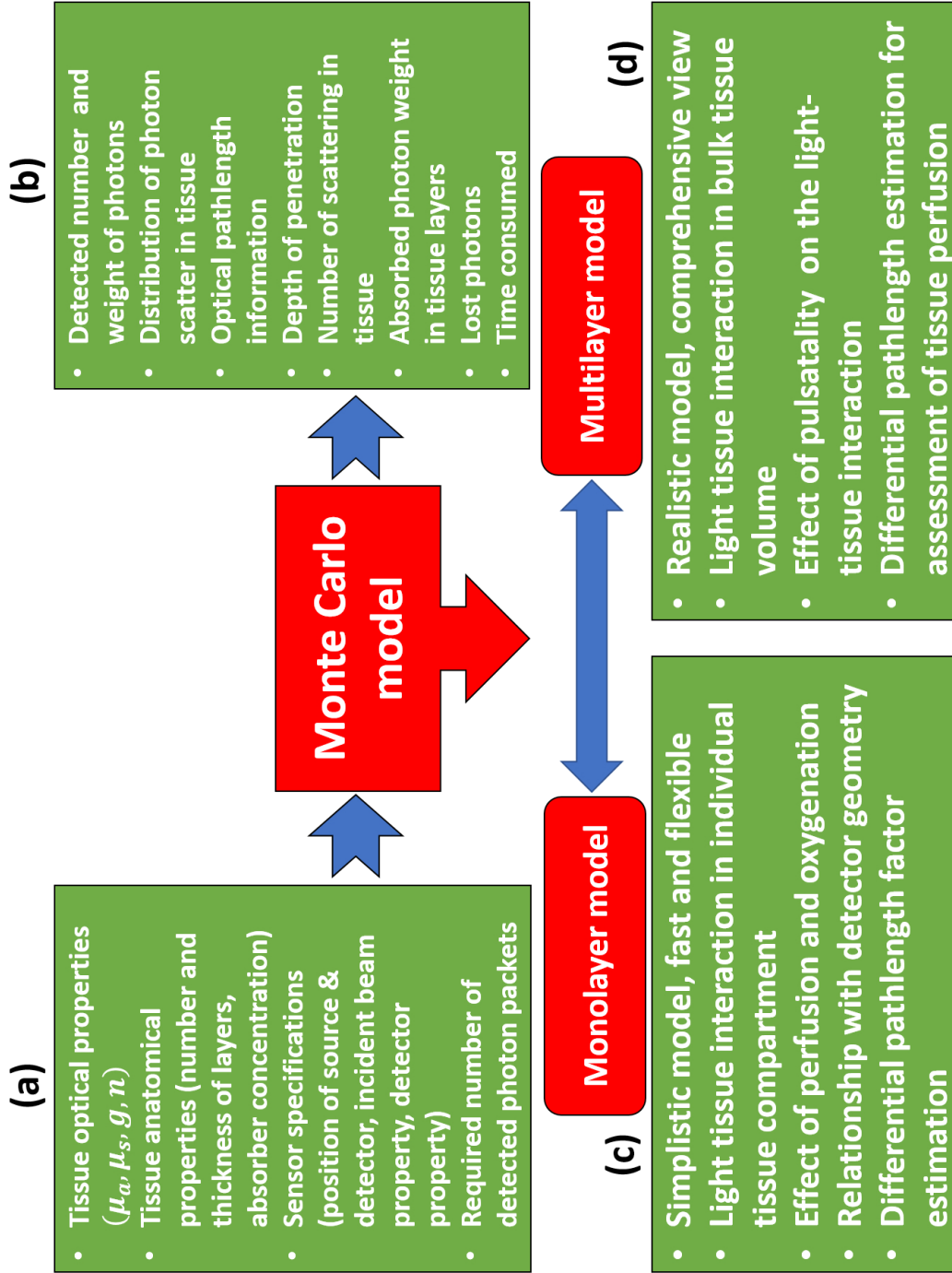


Figure 6.9: Flowchart shows the steps for implementation and execution of Monte Carlo strategy in the present work. The blocks (a) and (b) represent the ins and outs of the core Monte Carlo procedure. The blocks (c) and (d) point the features and applications of the monolayer and multilayer models.

6.3.2 Monolayer and multilayer model

On the basis of the level of heterogeneity induced in the tissue model, there were two categories of the MC approach: monolayer modelling and multilayer modelling.

A monolayer model consisted of a single homogeneous layer of tissue defined by its optical properties, for example, dermal skin, fat, muscle, brain matter etc. Although a single layer of tissue cannot be isolated in the case of *in vivo* experiments or practical applications with human subjects, such *in vitro* experiments are possible in the lab environment. Studies with a single layer of tissue provided an insight into the precise nature of anatomical and optical properties exhibited by particularly that layer. Several obvious advantages associated with the monolayer model, such as, simplicity to design, flexibility to induce any physiological variations, and of course, fast computational speed. In this work, the monolayer model was initially explored for validating the implementation protocols, and was further executed to investigate the light-tissue interactions in a perfused tissue.

On the other hand, a multilayer tissue model consisted of multiple layers of tissue with different optical properties. Numbers of individual homogeneous monolayers combined to form a heterogeneous multilayer tissue model. The level of the heterogeneity of a multilayer model depended on the application. In this work, multilayer models of human finger and forearm were simulated and explored for detail investigation on light-tissue interaction in photoplethysmography.

The monolayer model complemented the multilayer models, whereas the multilayer model presented a comprehensive view of the light-tissue interaction in the bulk tissue of interest. Therefore, studies with both the models were equally important in the thesis.

6.3.3 Execution of the model

This section describes the execution of the MC model. The outputs from the model which were recorded for all applications were:

- **Distribution of photon scattering** was the density plot of the position co-ordinates of the scattering centres distributed in the three-dimensional geometry.

- **Depth of penetration** was the maximum perpendicular distance from the tissue surface along the negative z-axis covered by a photon. The mean of the highest absolute magnitudes of the z-coordinate of each detected photon gave the quantification of the penetration depth
- **Optical path** was the sum of the step sizes (according to Eq. 6.32) a photon takes to travel from the source to detector.
- **Weight** of the detected photon was recorded as ‘reflectance’ or ‘transmittance’ depending on the detection geometry. Also, the weight of the absorbed photon in each layer of tissue was scored.

Two different photon capture techniques were used for the detection of photons, which are detailed below.

- **Fixed detector technique:** For the demonstration of the interaction events within tissue, the model was executed for a fixed source-detector separation d . In this case, a given number of photon clusters were detected when they crossed the boundary and reached the detector area.
- **Moving detector technique:** applications where a very large number of photons had to be simulated through a vast range of source-detector separations, this technique was used. Consider photons had to be detected at n separations (from source placed at the origin) in ascending order: d_1, d_2, \dots, d_n . In this case, it was very time consuming to detect photons separately in all distances. Instead, photons were detected whenever they cross the boundary anywhere within the maximum separation d_n , and the distance of the emerging point (having a co-ordinate $(x, y, 0)$) from the source (i.e., origin $(0, 0, 0)$) was calculated as:

$$d = \sqrt{x^2 + y^2} \quad (6.43)$$

The detector was basically simulated as a sliding window of a width equal to the detector diameter. The information on the detected photons in each sliding detector position at different distances were calculated by accumulating the data in the area defined by adequate bin sizes (i.e., detector diameters), and obtaining the histogram plots for optical path, depth, weight etc.

Both fixed and moving detector technique were used for the reflective mode investigations. For the transmissive mode, only the fixed detector technique was used. The applications of these techniques will be discussed in the following chapters in the thesis.

6.4 Summary

In the first section of this chapter, detail methodology for developing the MC model for this work has been described. Incidence of photon as a cluster has been considered in the model that is initiated with a weight equals to unity, and that weight gradually decays due to the absorption losses within the tissue medium, and after a certain threshold the photon cluster is terminated or propagated based on a probability check. The propagation of the photon cluster within the medium depends on the randomly generated pathlengths, and scattering angles. The model also incorporates the provision for the corrections due to reflection at the surface and the boundary. For the sampling of random variables, pseudo-random numbers (having values number between 0 and 1) were generated repeatedly. Since the cumulative distribution function of the random number and the variable was shown to have an one-to-one correspondence, the variables could be generated randomly as functions of the random numbers as many times as required. The methodology follows the light-tissue interaction theory discussed in Chapter 3. The assumptions for the model have been discussed and the necessary calculations are shown. In the second section of the chapter, details on the basic protocols for implementing the model have been discussed. The inputs and outputs of the model were illustrated. The main feature of the Monte Carlo strategy in this thesis are the simultaneous application of monolayer and multilayer tissue models. With the flowchart of the implementation detail, the importance of both kinds of models have been addressed in this chapter. The two execution strategy of the photon detection, namely, fixed detector and moving detector techniques have been described which will be used frequently in the thesis. The specifications about the models will be discussed later on along with the applications in the thesis. The modelling strategy and protocols discussed in this chapter will be verified in next chapter.

CHARACTERISATION AND EVALUATION OF THE MONTE CARLO MODEL

7.1 Introduction

The process of development of the Monte Carlo model has been discussed in the last chapter. The features of the model will be characterised in this chapter. Before relying on the numbers produced by a model, it is important to validate the results. This chapter will validate the results produced using the developed Monte Carlo model by comparing those with the already established analytical solutions. The features of the model, that has been defined in previous chapter, will be characterised by the simulated examples in this chapter. Also, the accuracy of the model will be verified in the chapter. For the purpose of characterisation and validation, the monolayer tissue volumes were simulated in this chapter.

7.2 Characterisation of the model

The recipe of the MC simulation was explained in Chapter 6. This will be further illustrated in this chapter by an example of simulation. The typical optical path of a single photon cluster simulated in a tissue medium is shown in Figure 7.1. As described in the last chapter, the tissue volume was characterised by its optical properties:

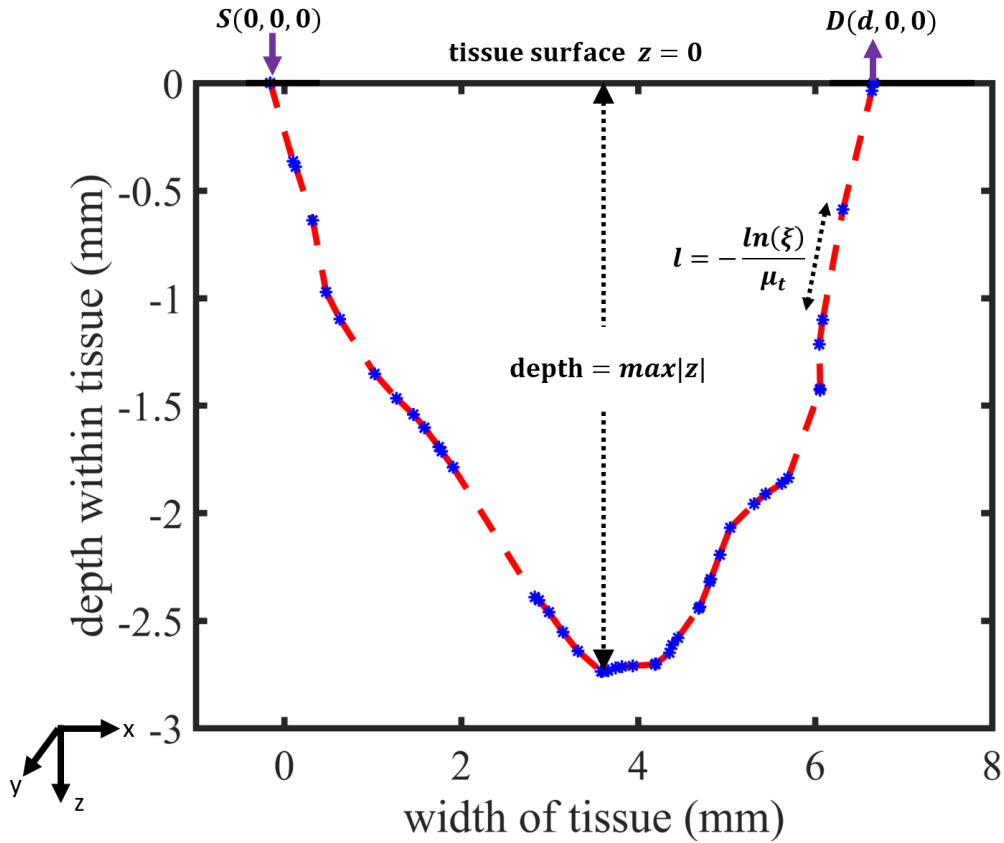


Figure 7.1: A typical path of a photon cluster traced in a medium is shown in a 2D projection (x-z plane) of the 3D model. Optical fibre source S and detector D are placed at the points (0,0,0) and (d,0,0) on the tissue surface $z = 0$ in this reflectance geometry. The blue dots are the positions of the photon cluster. Red dotted lines are the pathlength l . The plot describes the physical processes described in Figure 3.4.

$\mu_s = 36.36 \text{ mm}^{-1}$, $\mu_a = 0.09 \text{ mm}^{-1}$, $g = 0.876$, $n_i = n_t = 1$. The tissue specifications described the optical properties of the white matter of the human brain at 810 nm wavelength [Yaroslavsky *et al.*, 2002]. The 2D projection (x-z plane) of the 3D model is demonstrated in Figure 7.1. Source S was placed at the origin (0,0,0) of the Cartesian co-ordinate system, and detector D was placed at the point (d,0,0). Here, the optical fibre probe was used. The radii and numerical apertures for both the source and detector were kept the same, i.e., 1 mm and 0.39. In this reflectance geometry, both source and detector were placed on the tissue surface $z = 0$. The blue dots are the photon scatter positions. Red dotted lines joining the photon positions are the pathlength l in the simulated result. The maximum value of absolute z-coordinate presents the depth of penetration, and the angle between two consecutive scatter positions is the deflection angle θ . This also corresponds

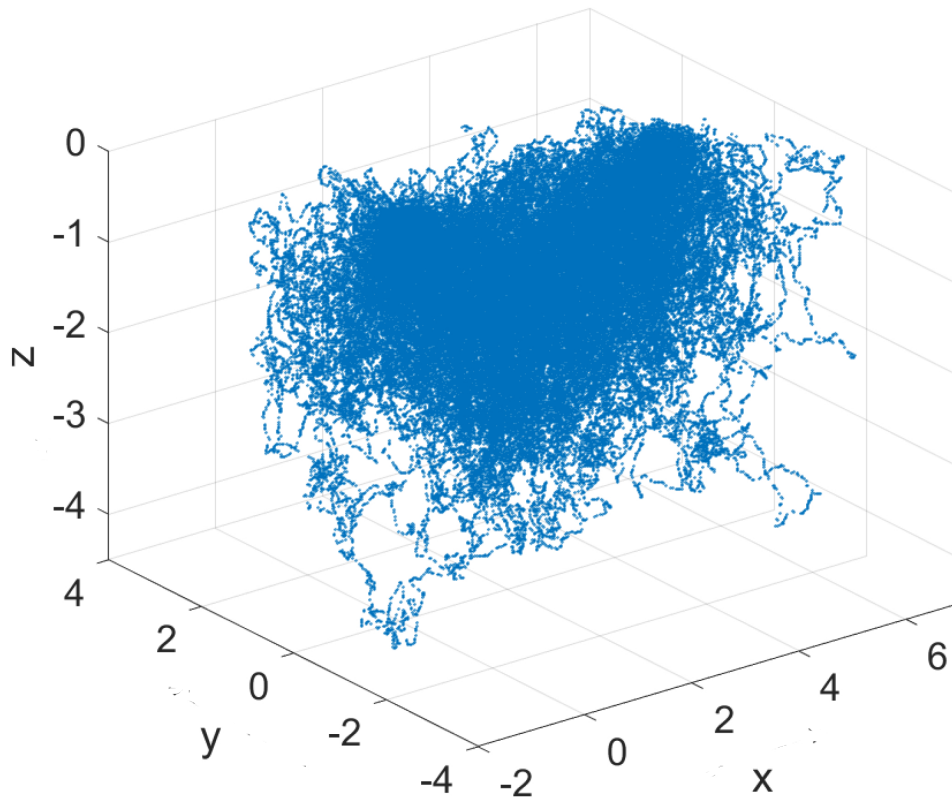


Figure 7.2: Scatter-plot of Monte Carlo simulated photon cluster distribution in tissue medium is presented in the (x,y,z) co-ordinate system. The path of the photon clusters from a source placed at origin $(0,0,0)$ and the detector $(4,0,0)$ in a reflectance geometry are shown. The randomness of the optical path is due to the random scattering of photon. Negative z -direction indicates depth within tissue.

to the description of scattering angle and mean free pathlength described in Figure 3.4. in the Chapter 3. The deflection angles generated in the tissue medium are small, leading to more forward scattering. The free pathlengths are randomly generated each time. All the variables used here have been already introduced in Chapter 6.

The scatter-plot distribution of the interaction events (scattering+absorption) through which the photon clusters propagated through the volume of tissue is shown in Figure 7.2. The plot shows the randomness of the photon cluster which was simulated by the random sampling of the step sizes and the scattering angles. A small number of photon clusters (10^3) were simulated. Although the scatter-plots are easy to compute in the MATLAB platform, such plots are inconvenient for simulating a very high number of photons.

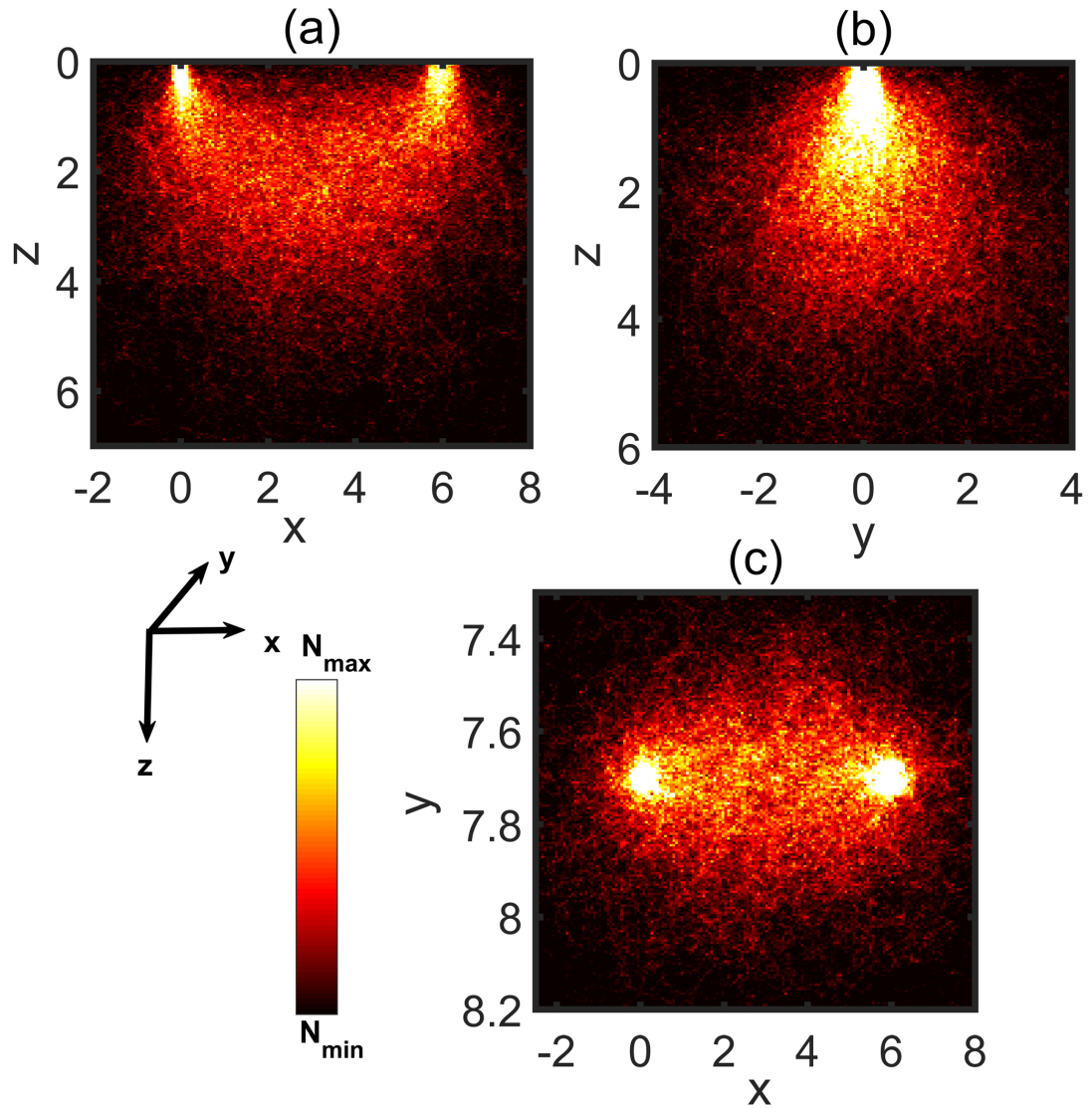


Figure 7.3: Density-plot of Monte Carlo simulated scatter distribution for photon clusters propagating through tissue from source to detector separated by a distance 6 mm is presented in the (x,y,z) co-ordinate system. Distribution in the three planes are shown separately: xz plane in (a) shows the direct cross-sectional view, yz plane in (b) shows lateral cross-sectional view, and the xy plane in (c) shows the top view of the photon scatter distribution from source to detector. Colourbar shows the distribution between the minimum and maximum number of scattering events (i.e., interaction events).

Instead, density-plots need to be used for handling a large number of data. Figure 7.3 presents the same scatter-plot in the form of density-plot. Images from the three different planes: xy , yz and xy are illustrated figures (a), (b) and (c) respectively. The colourbar represents the distribution of the number of scattering N between its minimum value $N_{min} = 0$ and its maximum value $N_{max} = 66 \times 10^4$. The brighter shade near the source and the detector in Figure 7.3(a) indicates the occurrence of the maximum scattering events in that region. The darker shade deeper within tissue refers to less number of scattering events. In the fixed detector technique (described in Chapter 6), the mean penetration depth of the photon clusters was calculated by averaging the maximum of absolute z co-ordinate of the photons, and the mean optical pathlength was calculated by averaging the total step sizes taken by the photons through tissue.

It should be noted that in this thesis, the Monte Carlo is discussed to simulate the light propagation through tissue to be detected in some specific geometries. Therefore, all previous images shown in this chapter are the path of photon clusters only that are detected in the reflectance geometry. However, if no detector is placed on the tissue, light traverses freely through it until they leave the tissue or become very weak to propagate further. An instance of the distribution of photon clusters in a detector-free tissue medium, having a source placed at the origin, are shown in Figure 7.4. In Figure 7.4 (a), a typical path of a single photon cluster is shown which starts from the point A, loses its energy (i.e., 'weight') through the absorption events and finally, is terminated at point B where it becomes too weak to survive (i.e., weight falls below w_{th}). In Figure 7.4(b), the scatter-plot of a 100 numbers of simulated photon clusters in the medium is shown. Since there is no cut-off criteria for the photon clusters, they follow random paths in any directions. Different colours shown the different optical paths, however, those are difficult to isolate because of their randomness. Figure 7.4 is presented for a complete understanding of the photon cluster distribution in a medium, however, in all further applications in this thesis, only the path of the detected photons clusters will be shown.

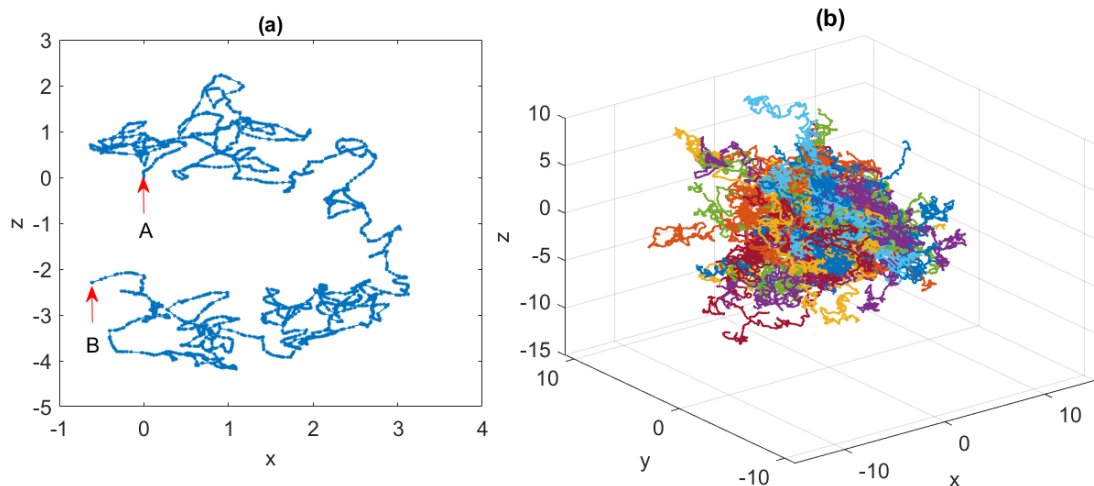


Figure 7.4: A typical distribution of *all* photon clusters in a medium is presented, i.e., the photon path is not restricted with any detection criteria. No photons beyond $z=0$ are discarded, and the only rule of termination of photon propagations is the weight of the photon falling below a threshold. The photon clusters are incident from a source placed at the origin $(0,0,0)$. A typical path of a photon cluster is shown in (a) in a 2-D geometry (xz plane). A and B are the positions of the start and end of the photon propagation, respectively. The typical paths of 100 photon clusters are shown in (b) in a 3D geometry (xyz plane). The optical paths appear to be randomly distributed. Different colours represent the different path of the photon clusters.

7.3 Evaluation of the model

The Monte Carlo model was verified by cross-checking with pre-validated results in the four different cases below.

Case I: The developed MC model was comprehensively validated through comparing the results of simulated diffuse reflectance R_d in a semi-infinite medium with: (a) the analytical result by [Giovannelli, 1955], (b) the results of adding doubling method (as mentioned in Chapter 5) by [Prah, 1988], and (c) the MCML code developed by [Wang *et al.*, 1995] (as stated in Chapter 5). The tissue medium was considered to have isotropic scattering property and a different refractive index than the outside medium. The parameters used for simulation in this case were: $n_i = 1.5$, $n_t = 1$, $\mu_a = 1 \text{ mm}^{-1}$, $\mu_s = 9 \text{ mm}^{-1}$, and $g = 0.0$. Ten simulations each with 5×10^4 photon clusters were iterated, as the same parameters were used in MCML application by [Wang *et al.*, 1995]. The calculated values of R_d and the standard error (i.e., deviation from the analytical value) are presented in

Table 7.1. The standard error was found to be minimal in the developed MC algorithm result.

Table 7.1: Simulated results of diffuse reflectance (R_d) compared with pre-validated results.

<i>References</i>	R_d	<i>Error</i>
Giovanelli [Giovanelli, 1955]	0.2600	–
Prahl [Prahl, 1988]	0.26079	0.00079
Wang [Wang <i>et al.</i> , 1995]	0.25907	0.00170
<i>Developed MC</i>	0.0.26029	0.0.00029

Case II:

The results of MC simulated diffuse reflectance R_d and transmittance T_d for a slab having finite thickness of 0.2 mm were compared with: (a) the results tabulated by [Hulst, 1957], (b) results obtained by [Prahl, 1988] using adding-doubling method, and (c) the results using MCML by [Wang *et al.*, 1995]. The tissue medium was considered to exhibit anisotropic scattering and to have the same refractive index as that of the outside medium (i.e., air). The parameters used for the simulation were: $n_i = n_t = 1$, $\mu_a = 1 \text{ mm}^{-1}$, $\mu_s = 9 \text{ mm}^{-1}$, and $g = 0.75$. The compared results are presented in Table 7.2. It was seen that the values of simulated R_d and T_d were in fair agreement with analytical and pre-validated data, with a very minimal standard error.

Table 7.2: Comparison of MC simulated total reflectance and transmittance with the analytical results for an anisotropic scattering tissue having matched boundary.

<i>Reference</i>	R_d	<i>Error</i>	T_d	<i>Error</i>
van de Hulst [Hulst, 1957]	0.0973	–	0.66096	–
Prahl [Prahl, 1988]	0.09711	0.00033	0.66159	0.00049
Wang [Wang <i>et al.</i> , 1995]	0.09734	0.00035	0.66096	0.00020
<i>Developed MC</i>	0.097397	0.000007	0.66074	0.00022

In Case I and case II, the energy conservation law was also verified to check the accuracy of the model. According to the law of energy conservation (which is also the basis of Radiative Transfer formalism discussed in Chapter 2), the total weight of the photon cluster should be maintained always. Therefore, the sum of the absorbance (absorbed weight, A), the diffuse reflectance (reflected weight, R_d) and the diffuse transmittance (transmitted weight, T_d) should always be equal to the incidence weight of the photon cluster, $w = 1$. In case I, $R_d = 0.2600$, $A = 0.7397$, so that $R_d + A = 1$. No transmittance

was recorded in Case I so $T_d = 0$. In case II, $R_d = 0.09737$, $T_d = 0.66074$, $A = 0.2419$, resulting in $R_d + T_d + A = 1$. Hence, the energy was conserved in both cases of Monte Carlo application.

Case III:

The results of transmittance and reflectance in a medium with the same refractive index as the outside medium (relative refractive index = 1) and exhibiting isotropic scattering were produced by the present MC model and were compared with the results: (a) tabulated by van de Hulst [Hulst, 1957], (b) the results of the adding-doubling method by Prahl [Prahl, 1988], and (c) the MC programs developed by van der Zee [Van der Zee, 1992] in Table 7.3. The results were obtained for a set of four values for albedo ($a = \frac{\mu_a}{\mu_t}$), and four values of a slab thickness t for each albedo, respectively with data. Results were averaged over 10^5 number of simulated photon clusters. The results showed fair agreement between the simulated and tabulated data.

Table 7.3: Comparison of developed Monte Carlo (MC) reflectance and transmittance simulations for an isotropic scattering slab with known thickness t and albedo a with the data tabulated by van de Hulst (vdH) [Hulst, 1957], van der Zee (vdZ) [Van der Zee, 1992] and Prahl (P) [Prahl, 1988].

t (mm)	<i>Reflectance</i>				<i>Transmittance</i>			
	MC	vdH	vdZ	P	MC	vdH	vdZ	P
$a = 0.4$								
0.25	0.0368	0.0357	0.037	0.0356	0.8112	0.8136	0.8120	0.8136
0.5	0.0550	0.0553	0.0524	0.0553	0.6596	0.6577	0.6610	0.6577
1.0	0.0737	0.0734	0.0716	0.0734	0.4233	0.4250	0.4260	0.4251
4.0	0.0838	0.0833	0.0837	0.0833	0.0270	0.0272	0.0272	0.0272
$a = 0.8$								
0.25	0.0833	0.0824	0.0837	0.0824	0.8581	0.8594	0.8580	0.8595
0.5	0.14130	0.1401	0.1430	0.1401	0.7353	0.7378	0.7340	0.7378
1.0	0.2073	0.2109	0.2090	0.2108	0.5451	0.5414	0.5440	0.5414
4.0	0.2844	0.2840	0.2870	0.2840	0.0754	0.0751	0.0754	0.0751
$a=0.9$								
0.25	0.0980	0.0965	0.0975	0.0965	0.8713	0.8733	0.8730	0.8733
0.5	0.1701	0.1690	0.1650	0.1690	0.7649	0.7653	0.7710	0.7654
1	0.2671	0.2674	0.2660	0.2674	0.5925	0.5916	0.5940	0.5916
$a=0.99$								
0.25	0.1122	0.1101	0.1090	0.1101	0.8846	0.8867	0.8860	0.8867
0.5	0.2017	0.1989	0.2030	0.1989	0.7910	0.7940	0.7900	0.7941
1	0.3361	0.3329	0.3290	0.3329	0.6478	0.6509	0.6550	0.6510
4	0.6444	0.6450	0.6450	0.6450	0.2765	0.2755	0.2760	0.2755

Case IV:

The reflectance and the transmittance for a tissue medium having scattering anisotropy were tabulated by van de Hulst [Hulst, 1957], which was reproduced by Prahl [Prahl, 1988] and P. van der Zee [Van der Zee, 1992]. Results simulated by the developed MC code with the same input variables, i.e., the HG scattering phase function with g values of 0.5, 0.875, and for albedo, $a = 0.9, 0.99$, each for thickness 0.5, 1 and 4 mm of the tissue slab are presented in Table 7.4. A 10^5 number of photon clusters were simulated. The average transmittance and reflectance were calculated. Good agreement was seen in all cases.

Table 7.4: Comparison of developed Monte Carlo (MC) reflectance and transmittance simulations for an isotropic scattering slab with known thickness t and albedo a with the data tabulated by van de Hulst (vdH) [Hulst, 1957], van der Zee (vdZ) [Van der Zee, 1992] and Prahl (P) [Prahl, 1988].

t (mm)	<i>Reflectance</i>				<i>Transmittance</i>			
	MC	vdH	vdZ	P	MC	vdH	vdZ	P
$a = 0.4, g=0.5$								
0.5	0.0714	0.0720	0.0739	0.0720	0.8681	0.8672	0.8650	0.8672
1	0.1294	0.1298	0.1290	0.1298	0.7397	0.7391	0.7390	0.7391
4	0.2617	0.2612	0.2620	0.2612	0.2498	0.2505	0.2490	0.2505
$a = 0.99, g=0.5$								
0.5	0.0862	0.0879	0.0874	0.0878	0.9074	0.9057	0.9060	0.9057
1	0.1694	0.1707	0.1690	0.1707	0.8158	0.8145	0.8160	0.8145
4	0.4687	0.4698	0.4670	0.4698	0.4537	0.4527	0.4550	0.4527
$a=0.9, g=0.875$								
0.5	0.0122	0.0125	0.0110	0.0125	0.9363	0.9354	0.9350	0.9354
1	0.0242	0.0238	0.0226	0.0238	0.8702	0.8701	0.8690	0.8702
4	0.0653	0.0657	0.0650	0.0658	0.5204	0.5212	0.5220	0.5212
$a=0.99, g=0.875$								
0.5	0.0151	0.0157	0.0155	0.0157	0.9795	0.9789	0.9790	0.9790
1	0.0321	0.0327	0.0322	0.0327	0.9564	0.9558	0.9560	0.9558
4	0.1413	0.1417	0.1400	0.1417	0.8008	0.8001	0.8020	0.8002

7.4 Correlating the optical parameters in the model

In order to check the effect of the individual optical parameters on the model behaviour, three sets of simulations were run and the output variables (e.g., mean optical path, absorbance, reflectance and transmittance) were measured. In all cases, the outputs were averaged over 50,000 simulations.

Case I:

According to Figure 7.5, MC model was executed for the absorption coefficient values from $0-10 \text{ mm}^{-1}$ with a scattering coefficient 50 mm^{-1} and an anisotropy factor 0.9 in a semi-infinite slab of 1 mm thickness with a refractive index matched boundary. As shown in Figure 7.5(a), the mean optical paths decreased with increasing absorption coefficient. The obvious reason was that the most of the photon weight was absorbed before it travelled a long distance in the medium. This explanation was supported by result in Figure 7.5 (b), (c) and (d) respectively. Results showed that the absorbance was increasing, and the reflectance and transmittance were decreasing. Higher values of the scattering coefficient and anisotropy factor were considered to simulate the highly forward scattering in the tissue medium.

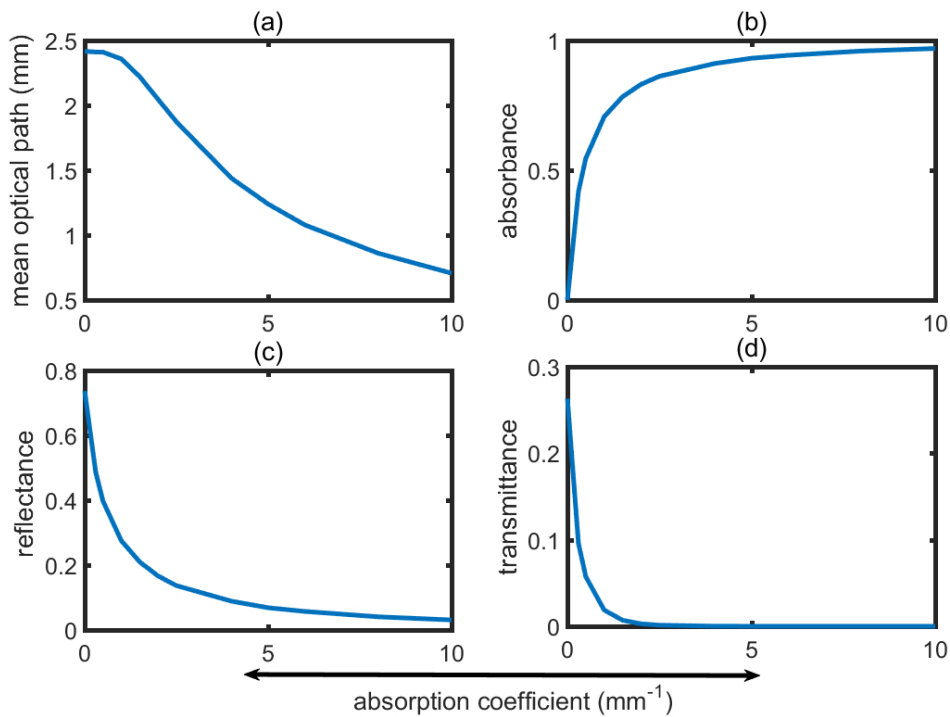


Figure 7.5: Monte Carlo simulated plots for mean optical path (a), absorbance (b), reflectance (c) and transmittance (d) are presented for a range of absorption coefficient values from $0-10 \text{ mm}^{-1}$ with scattering coefficient 50 mm^{-1} and anisotropy factor 0.9 in a semi-infinite slab of 1 mm thickness and refractive index matched boundary. Number of photon clusters simulated is 50,000.

Case II:

According to Figure 7.6, MC model was executed for the scattering coefficient values

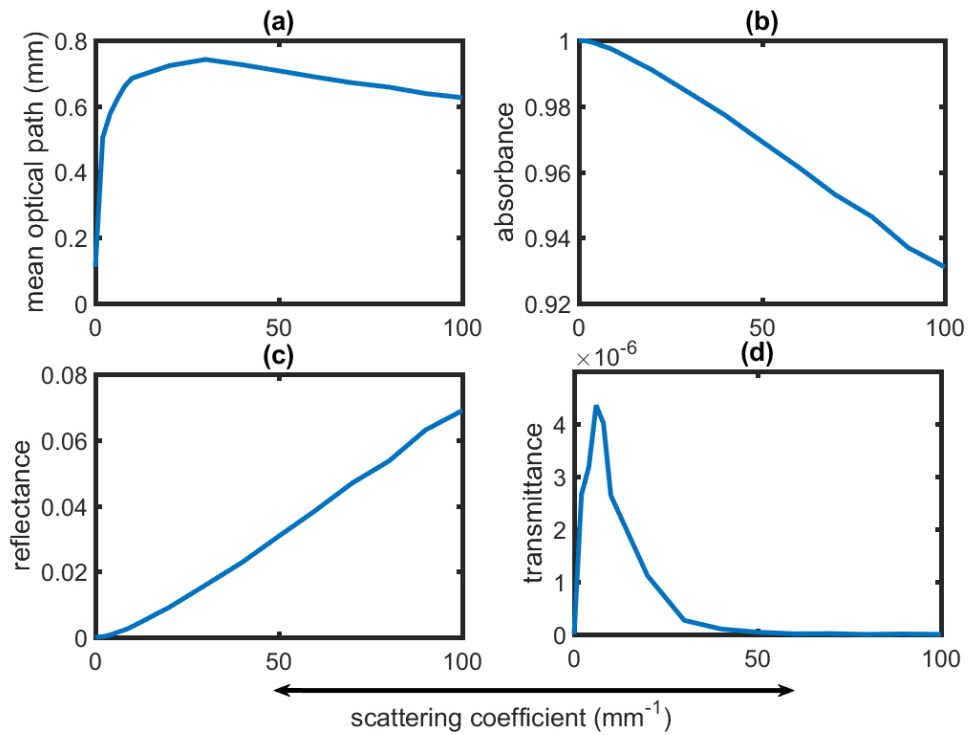


Figure 7.6: Monte Carlo simulated plots for mean optical path (a), absorbance (b), reflectance (c) and transmittance (d) are presented for a range of scattering coefficient values from 0-100 mm^{-1} with absorption coefficient 10 mm^{-1} and anisotropy factor 0.9 in a semi-infinite slab of 1 mm thickness and refractive index matched boundary. Number of photon clusters simulated is 50,000.

from 0-100 mm^{-1} with an absorption coefficient of 10 mm^{-1} , and an anisotropy factor of 0.9 in a semi-infinite slab of 1 mm thickness and refractive index matched boundary. As shown in Figure 7.6, optical path initially increased with the scattering coefficient, and then slowly decreased. This can be explained by the dependence of the optical pathlength on the total interaction coefficient $\mu_t = \mu_a + \mu_s$. Usually in biological tissue, $\mu_s \gg \mu_a$. In Figure 7.6, the high scattering region is the part where the optical path slowly decreased with the scattering coefficient. However, for $\mu_s \sim \mu_a$, i.e., in the beginning of the plot, the optical path increased sharply with the scattering coefficient. Since in this thesis, the subject of interest is the biological tissue, we should mainly concentrate on the part where $\mu_s > \mu_a$. The absorbance was found to fall sharply with an increasing scattering coefficient which is explicable by the measurement of absorbed photon weight: $\Delta w = w \cdot \left(\frac{\mu_s}{\mu_t}\right)$. Thus, the greater is the value of μ_s , the lower is the absorbance Δw . For the reverse reason, the reflectance increased with the increase of μ_s . The change in transmittance with the

increasing scattering coefficient could be related to the change in optical pathlength. Initially, with the higher optical paths, photons tended to cross the medium and transmit through it. However, with increasing scattering coefficient, the pathlength values dropped, i.e., lesser photons were able to transmit through tissue which resulted in a drop in the transmittance values.

Case III:

In Figure 7.7, MC model was executed for a range of anisotropy factor values from 0.1-0.9 with an absorption coefficient of 10 mm^{-1} and a scattering coefficient of 50 mm^{-1} in a semi-infinite slab of 1 mm thickness and refractive index matched boundary.

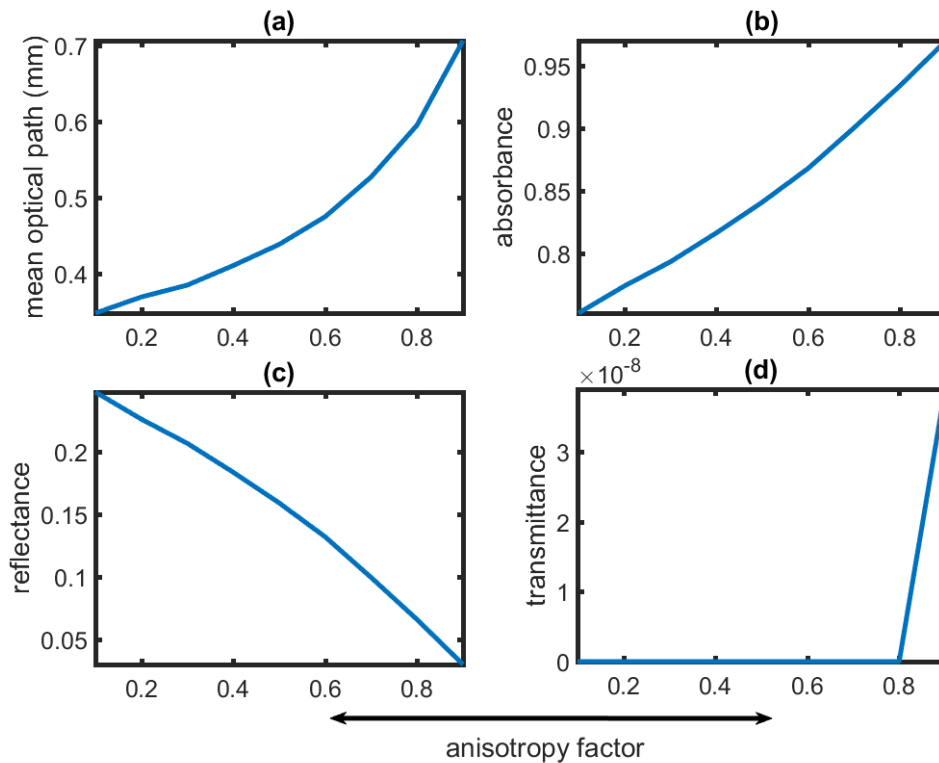


Figure 7.7: Monte Carlo simulated plots for mean optical path (a), absorbance (b), reflectance (c) and transmittance (d) are presented for a range of anisotropy factor values from 0.1-0.9 with absorption coefficient 10 mm^{-1} and scattering coefficient 50 mm^{-1} in a semi-infinite slab of 1 mm thickness and refractive index matched boundary. Number of photon clusters simulated is 50,000.

The optical path was found to be increasing with g . An increase in g indicated a gradual increase of the dominance of the forward scattering. This led the photons to take longer optical paths within the tissue. The increase in absorbance with g was the

result of an increased number of interactions in tissue. With increasing g , the reduced scattering coefficient of tissue $\mu'_s = \mu_s(1 - g)$ decreased. This resulted in smaller scattering angles and more forward scattering. Thus the number of interactions increased, which resulted in increasing absorbance. Again, increasing forward scattering led the photons to travel through higher values of optical paths from the source to the detector. Due to higher absorbance, less number of photons transmitted through tissue resulting in lower reflectance for high g . For smaller values of g , due to less forward scattering, most of the photon clusters reflected, and almost no photon clusters transmitted through tissue. With increasing g , forward scattering increased, resulting in increasing absorbance, and very low transmittance. Thus, the overall transmittance value was very small. A very small amount of photon weight (10^{-8}) transmitted only at a very high g value.

In all the above cases (Case I, II and III), for each value of the input variable, the values of reflectance, transmittance and absorbance were noted, and each time the energy conservation relationship $R_d + T_d + A = 1$ was verified.

7.5 Summary

In the first part of the chapter, the variables of the Monte Carlo model have been characterised. Introducing the parameters of the model was important to relate to the descriptions given in the following chapters. In the second part of the chapter, results from the model have been cross-validated. Different sets of simulations were performed to reproduce the results from the analytically obtained or re-validated data. All four cases of the simulation showed excellent agreement with the pre-validated results, and the correlations between the input and output variables have been demonstrated. In the third part of the chapter, the correlation between the basic input parameters (absorption and scattering coefficient, and anisotropy factor) and output variables (optical pathlength, absorbance, reflectance and transmittance) have been demonstrated. The validation and characterisation of the basic model make it a reliable and executable tool for the investigation of the light-tissue interaction of *any* bio-optical application. Based on the platform stated by this initial study, the following chapters will focus on investigating the light-tissue interaction in PPG.

INVESTIGATING LIGHT-TISSUE INTERACTIONS IN REFLECTANCE PHOTOPLETHYSMOGRAPHY USING MONOLAYER PERFUSED SKIN MODEL

8.1 Introduction

In this chapter, the development and execution of a single layer Monte Carlo model of perfused skin tissue will be presented. Perfusion is an important factor in the PPG-based measurement systems relying on the changes in the perfusion state (i.e., the volume of blood) in tissue. The model was executed in a dual wavelength, reflective mode PPG set-up. Pulse oximetry is the most common application of PPG which usually uses a dual wavelength setting. The results presented in the chapter, therefore, elucidate the fundamental properties of a reflective mode pulse oximeter as well. The operating wavelengths were 660 nm (red) and 940 nm (infrared), two commonly used wavelengths in pulse oximetry. The results presented in this chapter primarily concentrate on the light-tissue interaction in a perfused skin tissue in its static and pulsatile state.

8.2 Background

The last chapter addressed the relationship between the output variables and the input parameters of the basic MC model. To apply the model for the PPG that measures the

volumetric changes in blood and the pulse oximetry that measures the oxygen saturation of arterial blood, additional input parameters indicating the physiological state of tissue (for example, blood oxygen saturation and blood volume) were required. A perfused skin tissue layer was chosen as the ROI of the present study. For a non-invasive application of PPG, the most common application site is the skin. Also, pulse oximetry primarily concentrates on monitoring the peripheral perfusion, i.e., cutaneous and subcutaneous blood. This justifies the choice of perfused skin for the study.

For a PPG-based measurement system relying on the change of blood volume with the cardiac cycle, the 'pulse' plays a vital role. The pulsatility in the acquired PPG signal is also a key factor for the measurement with a pulse oximeter. Therefore, for a study related to PPG and pulse oximetry, a model should be able to include the pulsatility.

Commercial pulse oximeters are traditionally calibrated empirically by the manufacturers. The method involves a controlled study on a number of healthy volunteers. Although this method is straight forward, it has an obvious ethical restriction to desaturate the subject below 60%. As a result, R values (stated in Chapter 5) for a wide range of lower oxygen saturations have to be extrapolated [Severinghaus *et al.*, 1989]. In clinical practice, the accuracy of a pulse oximeter reading at very low oxygen saturations are not very important since patients are usually maintained at higher oxygen saturation level [Wukitsch *et al.*, 1988]. Also, with the recent advancement in signal processing techniques, pulse oximeters show a high level of accuracy. Nevertheless, the knowledge of PPG at very low saturation and blood volume is important for a comprehensive understanding in this field, which has never been addressed before. Such an understanding is significant in cases such as profound hypoxaemia (for example, cyanotic heart disease) for whom a 10% underestimation or overestimation of the SaO_2 values might lead to brain damage [DeMeulenaere, 2007; Fanconi, 1989].

Poor peripheral pulsation can result from several conditions such as hypotension, hypothermia, low cardiac output, hypovolemia, peripheral vascular disease, septic shock, infusion of vasoactive drugs, proximal blood pressure cuff inflation, leaning on an extremity, Raynaud's phenomenon etc. [Preston and Kelly, 2016; Engel and Kochilas, 2016; Baheti and Laheri, 2014]. In cases of compromised perfusion, it is often difficult to obtain good PPG signals. A controlled investigation of the tissue-optical parameters with blood

volume should be able to explain such a behaviour in PPG.

The Beer-Lambert law based theoretical description for PPG and pulse oximetry assumed no dependence of the optical path on the operating wavelength, as discussed in Chapter 5. However, in Chapter 7 it was seen that the optical pathlengths changed considerably for different optical properties. Since the optical properties vary with the operating wavelength, the approximation in the PPG theory might not be valid. There are published works that explained the dependence of the optical path on the wavelength [Sakaguchi *et al.*, 2007; Umeyama and Yamada, 2009; Nitzan and Taitelbaum, 2008], however, no investigation is available so far with a specific interest in photoplethysmography. Such an investigation, therefore, is required for an extensive understanding.

The present work has been motivated by such requirements existing in the field as discussed above in order to understand the fundamental working principle of PPG and pulse oximetry. Implementation and execution of the MC model for this purpose will be described in the following sections.

8.3 Model description

8.3.1 Monolayer model with static perfusion

8.3.1.1 Tissue characterisation

The tissue layer was presented by a slab of infinite dimensions and was characterised by its optical properties, e.g., μ_a , μ_s , and g . Considering the volumetric optical properties of the medium, as stated in the general concept of the model in Chapter 6, the ‘perfused’ tissue layer was assumed to be a homogeneous mixture of skin-dermis and blood (comprising the main absorbers: oxyhaemoglobin and deoxyhaemoglobin). The effective optical properties incorporated the volumetric contributions from the tissue-components. The total absorption coefficient μ_a of a layer of dermis perfused with a volume fraction of blood V and a total oxygen saturation S_tO_2 (i.e., the total oxygen saturation in the arterial, venous and capillary blood) was written as the sum of the individual absorption coefficients of the components [Schmitt, 1991; Wang and Tuchin, 2013; Meglinski and

Table 8.1: Optical properties of tissue constituents (in unit of mm^{-1})

λ (nm)	bloodless skin dermis		oxygenated blood (Hct=0.45)		deoxygenated blood (Hct = 0.45)	
	$\mu_{a_{skinbaseline}}$	$\mu'_{s_{skinbaseline}}$	$\mu_{a_{HbO_2}}$	$\mu'_{s_{HbO_2}}$	$\mu_{a_{Hb}}$	$\mu'_{s_{Hb}}$
660	0.0286	2.2336	0.15	1.3844	1.64	1.156
940	0.0245	0.9501	0.65	1.3187	0.43	1.124

Matcher, 2003]:

$$\mu_a = (1 - V) \cdot \mu_{a_{skinbaseline}} + V \cdot [S_t O_2 \mu_{a_{HbO_2}} + (1 - S_t O_2) \mu_{a_{Hb}}] \quad (8.1)$$

where $\mu_{a_{skinbaseline}}$ is the absorption coefficient of dermis, $\mu_{a_{HbO_2}}$ and $\mu_{a_{Hb}}$ are the absorption coefficients of oxygenated and deoxygenated blood respectively having a haematocrit (Hct) of 45%. The total oxygen saturation $S_t O_2$ was given by,

$$S_t O_2 = \frac{[HbO_2]}{[Hb] + [HbO_2]}, \quad (8.2)$$

where $[HbO_2]$ and $[Hb]$ were the concentrations of oxyhaemoglobin and deoxyhaemoglobin, respectively in the total blood volume, i.e., the all blood found in the arterial, capillary and venous blood compartments.

The baseline skin absorption coefficient (i.e., the co-efficient for bloodless skin) at wavelength λ was expressed (in the unit of mm^{-1}) as [Jacques, 1998; Simpson *et al.*, 1998]:

$$\mu_{a_{skinbaseline}} = 0.244 + 85.3 \cdot e^{-\frac{\lambda-154}{66.2}} \quad (8.3)$$

The reduced scattering coefficient of bloodless dermis was estimated from the contribution of dermis collagen fibres as given by [Jacques, 1998; Simpson *et al.*, 1998]:

$$\mu'_{s_{skinbaseline}} = (2 \times 10^4) \lambda^{-1.5} + (2 \times 10^{11}) \lambda^{-4}. \quad (8.4)$$

The values of the absorption and reduced scattering coefficient at 660 nm and 940 nm for skin dermis (calculated using above equation), and for the oxygenated and deoxygenated blood (adapted from [Bosschaart *et al.*, 2014]) are given in Table 8.1. The anisotropy factor value for the perfused skin tissue was considered to be $g = 0.95$ at both wavelengths, and the refractive index of the tissue layer was considered to be $n = 1$. The model was executed for a range of volume and oxygen saturation of the perfused skin. The blood volume was varied from 2.5% to 10% in the tissue volume, and the total oxygen saturation

was varied between 50% to 100%. In each case the optical path and detected reflectance were calculated.

8.3.1.2 Implementation details

The MC code was initially executed to find the distribution of scattering events within perfused tissue and its variation with the distance between source and detector. Fixed detector technique described in Chapter 6 was used for the photon capture. In addition to the described reflectance sensor geometry with circular source and detector both having radii of 0.1 mm, in this case a numerical aperture (NA) was considered for both source and detector so that the light was guided within the cone of acceptance. The photons were simulated for the two fixed source-detector distances 3 mm and 6 mm, at the red and infrared wavelengths. In this fixed detector set up, a 10^4 photon clusters were detected (with total simulated photon clusters $10^8 - 10^9$) for each source-detector separation at each wavelength.

MC code was executed separately for investigating the differential mean optical path (MOP) and total diffuse reflectance (W) of photons through tissue. The circular source had a radius of 0.05 mm and NA 0.39, and the circular detector had a radius of 0.05 mm and NA 0.39. The model was executed at different blood volumes for a range of total oxygen saturations using the moving detector technique. In this case, the detector was simulated as a sliding window of a width equal to the detector diameter (0.1 mm). The photon exiting from the tissue surface was detected if it had fallen within the NA of the detector fibre. The distance of its point of exit (on the plane $z = 0$) from the origin was calculated from its position co-ordinates following the equation:

$$d = \sqrt{(x^2 + y^2)}. \quad (8.5)$$

Meanwhile, other quantities (e.g., total optical path and remaining weight) associated with the detected photon were recorded. In this moving detector set up, a total 10^{10} photon clusters were detected within a maximum source-detector spacing of 8 mm. Since pulse oximeters normally use small source-detector separations, simulations were not run further to detect photons at $d > 8$ mm to avoid excessive computation time. Also, no photons were detected below $d = 0.1$ mm, where source and detector superposed. Finally,

the average optical path and weight of the photon clusters were detected within the sliding window of width 0.1 mm were calculated.

8.3.1.3 Calculation of mean optical path, mean penetration depth and reflectance

Let us consider a j^{th} photon cluster travels from the source to detector through N number of randomly generated step sizes (in other words, through N number of scattering-absorption interaction events, or number of scattering). For any i^{th} step, the generated step size l_i was given by:

$$l_i = -\frac{\ln(\xi_i)}{\mu_t} \quad (8.6)$$

Therefore, the total optical path of the j^{th} photon cluster was:

$$OP_j = \sum_{i=1}^N l_i. \quad (8.7)$$

For a total detected number of photons N_p , the mean optical path (MOP) was calculated as:

$$MOP = \frac{1}{N_p} \sum_{j=1}^{N_p} OP_j \quad (8.8)$$

The mean penetration depth MD of the detected photons within a certain source detector separation was calculated as the mean of the depths (i.e., the maximum distance covered along negative z-axis) of the photons. Similarly to MOP , considering D_j to be the depth of penetration of the j -th photon cluster, the mean depth calculated over N_p number of photon clusters which was given by,

$$MD = \frac{1}{N_p} \sum_{j=1}^{N_p} D_j \quad (8.9)$$

The detected diffuse reflectance (W) was defined as the sum of normalised statistical weights of the N_p detected photon clusters as the following equation [Meglinski and Matcher, 2003]:

$$W = \frac{1}{N_p \cdot w} \sum_{j=1}^{N_p} w_{o_j} \quad (8.10)$$

where w and w_o are in the incident and detected weight of a photon cluster, with $w = 1$.

8.3.2 Monolayer model with pulsatility

The pulsatility was introduced in the monolayer model by simulating the different states of perfusion corresponding to systole and diastole. In this model, instead of total blood volume and oxygen saturation, arterial and venous blood contributions were incorporated separately. There is not many literature particularly stating the distribution between the arterial and venous blood. However, based on the available literature [Williams *et al.*, 1989; Reuss, 2005; Wang and Tuchin, 2013], the ratio of arterial and venous blood was considered to be 1:1, and the value of venous oxygen saturation S_vO_2 was kept 10% lower than the arterial oxygen saturation. These values were approximated based on the information from textbook and published literature. Although these parameters may vary between different locations and physiological states of the subject, an ideal situation was assumed here. In the present modelling approach, the main focus was to asses the relative absorbances in PPG and PO at the operating wavelengths, thus the current assumption did not compromise the accuracy of the model. The main variables in the static model (V and S_tO_2) were related to the variables of the pulsatile model (V_a , V_b and S_aO_2 , S_vO_2), as:

$$\begin{aligned} V &= V_a + V_b \\ S_tO_2 &= S_aO_2 + S_vO_2. \end{aligned} \tag{8.11}$$

The diastole phase was achieved by assuming a nominal arterial blood volume of $V_a(dia) = 50\%$ in the dermal tissue, and the systole was obtained by increasing the blood volume by 20% so that $V_a(sys) = 70\%$. The model was executed for a range of S_aO_2 . The reflectance and the mean optical paths were detected in systolic and diastolic phases using the ‘fixed detector’ technique at a source-detector separation of 6 mm. The model was explored to generate the curve for ‘ratio of ratios’ R (Chapter 5) as a function of S_tO_2 . Recalling Eq. 5.10 from Chapter 5, R was written in the form:

$$R = \frac{\frac{\Delta I(r)}{I_d(r)}}{\frac{\Delta I(ir)}{I_d(ir)}}. \tag{8.12}$$

Here, the difference between diastolic and systolic intensities was expressed as $\Delta I = I_d - I_s$. In this model, the detected intensity was considered equivalent to the reflectance as already stated earlier. Therefore, above expression for R could be written in the form of

the systolic and diastolic reflectance (W_s and W_d respectively):

$$\begin{aligned}
 R &= \frac{\frac{\Delta W(r)}{W_d(r)}}{\frac{\Delta W(ir)}{W_d(ir)}} \\
 &= \frac{1 - \frac{W_s(r)}{W_d(r)}}{1 - \frac{W_s(ir)}{W_d(ir)}}.
 \end{aligned} \tag{8.13}$$

8.4 Distribution of scattering events

Examples of the photon scattering distributions within the dermis containing 7.5% blood at a $S_tO_2 = 60\%$ are given in Figure 8.1. The distribution of the scattering events at 660 nm and 940 nm are shown for $d = 3$ mm in Figure 8.1(a) and Figure 8.1(b), and for $d = 6$ mm in Figure 8.1(d) and Figure 8.1(e), respectively. The simulations provided full 3D description of the distribution of the photon scattering, however, only its projection in the xz plane was shown in the figure. The colourbar represented the number of scattering N within tissue.

In all cases, the photon clusters followed a ‘banana’ shaped path distribution from the source to the detector. As expected, the number of scattering events N was the highest near the source and the detector, and decreased at deeper penetration depths. The number of scattering was directly related to the number of photon clusters. The more number of photons accumulated in one region, the more number of overall scattering was found. Conclusively, the number of photons gradually decreased along the depth within the tissue. An important observation from the figure was that the red and infrared photons distributed themselves differently in tissue. The infrared photons appeared to be more dispersed, whereas the red photons appeared to be clumped. This can be explained as the result of the different scattering coefficients. The infrared scattering co-efficient was lower than the red scattering co-efficients for all tissue components according to Table 8.1. The lower is the scattering co-efficient, the higher is the free pathlength. Thus the distance between two consecutive scattering events for infrared photon was higher compared to the red photon. As a result, the number of scattering of red photons was much higher compared to the infrared photons.

Comparative histograms of the optical pathlengths (OP) at red and infrared wavelengths at $d = 3$ mm and 6 mm were shown in Figure 8.2 (a) and (b) respectively. Differ-

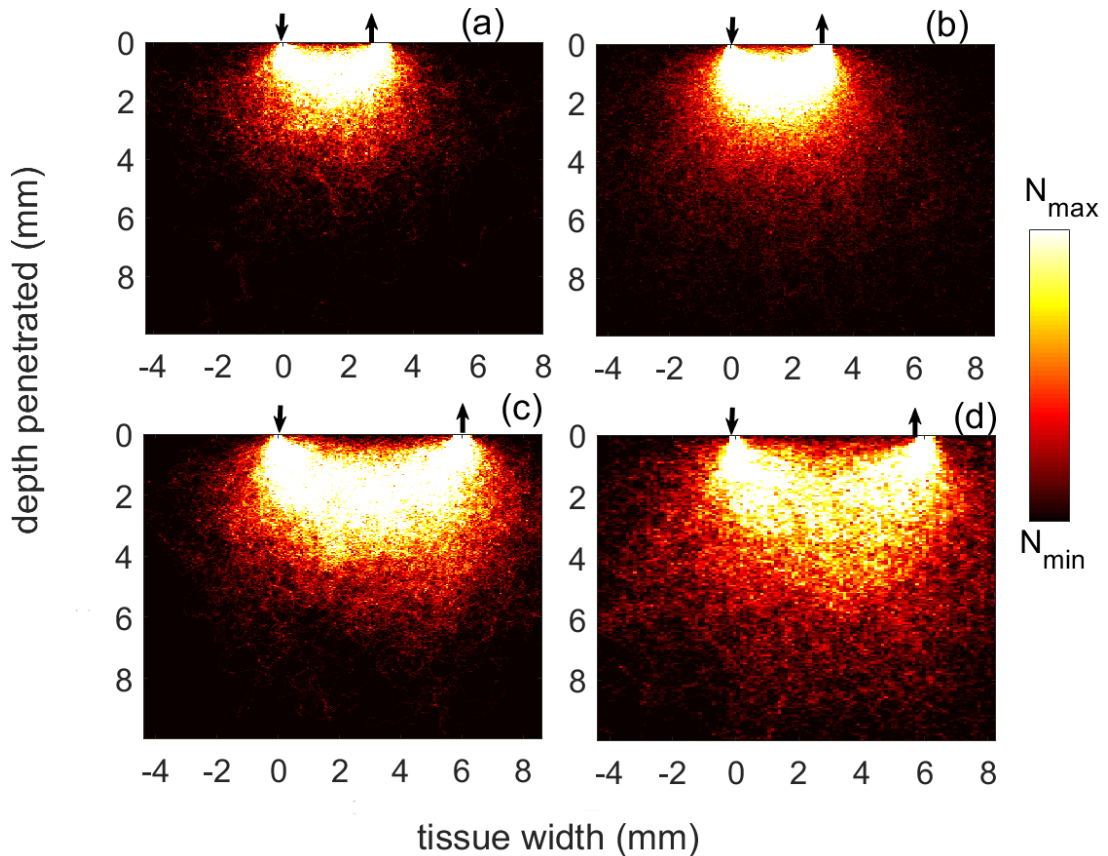


Figure 8.1: Density-plots for distribution of photon scatter in monolayer dermal skin tissue containing blood volume 7.5% at a total oxygen saturation of 60% are shown. Results for a source-detector separation, $d=3$ mm and $d = 6$ mm at 660 nm are shown in (a) and (c), respectively. Results for $d = 3$ mm and $d = 6$ mm at 940 nm are shown in (b) and (d), respectively. The colourbar indicates the number of scattering events (N). Each figure shows a 2-D projection of a 3-D distribution of photon clusters. For comparison, all colourmaps are shown within the same axis limits. The optical path of only detected photon clusters are shown here.

ences in the distribution of optical paths at red and infrared wavelengths were apparent for both source-detector separations. The histogram plots further showed the tendency of infrared photons to take shorter optical path compared to red photons. The difference between the red and infrared optical paths increased for $d = 6$ mm compared to $d = 3$ mm. Since the same number of photons were detected at both d , the optical pathlengths were lesser at 6 mm than at 3 mm as expected.

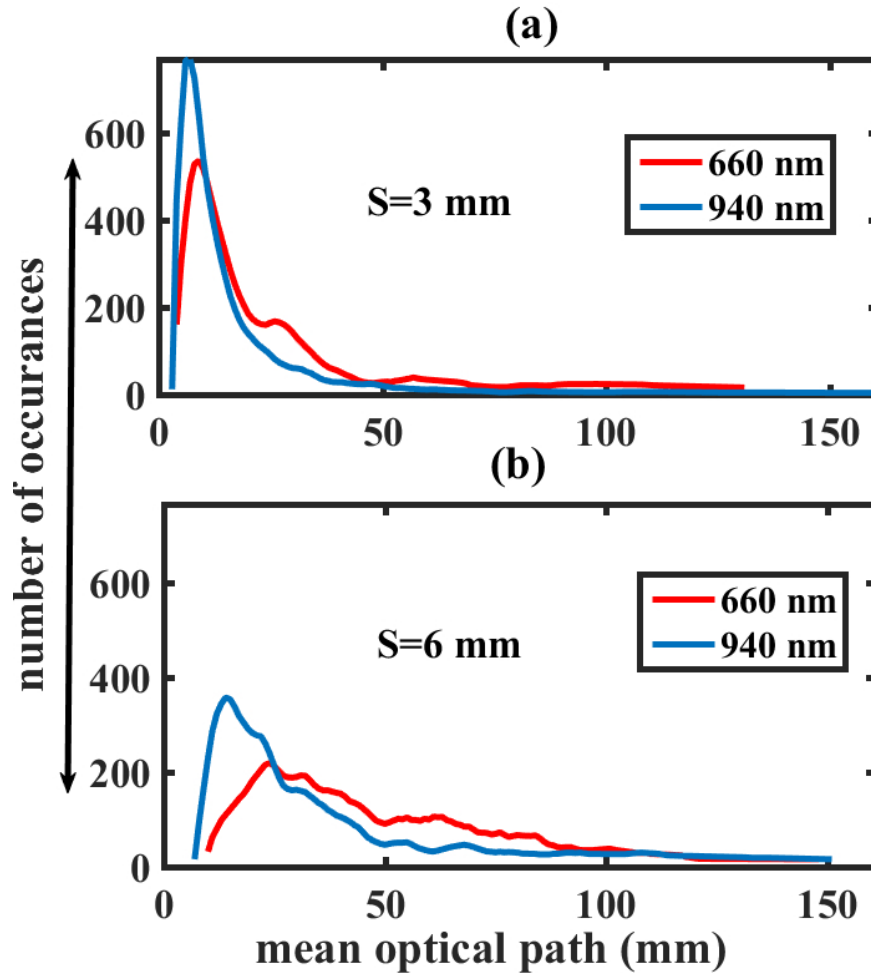


Figure 8.2: Comparative histogram plots of the optical pathlengths at red and infrared wavelengths are shown. Results for $d = 3$ mm and $d = 6$ mm are shown in (a) and (b), respectively. The plots are presented in the same axes limits. These plots correspond to the scatter-density plot shown in Figure 8.1.

8.5 Mean optical path and reflectance as function of blood volume

In Figure 8.3, the variation of mean optical path and the diffuse reflectance as functions of the source-detector separations are shown. Simulation was carried out for variable volume fractions of blood at a fixed oxygen saturation 60%. In both wavelengths MOP was reduced for higher blood volumes as shown in Figure 8.3 (a) and (c). Vertical axis limits show that the infrared pathlengths are shorter than red pathlengths. In Figures 8.3 (b) and (d), it was seen that the reflectance decreased considerably with increasing blood volumes at both wavelengths.

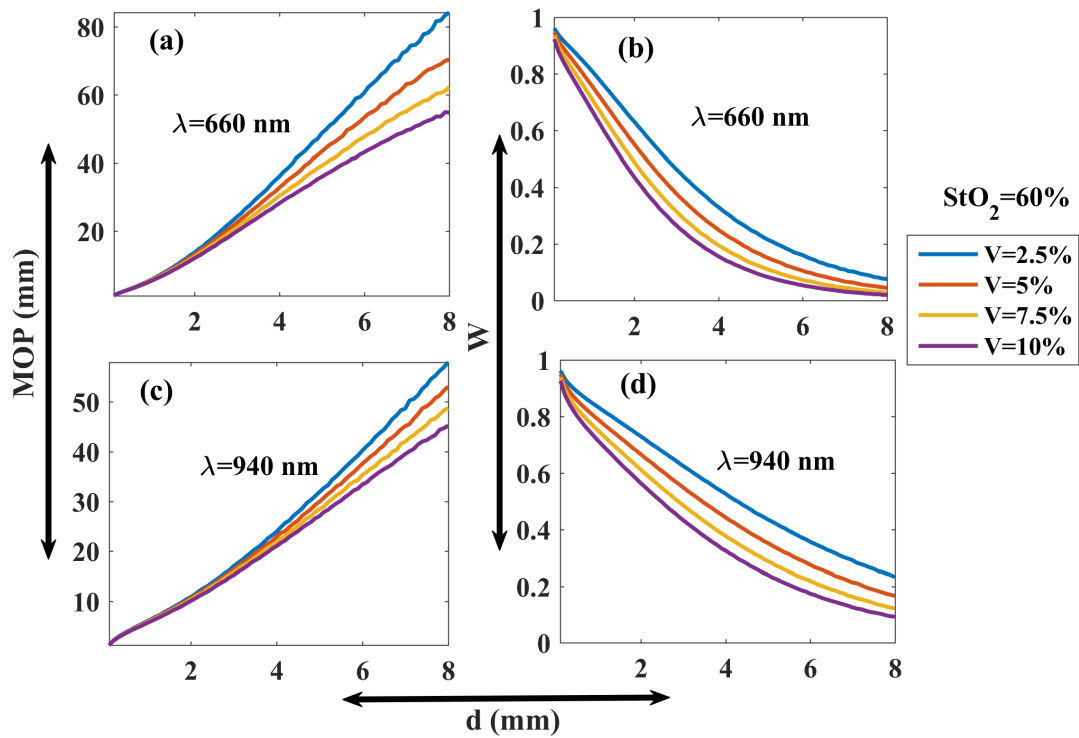


Figure 8.3: Mean optical path (MOP) and diffuse reflectance (W) of the photon clusters as function of source-detector separation (d) are shown. Results for MOP and W at a fixed $StO_2 = 60\%$ for $V = 2.5 - 10\%$ for $\lambda = 660$ nm are shown in (a) and (b), respectively. For the same parameters, the results for $\lambda = 940$ nm are shown in (c) and (d), respectively.

8.6 Mean optical path and reflectance as function of blood oxygen saturation

In Figure 8.4, the variation of mean optical path and reflectance were plotted as functions of d. The oxygen saturation was varied through 50%-100% at a fixed blood volume 7.5%. Red optical paths increased considerably with the increasing saturations. The maximum MOP was at 100% oxygen saturation. Infrared optical paths varied slightly with varying V and increased with increasing blood volume. This observation was opposite to the case of red light. Red light was attenuated more at lower saturation. Infrared attenuation changed very slightly with saturations with a maximum value at 100% saturation.

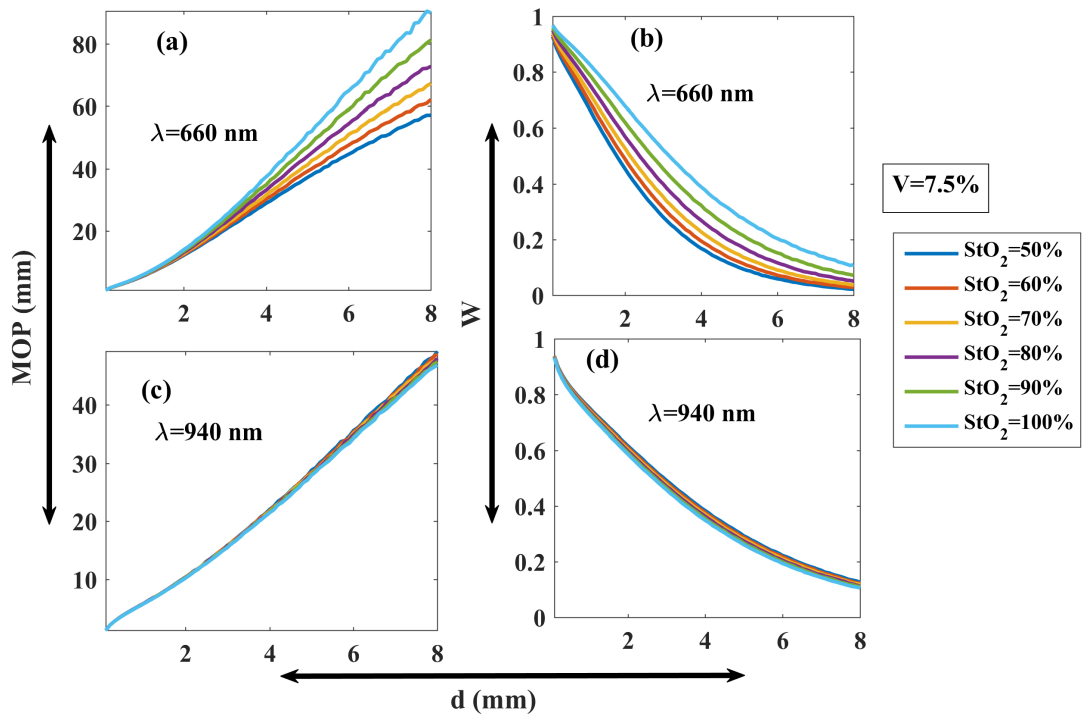


Figure 8.4: Mean optical path (MOP) and diffuse reflectance (W) of photon clusters as functions of source-detector separation (d). Results are shown at a fixed $V = 7.5\%$ for $S_tO_2 = 50 - 100\%$ for $\lambda = 660$ nm in (a) and (b); and for $\lambda = 940$ nm in (c) and (d), respectively.

8.7 Differential red and infrared mean optical path, mean penetration depth and reflectance

The dependence of the mean optical path with the source-detector separation, blood volume and the total blood oxygen saturation were observed in Figures 8.3 and 8.4 which motivated further investigation of this relationship through a range of parameters. MC simulation results exhibiting mean optical path as a function of source detector separation are presented. The simulation for skin tissue containing different blood volumes (i.e., $V = 2.5\%$, 5% , 7.5% and 10%) for a range of tissue oxygen saturations (i.e., $S_tO_2 = 50 - 100\%$ with an interval of 10%) are shown in Figure 8.5. The photons took longer paths at the red wavelength compared to infrared for all blood volume and oxygen saturation values. For $S_tO_2 = 50 - 80\%$, the difference between red and infrared optical paths decreased with increasing blood volume. However, for very high S_tO_2 ($90 - 100\%$) the differences in red-infrared optical path increased with increasing blood volume. The differences in

red-infrared optical path, thus, increased with blood oxygen saturation but decreased with blood volume (except at very high S_tO_2 , i.e., approximately 100%).

The percentage changes of the optical path between red wavelength (MOP (R)) and infrared wavelength (MOP (IR)) at a certain source-detector spacing $d = 6$ mm is illustrated in Figure 8.6. The percentage change ΔMOP is calculated as:

$$\Delta MOP = \frac{MOP(R) - MOP(IR)}{MOP(IR)} \times 100\%. \quad (8.14)$$

Clearly, positive values of ΔMOP showed that MOP (R) was greater than MOP (IR). ΔMOP decreased with V at lower S_tO_2 (50 – 80%) but the variation gradually decreased with higher S_tO_2 . For a very high S_tO_2 (90 – 100%), ΔMOP increased with V . Results of the variation of the mean optical path with blood volume and oxygen saturation shown in Figure 8.5 and Figure 8.6 are consistent with the observations in Figure 8.3 and Figure 8.4.

The Monte Carlo simulation results for the mean penetration depth, as a function of d for different volume fractions of blood with a range of total oxygen saturation of blood, are shown in Figure 8.7. The depth of penetration increased directly with the increasing source-detector separation. For lower blood volume and oxygen saturation, infrared photons penetrated deeper than the red photons. However, for higher saturation and higher blood volume, the difference between red and infrared penetration depths were smaller. For $S_tO_2 = 100\%$ and $V = 10\%$, red and infrared photons penetrated through almost the same depth within tissue. From Figures 8.5 and 8.7, it is concluded that the variation in the optical path and the penetration depth were not identical, i.e., a higher optical path did not refer to a higher penetration depth in tissue. As very clearly seen in Figure 8.7 and Figure 8.5, infrared optical path was lower compared to red but the penetration depth was mostly higher for infrared. This can be predicted from the scattering distribution plot in Figure 8.1, that the infrared photons are likely to penetrate deeper due to their lower scattering coefficient and higher free pathlength.

The Monte Carlo simulation results for diffuse reflectance W , as a function of d for different volume fractions of blood with a range of total oxygen saturation of blood, are shown in Figure 8.8. As expected, in Figure 8.8 it was seen that W decreased with increasing source-detector separation. This observation supports the Beer-Lambert law

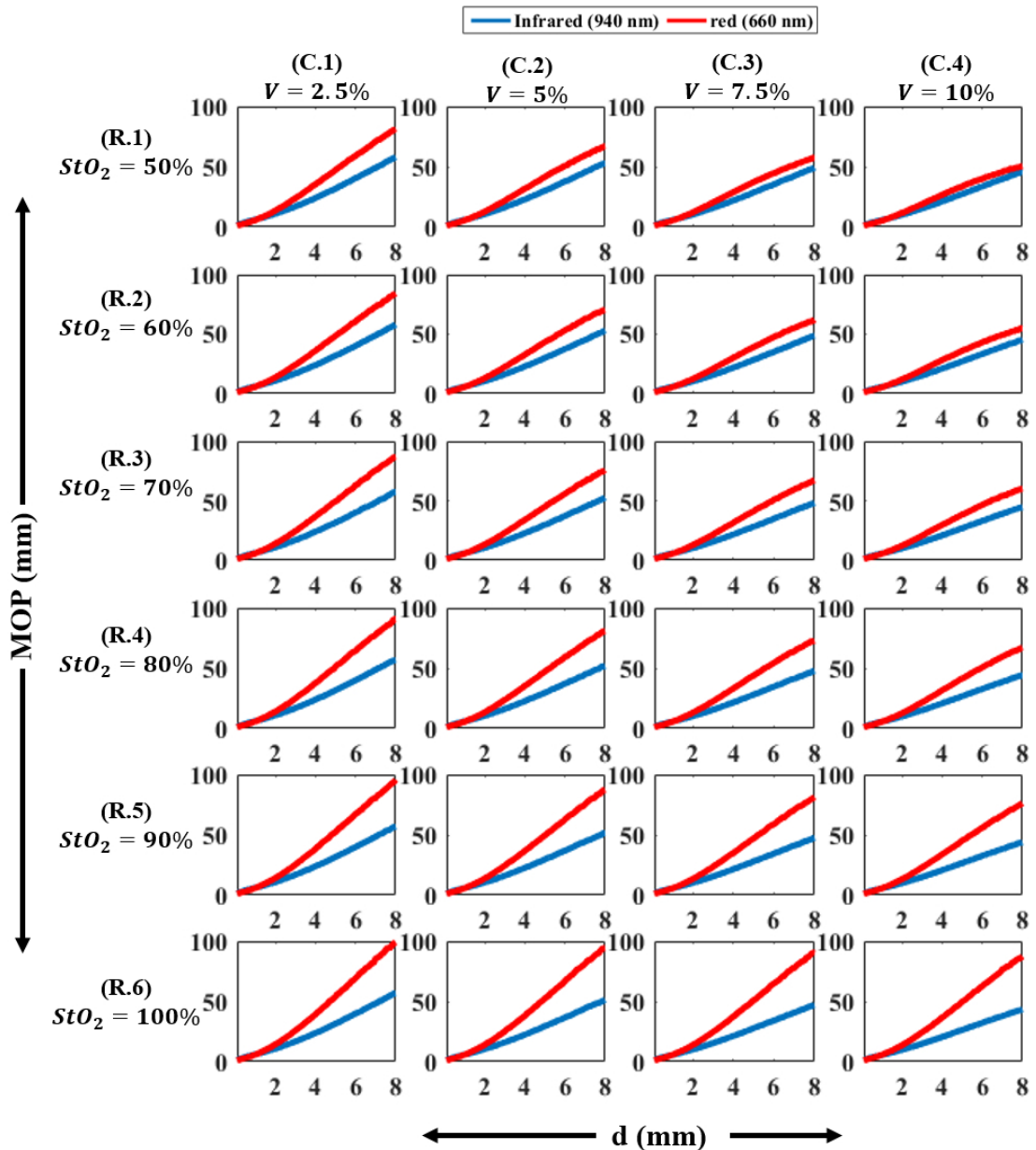


Figure 8.5: Differential mean optical path (MOP) between red and infrared wavelengths as a function of source-detector separation (d) for perfused dermal skin tissue is shown. Results for $S_tO_2 = 50\%, 60\%, 70\%, 80\%, 90\%$ and 100% are presented in the rows (R.1), (R.2), (R.3), (R.4), (R.5) and (R.6) respectively. For each saturation, the differential mean optical path for $V = 2.5\%, 5\%, 7.5\%$ and 10% are shown in the columns (C.1), (C.2), (C.3) and (C.4) respectively. For comparison, all graphs are plotted within the same axis limits. The red and blue lines represent MOP at red (660 nm) and infrared (940 nm) light respectively.

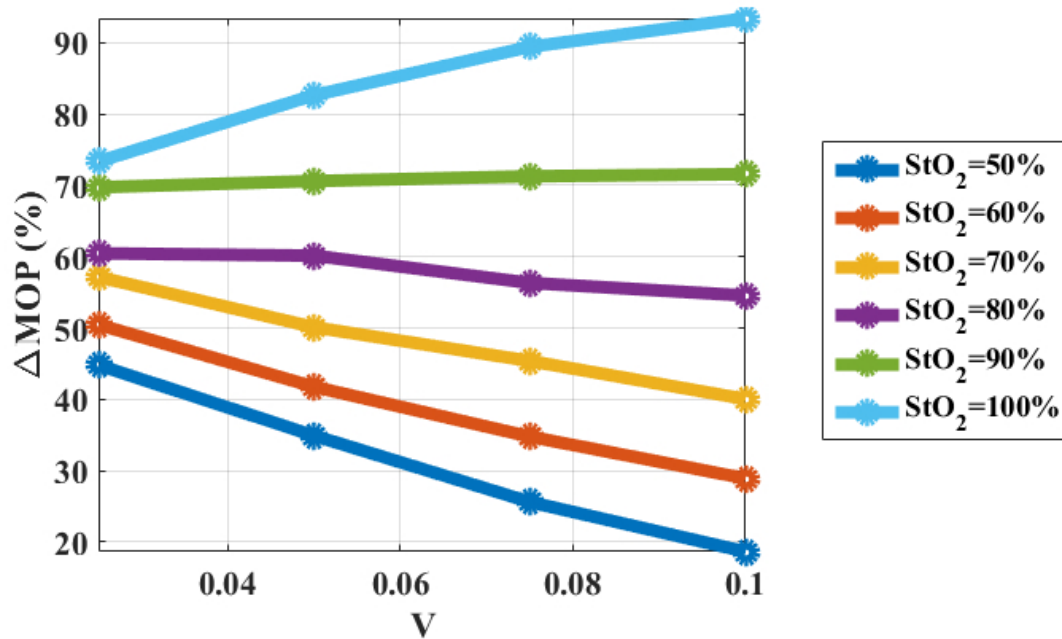


Figure 8.6: Percentage change in the mean optical path between red and infrared light (ΔMOP) is shown. Results were calculated for a source-detector separation 6 mm as a function of blood volume (V) for total oxygen saturations $S_tO_2 = 50\%, 60\%, 70\%, 80\%, 90\%$ and 100% . The markers represent data points at fractional blood volume $V = 0.025, 0.05, 0.075$ and 0.1 . ΔMOP decreases with V for lower S_tO_2 ($\sim 50-80\%$) increases with V for higher S_tO_2 ($\sim 100\%$).

that the attenuation of light increases with increasing distance traversed through tissue. The difference in the decremental rate with d of the reflectance between red and infrared varied according to both the blood volume and blood oxygen saturation. Results showed that red light was more attenuated than infrared at oxygen saturations 50-80%, with a decrease in the difference in attenuation at higher blood volume. However, at very high oxygen saturations (90-100%), infrared light was attenuated more than red light, which is mostly visible for high blood volumes (7.5-10%). The difference in attenuation, thus, decreased with increasing blood volume as well as increasing blood oxygen saturation.

Relating Figures 8.5, 8.7 and 8.8, it is seen that at lower saturation and blood volume, detected infrared reflectance was higher when the penetration depth was also higher although the optical path was lower. Even though red light took higher mean optical path-length, it penetrated less because its direction was deviated more frequently than infrared due to smaller free pathlengths. Also for the same reason, i.e., the increased number of interactions, red photons were absorbed more frequently than infrared while travelling

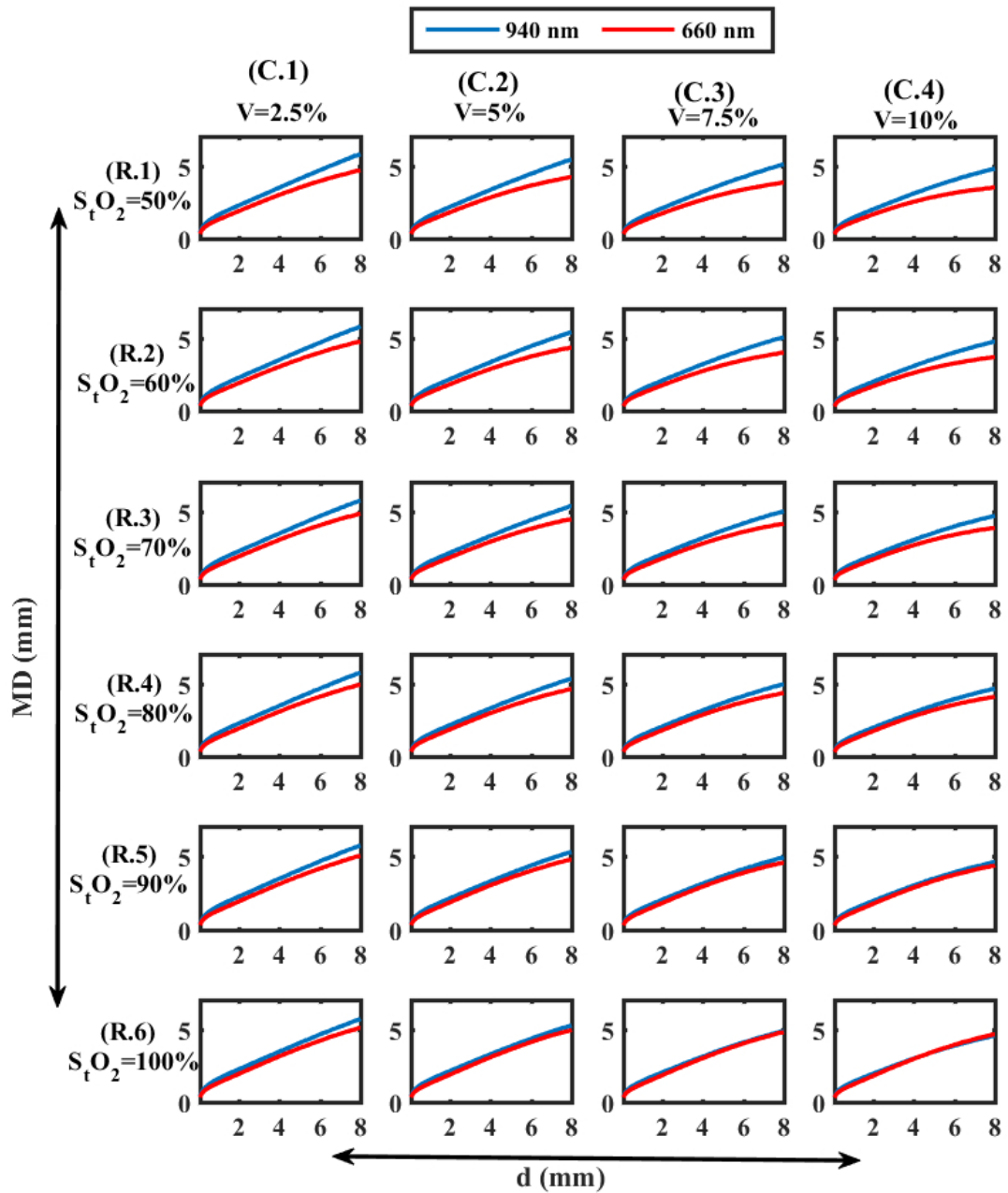


Figure 8.7: Differential mean penetration depth (MD) between red and infrared wave-lengths as a function of source-detector separation (d) for perfused dermal skin tissue is shown. Results for $S_tO_2 = 50\%$, 60% , 70% , 80% , 90% and 100% are presented in the rows (R.1), (R.2), (R.3), (R.4), (R.5) and (R.6) respectively. For each saturation differential mean optical path for $V = 2.5\%$, 5% , 7.5% and 10% are shown in the columns (C.1), (C.2), (C.3) and (C.4) respectively. For comparison, all graphs are plotted within the same axis limits. The red and blue lines represent MD at red (660 nm) and infrared (940 nm) light respectively.

from the source to the detector, resulting in lower remaining weight in the detection end. Also, the absorption coefficient of skin was higher in red than infrared. The oxygenated blood absorbed less red light than infrared, whereas the deoxygenated blood absorbed more red light than infrared. When blood volume was small, the optical properties of skin dominated over the oxy and deoxyhaemoglobin properties in the entire tissue volume. Consequently, red light was more attenuated than infrared at any oxygen saturation values. For higher blood volume, the optical properties of oxy and deoxyhaemoglobin were dominant. When oxygen saturation was low, the optical properties of deoxyhaemoglobin dominated, resulting in higher absorption in red light and higher detected reflectance in infrared light. But for higher blood volume and higher oxygen saturation, optical properties of oxyhaemoglobin dominated, resulting in higher absorption in infrared. As the cumulative effect of all components, red detected reflectance became almost the same or slightly higher than the infrared for a very high oxygen saturation ($\sim 100\%$), as seen in the row (R.6) of Figure 8.8. At the high blood volume and high oxygen saturation (e.g., $V = 10\%$ and $S_tO_2 = 100\%$), for smaller source-detector separation, red reflectance was higher than infrared reflectance, however for longer source-detector separation the case reversed. It can be explained from the analogy with Figure 8.7, where for the same state of perfusion and oxygenation, the depth penetrated by red light was slightly higher than infrared at higher source-detector separation, resulting in slightly higher red light absorption and therefore, gradually lower detected reflectance with increasing source-detector separation.

Similar to the percentage changes in MOP, percentage change between red and infrared detected reflectance and the mean penetration depth (ΔW and ΔMD , respectively) are calculated as:

$$\Delta W = \frac{W(R) - W(IR)}{W(IR)} \times 100\%; \quad (8.15)$$

$$\Delta MD = \frac{MD(R) - MD(IR)}{MD(IR)} \times 100\%. \quad (8.16)$$

Percentage changes in optical path, mean optical penetration depth and relative diffuse reflectance at different physiological states at a certain source-detector spacing 6 mm are presented in Table 8.2. Negative values of ΔW and ΔMD showed lower values in red than infrared in all cases only except very high $S_tO_2 \sim 100\%$ and high $V \geq 7.5\%$.

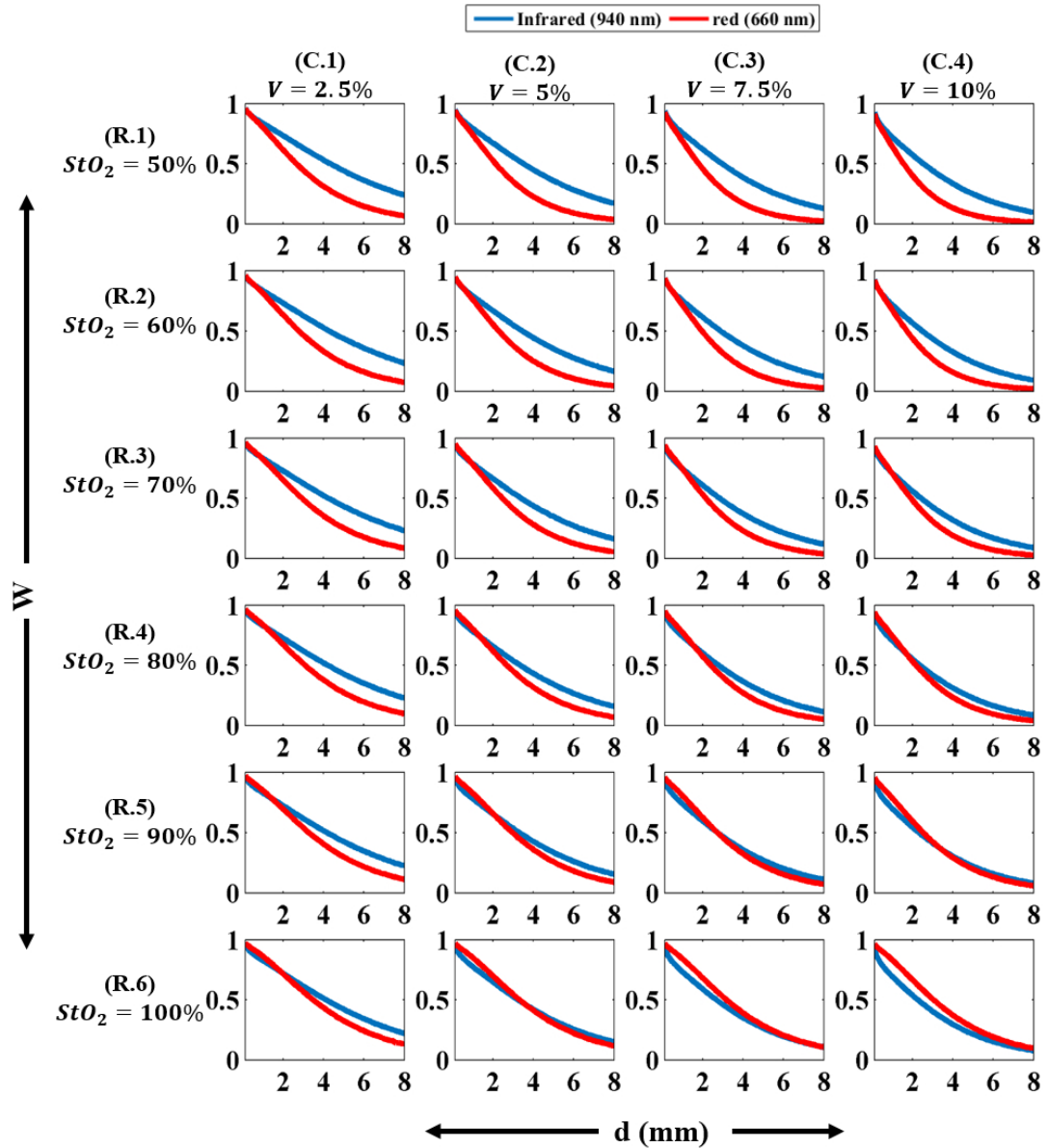


Figure 8.8: Differential reflectance (W) between red and infrared wavelengths as a function of source-detector separation (d) for perfused dermal skin tissue is shown. Results for $S_tO_2 = 50\%, 60\%, 70\%, 80\%, 90\%$ and 100% are presented in the rows (R.1), (R.2), (R.3), (R.4), (R.5) and (R.6) respectively. For each saturation differential mean optical path for $V = 2.5\%, 5\%, 7.5\%$ and 10% are shown in the columns (C.1), (C.2), (C.3) and (C.4) respectively. For comparison, all graphs are plotted within the same axis limits. The red and blue lines represent W at red (660 nm) and infrared (940 nm) light respectively.

Table 8.2: Percentage change in mean optical path ΔMOP , reflectance ΔW and mean penetration depth ΔMD with blood volume V and total blood oxygen saturation S_tO_2 for a certain source-detector separation of 6 mm.

V	S_tO_2	ΔMOP	ΔW	ΔMD
2.5%	50%	+44.79%	-59.70%	-18.90%
	60%	+50.48%	-55.01%	-16.95%
	70%	+57.16%	-50.62%	-15.49%
	80%	+60.48%	-43.96%	-13.39%
	90%	+69.74%	-38.31%	-11.70%
	100%	+73.35%	-29.44%	-10.25%
5%	50%	+34.91%	-68.50%	-22.14%
	60%	+41.76%	-61.84%	-18.43%
	70%	+50.11%	-54.05%	-16.28%
	80%	+60.15%	-43.74%	-11.91%
	90%	+70.61%	-30.96%	-9.07%
	100%	+82.65%	-13.21%	-5.47%
7.5%	50%	+25.61%	-73.45%	-25.15%
	60%	+34.78%	-66.91%	-20.66%
	70%	+45.39%	-57.06%	-15.94%
	80%	+56.33%	-43.20%	-11.25%
	90%	+71.28%	-23.84%	-5.97%
	100%	+89.43%	+5.24%	-1.44%
10%	50%	+18.65%	-76.78%	-28.24%
	60%	+28.91%	-69.28%	-23.09%
	70%	+40.94%	-58.29%	-16.92%
	80%	+54.56%	-42.55%	-11.39%
	90%	+71.58%	-15.99%	-4.32%
	100%	+93.43%	+25.66%	1.74%

The conclusions drawn from the steady state monolayer skin tissue simulation can be summarised as stated below:

- **Low V , low S_tO_2 :** At low blood volume, optical properties of skin tissues dominate. Skin has lower absorption and scattering coefficient in infrared than red light. Therefore, the total interaction coefficient is also lower in infrared than in red, resulting in longer free path length in infrared, i.e., $MOP(R) > MOP(IR)$. Consequently, red photons are subjected to more frequent scattering events which do not let them to penetrate very deep within tissue so that $MD(R) < MD(IR)$. Also, due to an increased number of absorption, more photon weight is absorbed in tissue so that $W(R) < W(IR)$.
- **High V , low S_tO_2 :** Due to high blood volume, the optical properties of blood

dominate. Because of low oxygen saturation, optical properties of deoxyhaemoglobin dominate. Deoxyhaemoglobin being more absorbing and scattering in red than infrared, the scenario is the same as the above. However, the difference between red-infrared scattering coefficient for deoxyhaemoglobin is not that great as in skin baseline. Therefore, although the red optical path is higher than infrared, the difference is comparatively low. The effect on mean penetration depth and the reflectance is almost similar as in the case above.

- **High V , high S_tO_2 :** Optical properties of oxyhaemoglobin is predominant. Although optical path is much higher in red than in infrared, both mean penetration depth and the detected reflectance are almost identical.

8.8 Reflectance and ‘ratio of ratios’ as function of oxygen saturation

Pulsatile monolayer model described in the subsection 8.3.2 was executed to determine the reflectance in systole and diastole at red (660 nm) and infrared (940 nm). Results are shown as a function of arterial oxygen saturation with a source-detector separation of 6 mm. In Figure 8.9 (a), the red reflectance (660 nm) was found to be lower than infrared (940 nm) reflectance for low arterial oxygen saturation values. However, it gradually increased with increasing oxygen saturation. At high saturation values (90 – 100%), it exceeded the infrared reflectance. This observation agrees with the static model result in Figure 8.8, where the red reflectance exceeded the infrared at high oxygen saturations. The diastolic reflectance (shown in red line in plot) was always higher than the systolic reflectance (shown in green light in the plot). This was expected due to the higher absorption of light at higher blood volume in systolic phase.

The ‘ratio of ratios’ R was calculated from Eq. 8.13 as a function of arterial oxygen saturation. As shown in the Figure 8.9 (b), the calculated values of R at each S_aO_2 produced an almost linear curve. This nature of the simulated calibration curve was similar to the available calibration curve, presented in Figure 5.5.

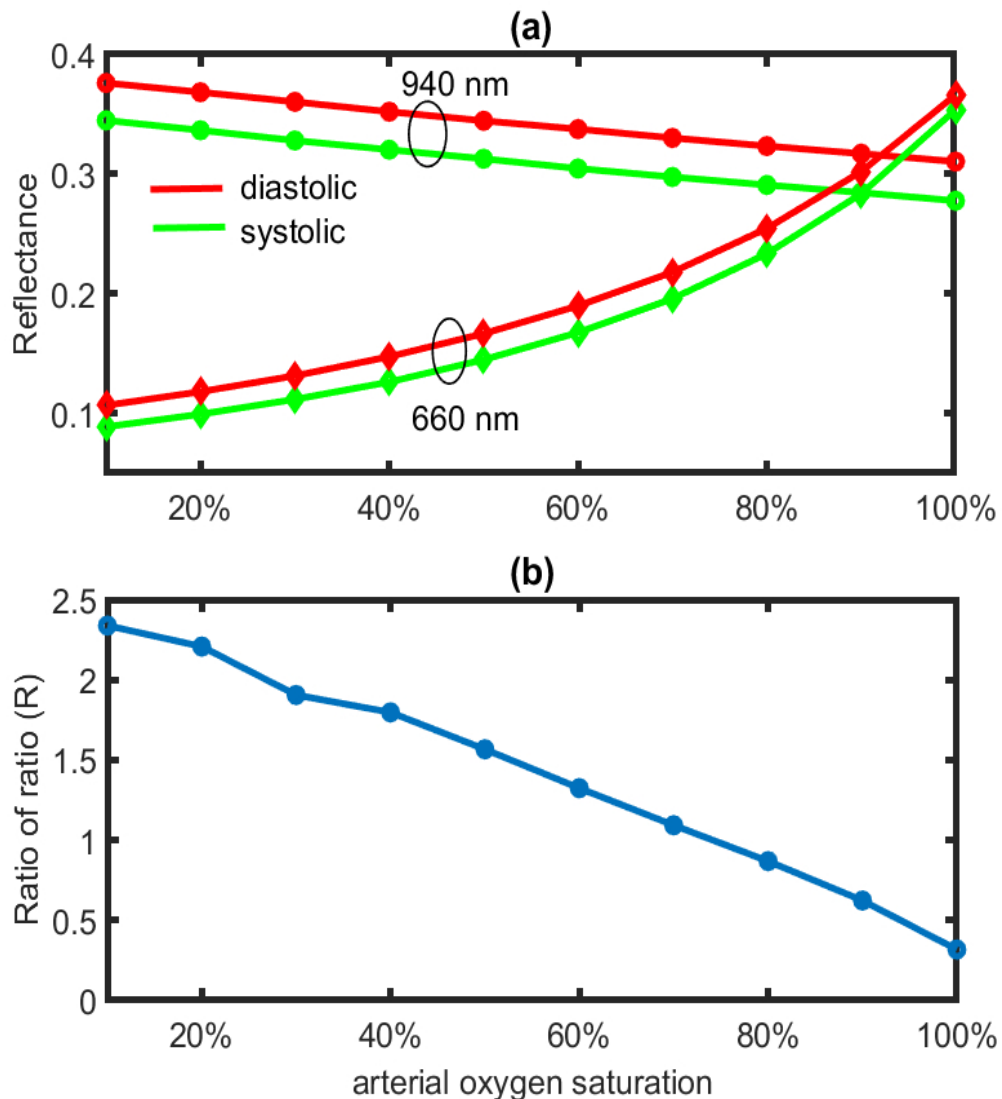


Figure 8.9: Simulated results from a monolayer pulsatile model is presented. Reflectance in systole and diastole at red (660 nm) and infrared (940 nm) wavelengths are shown as a function of arterial oxygen saturation (a). Calculated ‘ratio of ratios’ R from the reflectance as a function of arterial oxygen saturation is presented (b), which produces the ‘calibration curve’ of the present reflectance mode monolayer pulse oximetry model. The data points at individual oxygen saturation values are denoted by the markers.

8.9 Summary

In this chapter, a monolayer static and a pulsatile Monte Carlo model of perfused skin was explored for rigorous analysis of the fundamental tissue-optical variables in a dual wavelength PPG system such as pulse oximeter. The output variables of the model were the distribution of the interaction events, mean optical path, mean penetration depth, and

detected reflectance etc. The input parameters were the tissue optical properties, blood volume, total oxygen saturation of blood, and source-detector separation etc. The optical path and the penetration depth were found to vary differently with the input variables. The wavelength dependence of the output variables were quantified. From the pulsatile modality of the PPG model, the 'ratio of ratios' were calculated as a function of the total blood oxygen saturation, which produced a shape close to the 'calibration curve' of the pulse oximeters. The extensive studies with the monolayer skin tissue model enlightened the light-tissue interactions in PPG. The next chapter will concentrate on investigation with a further detailed multilayer tissue-model.

INVESTIGATING LIGHT-TISSUE INTERACTIONS IN REFLECTANCE AND TRANSMITTANCE FINGER PHOTOPLETHYSMOGRAPHY

9.1 Introduction

In the last chapter, an investigation with a single layer of tissue analysed the light-tissue interactions in photoplethysmography and pulse oximetry. Although a monolayer model-based study has its own significance, in order to describe the complex structure of the biological tissue, a multilayer model-based study is a necessity. Different regions of interests (ROI) of the body exhibit different anatomical and optical characteristics [Williams *et al.*, 1989]. Defining an ROI is important for an investigation dedicated to a specific bio-optical application. In this chapter, the Monte Carlo simulation of light-tissue interaction in a finger ROI will be described.

9.2 Background

The previous study with the single layer of skin tissue unravelled much useful information on PPG and pulse oximetry. However, that study was limited to the reflective modality only. Since a semi-infinite tissue volume was modelled, it could not be implemented for a study on the transmissive mode. Moreover, no details on the tissue-heterogeneity were

included to the previous model. With the confidence built from the results with single layer tissue, the present study is focussed on the light-tissue interactions through a heterogeneous volume of human finger pertinent to PPG and pulse oximetry. The finger tissue, being the most common site for the clinical measurement of the peripheral oxygen saturation using pulse oximetry, was chosen as the ROI. The model was executed in both reflective and transmissive modalities of the system at the two commonly used wavelengths (660 nm and 940 nm) in pulse oximeters.

9.3 Description of the finger tissue model

The schematic diagram of the tissue volume used for the study is shown in Figure 9.1. A three-dimensional slab geometry was chosen to represent the simulated tissue volume which was a small cubic section of the finger (as shown in Figure 9.1(a) by a red dotted block). The stratification and dimensions of the tissue layers and sublayers were determined by surveying various histological images and consulting text books and published literature [Wang and Tuchin, 2013; Meglinski and Matcher, 2003; Williams *et al.*, 1989; Tuchin *et al.*, 2011; Doronin and Meglinski, 2011; Doronin, 2014]. The heterogeneous volume of the finger had a width of 1.3.cm, and consisted of the layers: skin (0.95 mm thick), fat (0.55 mm thick), muscle (10 mm thick), and then fat (0.55 mm thick) and skin (0.95 mm thick) in reverse order. The muscle tissue contained a cylindrical bone at a depth of 3 mm with a radius of 2 mm.

The skin layer comprised six sublayers: stratum corneum, epidermis, papillary dermis, upper blood net dermis, reticular dermis and deep blood net dermis [Wang and Tuchin, 2013; Salasche and Bernstein, 1988]. The pulsating arterial blood flow was simulated by a proportional increase in blood volume. It was assumed that the pulsatile changes in the arterial blood mainly manifested in the dermal tissue sublayers rather than sub-dermal fat, bone, and muscle [Reuss and Siker, 2004; Tuchin, 2007; Doronin *et al.*, 2011]. To achieve the pulsatility, blood volumes in all the dermal sublayers during ‘systole’ were incremented twice as much as in ‘diastole’. Following the similar assumption as stated in Chapter 8, the ratio of arterial and venous blood fraction in the dermal tissue layers was considered as 1:1. Venous oxygen saturation (SvO_2) was considered 10% lower than

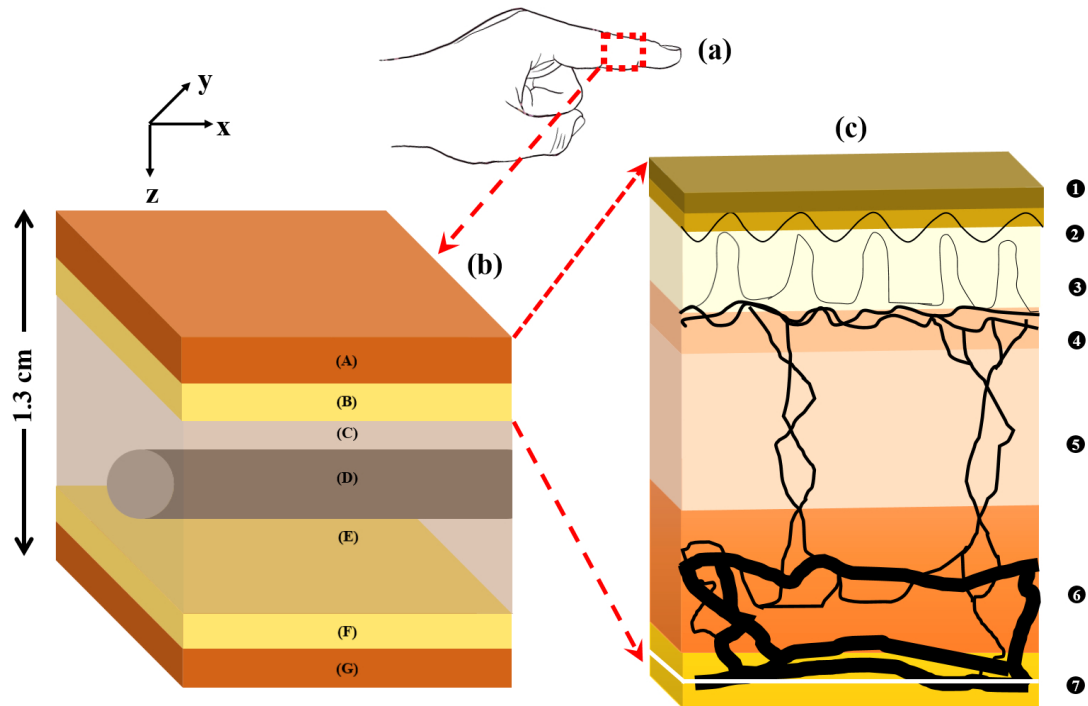


Figure 9.1: Description of the multilayer finger tissue model is presented. The selected cubic section of the finger (a) has the layers and sublayers as illustrated in (b). The volume of finger section is represented by a semi-infinite slab geometry of a thickness of 1.3 cm. It consists of the tissue layers: skin (A), fat (B), muscle (C & E) containing a cylindrical bone layer (D), and then the fat (F) and skin (G) in reverse order. Skin layer consists of several sublayers which are illustrated in (c). The sublayers are: (1) stratum corneum, (2) epidermis, (3) papillary dermis, (4) upper blood net dermis, (5) reticular dermis, and (6) deep blood net dermis. The 6-th sublayer of the skin is connected with the next layer which is fat (7) through blood vessels.

the arterial oxygen saturation (SpO_2). An epidermal melanin concentration of 10% was considered in the model. The contribution of the water present in the dermal tissue sublayers were taken into consideration. The thickness (t), and the volume fraction of diastolic blood and water (V_b and V_w , respectively) present in the dermal tissue layers were adapted from textbook and literature [Reuss and Siker, 2004; Williams *et al.*, 1989; Tuchin, 1993; Wang and Tuchin, 2013; Bashkatov *et al.*, 2016; Tuchin, 1997; Jacques, 1998]. The thickness of the dermal sublayers, and the distribution of the water and blood content in them are illustrated in Table 9.1.

Table 9.1: Stratification of dermal sublayers.

serial no.	Dermal sublayer	t (mm)	V_b	V_w
1	stratum corneum	0.02	0	0.05
2	epidermis	0.25	0	0.2
3	papillary dermis	0.1	0.04	0.9
4	upper blood net dermis	0.08	0.3	0.6
5	reticular dermis	0.2	0.04	0.7
6	deep blood net dermis	0.3	0.1	0.7

The effective absorption coefficient of the dermal tissue sublayer considered the volumetric contribution of the all absorbers, namely, the main two haemoglobin species (oxyhaemoglobin and deoxyhaemoglobin), water and melanin.

The baseline absorption coefficient $\mu_{a_{baseline}}$ (i.e., the absorption coefficient of the skin tissue in absence of any other chromophore) at an operating wavelength λ was given by [Saidi, 1992; Jacques, 1998]:

$$\mu_{a_{baseline}} = 7.84 \times 10^7 \lambda^{-3.255} \quad (9.1)$$

The absorption coefficient of any i-th sublayer of skin (only except epidermis) was written as:

$$\mu_{a_i}(\lambda) = V_{A_i} \mu_{a_{A_i}}(\lambda) + V_{V_i} \mu_{a_{V_i}}(\lambda) + V_{w_i} \mu_{a_{w_i}}(\lambda) + [1 - (V_{A_i} + V_{V_i} + V_{w_i})] \mu_{a_{baseline_i}} \quad (9.2)$$

where V_{A_i} and V_{V_i} are the arterial and venous blood volume, respectively, in the i-th sublayer (i.e., $V_{A_i} : V_{V_i} = 1 : 1$ or, $V_{A_i} = V_{V_i} = V_{b_i}/2$); and $\mu_{a_{A_i}}$, $\mu_{a_{V_i}}$, $\mu_{a_{w_i}}$ are respectively the absorption coefficients of the arterial blood, venous blood and water present in the i-th sublayer.

The absorption coefficients of arterial and venous blood attributed to the absorption properties of oxy and deoxyhaemoglobin, as stated in the following equations:

$$\begin{aligned} \mu_{a_A}(\lambda) &= S_a O_2 \mu_{a_{HbO_2}}(\lambda) + (1 - S_a O_2) \mu_{a_{Hb}}(\lambda) \\ \mu_{a_V}(\lambda) &= S_v O_2 \mu_{a_{HbO_2}}(\lambda) + (1 - S_v O_2) \mu_{a_{Hb}}(\lambda) \end{aligned} \quad (9.3)$$

where $\mu_{a_{HbO_2}}$ and $\mu_{a_{Hb}}$ are the absorption coefficients of oxy and deoxyhaemoglobin, and $S_a O_2$ and $S_v O_2$ are the arterial and venous oxygen saturation respectively. According to the consideration in the model, $S_v O_2 = S_a O_2 - 10\%$.

The first two layers in skin, i.e., the stratum corneum and epidermis did not contain blood. The absorption coefficient of the stratum corneum was calculated using above

Table 9.2: Optical properties of tissue layer in finger tissue model.

Tissue component	$\mu_a(mm^{-1})$		$\mu_s(mm^{-1})$		g
	660 nm	940 nm	660 nm	940 nm	
skin	-	-	25.62	15.68	0.9
fat	0.0104	0.0170	6.20	5.42	0.8
muscle	0.0816	0.0401	8.61	5.81	0.5
bone	0.0351	0.0457	34.45	24.70	0.92
oxyhaemoglobin	0.15	0.65	-	-	-
deoxyhaemoglobin	1.64	0.43	-	-	-
water	0.0036	0.2674	-	-	-

equation with $V_b = 0$. Epidermal layer contained the absorber melanin. The melanin absorption coefficient $\mu_{a_{mel}}$ at a wavelength λ was determined from the following equation [Jacques and McAuliffe, 1991]:

$$\mu_{a_{mel}}(\lambda) = 6.6 \times 10^{10} \times \lambda^{-3.33}. \quad (9.4)$$

The epidermal absorption coefficient $\mu_{a_{epi}}$ was, therefore, written as the cumulative effect of the absorption coefficients of water and melanin:

$$\mu_{a_{epi}}(\lambda) = V_{mel}\mu_{a_{mel}}(\lambda) + V_{w_{epi}}\mu_{a_w}(\lambda) + [1 - (V_{mel} + V_{w_{epi}})]\mu_{a_{baseline}}(\lambda). \quad (9.5)$$

The haematocrit of blood was considered to be 45%. The absorption coefficients of the blood constituents (Hb and HbO_2) and water were adapted from literature [Bosschaart *et al.*, 2014; Laufer *et al.*, 1998; Steinke and Shepherd, 1988; Hale and Querry, 1973]. The absorption coefficients of subdermal fat and muscle were adapted from the published data measured from human skin [Simpson *et al.*, 1998]. Due to lack of data on the optical properties of a finger bone, the optical properties of the skull bone were used for the simulation [Bashkatov *et al.*, 2016]. The scattering coefficient and anisotropy factor of skin, muscle and bone were adapted from published studies [Simpson *et al.*, 1998; Bashkatov *et al.*, 2016]. The optical properties of the tissue layers used in the model are presented in Table 9.2.

The assumptions and considerations in the model were based on the ideal situations. In reality, however, the biological tissue is a highly heterogeneous and complex structure, with the variable spatial distribution of blood and other chromophores in different depths [Meglinski and Matcher, 2002]. The content of blood in tissue layers also can vary in amount and distribution [Renkin *et al.*, 1984; Goldsmith, 1991]. The thickness of the layers

is subjected to vary from person to person. Efforts were made to choose the parameters to simulate the model close to reality, replicating the ideal situation for a normal healthy human being.

9.4 Method of execution

The MC model was executed for the reflectance and transmittance modalities of PPG. In the reflectance mode, the optical source and detector were placed 5 mm apart on the tissue surface. In transmittance mode, the source and detector were placed at two opposite surfaces of the tissue site, i.e., 13 mm apart. A Gaussian beam of 1 mm radius was made incident to the tissue surface that propagated through the tissue medium to be detected at a circular detector of radius 1 mm. The model was executed to record the distribution of scattering and absorption events in different geometries through the finger tissue volume using the ‘fixed detector technique’ (Chapter 6). The optical path at the red and near-infrared wavelengths were also investigated. Further, the model was explored to record the ‘intensity’ of detected photon clusters. Here, the term ‘intensity’ I refers to the total weight of the detected photon clusters relative to the total weight of the incident photon clusters, which is generally known as ‘reflectance’ or ‘transmittance’ (depending on the source-detector positions). Denoting the ‘pulsatile intensity’ (i.e., the difference between the diastolic and systolic intensity) by ΔI , the normalised pulsatile intensity I_N was represented as:

$$I_N(\lambda) = \frac{\Delta I(\lambda)}{I_{diastole}(\lambda)} \quad (9.6)$$

The graphs resembling the ‘calibration curves’ of the pulse oximeter were generated at both modalities by computing the ‘ratio of ratios’ (R), i.e., the ratio of the red to the infrared (ir) normalised pulsatile intensity as a function of arterial blood oxygen saturation ($S_aO_2 = 10 - 100\%$):

$$R = \frac{I_N(red)}{I_N(ir)}. \quad (9.7)$$

The model investigated the relationship among the penetration depth, optical path and source-detector separation in a reflectance geometry. The mean penetration depth was calculated as the mean of the highest depths penetrated by each photon cluster. The mean

optical path was calculated as the mean of the total simulated pathlengths of all detected photon clusters using the ‘moving detector technique’ (Chapter 6).

The transmittance mode MC model was employed to quantify the contribution of each tissue layer to the total light-absorbance. Absorbance A in its normalised form at any wavelength λ was expressed as:

$$A(\lambda) = \frac{\Delta A(\lambda)}{A_{diastolic}(\lambda)}, \quad (9.8)$$

$\Delta(A)$ corresponding to the change in absorbance between systole and diastole.

The relative absorbance at the optical wavelengths 660 nm and 940 nm were expressed in terms of the ‘modulation ratio’ of the normalised absorbances, R_M [Mannheimer *et al.*, 1997]:

$$R_M = \frac{A(red)}{A(ir)}. \quad (9.9)$$

9.5 Simulated results of the interaction events

The simulated distribution of the light-tissue interaction events through the finger tissue in reflectance and transmittance modalities of PPG are shown in Figure 9.2. An example of typical distributions of the interaction events while the light traverses through the tissue from the source to the detector at an arterial oxygen saturation value $S_aO_2 = 90\%$ is shown here. In reflective geometry, the photons were simulated from a source (S) to a detector (D) placed 5 mm apart on the top surface of the tissue. In the transmissive geometry, the source and detector were supposed to be placed at two opposite surfaces of the tissue. Therefore, the depth of penetration of the photons in the reflective geometry depended on the source-detector separation, whereas for the transmissive mode the penetration depth was fixed, i.e., equal to the thickness of the tissue. The number of interaction events N (i.e., scattering and absorption events) along the depth within the tissue volume for red (660 nm) and infrared (940 nm) wavelengths are shown for the reflective geometry in Figures (a) and (b), and for the transmissive geometry in Figures (c) and (d) respectively. In the reflective mode, the maximum number of interactions was found in the upper layers of the tissue volume, i.e., the dermal sublayers. The maximum penetration depth was till the muscle layer and no photon passed beyond the muscle layer in both red and infrared wavelengths (i.e., penetration depth ≤ 11.5 mm). In

the transmissive mode, the maximum numbers of interaction events occurred near the source and the detector, which were limited to dermal sublayers. Also, a large number of interaction events were observed in the bone part of the finger. In all four simulations, the detected number of photon clusters were 10^8 . Typical time taken for detecting these many photon clusters in parallel programming configuration were 3 hours and 3.50 hours for reflective and transmissive modes respectively.

To quantify the distribution of the optical pathlength and the penetration depth in the reflective PPG, the histogram plots of these variables at both wavelengths were plotted in Figures 9.3 (a) and (b) respectively. The maximum number of occurrences were found in the smaller depths ($\leq 1.5\text{mm}$), i.e., primarily in the dermal tissue region. This observation agreed with Figure 9.2 (a). Maximum depth of penetration for both wavelengths concluded that almost no photons pass through the muscle layer, i.e., beyond 12 mm. The number of photons penetrated deeper was higher in infrared compared to red. In the histogram for optical pathlength, the number of infrared photons having smaller optical pathlength was higher than red. This observation is consistent with the results from the previous monolayer model where the infrared photons penetrated deeper yet had smaller optical pathlengths compared with red photons. The similar histogram plots for the transmissive modality of PPG are shown in Figure 9.4. The histogram plots of the penetration depth and the optical paths taken by the photon clusters from the source to the detector placed on the top and bottom surface of the finger tissue are shown in (a) and (b) respectively. The penetration depth followed the profile of the distribution of the scattering as shown in Figure 9.2(b). The maximum occurrence were seen in the depth of the bone tissue layer, i.e., the photons were interacted (or scattered) for the maximum number in the bone layer. This is explained by the very high scattering coefficient of bone 34.45 mm^{-1} for red and 24.70 mm^{-1} for infrared. The number of events are the lowest in the fat tissue layer. The second highest number of interactions occur in the dermal layer. In all cases the red number of scattering is higher. It should be noted that in transmissive mode, all photons had to penetrate all the sublayers of tissue in order to be detected, thus the total penetrated depth by both red and infrared photons were the same (i.e., equal to the thickness of the tissue 13 mm) which is seen in the Figure 9.4. The frequency of interactions at different depths and optical pathlengths in finger varied between the red

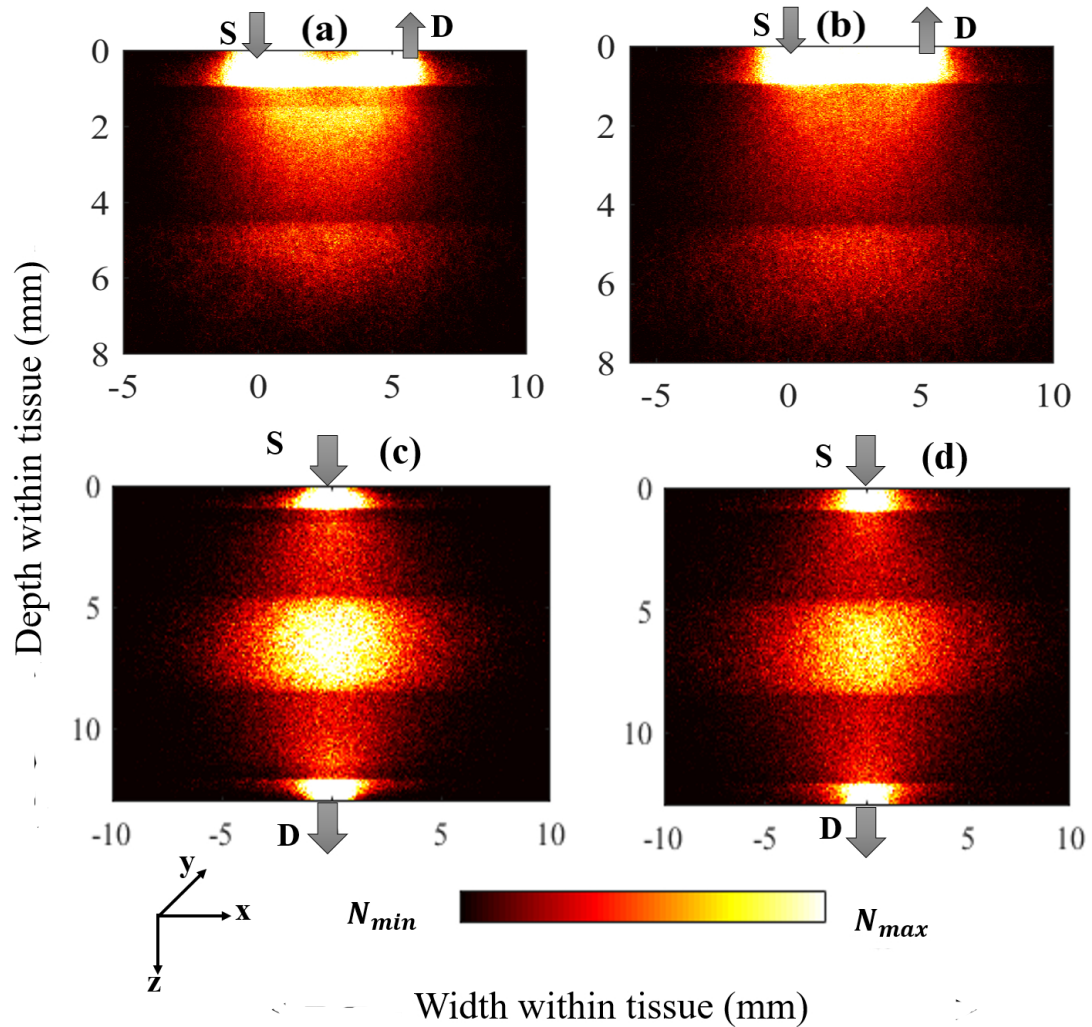


Figure 9.2: Density plots of the interaction events (i.e., scattering and absorption) while light passes through the finger tissue-volume at 660 nm and 940 nm are shown for the two modalities of Photoplethysmography: reflective modality in (a) and (b), and transmissive modality in (c) and (d), respectively. The plots are the xz -plane projection of the 3D simulation in the (x,y,z) Cartesian co-ordinate system. The optical source S and detector D are placed at a separation $d = 5$ mm on the same side of finger in the reflective geometry, and those are placed at two opposite surfaces of finger in the transmissive geometry. The colourbar represents the distribution of the number of interaction events (N) between its maximum and minimum values. All the plots are presented in the same axes limits. Optical paths of the detected photon clusters only have been shown.

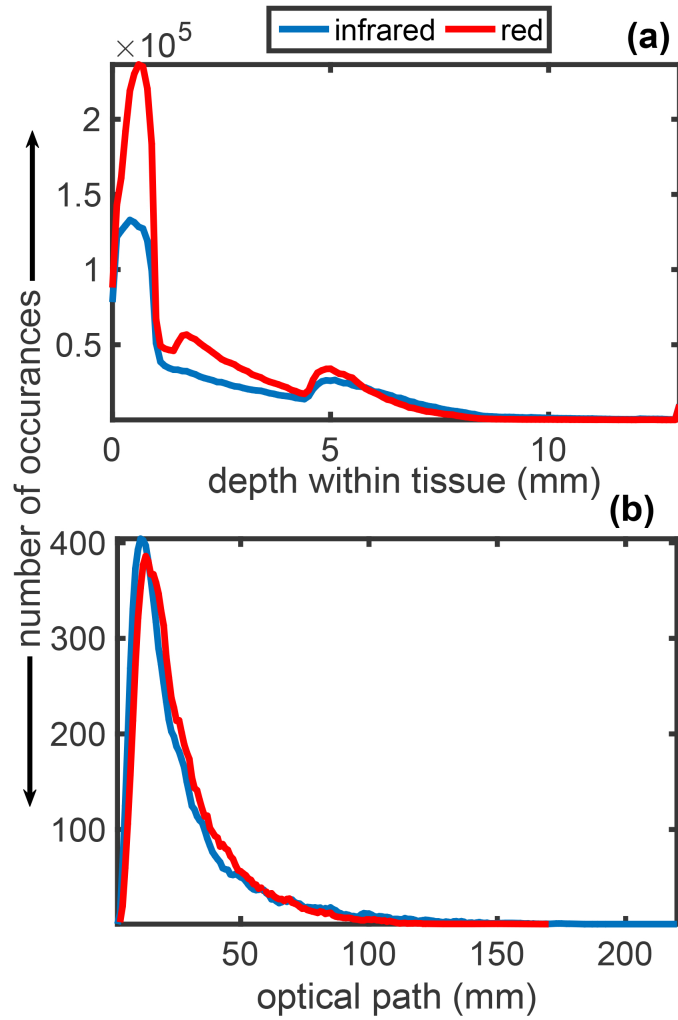


Figure 9.3: Histogram plots of the penetration depth (a) and the optical pathlength (b) taken by the detected photon clusters at red (660 nm) and infrared (940 nm) in the reflective PPG setting with a source-detector separation of 5 mm, placed on the top surface of finger tissue are shown.

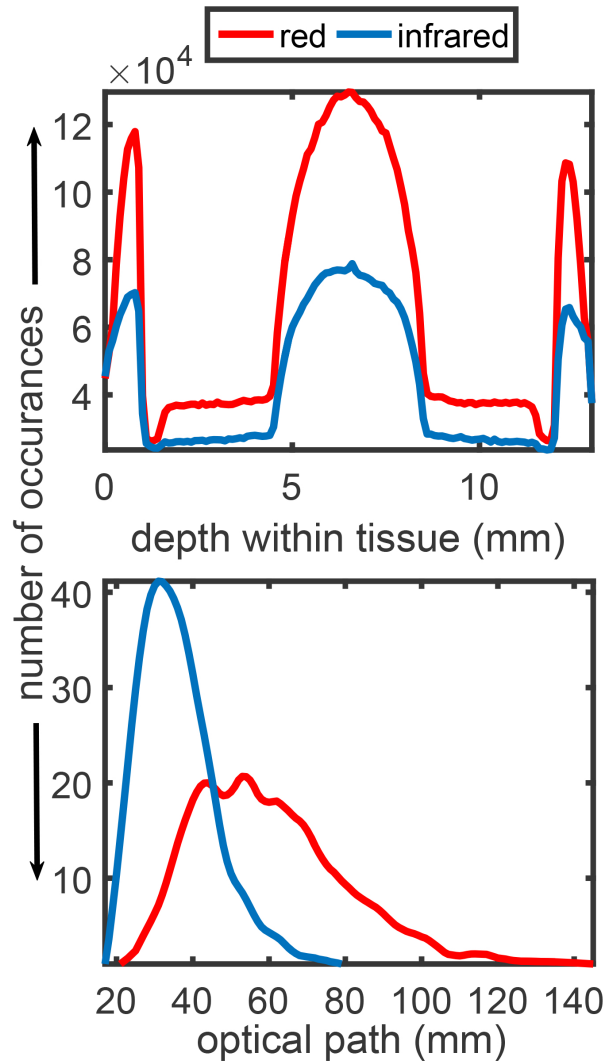


Figure 9.4: Histogram plots of the penetration depth (top) and the optical pathlength (bottom) by the detected photon clusters at red (660 nm) and infrared (940 nm) in the transmissive PPG setting with the optical source and the detector placed on the opposite surfaces of the finger tissue are shown.

and infrared light. Red photons having higher scattering coefficient than infrared, were tending to take higher optical paths despite penetrating through the same depth. This is validated in Figure 9.4, where it is seen that the number of photons having longer optical path is higher in red compared to infrared. To penetrate the same thickness of finger, the infrared photons used to take pathlengths up to 80 mm, whereas the red optical pathlength extended up to 140 mm.

9.6 Reflectance, Transmittance and Ratio of ratios

In Figures 9.5 (a) and (b), the detected reflectance and transmittance recorded in the reflective and transmissive PPG geometries are presented as functions of arterial oxygen saturation. The geometrical setting of PPG system were the same as stated in the previous section. The overall transmittance was shown to be higher than the overall reflectance for both red and infrared wavelengths at systole and diastole. For example, at 90% oxygen saturation, the infrared diastolic transmittance was 2.89×10^{-2} , which was about 10^5 times higher than the infrared systolic reflectance, i.e., 5.27×10^{-8} . Apparently, reflectance and transmittance for the red light very slowly increased with the arterial oxygen saturation, whereas the same for infrared light gradually decreased. The diastolic values of the reflectance and transmittance were shown to be slightly higher than the systolic values in all cases.

The calculated normalised pulsatile reflectance and transmittance were shown in Figures 9.5(c) and (d), respectively. Although the values of the individual detected intensities varied greatly between the reflectance and transmittance mode, the normalised pulsatile intensities (i.e., the ratio of the pulsating signal to the diastolic intensity) were almost identical in both the modes. For example, the infrared normalised reflectance was 0.18, i.e., almost equal to the infrared normalised transmittance 0.10. The red normalised intensity was higher than the infrared normalised intensity in both the modes.

The ratio of the normalised red and infrared amplitudes, i.e., R , was plotted as a function of the arterial oxygen saturation in Figure 9.5(e). These plots resembled the ‘calibration curves’ of the Pulse Oximeter. The calibration curves for the reflective and transmissive modalities were found to be strongly correlated. Using the in-built

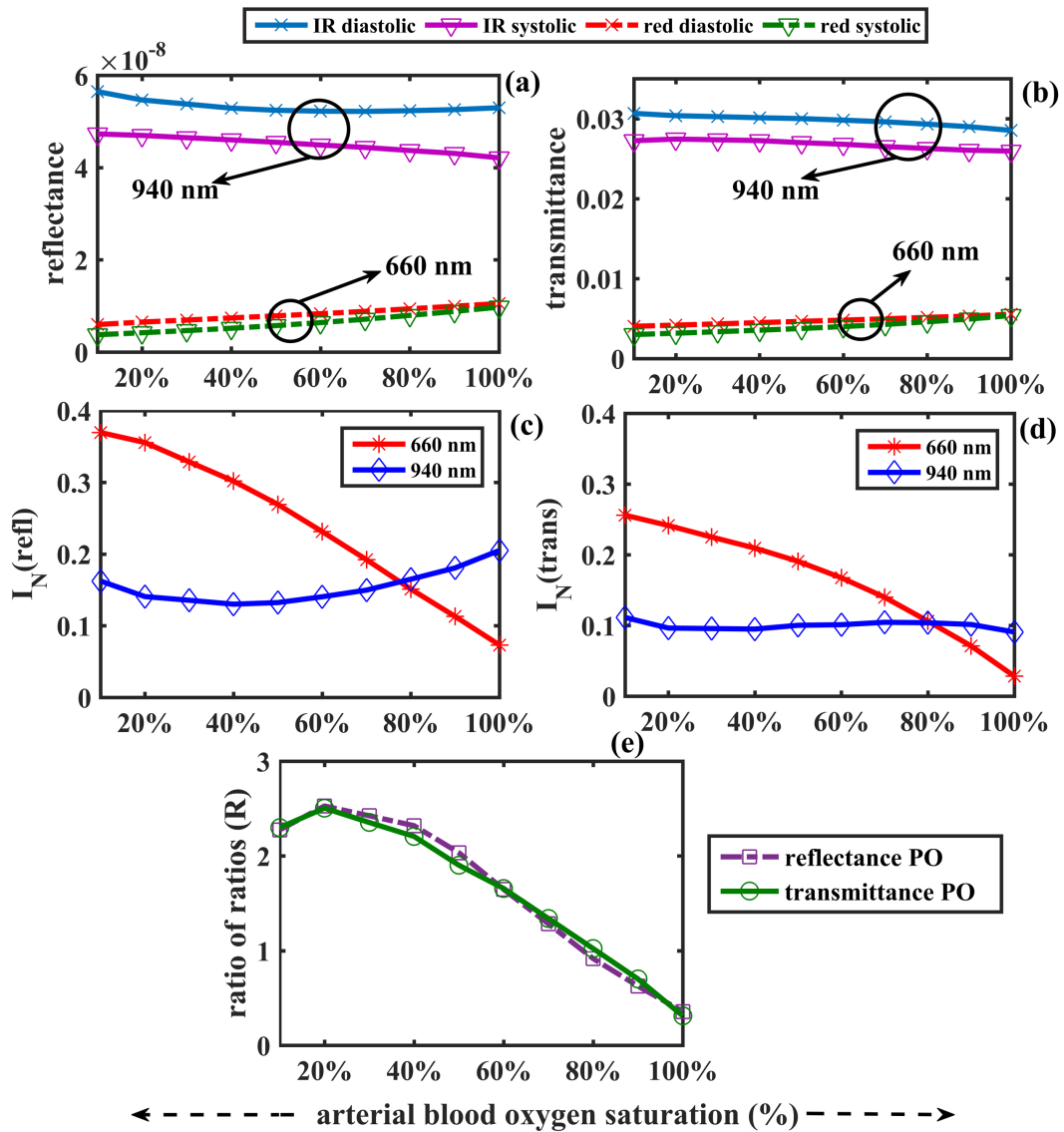


Figure 9.5: Detected reflectance and transmittance in the reflective and transmissive PPG geometries are shown in (a) and (b), respectively. The upper solid line pairs represent diastolic and systolic states at infrared wavelength (940 nm) and the lower dashed line pairs represent diastolic and systolic states at red wavelength (660 nm). The normalised reflectance and the normalised transmittance, as functions of arterial blood oxygen saturation, are plotted in (c) and (d). The ‘ratio of ratios’ R is plotted against the arterial blood oxygen saturation in (e), resembling the ‘calibration curves’ for both the reflectance and transmittance mode pulse oximeter.

correlation calculator in MATLAB, the correlation factor was found to be $r = 0.996$.

A high number of interaction events for red light led to more absorption in photon clusters, resulting in higher detected intensity for infrared light compared to red light at both the reflective and transmissive mode. The systolic increase in blood volume in the dermal sublayers resulted in more absorption in systolic states, and thus, higher detected reflectance and transmittance values in diastole compared to systole at all arterial blood oxygen saturations (10-100%) occurred. The ‘pulse’, i.e., the difference in systolic and diastolic amplitude (AC component of PPG), was normalised by the diastolic intensity (DC component of PPG) to obtain the ‘ratio of ratios’ (described in Chapter 6), that was plotted as a function of oxygen saturation to produce the ‘calibration curve’, which was the technical characterisation of the pulse oximetry set up. The similar patterns and values of normalised reflectance and transmittance, and the correspondence between the calibration curves obtained in reflective and transmissive modes show that the functions of the pulse oximeters do not greatly depend on the geometry chosen.

The limitations regarding the empirical calibration of pulse oximeters have been discussed in Chapter 8. The inadequacy of data in low arterial oxygen saturations may not influence the traditional SpO_2 reading by pulse oximetry, in fact, most of the pulse oximeters provide a consistent accuracy of $\pm 2\%$ in clinical measurements. Still such information is invaluable in cases such as septic shock where very low oxygen saturation in the peripheral proximities take place, often together with severe hypoxaemia where studies have shown an overestimation of the pulse oximeter readings [Wilson *et al.*, 2010].

9.7 Mean optical path and mean depth of penetration

The source-detector separation in a transmittance mode geometry was fixed. For investigation with variable source-detector separation, therefore, the reflective geometry was chosen. The the mean optical path and the mean penetration depth as functions of source-detector separation for a range of arterial oxygen saturation (SaO_2) were recorded. Results for the simulation of the optical pathlengths and the penetration depths at $SaO_2 = 10\%, 30\%, 50\%, 70\%$, and 90% are shown in Figure 9.6(a)-(e) and (f)-(j), respectively. The source-detector separation d was varied from 1 mm to 10 mm, with a gap of 1

mm between two consecutive detections. The total number of detected photon clusters in the range of source-detector separations was 10^{10} . The ‘moving detector’ technique was followed for the calculations. The simulations were performed at both the red and infrared wavelengths, at systolic and diastolic states. The mean optical path was found to increase almost linearly with d . The maximum optical path was taken by any photon cluster to reach the maximum distance between source and detector ($d = 10$ mm) was 60 mm. The penetration depth increased sharply with an initial increase of d , however, the increment rate fell for higher d . Interestingly, no photon passed through finger beyond the depth 8 mm, even for a high source-detector separation $d = 10$ mm. For all cases, the systolic and diastolic optical path and penetration depths appeared almost same, and varied between the red and infrared wavelengths, especially at higher source-detector separations ($d > 5$ mm).

The wavelength dependence of the mean optical path (MOP) and the mean penetration depth (MD) were quantified as the percentage change between their values at 660 nm and 940 nm (ΔMOP and ΔMD) following the equations:

$$\begin{aligned}\Delta MOP &= \frac{MOP(ir) - MOP(red)}{MOP(ir)} \\ \Delta MD &= \frac{MD(ir) - MD(red)}{MD(ir)}\end{aligned}\tag{9.10}$$

The percentage changes in the mean optical path and penetration depth at $d = 3$ mm, 5 mm, 7 mm and 9 mm for $S_aO_2 = 10 - 100\%$ are presented in Figures 9.7 (a) and (b) respectively. The negative values of ΔMOP at $d = 3$ mm referred to the lower optical path at 940 nm compared to 660 nm wavelength. With increasing d , the infrared optical path became higher than the red optical pathlength. With increasing oxygen saturation, the difference between red and infrared optical path slowly decreased. All positive values of ΔMD , on the other hand, indicated that the penetration depth in infrared light was always higher than red. The difference in the penetration depth between red and infrared light did not exhibit any significant variation with increasing oxygen saturation.

The optical pathlengths were found to increase almost linearly with d . Also, the physical optical pathlengths were much higher than the geometric pathlength (i.e., the source-detector separation). These two observations followed the modified Beer-Lambert law (Chapter 2). Optical pathlengths depended on both the absorption and scattering

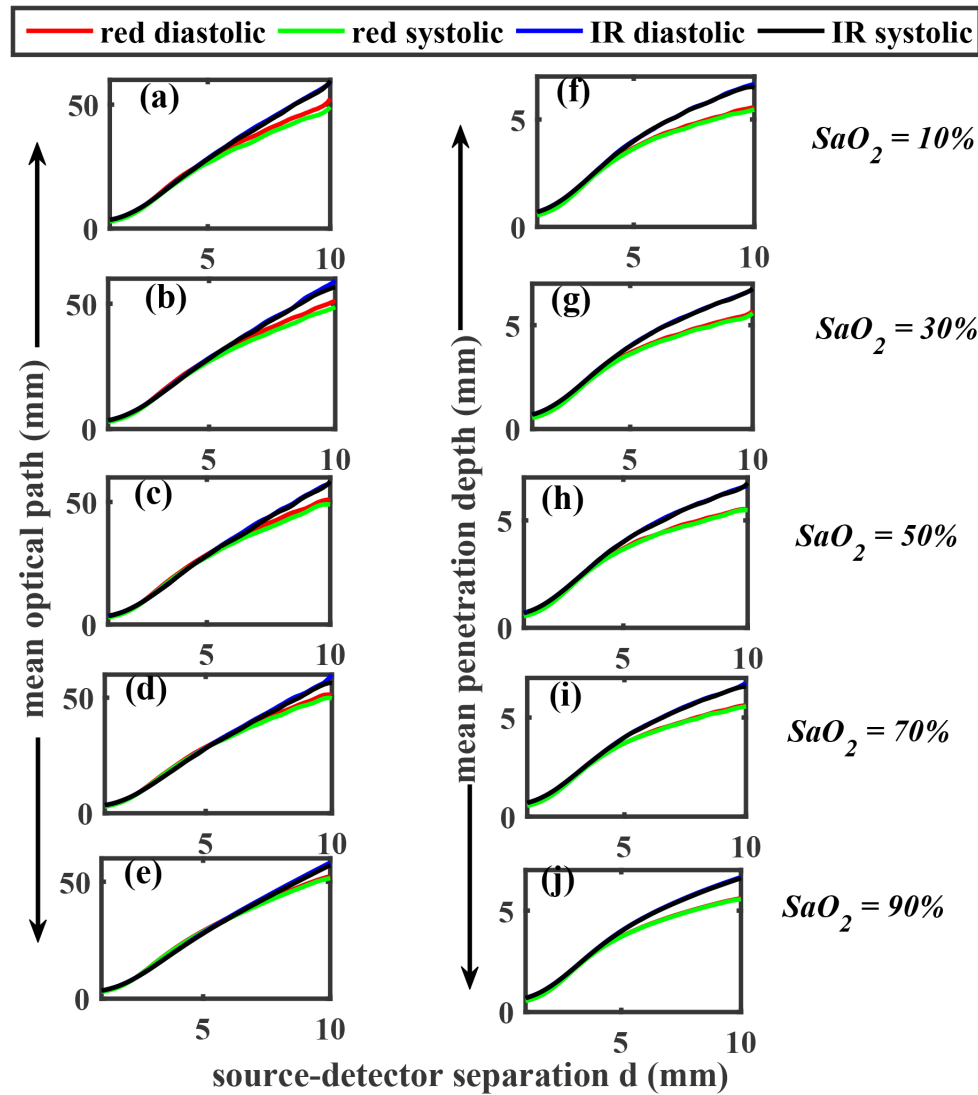


Figure 9.6: The mean optical path and the mean depth of penetration, at red (660 nm) and infrared (940 nm) wavelengths for both systolic and diastolic states, recorded at different source-detector separations ($d = 1-10$ mm) at arterial oxygen saturations 10%, 30%, 50%, 70% and 90% are shown in (a)-(e) and (f)-(j) respectively.

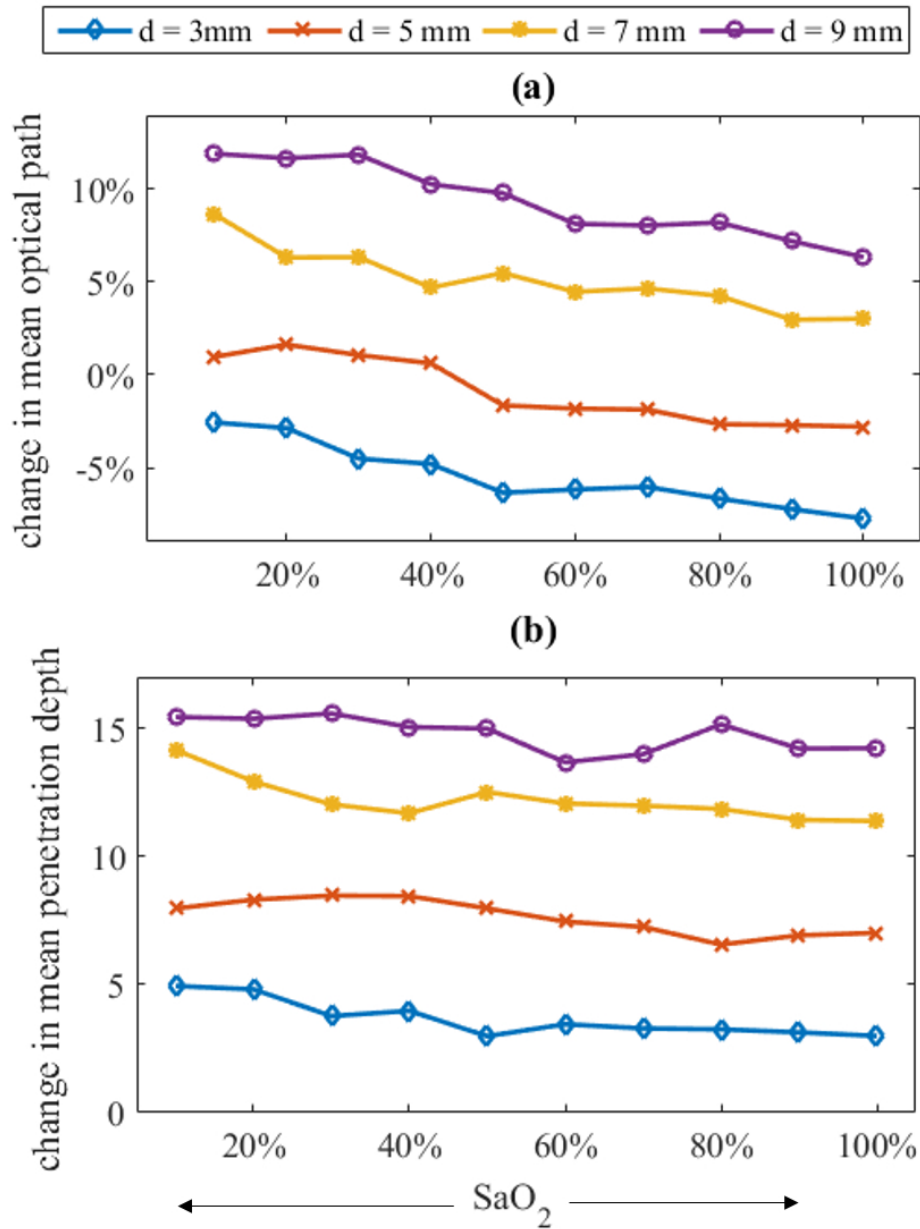


Figure 9.7: At source-detector separations $d = 3$ mm, 5 mm, 7 mm, and 9 mm, the calculated percentage changes in diastolic mean optical path ΔMOP between the red and infrared at $SaO_2 = 10 - 100\%$ are presented in (a). At the same source-detector separations, the calculated percentage change in diastolic mean penetration depth ΔMD are presented in (b). The different colours of the line plots as stated in the legend present different source-detector separations, and the markers represent the data points.

coefficients of the tissue layers. Since the effective absorption coefficient changed with the change in oxygen saturation, the optical pathlength also varied with the blood oxygen saturation, as seen in Figure 9.6(a)-(e). In the shorter source-detector separations, i.e., when photons mainly localised near the dermal sublayers, red photons took higher path than infrared photons. However, at higher source-detector separations, the higher infrared optical path compared to red was attributed to the distinct optical properties of muscle and bone.

The information of the penetration depth is important to understand the PPG light-tissue interaction. The method such as diffusion approximation is incapable of providing with correct information on penetration depth for a system like PPG where the source-detector separation is normally very small (\sim mm). The simulated result showed that the infrared light always penetrated higher than the red light as depicted in Figure 9.6 (f)-(j). The change in penetration depth with increasing oxygen saturation is an indicative of the dependence of the depth on the absorption coefficient (as scattering coefficient has no dependence on the oxygen saturation). The difference between the red and infrared depth of penetration sharply increased with the increasing source-detector separation and slowly decreased with increasing oxygen saturation.

From Figure 9.6, it is seen clearly that for lower source-detector separations ($d \leq 5$), red and infrared optical paths were almost the same, so were the depth of penetration. For higher separations, however, the difference increased considerably. From the observation, it is advisable that for the best result using reflective PPG setting, a small source-detector separation (~ 5 mm) should be chosen.

9.8 Normalised absorbances and modulation ratio

To retrieve the information on the absorption from each layer of the tissue, it photons need to pass through all tissue layers. While travelling from source to detector in the reflective modality PPG, light does not pass through all layers of the finger, as seen in earlier sections. Therefore, this study was performed on the transmissive modality of the system only. The distribution of relative absorbances in each tissue layer is illustrated in Figure 9.8. The amount of absorbances in each layer is presented in Table 9.3. It should

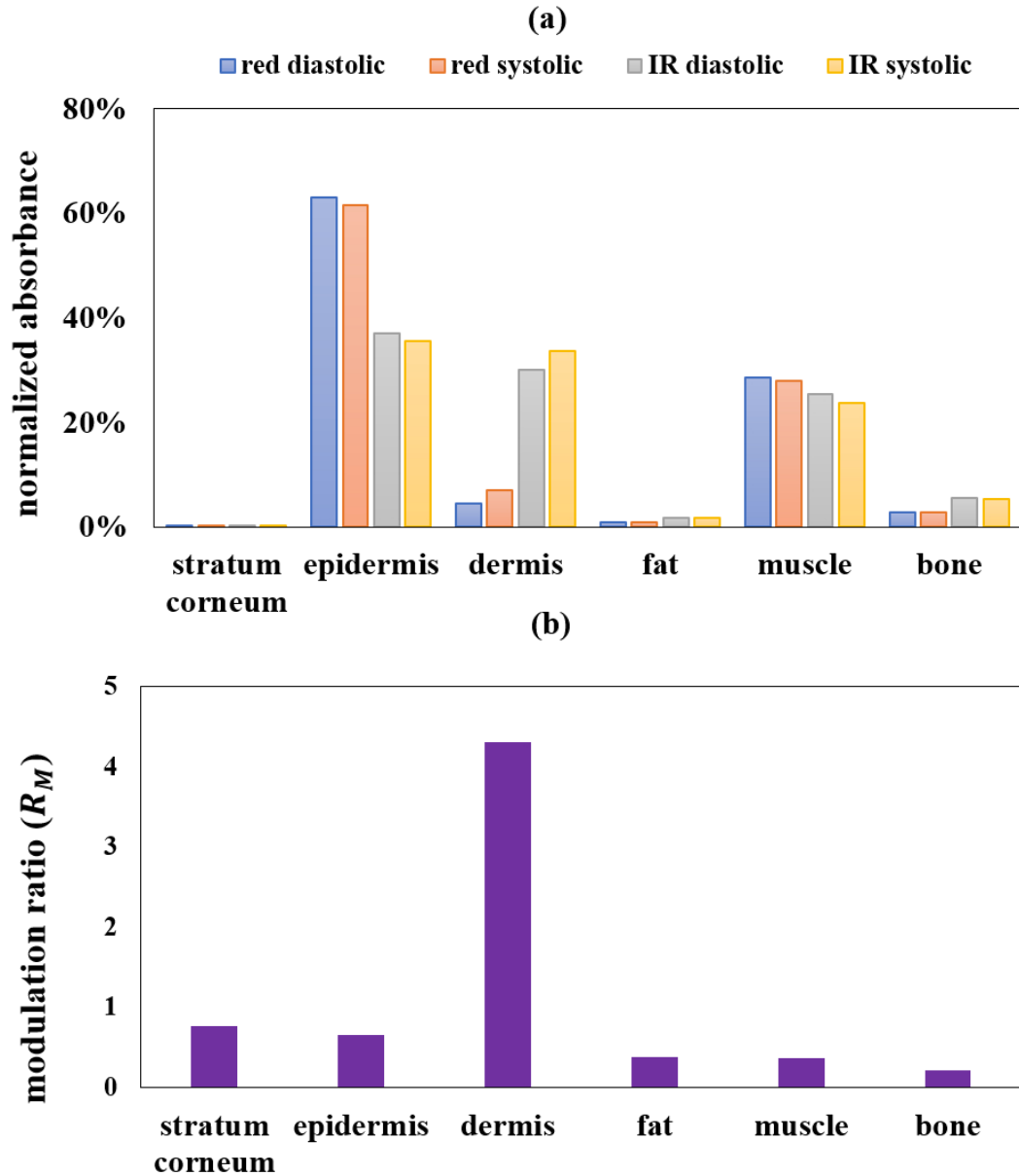


Figure 9.8: Barplot showing the distribution of the normalised absorbances ($A(\lambda)$) is presented in (a). The normalised absorbance was derived at different tissue layers in a transmissive modality of PPG at red (660 nm) and infrared (940 nm) wavelengths during systolic and diastolic phases of tissue perfusion. The absorbance modulation ratio $R_M = \frac{A(red)}{A(ir)}$ calculated for each tissue each layer is shown in (b).

Table 9.3: Simulated distribution of relative absorbances and modulation ratio in tissue layers

Tissue layers	Red diastolic	Red systolic	Infrared diastolic	Infrared systolic	R_M
Stratum corneum	0.12%	0.12%	0.09%	0.09%	0.77
epidermis	63%	61%	37.07%	35.57%	0.66
dermis	4.53%	6.97%	29.99%	33.74%	4.30
fat	0.82%	0.79%	1.79%	1.64%	0.37
muscle	28.58%	27.89%	25.50%	23.75%	0.36
bone	2.83%	2.79%	5.56%	5.21%	0.21

be noted that the absorbance in the dermis is presented as a whole and not as separate absorbances by sublayers.

The maximum absorbances at both red and infrared systole and diastole were seen in the epidermis layer. The minimal absorption was found in the stratum corneum, then in fat, bone, muscle and dermis. The absorbances in the dermal layer exhibited a large difference between the infrared and red wavelengths (e.g., in diastole, 29.99% and 4.53% which is about 7 times).

The relative difference in the absorbances of light between red and infrared wavelengths is the main working principle of pulse oximetry. Although this principle is well-known, the contribution of the different layers in the absorbance was never investigated earlier. Such an information is of fundamental importance for a comprehensive understanding of PPG and pulse oximetry mechanism. In Figure 9.8, the epidermal layer appeared to absorb the maximum amount of red (~60%) and infrared (~35%) light, which was attributed to the presence of a 10% melanin concentration in the epidermal volume. High absorbances were found in the muscle, bone and dermal layer, and the maximum amount of relative absorbance (hence the highest R_M) was found in the dermis, and the minimum was found in the bone. This also pointed towards the fact that the dermal sublayers were mainly responsible for the pulsatile signal, to which the contribution of bone was the minimal. This is an important observation as the optical properties of the bone layer used in the simulated tissue volume were approximated. All previously published modelling studies available related to the light-tissue interaction in finger or arm excluded the bone layer from their simulation stating that bone is highly scattering and reflecting [Schmitt, 1991; Doronin *et al.*, 2011]. In the present simulation, cranial

optical properties were used due to lack of information on finger bone. Simulated results showed, however, that the contribution of the dermis in the PPG waveform was much higher compared to any other layer, and bone had the minimum impact. These results justify the approximation of the bone optical properties in the simulated tissue volume.

9.9 Summary

In the present paper, the interaction of light at two wavelengths (660 nm and 940 nm) with a three-dimensional volume of finger tissue has been shown using a Monte Carlo model. The model has been executed at the reflective and transmissive modalities to investigate the distribution of scattering, detected intensities, the ratio of ratios, optical path, penetration depth, relative absorbances and absorbance modulation ratio. The comparative study between the reflective and transmissive modalities has given an insight into the pulse oximetry mechanism. The demonstration of the change in optical path and penetration depth with the source-detector separation are crucial to systematise the sensor geometry in a reflectance optoelectronic setting. Characterisation of the depth-specific absorbances elucidates the contribution of each layer of the tissue model in the PPG. The studies presented in this paper are useful in a broad area of applications using PPG, and also other similar optical systems.

DIFFERENTIAL PATHLENGTH FACTOR ESTIMATION AND PERFUSION ASSESSMENT BY PHOTOPLETHYSMOGRAPHY

10.1 Introduction

In previous chapters, the Monte Carlo model has been explored to understand the basic light-tissue interactions in PPG and pulse oximetry. From both the monolayer and multi-layer model based studies, the dependence of the optical path with the source-detector separation has been observed. The simulated optical pathlength (l) has been shown to be considerably higher compared to the geometrical pathlength (i.e., the source detector separation, d) in the previous results. In a highly scattering medium such as biological tissue, the physical pathlength of the photon is related to the geometrical pathlength by the Differential Pathlength Factor DPF , which was introduced during describing the modified Beer-Lambert law in Chapter 3. The relationship between the geometrical and physical optical pathlength is stated as:

$$l = DPF \cdot d. \quad (10.1)$$

The results presented in the previous chapters revealed the importance of the studies focussed on the optical path and DPF in PPG which has never been investigated before. In this chapter, a monolayer model of perfused skin and a multilayer model of human

forearm will be explored to investigate DPF in PPG. The simulated DPF for forearm will be further utilised to assess the tissue perfusion from PPG. Using the simulated DPFs at 660 nm and 880 nm, the time-change in concentration in the main two haemoglobin species of blood, namely, oxyhaemoglobin and deoxyhaemoglobin, will be evaluated from the experimentally obtained PPG signal from healthy volunteers. Additionally, the results obtained using the simulated DPF will be compared with the same obtained using approximated DPF, and the errors induced due to the approximations will be evaluated.

10.2 Background

The concept of DPF is fundamental in light-tissue interaction theory starting from Beer-Lambert law, as stated before. However, all the published studies on DPF associate with only one certain type of bio-optical system, namely, ‘Near Infrared Spectroscopy (NIRS)’. NIRS is a well-known biomedical diagnostic technique relying on the application of the modified Beer-Lambert law for measurement of tissue oxygenation and perfusion. Investigation on DPF is a very crucial part of NIRS studies, and many works have been pursued for estimating the values and the properties of DPF in NIRS at different tissue sites [Pellicer and del Carmen Bravo, 2011; Scheeren *et al.*, 2012; Jue and Masuda, 2013; Murkin and Arango, 2009; Hiraoka *et al.*, 1993; Delpy and Cope, 1997; Duncan *et al.*, 1995; Delpy *et al.*, 1988; Essenpreis *et al.*, 1993; Kohl *et al.*, 1998].

The recent works by Abay *et al.* [Abay and Kyriacou, 2015, 2018] have demonstrated the feasibility of using the Photoplethysmography signal for estimating changes in oxyhaemoglobin (HbO_2), deoxyhaemoglobin (Hb), and total haemoglobin (tHb) as in NIRS. This has been achieved by splitting dual-wavelength PPG signals into AC and DC components, and applying the modified Beer-Lambert law to the DC component. Since the same PPG signals can also be used to estimate the conventional SpO_2 , this approach allows the same signals captured during pulse oximetry for also determining other haemodynamic parameters (i.e., concentrations of oxy and deoxyhaemoglobin), in addition to measuring the oxygen saturation, in clinical settings. That might eventually lead pulse oximetry to be used as a tool for measurement of arterial oxygen saturations and for the assessment of tissue perfusion changes. Although being relatively easy to apply this approach, not

requiring any additional instrumentation to the conventional pulse oximetry technology, this procedure has been restricted by the unknown DPF. In the existing literature, the optical path and DPF have been evaluated for longer source-detector separations normally used for NIRS (>10 mm) [Duncan *et al.*, 1995; Van der Zee *et al.*, 1992]. The available information is unlikely to match the shorter source-detector separations which are ideally around 5-6 mm (as observed in Chapter 9). Also, in previous studies, DPF values have not been assessed at the wavelengths pertinent to PPG. The inadequacy of available data on the PPG DPF, therefore, limits the scope of tissue perfusion assessment from PPG. This limitation is possible to resolve with a better knowledge on the fundamental light-tissue interaction details behind the PPG system. With this motivation, the work presented in the chapter is focussed to estimate the DPF in PPG for the first time using Monte Carlo simulations, and to apply this knowledge gained from the study for the assessment of tissue perfusion using PPG.

Let us recall the modified Beer-Lambert law for a highly scattering medium such as biological tissue as introduced in Chapter 3. According to the law, the absorbance of light of an wavelength λ in tissue medium is represented as the product of the extinction coefficient ϵ of the medium, concentration c of the absorber and physical (or differential) optical pathlength l as stated below:

$$A_{\lambda} = \epsilon_{\lambda} \cdot l_{\lambda} \cdot c + G. \quad (10.2)$$

With the consideration that the main absorbers present in the tissue medium are oxyhaemoglobin (HbO_2) and deoxyhaemoglobin (Hb), the above equation can be written as:

$$A_{\lambda} = (\epsilon_{HbO_2\lambda} \cdot C_{HbO_2} + \epsilon_{Hb\lambda} \cdot C_{Hb}) \cdot l_{\lambda} + G \quad (10.3)$$

where $\epsilon_{HbO_2\lambda}$ and $\epsilon_{Hb\lambda}$ are the extinction coefficients of oxyhaemoglobin and deoxyhaemoglobin, respectively, and C_{HbO_2} and C_{Hb} are the concentrations of oxyhaemoglobin and deoxyhaemoglobin, respectively. Considering G to be constant over time, a differential approach of the modified Beer-Lambert law is applied that permits the calculation of changes in concentrations relative to an initial nominal or a baseline value. Expressing the differential pathlength in terms of the geometrical pathlength (i.e., the source-detector separation) d and the differential pathlength factor at the wavelength, DPF_{λ} , above

equation reduces to:

$$\Delta A_{\lambda} = (\epsilon_{HbO_2\lambda} \cdot \Delta C_{HbO_2} + \epsilon_{Hb\lambda} \cdot \Delta C_{Hb}) \cdot d \cdot DPF_{\lambda}. \quad (10.4)$$

This expression indicates a change in absorbance due to a change in the overall blood volume in tissue, or in other words, due to the change in concentration of the oxy and deoxyhaemoglobin in the tissue. This fundamental equation is the basis of NIRS measurements [Kohl *et al.*, 1998; Delpy and Cope, 1997; Matcher *et al.*, 1994].

Using the above equation in the two wavelengths used in pulse oximetry, at red and infrared (ir) wavelengths, a set of two linear equations are obtained:

$$\Delta A_{red} = (\epsilon_{HbO_2_{red}} \cdot \Delta C_{HbO_2} + \epsilon_{Hb_{red}} \cdot \Delta C_{Hb}) \cdot d \cdot DPF_{red} \quad (10.5)$$

$$\Delta A_{ir} = (\epsilon_{HbO_2_{ir}} \cdot \Delta C_{HbO_2} + \epsilon_{Hb_{ir}} \cdot \Delta C_{Hb}) \cdot d \cdot DPF_{ir} .$$

The two linear equations are solved to determine the concentration changes in oxy and deoxyhaemoglobin as:

$$\Delta C_{HbO_2} = \frac{\frac{\Delta A_{red} \epsilon_{Hb_{ir}}}{DPF_{red}} - \frac{\Delta A_{ir} \epsilon_{Hb_{red}}}{DPF_{ir}}}{d[\epsilon_{HbO_2_{red}} \epsilon_{Hb_{ir}} - \epsilon_{Hb_{red}} \epsilon_{HbO_2_{ir}}]} \quad (10.6)$$

$$\Delta C_{Hb} = \frac{\frac{\Delta A_{ir} \epsilon_{HbO_2_{red}}}{DPF_{ir}} - \frac{\Delta A_{red} \epsilon_{HbO_2_{ir}}}{DPF_{red}}}{d[\epsilon_{HbO_2_{red}} \epsilon_{Hb_{ir}} - \epsilon_{Hb_{red}} \epsilon_{HbO_2_{ir}}]} \quad (10.7)$$

Once ΔC_{HbO_2} and ΔC_{Hb} are calculated, the time changes in total haemoglobin concentration ΔC_{tHb} is derived as the sum of the two haemoglobins species.

$$\Delta C_{tHb} = \Delta C_{HbO_2} + \Delta C_{Hb} \quad (10.8)$$

The impact of DPF in the quantification of ΔC_{HbO_2} and ΔC_{Hb} , therefore, are seen from Eqs. 10.6 and 10.7. An approximation in the DPF value might cause a systematic error in the estimated concentration changes. The error induced by an approximation on the DPF value can be estimated by calculating the ‘cross-talk’ and the ‘absolute error’.

Cross talk relates to the separability of the mixed optical signals into ΔC_{HbO_2} and ΔC_{Hb} , and it is defined as the quantity of ΔC_{HbO_2} that is reflected into ΔC_{Hb} and vice-versa. The cross talk error (CT) due to inaccuracies in the optical pathlengths is expressed as [Strangman *et al.*, 2003; Uludağ *et al.*, 2004]:

$$CT_{i \rightarrow j} = \frac{-\epsilon_{i_{red}} \epsilon_{i_{ir}}}{\epsilon_{i_{red}} \epsilon_{j_{ir}} - \epsilon_{j_{red}} \epsilon_{i_{ir}}} \cdot [k_{red} - k_{ir}] \quad (10.9)$$

where ϵ_i is the extinction coefficient of either oxyhaemoglobin or deoxyhaemoglobin, and ϵ_j is the extinction coefficient of the other haemoglobin species. $CT_{i \rightarrow j}$ represents the crosstalk from the chromophore i to the chromophore j , and it is different in sign and magnitude from $CT_{j \rightarrow i}$, which, in turn, is the crosstalk from the chromophore j to chromophore i . The terms k_{red} and k_{ir} are the relative pathlength factors in red and infrared optical wavelengths, respectively [Strangman *et al.*, 2003; Uludağ *et al.*, 2004] and mathematically represent the amount of error in the optical pathlengths at each wavelength. Here, DPF simulated by the Monte Carlo model is defined as the ‘real’ DPF (i.e., DPF_{MC}). The approximated value of DPF based on the assumption of wavelength-independence is denoted as DPF_{appr} . Hence, the relative pathlength is expressed as the ratio between the accurate and estimated DPFs [Strangman *et al.*, 2003]:

$$k_\lambda = \frac{DPF_{MC_\lambda}}{DPF_{appr_\lambda}}. \quad (10.10)$$

Cross talk provides the qualitative error information between the concentrations, measured using real (simulated, in this case) and approximated DPF values.

The quantitative (or absolute) errors between the concentration measured in two ways (E_{Hb} and E_{HbO_2} , respectively, for deoxy and oxyhaemoglobin) can be derived directly using the following equations:

$$\begin{aligned} E_{HbO_2} &= \Delta C_{HbO_{2appr}} - \Delta C_{HbO_{2MC}} \\ E_{Hb} &= \Delta C_{Hb_{appr}} - \Delta C_{Hb_{MC}} \end{aligned} \quad (10.11)$$

where the concentration-change in Hb, determined using simulated and approximated DPFs, are $\Delta C_{Hb_{MC}}$ and $\Delta C_{Hb_{appr}}$, respectively and the concentration-change in HbO_2 determined using simulated and approximated DPFs are $C_{HbO_{2MC}}$ and $C_{HbO_{2appr}}$, respectively.

10.3 Methodology

The work in this chapter can be divided into three main sections. The first phase of work is the investigation of the DPF in a perfused skin tissue layer at different states of perfusion and oxygenation. This work is an extension from the monolayer model-based study presented in Chapter 8. The second part of the work includes the investigation of DPF

with a multilayer tissue model. A human forearm model was used for this purpose. The third part of the work utilised the estimated DPFs for forearm to assess the tissue perfusion (by determination of the time-change in concentration of oxy and deoxyhaemoglobin) from the PPG signal recorded from the forearm as a part of an *in vivo* experimental study. This part also estimated the cross-talk and the absolute error between for the results obtained using approximated DPF values.

The parameters for the monolayer model of the perfused skin has already been described in Chapter 8 and the same model was used for the assessment for DPF for different blood oxygen saturation and blood volumes in this chapter. The parameters for the multilayer model of forearm will be discussed in this chapter.

10.3.1 Description of multilayer tissue model

A heterogeneous volume of human forearm was modelled which replicated the location for the experimental PPG measurement. Experimentally, the signal was acquired from the volar side of the brachioradialis muscle of left forearm, which will be shown later in Figure 10.2. In Figure 10.1, the location of the PPG sensor on the hand, and the anatomical configuration of the tissue volume beneath the sensor are presented. The anatomical structure presented in Figure 10.1(B) was presented by a simplified tissue model presented in Figure 10.2. A three-dimensional slab geometry was chosen to represent the volume of the forearm which was interrogated by red (660 nm) and infrared (880 nm) light. In order to reconstruct a multilayer tissue model, the anatomical properties of the forearm were determined by surveying the published literature [Doronin *et al.*, 2011; Tuchin *et al.*, 2011; Meglinski and Matcher, 2003; Williams *et al.*, 1989; Schmitt, 1991] and analysing histological images. The first six layers starting from the top represented the dermal sub-layers of the skin (stratum corneum, epidermis, papillary dermis, upper blood net plexus, reticular dermis, and deep blood net plexus) and they were followed by the subdermal fat layer and the muscle layer. This order represented the first half of the tissue model, and was replicated in reverse order in the other half of the model. Overall, the multilayer tissue model comprised 15 layers, with a total thickness of 4 cm and an infinite width (considering the spatial distribution of the photons to be much smaller than the width of the human forearm). The schematic of the multilayer tissue

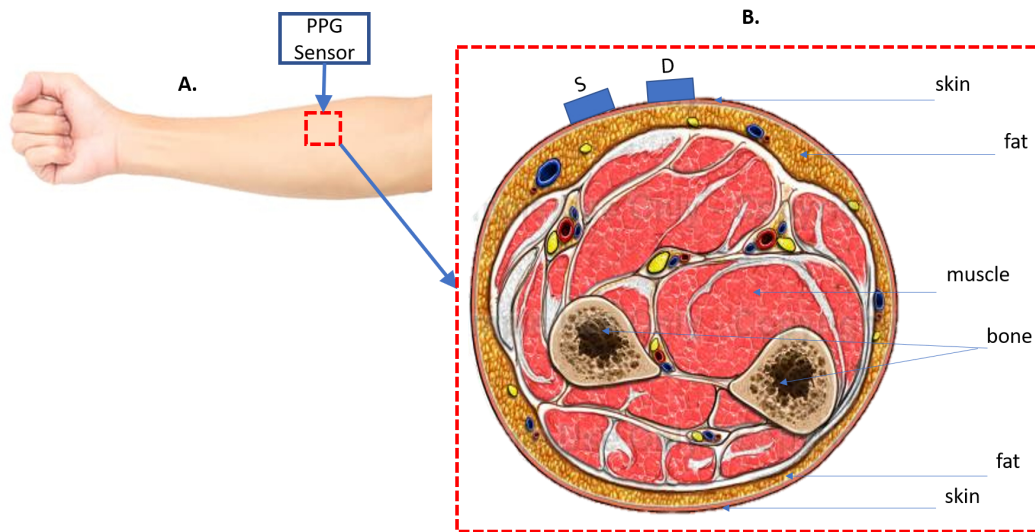


Figure 10.1: The location of the PPG sensor on the forearm (A) and the anatomy of the volume of tissue in that location (B) are presented. This figure corresponds to the actual experimental set up presented in Figure 10.3. S and D represent the approximate locations of the optical source and detector of the PPG sensor, placed on the volar side of the brachioradialis muscle of left forearm. The anatomical description is adapted from the text book [Netter, 2017].

model in the reflectance photoplethysmography setting at a source-detector separation of 5 mm is shown in Figure 10.2.

The stratification of the layers of the forearm tissue are illustrated in Table 10.1. The volume of blood (V_b) and water (V_w) in each layer were used to simulate the overall perfusion and hydration of the tissue, and the values were adapted from textbook [Wang and Tuchin, 2013]. The arterial oxygen saturation of blood in all layers was considered 92%, with an arteriovenous oxygen saturation difference of 10%, an arteriovenous blood concentration ratio 1:1 and a haematocrit of 45% [Wang and Tuchin, 2013; Bosschaart *et al.*, 2014; Jacques, 1998]. The individual absorption and scattering coefficients and anisotropy factor were adapted from published literature [Simpson *et al.*, 1998; Matcher *et al.*, 1994; Kohl *et al.*, 1998; Bosschaart *et al.*, 2014; Steinke and Shepherd, 1988]. The effective absorption coefficient was calculated using the same formulations described in Chapter 9. Refractive index of tissue layers was 1.4, and the external (air) refractive index was 1.

The model used in this work did not include the optical properties of the bone layer. Due to the high scattering and reflecting optical characteristics of bone, especially in a

Table 10.1: Stratification order and properties of the tissue layers used for modelling the forearm. The thicknesses are presented with the volume distribution of blood and water in each layer.

Tissue layer	Thickness (mm)	C_{blood}	C_{water}	$\mu_a (mm^{-1})$			$\mu'_s (mm^{-1})$		g
				660 nm	880 nm	880 nm	660 nm	880 nm	
1. Stratum corneum	0.02	0	0.05	0.0497	0.0222				
2. Epidermis	0.1	0	0.2	2.7316	1.0592				
3. Papillary dermis	0.2	0.04	0.5	0.0931	0.0548				
4. Upper blood net plexus	0.1	0.3	0.6	0.5128	0.1666		2.562	1.681	0.9
5. Reticular dermis	1.23	0.04	0.7	0.0834	0.0620				
6. Deep blood net plexus	0.12	0.1	0.7	0.1814	0.0869				
7. Subdermal fat	3.23	0.05	0.7	0.0998	0.0661		1.24	1.09	0.8
8. Muscle	30	0.35	0.6	0.5944	0.1874		0.8610	0.635	0.9

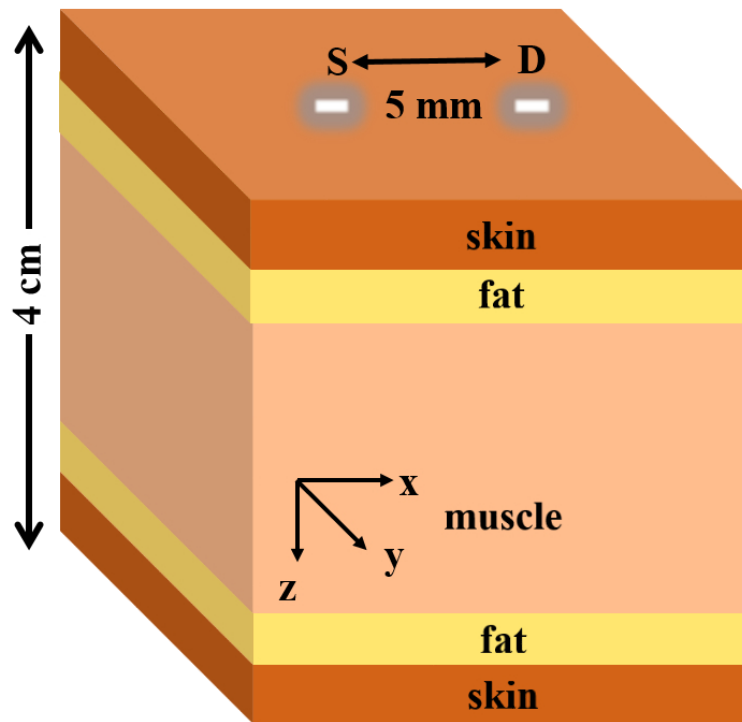


Figure 10.2: Schematic of tissue layers of human forearm model presented in a three-dimensional Cartesian co-ordinate system. The model comprises of the layers skin, fat, muscle, and again fat and skin respectively (skin sublayers are not shown separately). The depth of tissue is along the negative z-axis. Total tissue thickness is 4 cm. In the reflectance PPG setting, the optical source (S) and detector (D) are placed at a distance of 5 mm, however the distance in the simulation was varied. This schematic is a simplified form of the anatomical structure shown in Figure 10.1B.

small source-detector separation used in this study, the photons scattered within the bone were very unlikely to survive until they reach the detector [Schmitt, 1991; Williams *et al.*, 1989]. Also, there was not enough study describing the optical properties of forearm-bone. Additionally, from the previous chapter, by investigating with the finger tissue layers, it was found the bone has a minimum impact in PPG light tissue interactions. Therefore, the presence of bone layer in the forearm (radius and ulna, which are two cylindrical bones, deep below the skin and surrounded by muscle tissue) were not considered in the model.

10.3.2 Execution strategy

Both the monolayer and multilayer models were executed in the moving detector technique (described in Chapter 6) for capturing a 10^{10} number of photon clusters throughout

a range of source-detector separations.

If the path of the photon cluster through the tissue volume from the source to the detector is simulated through small step sizes s (where each value of s is different), the total optical path S of the photon cluster will be the sum of these small steps:

$$S = \sum_i s. \quad (10.12)$$

The mean optical pathlength (also differential pathlength) l is the average of the total optical pathlengths of all photons detected in a certain source-detector separation (which is also the geometrical pathlength) d at a certain wavelength λ :

$$l_{\lambda_d} = \bar{S}_{\lambda}. \quad (10.13)$$

According to the definition of differential optical path, the DPF at the same geometrical and optical pathlength at that wavelength is calculated as:

$$DPF_{\lambda_d} = \frac{l_{\lambda}}{d}. \quad (10.14)$$

In this work, for both the monolayer and multilayer models DPFs were calculated through a range of source-detector separation d . The monolayer model was executed at the wavelengths 660 nm and 940 nm. The multilayer model was executed at the wavelengths 660 nm and 880 nm. Both the wavelengths 880 nm and 940 nm are commonly used to detect the PPG signals in pulse oximetry [Patel *et al.*, 2018; Budidha *et al.*, 2018].

Usually, shorter source-detector separations (< 10 mm) are used in PPG measurements, whereas larger source-detector separations (> 10 mm) are used in NIRS measurements. Depending on the usual application, the range of source-detector separations used in this study for modelling light-tissue interactions were divided into two sections: d_{PPG} that was varied between 1-10 mm, and d_{NIRS} that was varied from 10 mm to 40 mm. Although the work primarily focussed on the determination and application of DPF for PPG, the NIRS region was also modelled for a more comprehensive understanding.

The monolayer model was executed in the PPG region only, demonstrating DPF values through d_{PPG} ($1 < d(mm) < 10$) at red and infrared wavelengths. The multilayer model was executed at through the ranges of d_{PPG} and d_{NIRS} ($1 < d(mm) < 40$). The simulated DPF values from the multilayer model were further utilised in the experimentally obtained PPG signal.

10.3.3 Experimental setting and data analysis

As already stated, initial attempts to assess tissue perfusion using PPG was restricted with an insufficient information on optical pathlength. Also from Eq. 10.6 and Eq. 10.7, it is apparent that an inaccurate selection of DPF may cause systematic errors in the estimated concentration changes [Boas *et al.*, 2001; Uludağ *et al.*, 2004; Strangman *et al.*, 2003]. Thus, using the simulated DPF values, the time change in concentration was determined from the physiological signal recorded from healthy volunteer, and compared with the result with not using the DPF values. The DPF values derived from the MC model were used for determining changes in the concentration of oxyhaemoglobin and deoxyhaemoglobin from in-vivo PPG measurements acquired from the forearm. The measurements were collected as a part of a previous study by [Abay and Kyriacou, 2015]. The experimental set up for recording the PPG signal of the volunteer is shown in Figure 10.3. The processing unit ZenPPG was used for acquiring the PPG data, the details of which can be found in the work by [Budidha *et al.*, 2018]. The collected data consisted of raw PPG signals (AC + DC) acquired at two wavelengths, red (660 nm) and infrared (880 nm), from a reflectance PPG sensor positioned on the volar side of the left forearm. The reflectance PPG sensor comprised two red (660 nm) LEDs, two infrared (880 nm) LEDs, and a photodiode. The LEDs and photodiode were placed at a centre-to-centre distance of 5 mm.

The protocol consisted of a sequence of vascular occlusions, which aimed to induce changes in blood flow in the measurement area and they were performed by manually inflating a cuff positioned around the upper left arm (on the volar side of the brachioradialis muscle) of 21 healthy volunteers (13 males and 8 females having the mean age of 31.05 years with a standard deviation of 7.55). Ethical approval was granted by the Senate Research Ethics Committee at City, University of London and written consent was sought from the volunteers before commencing of the investigation. Subjects with a history of cardiovascular disorders were excluded from the study.

The protocol started with 5 min of baseline measurements, followed by two minutes of venous occlusion (60-mmHg occlusion pressure), 2 min of recovery (no pressures), and two final minutes of total vascular occlusion (occlusion pressure 20-mmHg over the

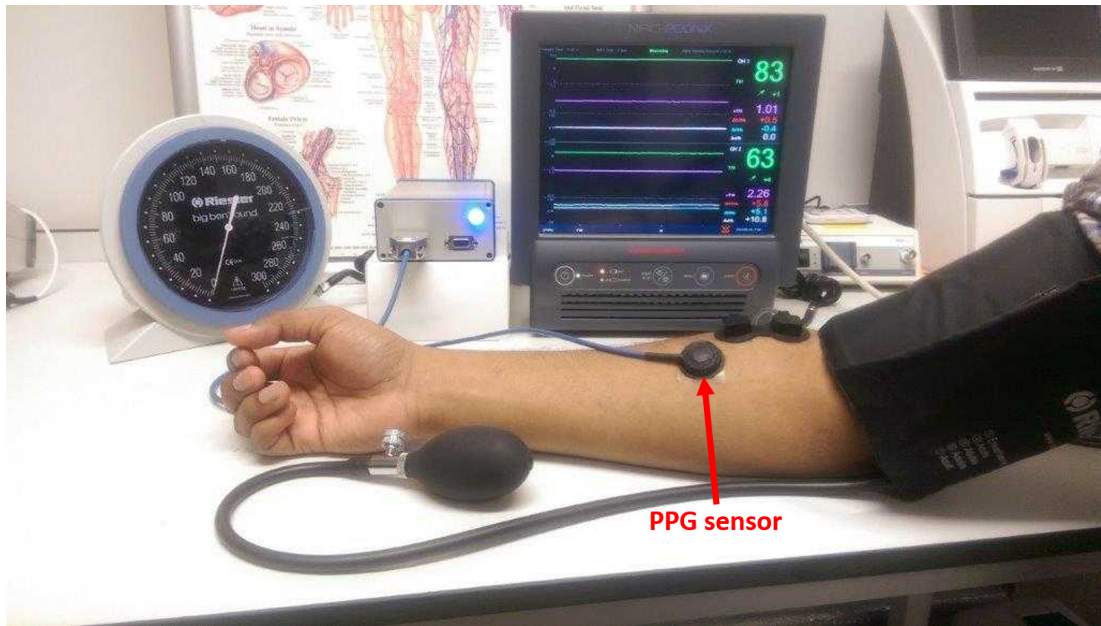


Figure 10.3: The experimental set-up for acquiring the PPG signal is shown. The PPG sensor is placed at the volar side of the left forearm of the volunteer.

systolic pressure). The post-processing of the signals was performed on MATLAB. The DC components were obtained with a low-pass zero-phase digital filter (cut-off frequency: 0.1 Hz). A more detailed description of the protocol and the reflectance PPG sensor can be found in the published work by [Abay and Kyriacou, 2015].

In order to investigate the effects of DPF approximations on ΔC_{HbO_2} and ΔC_{Hb} estimated from PPG measurements, the error-analysis was carried out with three different sets of approximated data. The ‘real’ situation was considered when the DPF values for red and infrared optical wavelengths obtained through the MC simulation ($DPF_{MC_{red}}$ and $DPF_{MC_{ir}}$), were utilised for calculating ΔC_{HbO_2} and ΔC_{Hb} from the PPGs acquired from the forearm. This situation was considered as ‘real’ in this case as the DPFs were obtained from the simulation of a realistic model and no assumption or approximation was made regarding the optical pathlength (i.e., $DPF_{red} \neq DPF_{ir}$).

In the approximated conditions, the wavelength-independence of DPF was assumed (i.e., $DPF_{red} = DPF_{ir}$). The conditions are listed below:

- **Case A:** The DPFs for both wavelengths were set equal to the value simulated for the red wavelength (i.e., $DPF_{red} = DPF_{ir} = DPF_{MC_{red}}$).
- **Case B:** The DPFs for both wavelengths were set equal to the value obtained for the

infrared wavelength from the MC simulation (i.e., $DPF_{red} = DPF_{ir} = DPF_{MC_{ir}}$).

- **Case C:** The DPFs for both wavelengths were set equal to an experimentally determined DPF for NIRS measurements from the existing literature [Van der Zee *et al.*, 1992]. The parameter was measured from the adult forearm by the time of flight method at an optical wavelength of 761 nm, resulting in a value of 3.59 for long separation distances ($d > 2.5$ cm). Therefore, the DPFs at red and infrared wavelength in this experiment were approximated to be equal to 3.59 ($DPF_{red} = DPF_{ir} = 3.59$).

For each of the conditions where the DPFs were approximated (i.e., A, B, and C), the cross talk and absolute errors were assessed against the results obtained with the MC simulated DPFs (i.e., $DPF_{MC_{red}}$ and $DPF_{MC_{ir}}$), following the theory explained in Section 10.2. The cross talk between haemoglobin species was determined with the relative pathlength factor k_λ being set as the ratio between the DPF obtained at each wavelength from the MC simulation and the DPFs assumed at each of the three conditions above. For example, in Case A where $DPF_{appr} = DPF_A$, the relative pathlength at red wavelength was written after Eq. 10.10 as $k_{A_{red}} = \frac{DPF_{MC_{red}}}{DPF_{A_{red}}}$. The inaccuracies in the haemoglobin concentrations in the three conditions were assessed by determining the absolute error in the measurements. This was obtained for each haemoglobin species by computing the maximum difference between the concentrations estimated using simulated DPFs (DPF_{MC}) and approximated DPFs (DPF_{appr}). The error was then normalised to the full measurement range and expressed as a percentage error. The values across the population were presented as median and interquartile ranges (IQR).

10.4 DPF in monolayer perfused skin tissue

Differential pathlength factors were evaluated for a semi-infinite three-dimensional slab of perfused dermis tissue. Simulated results with this model (e.g., scattering distribution, optical pathlength, penetration depth etc.) have already been presented in Chapter 8. Dependence of optical path on the source-detector separation, with a change in optical pathlength between the red (660 nm) and infrared (940 nm) wavelengths were observed in the results discussed in Chapter 8. The dependence of the optical pathlength on the

source-detector separation was quantified by the differential pathlength factor, and the results are presented in this chapter. DPF in the perfused skin was evaluated for a range of total oxygen saturation ($S_tO_2 = 50 - 100\%$) and blood volume ($V_b = 2.5\%, 5\%, 7.5\%, 10\%$) for the source-detector separations in PPG region ($1 < d_{ppg} (mm) < 10$). The results are demonstrated in Figure 10.4. In Figure 10.4, considerable difference is observed between the red and infrared DPFs. The values of DPF is found to be changing with the blood volume as well as blood oxygen saturation. For a clearer observation, DPFs for a fixed blood volume $V_b = 10\%$ for different oxygen saturations, i.e., $S_tO_2 = 50\%, 60\%, 70\%, 80\%, 90\%$ as function of source-detector separations are presented in Figure 10.5. Red DPF increases slowly with increasing d but the rate of increase gradually decays with the increasing d . Considerable increase in red DPF with higher oxygen saturation is noticed. The infrared DPF, on the other hand, does not change considerably with blood oxygen saturation and slightly varies with increasing source-detector separation. Also, DPF values at a fixed $S_tO_2 = 90\%$ for different blood volumes, i.e., $V_b = 2.5\%, 5\%, 7.5\%, 10\%$ are shown in Figure 10.6. It is seen that for red wavelength, the DPF rises more sharply compared to infrared. With increasing blood volume, red and infrared DPF values decrease.

The results presented in Figures 10.4, 10.5 and 10.6 elucidate the dependence of DPF on many factors, e.g., source-detector separation, optical wavelength, physiological states such as blood volume and oxygen saturation of tissue etc. Therefore, for any further application, it is crucial to assess the DPF in the specific geometry for the specific tissue sample at a certain wavelength rather than any crude approximation. The dependence of DPF on the external factors such as the geometrical setting or the physiological states are more clearly visible in the red wavelength. Relatively lesser changes in the infrared wavelength is consistent with the previous observation by [Delpy *et al.*, 1988] where it was stated the DPF is independent of the source-detector separation at infrared wavelength region. For PPG applications where lower wavelengths also play vital role, therefore, an accurate assessment of the DPF at a certain source-detector separation is crucial for any related studies.

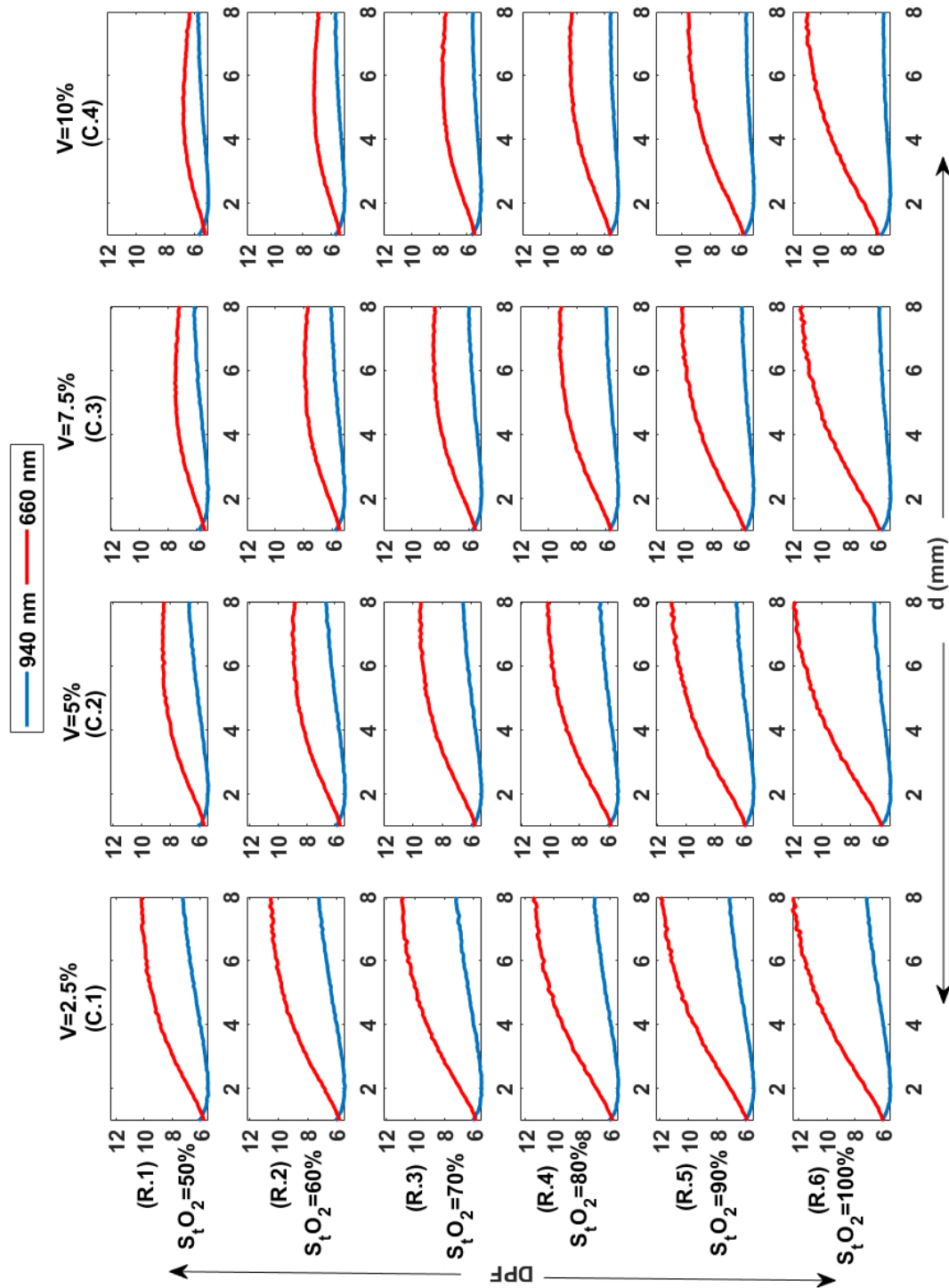


Figure 10.4: Differential Pathlength Factor is estimated in monolayer perfused skin dermis. DPFs in red (660 nm) and infrared (940 nm) are evaluated at source-detector separations 1-10 mm. Results for different blood volumes ($V_b = 2.5\%, 5\%, 7.5\%, 10\%$) are presented in the columns C.1-C.4, and that for different total oxygen saturations ($S_tO_2 = 50 - 100\%$) are presented in the rows R.1-R.6.

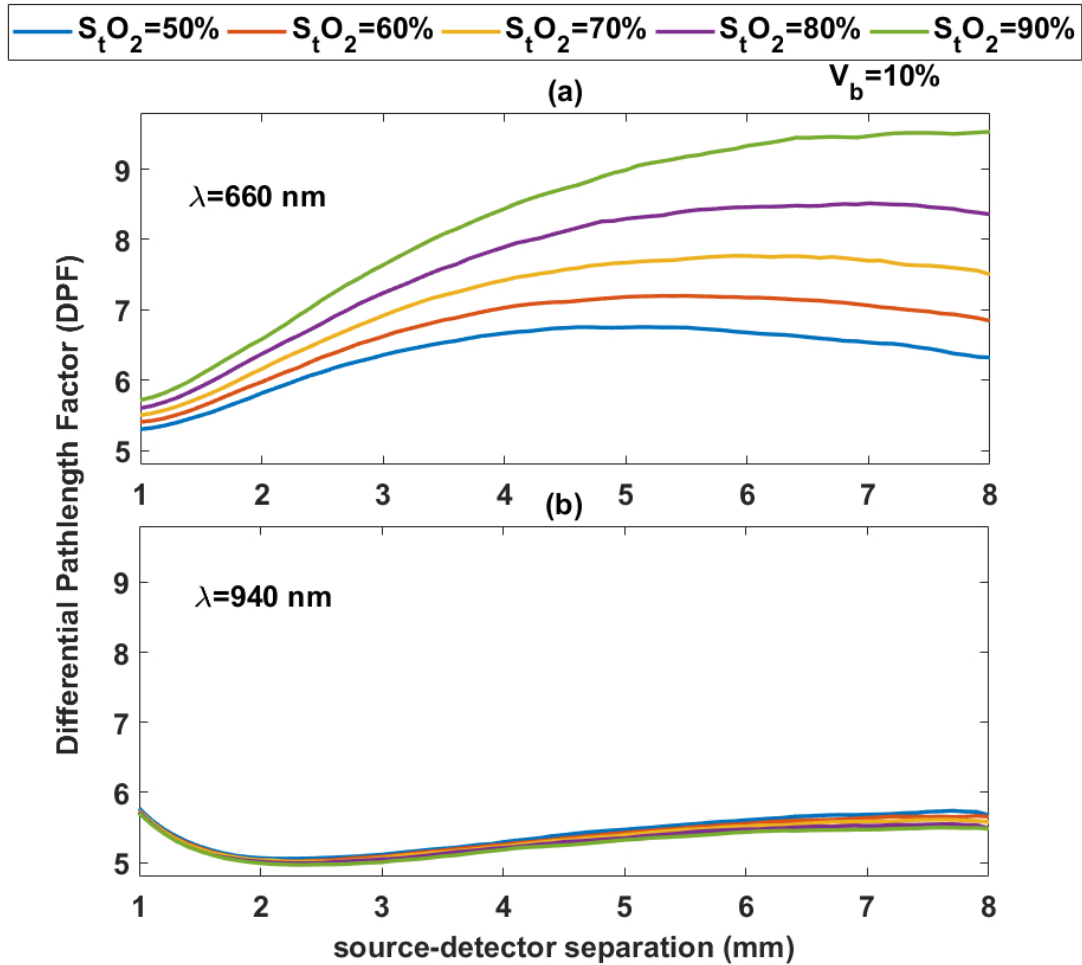


Figure 10.5: Differential Pathlength Factor in monolayer perfused skin dermis at a fixed $V_b = 10\%$ for different oxygen saturations $S_tO_2 = 50\%, 60\%, 70\%, 80\%, 90\%$. All plots are shown in the same axes limits.

10.5 Light-tissue interaction and DPF estimation in multilayer forearm tissue

Figure 10.7 shows the density plots of the simulated photon migration in the forearm at both red (660 nm) and infrared (880 nm) wavelengths. The plots show the colourmap of the scattering events N for red and infrared reflectance PPG measurements, acquired with an interoptode separation distance of 5 mm. The maximum number of photon scattering events is found within the top few layers, especially in the proximity of the light source and detector. The photon scattering distribution clearly decreases with increasing depth. It is noticeable that the majority of the scattering events for both wavelengths take place

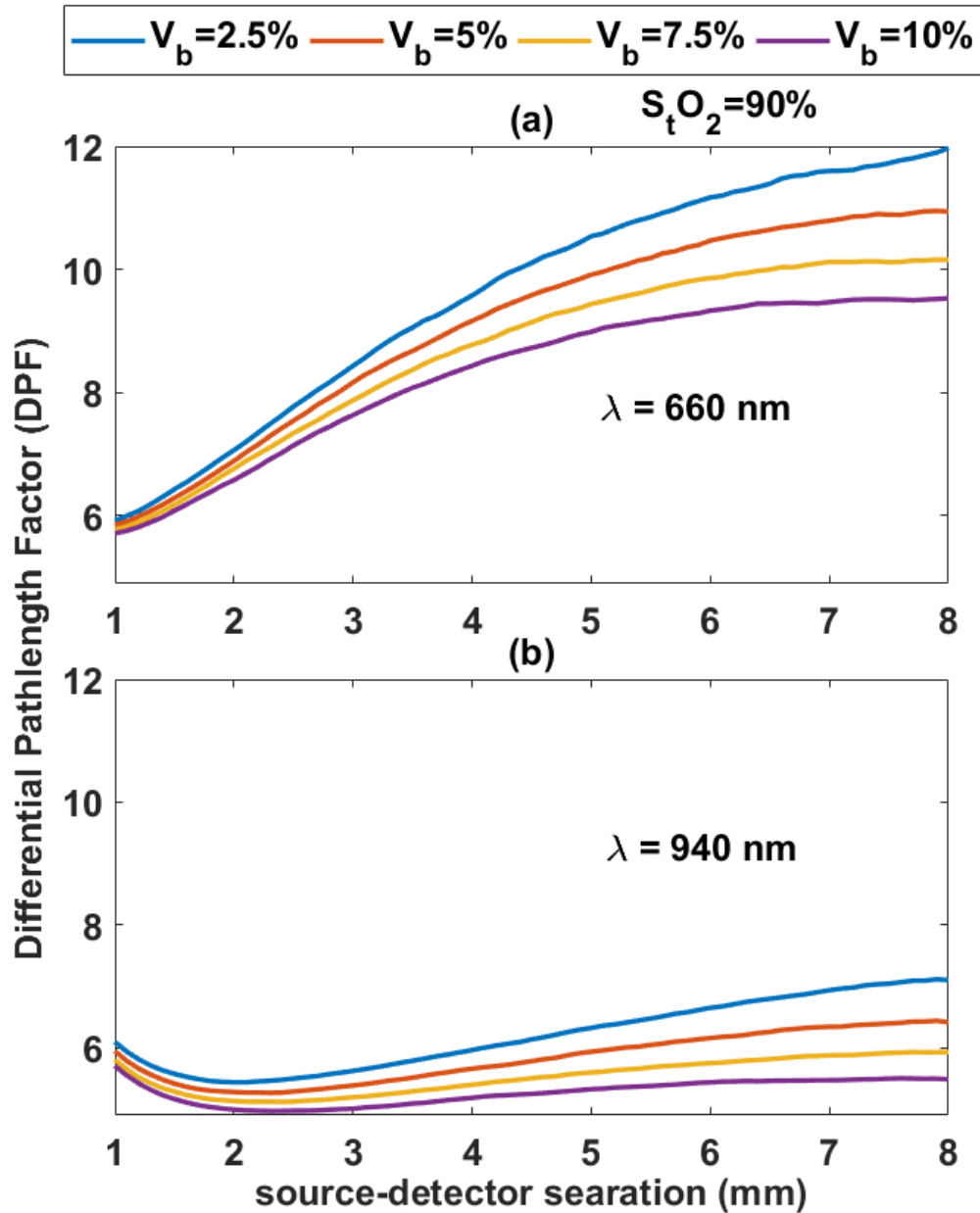


Figure 10.6: Differential Pathlength Factor in monolayer perfused skin dermis at a fixed $S_tO_2 = 90\%$ for different blood volume $V_b = 2.5\%, 5\%, 7.5\%, 10\%$ are shown for red (660 nm) in (a) and for infrared (940 nm) in (b). All plots are shown in the same axes limits.

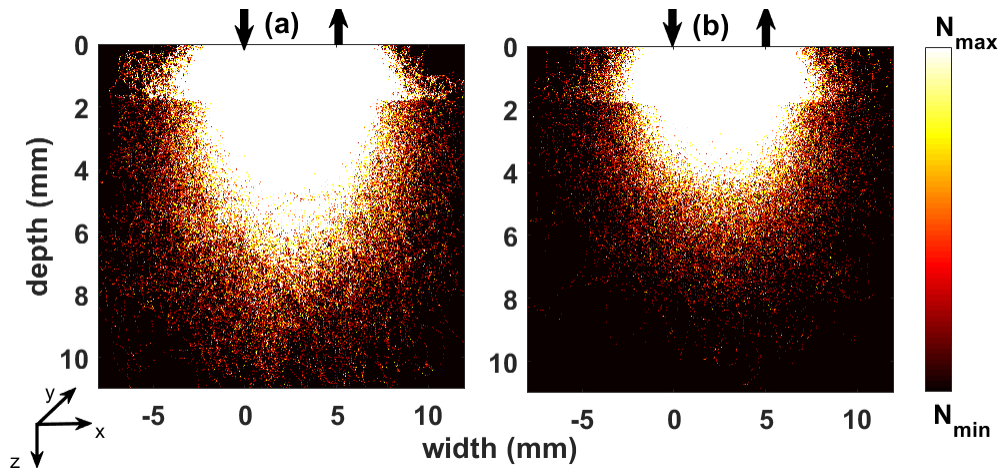


Figure 10.7: Simulated distributions of scattering events (N) through human forearm in PPG measurements at 880 nm (a) and 660 nm (b). The images are 2D projections of the 3D distribution, with a source-detector separation distance fixed at 5 mm. Only the photons that reach the detector from the source are shown. The images are scaled equally. Colourbar represents distribution between maximum (N_{max}) and minimum (N_{min}) values of number of scatter.

within the dermal skin layers, extending up to a depth of 1.77 mm. Almost no photons travel any deeper than the muscle tissue layer (i.e., 12 mm depth from the surface). In Figure 10.8, the scattering distributions for higher source-detector separations, which are beyond usual PPG specifications, and fall normally within the NIRS source-detector separation range, are shown. Simulations were carried out for the separations 15 mm, 25 mm and 35 mm. It is seen that the penetration depth increases slowly with increasing source-detector separation, although the maximum penetration depth by the photons did not exceed the muscle layer even for a very high source-detector separation.

Figures 10.9(a) and (b) show the simulated distributions of the mean optical path (or differential pathlength, l) and DPF in the forearm tissue volume at red and infrared wavelengths for source-detector separation distances ranging from 2 mm to 40 mm. As expected, the mean optical path l travelled by the photons increased with the separation distance d , indicating a deeper light penetration with increasing d . The differences in l and DPF at the two different wavelengths are clearly visible, with the optical path at 660 nm being higher than 880 nm, thus resulting in a greater DPF at the red wavelength. The plots in Figures 10.9(a) and (b) were divided into two application regions, depending on the source-detector separation distance d . The region A at shorter d , represents the typical application region of PPG measurements, whereas the region B indicates the applications

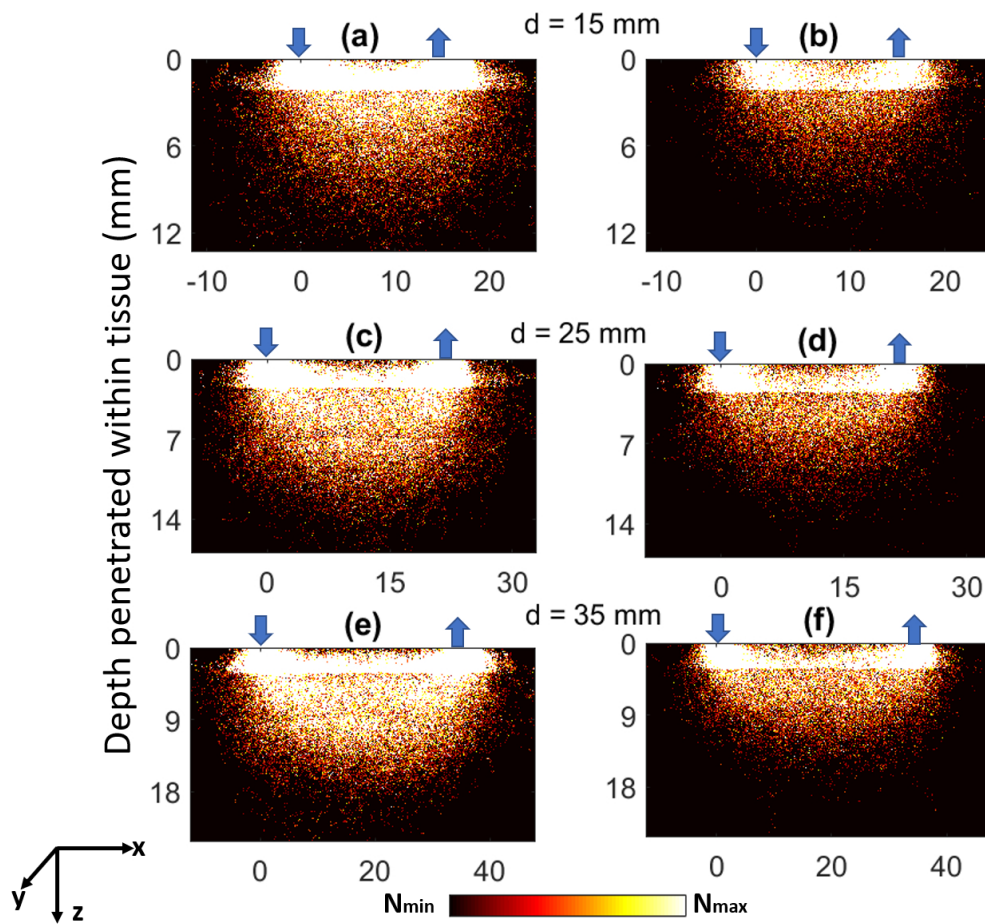


Figure 10.8: Simulated distributions of scattering events (N) through human forearm at 880 nm and 660 nm for larger source detector separations: $d = 15$ mm (a)-(b), $d = 25$ mm (c)-(d) and $d=35$ mm (e)-(f) respectively. The images are 2D projections of the 3D model. Only the photons that reach the detector from the source are shown. Colourbar represents distribution between maximum (N_{max}) and minimum (N_{min}) values of number of scatter.

with medium-large separation distances. The upper end of region B mainly represents NIRS applications, consisting in a very large source-detector separation distances ($d > 2.5$ cm). Interestingly, the increase of l with d in the PPG region (A) is much sharper compared to the NIRS region (B), resulting in a steep increase in DPF for lower d . For d larger than 30 mm (region B), the DPFs at both red and infrared wavelengths tended to an asymptote (constant DPF), with a concomitant decrease in the difference between red and infrared DPFs. Table 10.2 summarises some DPF values at 660 nm and 880 nm for different separation distances d commonly employed in PPG and NIRS measurements.

From the simulation results presented in Figures 10.7 and 10.8, it is observed that both the red and infrared light penetrate a certain distance within the tissue, with

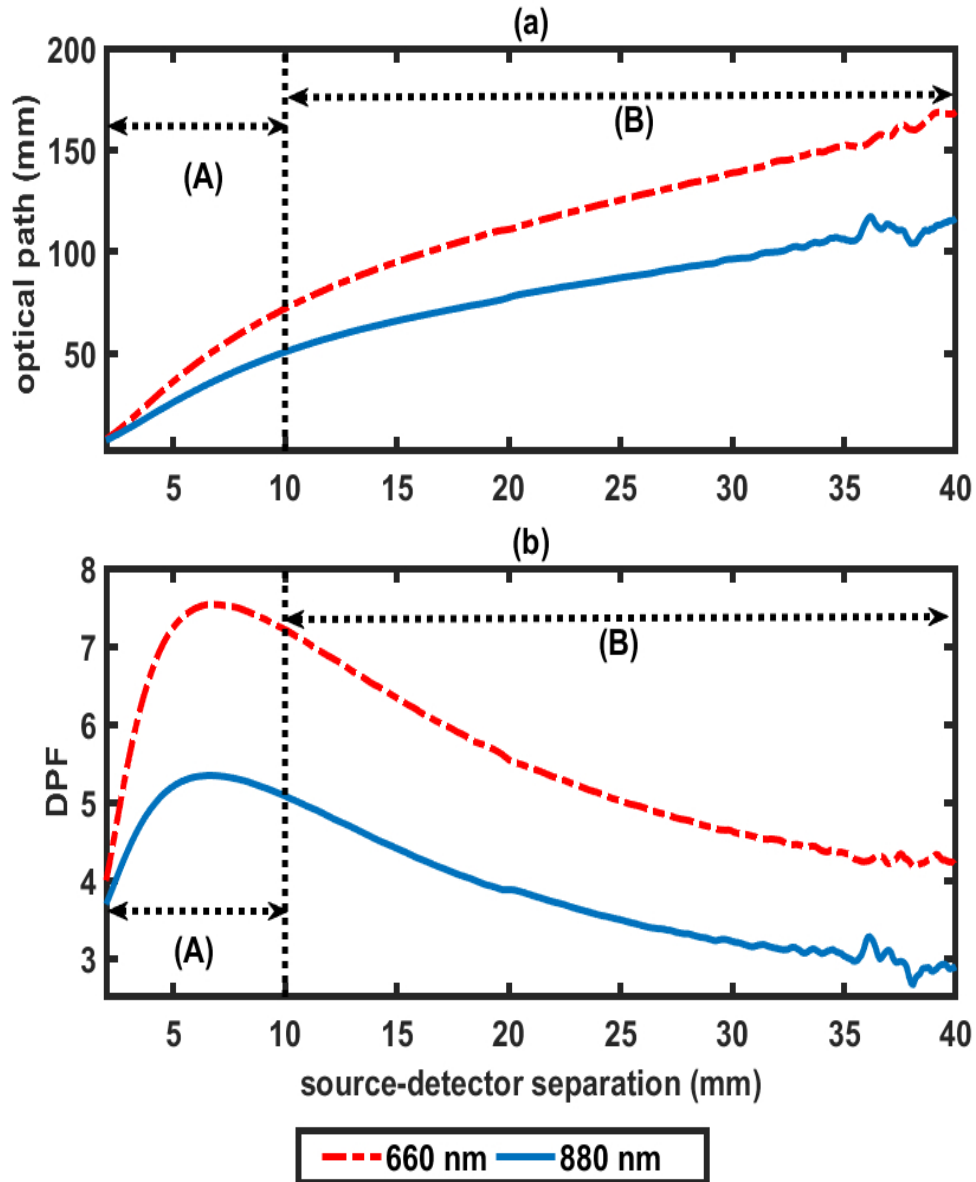


Figure 10.9: Mean Optical Path in mm (a) and Differential Pathlength Factor DPF (b) simulated through the human forearm at wavelengths 660 nm and 880 nm, as functions of source detector separation d . The region of shorter d is marked as (A) and the region at longer d is marked at (B), representing respectively the PPG and NIRS regions of measurements. Red dashed lines represent the results from 660 nm, whereas blue solid lines represent the 800 nm.

Table 10.2: Differential Pathlength Factor (DPF) at both red and infrared wavelengths for different source-detector separation distances d . The values are derived from the MC simulations of light transport through human forearm. The mean optical pathlength l can be calculated as $l = d \times DPF$.

Source-detector separation d (mm)	Differential Pathlength Factor (DPF)	
	660 nm	880 nm
2	3.998	3.70
3	5.542	4.398
4	6.649	4.915
5	7.242	5.203
6	7.487	5.323
7	7.532	5.337
10	7.213	5.077
20	5.547	3.876
30	4.628	3.215
40	4.218	2.905

maximum scattering in the first few layers of the skin and a reduction of scattering in the fat and muscle layers. The optical paths are mainly limited within the cutaneous and subcutaneous tissue region, which indicates that PPG would only provide information on the shallow tissue perfusion and not deep tissue perfusion as NIRS. In Figure 10.9, the two application regions investigated (regions A and B) show very different characteristics of the optical pathlength and DPF. Overall, the DPF for the red wavelength is always greater than infrared, thus highlighting a consistent wavelength-dependency of the DPF for short separation distances.

From the multilayer model study it is seen that DPF depends on scattering properties of tissue. The scattering coefficients of all tissue layers possess higher values in red wavelength compared to the infrared wavelength according to the tissue optical properties presented in Table 10.1. The effective optical properties of the tissue volume resulted in higher optical path for red photons for all source-detector separation. Consequently, DPF at 660 nm is consistently greater compared to 880 nm. The decline in the measured DPF values with increasing wavelength is as well observed in the literature by Duncan *et al.* in their experimental measurements of DPF on the forearm [Duncan *et al.*, 1995]. The variation in DPF with varying d observed in this study agrees with experimental measurements of DPF previously reported by van der Zee *et al.* [Van der Zee *et al.*, 1992]. In the study by van der Zee, the DPF was measured experimentally at d ranging from 10

mm to 60 mm. In their measurements on the forearm, the authors reported a gradual decrease in DPF with increasing interoptode distance, similarly observed in the present MC simulation. Also, it was observed that the measured DPFs were relatively constant for separation distances above 25 mm. The similarity of the results obtained from the present Monte Carlo studies with the published literature confirms the accuracy of the model. However, the DPF for separation d less than 10 mm (i.e., PPG applications) was never measured in any previous studies. Therefore, the present study can be considered as the first effort towards the assessment of DPF for PPG.

10.6 Experimental data analysis and error calculation

Figure 10.10 shows the changes in the concentration of HbO_2 and Hb from a subject, estimated from PPG signals in the three conditions A, B, and C (as described in Sec. 10.3). The trends in the changes of ΔC_{Hb} and ΔC_{HbO_2} indicate the variations in blood flow, either of venous or arterial nature, caused by the vascular occlusions. For comparison, the ΔC_{Hb} and ΔC_{HbO_2} obtained with the simulated DPFs are plotted as well in the same figure, showing how the approximations in the DPFs introduced some discrepancies in the estimation of ΔC_{Hb} and ΔC_{HbO_2} . The differences in the estimation of ΔC_{Hb} and ΔC_{HbO_2} were assessed by calculating the cross talk between the two haemoglobin species. Table 10.3 shows the values of cross talk calculated in all the three different conditions investigated, and it shows how the approximations in all three conditions resulted in a consistent cross talk between the haemoglobin species. The highest degree of cross talk for both haemoglobin species was observed in condition C, where a DPF for NIRS measurements was used for estimating ΔC_{Hb} and ΔC_{HbO_2} from PPG signals.

When compared with the results obtained with the DPFs from the MC simulations, the use of approximated DPFs for the estimation of ΔC_{Hb} and ΔC_{HbO_2} during occlusions also resulted in a consistent error in the quantification of the magnitude of change. Figure 10.11 shows the box-plots of the normalised percentage errors in ΔC_{Hb} and ΔC_{HbO_2} in the three different conditions. The normalised maximum errors in ΔC_{HbO_2} were 26.04 ($IQR = 21.76$ to 27.32)%, 9.90 ($IQR = 7.25$ to 12.28)%, 19.53 ($IQR = 15.16$ to 25.18)%, respectively, for conditions A, B, and C. The normalised errors for ΔC_{Hb} were 3.17

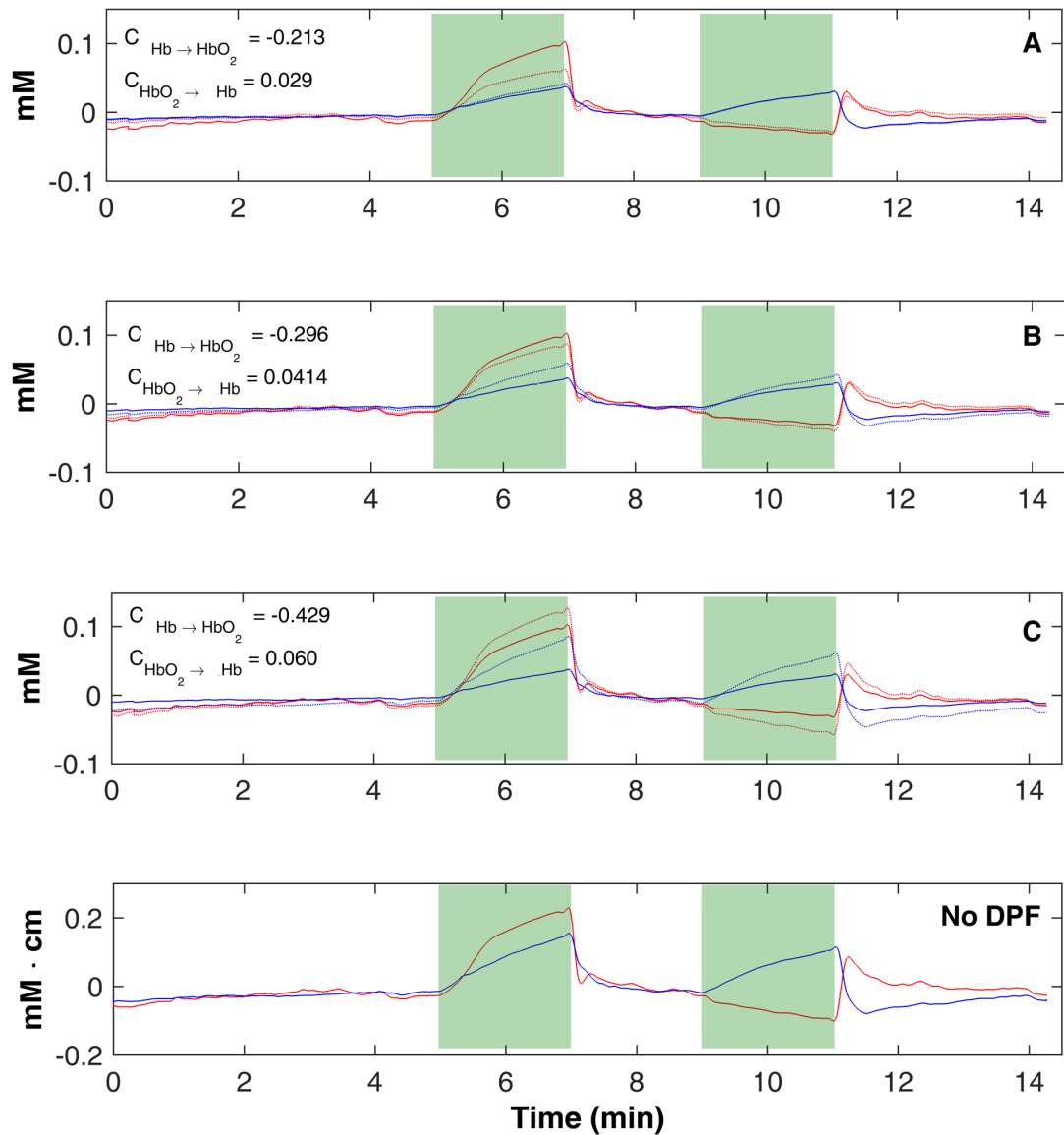


Figure 10.10: Changes in concentrations of oxyhaemoglobin HbO_2 (red traces) and deoxyhaemoglobin Hb (blue traces) estimated from a subject during the protocol in the three conditions investigated. The solid lines represent the changes estimated with the simulated DPFs, whereas the dotted lines represent the same estimated with the approximated DPFs. (a) ΔC_{HbO_2} and ΔC_{Hb} in condition A, (b) ΔC_{HbO_2} and ΔC_{Hb} in condition B, and (c) ΔC_{HbO_2} and ΔC_{Hb} in condition C. The bottom trace shows the ΔC_{HbO_2} and ΔC_{Hb} estimated without DPF (concentration \times optical pathlength). The shaded green areas indicate the duration of the venous occlusion (minutes 5 to 7) and total occlusion (minutes 9 to 11). For improved clarity, plots A, B, and C have been plotted with equal scales, whereas the last instance [(d) no DPF] has been plotted with a different scale in $mM \cdot cm$.

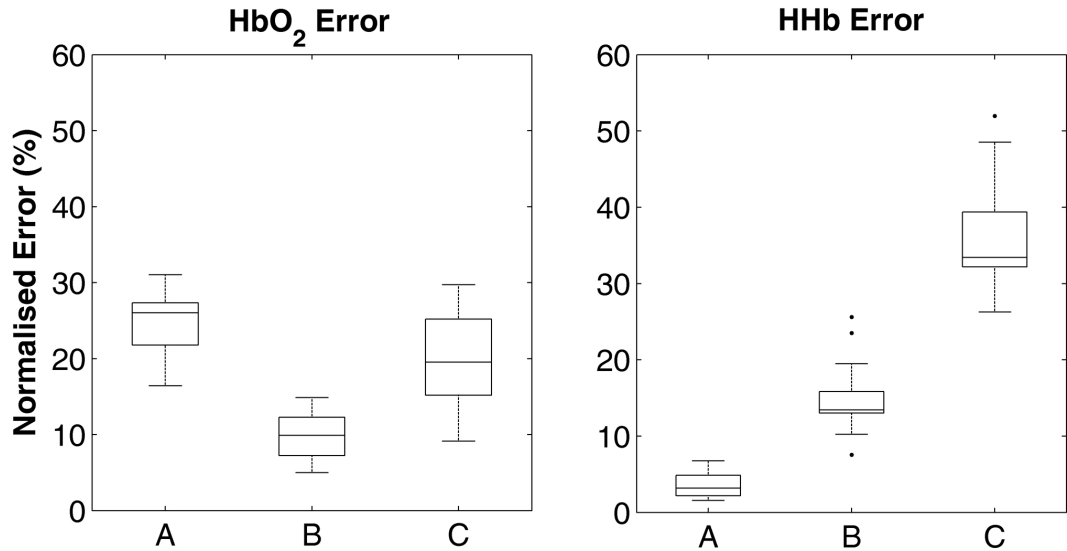


Figure 10.11: Box-plots of the normalised percentage errors of ΔC_{Hb} and ΔC_{HbO_2} in the three conditions (A, B, and C) investigated. The values represent the maximum absolute errors observed in ΔC_{Hb} and ΔC_{HbO_2} from the MC simulation condition, normalised to the full measurement ranges.

($IQR = 2.18$ to 4.85)%, 13.44 ($IQR = 13.00$ to 15.83)%, and 33.43 ($IQR = 32.18$ to 39.39)% for conditions A, B, and C, respectively.

Table 10.3: Cross talk between haemoglobin species calculated for the three conditions investigated. $CT_{Hb \rightarrow HbO_2}$ is the cross talk of deoxyhaemoglobin into oxyhaemoglobin, whereas $CT_{HbO_2 \rightarrow Hb}$ represents the cross talk of oxyhaemoglobin into deoxyhaemoglobin.

conditions	cross-talk	
	$CT_{Hb \rightarrow HbO_2}$	$CT_{HbO_2 \rightarrow Hb}$
A	-0.213	0.0297
B	-0.2965	0.0414
C	-0.4297	0.060

In all three cases of approximation, therefore, significant amount of error in the assessed concentration-changes of oxy and deoxyhaemoglobin were observed. These results clearly indicate that the assumption of the wavelength independence will lead to error in calculation, thus should not be considered. The maximum amount of cross talk between the haemoglobin species (in values of both $CT_{Hb \rightarrow HbO_2}$ and $CT_{HbO_2 \rightarrow Hb}$) were found in Case C, i.e., in the approximation of the NIRS DPF. Also, the maximum absolute error was calculated for Case C. This suggests that for the quantification of haemoglobin concentrations from PPG, the use of DPFs from the NIRS literature could cause significant measurement errors, therefore, should be avoided.

10.7 Summary

The present chapter primarily focussed on evaluating the DPF in PPG. The investigation was performed separately on a monolayer and a multilayer model. A thorough investigation of the dependence of DPF on wavelength, blood volume and blood oxygen saturation in the single perfused skin tissue layer was shown at 660 nm and 940 nm wavelengths. The values of DPF at 660 nm considerably shifted between different states of oxygen saturation and blood volume. DPFs for 940 nm were relatively constant. Results from the monolayer model motivated the study with a multilayer volume of forearm tissue layer. The model was explored to quantify the DPF in PPG at red (660 nm) and infrared (880 nm) wavelengths. The simulated DPF values were utilised to derive the time changes in concentrations of oxyhaemoglobin and deoxyhaemoglobin, based on the derivations from the modified Beer-Lambert law. To study the influence of the DPF values on the concentration measurements from PPG, recorded PPG signals from the human forearm was analysed using the simulated DPF. Simulated density plots showed the distribution of light-tissue interaction events through the tissue volume. Both red and infrared light penetrated a certain distance through tissue, with maximum scattering in the first few layers of the skin and a reduction of scattering in the fat and muscle layers. Through the two application regions (i.e. shorter source-detector separations for PPG and longer separations for NIRS) investigated in the simulation, the optical pathlength and DPF showed different characteristics. The DPF for the red wavelength was invariably higher than infrared. The observations displayed a consistent wavelength-dependence of the DPF, predominantly in the shorter separation distances usually used in PPG measurements.

DISCUSSION AND CONCLUSION

A concept-based technical design and optimisation of the geometrical parameters of an optical system used in biomedical applications require a clear understanding of the underlying light-tissue interaction. A robust bio-optical model (i.e., a model characterised by a combination of biological and optical properties) including the different tissue structure (i.e., monolayer and multilayer) at different geometries (reflective and transmissive modalities) of PPG has never explored in any earlier studies. The growing research interest in employing photoplethysmography for various applications and an inadequacy of the existing literature on the core PPG research were the driving factors of the thesis. There is clearly a deficit in knowledge on the fundamental tissue-optical variables in PPG such as the optical path, penetration depth, light absorbance by different tissue layers, distribution of scattering and absorption etc. It was previously known that the foundation of PPG and pulse oximetry lies on the relative absorbance of red and near infrared light by oxyhaemoglobin and deoxyhaemoglobin, however, no study evaluated the contribution of the different layers, sublayers, and absorbers present in a heterogeneous volume of tissue. Results presented in the thesis shed light on such information that is crucial for a better understanding of the PPG theory and its contribution to a plethora of applications.

Monte Carlo method was chosen for simulating the light-tissue interaction in photoplethysmography due to its significant advantages over other methods, for example, electromagnetic theory, random walk theory, diffusion approximation etc. The most im-

portant advantage of this approach was its ability to recreate the ‘randomness’ in the tissue medium. This was achieved by the random sampling of the optical variables such as photon pathlength, the angle of incidence, the angle of scattering etc. The anatomical heterogeneity and the wavelength-dependent optical properties of the tissue layers led to the realistic distribution of light-tissue interaction events in tissue. The anisotropy in the scattering events depended on the choice of the ‘phase function’. Henyey-Greenstein phase function was used to describe the randomised scattering in tissue. This phase function was chosen as it makes the photons to scatter more in the forward direction, and is accepted by previous researchers for tissue-optics modelling [Splinter and Hooper, 2006]. The corrections made at the boundary of the tissue-model compensated for the loss of photonic energy while entering or exiting the tissue surface. The model in the thesis was executed in two different modalities: reflective and transmissive and the geometrical positions of the optical source and detector were variable. The MC design provided the flexibility to operate the system through a very short as well as a very long source-detector separation, and thus, modelled the system suitable for both peripheral and deep tissue monitoring (i.e., PPG and NIRS regions). The MC model was also equipped with the facility to incorporate different types of optical source and detector. Hence, for different applications, the model was exposed to a beam from a point source, illumination from the optical fibre and the Gaussian type beam such as laser source. Incident light from the point source was used for the validation purposes. Optical fibre source was simulated for a few preliminary applications in this thesis, however, this can be used for any fibre-optic system for the non-invasive clinical measurements and monitoring [Phillips *et al.*, 2006; Hickey and Kyriacou, 2007; Hickey *et al.*, 2010]. In the most common PPG technology, usually, LEDs or laser diodes are used [Budidha *et al.*, 2018; Moyle, 2002; Silva *et al.*, 2003; Nitzan *et al.*, 2014]. Therefore, for the main applications in the thesis, Gaussian beam was used as the incident illumination.

Monte Carlo model developed in this thesis was validated against analytical results and checked with the standard law of energy conservation. Monolayer models were used for the validation and characterisation purpose. By cross-checking the model with pre-validated data, and defining the input and output variables of the model, confidence was built on the accuracy of the model. Throughout the thesis, the accuracy of each simulation

was verified against the law of energy conservation, i.e., the input weight of the photon clusters must have been equal to the sum of their absorbed, reflected and/ or transmitted weights. Another accuracy check was performed on the basis of the number of simulation (Q). It is known that the convergence rate of the Monte Carlo method is $1/\sqrt{Q}$ [Lapeyre *et al.*, 2003]. In the thesis, the minimum number of simulated photon clusters were 10^8 , and the maximum was 10^{10} . Therefore, the convergence rate was a minimum of 0.0001, and the maximum was 0.00001. Due to a very large number of iterations, the modelling results exhibited a high level of accuracy. Monte Carlo method has a well-known limitation regarding the time-consumption [Prahl, 1988; Wang *et al.*, 1995] which was considered in this work. A ‘variance reduction’ approach for the modelling was adapted that allowed a large number of photons to be simulated in a small processing time. Additionally, for simulating the mean optical path through a wide range of source-detector separation, implicit detection technique was used. Finally, the computer program was written in a multi-threaded platform that fastened the simulations considerably.

Modelling a highly heterogeneous structure like biological tissue needed a careful selection of the anatomical details and the optical properties. In the model, the optical and anatomical properties of the tissue layers were adapted from published literature, and by surveying the text-books on human anatomy and histology. The textbooks and existing literature contain the optical property and anatomical structure of the individual tissue components measured experimentally by dedicated research groups. Though now-a-days an increasing number of research groups are working in this core area of bio-photonics, still the works are numbered [Prasad, 2004; Wang and Tuchin, 2013]. In the thesis, efforts were made to choose the optical properties and the anatomical details carefully using the best resources available, and in cases of unavailability of the data, a rational approximation was made (for example, arterio-venous oxygen saturation difference, systolic increase in blood volume, bone optical properties etc.). In cases of sex or race based division of parameters, the average values were considered in the thesis. For example, melanin concentration in the simulation was considered to be 10% which was an average of Negroid and Caucasian skin [Jacques and McAuliffe, 1991]) since the aim of this thesis was to present an unbiased study. Besides, it is well known that the anatomical structure of tissue layers largely varies from person to person. Various factors of the test

subject could affect the anatomical properties of the tissue layers of the same region of interest in the body, for example, age, sex, complexion, fat content; physiological states during measurement such as skin or body hydration, state of perfusion, the position of the subject etc. In the thesis, an ideal situation was considered, i.e., simulations were carried out considering the test subject to be a healthy person at rest. However, the model was equipped with flexibilities to incorporate other states, such as low perfusion, skin dryness, pigmented skin etc. The basic tissue geometry was represented by a semi-infinite slab. Of course in reality tissue is not semi-infinite, however, considering the tissue dimensions to be much higher than the spatial distribution of photons, the approximation was valid. The tissue model used in this work, as mentioned previously, followed the ideal scenario. The assumptions and approximations might be slightly different from the experimental findings, however, the relative behaviour between the systole and diastole, and between red and infrared wavelengths will be the same.

The steps of the gradual development of the model have been demonstrated in the thesis. A homogeneous model of a single absorbing-scattering tissue layer was the first step that was used for the validation and characterisation purpose. In order to simulate a ‘perfused’ skin tissue, heterogeneity was added to the dermal layer by introducing absorbers (i.e., oxy and deoxyhaemoglobin) of different absorption coefficients. For this basic investigation of light-tissue interaction in a monolayer tissue, the skin was chosen as this is the most common ROI for the non-invasive optical application. This model was explored for several investigations in order to retrieve the behaviour of light through a perfused tissue layer in different settings and environments relevant to PPG, for example, ranges of source-detector separation, blood volume, blood oxygen saturation etc. The distribution of scattering for different source-detector separations at red and infrared wavelengths was shown. The density plot showed the distribution of the interaction events. According to the MC algorithm, after taking each step size l , the photon reached a new ‘site of interaction’ where it underwent the scattering and absorption events simultaneously. Therefore, the interaction sites were basically the position of the scatterer, and l was the ‘free pathlength’ between two consecutive interaction events. A higher number of scattering events was shown in red light compared with infrared due to the higher scattering coefficient of the red light. The dependence of the optical path, depth of

penetration and detected intensity were rigorously studied as functions of source-detector separation, blood volume and oxygen saturation. One of the main findings from the study was the dependence of the optical path on the operating wavelength in PPG. Therefore, the assumption of wavelength independence of the optical path found in the basic theoretical description of PPG has been proven to be invalid. The demonstration of the increasing optical pathlength and penetration depth with the source-detector separation proved that for deeper tissue monitoring, a larger source-detector separation was required.

The ‘pulsatility’ in the monolayer and the multilayer studies were achieved by the increment in blood volume in the dermal layer. The small source-detector separations used in PPG mainly interrogate with micro-circulation in the vascular tissue bed in the extremities of the body. The peripheral tissue is supplied with blood through arterioles and capillaries. However, capillaries are not pulsatile, thus, unlikely to contribute in the pulsatile signal captured in PPG [Kamshilin *et al.*, 2015]. Therefore, the pulsatility exists in the arterioles. In the tissue model, the arteriole was too thin ($\sim \mu m$) to be designed as a rigid cylinder (simulation with a large cylindrical blood vessel can be found in the appendix of the thesis). Instead, the volumetric contribution of the blood was considered in the tissue layer. In other words, the peripheral dermis was considered to be ‘perfused’ with a volume of blood which varied corresponding to the cardiac cycle, giving rise to the pulses.

In the finger tissue simulation, the optical properties of the cranial bone were incorporated due to the absence of any available data on the finger bone. Cranial and finger bones are optically different due to the variation of blood present. However, it has been found that the bone layer has the minimum impact on the relative absorbance of light in PPG. The maximum contribution to the absorbance was of dermis that has the modulation ratio of 4.30, whereas this was only 0.21 in bone. The high absorption of both red and infrared light in the epidermal layer indicated that melanin has an effect on the recorded PPG amplitude. However, a low absorption modulation ratio confirmed that skin colour does not influence the oxygen saturation sensing using a pulse oximeter where the ratios of the absorbances are evaluated. The correlation between the reflectance and transmittance mode calibration curves have stated that the pulse oximeter readings should not change depending on their modalities.

The dependence of the optical pathlength and penetration depth on the source-detector separation was noticeable in all simulated cases. Also, the wavelength-dependence of the pathlength and penetration depth increased with the increasing source-detector separation. In order to avoid any error caused by the differences in the optical path or depth penetrated by red and infrared wavelengths, a shorter source-detector separation for a reflectance mode sensor is advisable. Wavelength-dependence of the optical path and detected intensities at different source-detector distances in a general reflectance geometry were reported in earlier literature [Nitzan *et al.*, 2000; Meglinsky and Matcher, 2001], however, no investigation in a finger tissue volume has ever been addressed earlier. The data presented in the thesis, therefore, may be readily used for the optimisation of the reflectance finger PPG sensor.

The dependence of the optical path, mean penetrated depth and the mean reflectance and transmittance on blood volume and blood oxygen saturation is an important aspect of the thesis. The limitation of pulse oximetry in the conditions of very poor perfusion or very low oxygen saturation is well-documented [Wilson *et al.*, 2010; Baheti and Laheri, 2014; Preston and Kelly, 2016; DeMeulenaere, 2007; Engel and Kochilas, 2016]. Recent technological developments and the advanced data-processing tools have enabled pulse oximetry to maintain consistent accuracy of $\pm 2\%$, and any inconsistency in the SpO_2 reading usually can be avoided. Nevertheless, an in-depth knowledge of the correlation between the variables is very important to understand any potential sources of errors during the measurement, and to rule them out. In absence of any such previous studies, the results presented in this thesis will play an indispensable role to analyse the performance of PPG and pulse oximetry in a clinical setting.

The assessment of the Differential Pathlength Factor for PPG has never been attempted before. Recently, there is a huge interest in extending the horizon of the PPG applications beyond SpO_2 measurement, and acquiring adequate knowledge on the optical path and DPF opens the doors for new applications of PPG, especially in the assessment of tissue perfusion. Changes in peripheral perfusion can be an early sign of a global change in the parameter, indicating a serious health condition. Since the oxygen saturation level of the critical care patient is continuously monitored using a pulse oximeter, the same PPG signal can be used for the assessment of the peripheral tissue perfusion

without requiring any additional instrumentation. Determination of tissue perfusion using PPG, however, is not possible without an adequate knowledge of the DPF. The DPF simulated for the forearm tissue has exhibited unique behaviour through different ranges of source-detector separations, as well as at different wavelengths. The dynamic behaviour of the DPFs at short separation distances should be taken into consideration in the use of an appropriate DPF for the quantification of haemoglobin concentration changes from PPG signals. The cross-talk and the absolute error in the measured haemoglobin concentrations indicated the inefficiency of using an approximated DPF. The approximation that the NIRS DPF was the same as the PPG DPF caused the maximum cross-talk and error. This again points towards the significant mismatch between the behaviours of the DPFs in the PPG and NIRS regions. The studies with the monolayer model have exhibited the dependence of DPF on the volume and the (total) oxygen saturation of blood in the skin, especially in the red wavelength. Higher scattering and absorption in the lower optical wavelengths have been the main contributing factors for the dynamic behaviour of the red DPF with the input physiological, anatomical and geometrical variables. Therefore, a careful assessment of the DPF is essential for using the pulse oximeter, operating at red or lower wavelengths, for the applications such as peripheral perfusion monitoring.

In summary, a rigorous computational model of photoplethysmography has been developed, evaluated and executed for the reflective and transmissive modalities. A thorough investigation of the light-tissue interaction variables pertinent to PPG and pulse oximetry has been performed on a monolayer perfused skin tissue which has been followed by the investigation with heterogeneous tissue-structure of a finger. For the first time, an opto-anatomical model of a specific ROI has been explored for investigating the light-tissue interactions in both reflective and transmissive modalities of pulse oximetry. The multilayer model of the forearm tissue volume has been explored for the assessment of the differential pathlength factor of PPG, which has never been addressed before. Using the simulated DPFs in the PPG signals recorded from the forearm of healthy volunteers, the absolute concentration-changes in oxyhaemoglobin and deoxyhaemoglobin have been determined, exploring PPG as a potential tool for the perfusion assessment. The hypothesis and the results discussed in the thesis are invaluable for the prediction of any potential error, comprehending the origin of the signal and optimisation of the sensor

design.

This thesis has opened new pathways for further research in this field and hence some recommendations for future research are:

- As mentioned already, the models presented in the thesis approximate the ideal situation. The main focus of the applications of the model in the thesis has been to assess the relative functionality of PPG in the operating wavelengths, and investigating the influence of variations in all parameters were not in the scope of the study. However, the model can be employed in future to study the effect of the variations in the individual parameters of the model, for example variation in the ratio between arterial and venous blood, variation in the distribution of arterial and venous oxygen saturation, studying the effect of varying melanin and water concentration etc.
- In the thesis, the model has primarily focussed on the effect of optical, anatomical and physiological properties of tissue in PPG. However, the model also has the flexibility to include the mechanical properties. An instance of the investigation with the variation in artery radius has been shown in the appendix section. Such studies can be extended further for investigating the effect of the change in other mechanical properties such as elasticity and rigidity of the blood vessel on the light-tissue interaction.
- It has been stated in the thesis that different regions of interest in body exhibit different anatomy and physiology, which greatly affects the optical interaction with that region. Also, operating wavelengths play the most significant part to characterise the optical interactions in the tissue region. Modelling light-tissue interactions in other regions of interest (e.g., forehead) and at a range of wavelengths (i.e., green, mid and far infrared etc.), therefore, can be an important study, extending from the present model.
- The model in the thesis has been explored for reflectance and transmittance geometry. In reflectance mode, it has also been explored for various source-detector separations. An instance of multi-detector PPG model has been mentioned in the

appendix section of the thesis. The model can be executed for studying the effect of different location and orientation of the sensor on the tissue and such a study will be immensely helpful for designing new age wearable PPG sensors.

- PPG DPF has been addressed for the very first time in the thesis. This area is not well explored. The study can be extended to many directions, for example, to assess tissue perfusion using PPG from finger or forehead, to experimentally derive the DPF for a particular region of interest at a certain wavelength etc. Such studies can be useful for many potential applications in medical technology.

The theory, method, and results presented in the thesis undoubtedly contribute new knowledge to the ongoing research in the fields of PPG and Pulse Oximetry. Clearly, the information gained in this research enhances the understanding of the fundamental aspects of PPG and provides a new perception to all the community who is involved in the development of transcutaneous sensors based on PPG.



OTHER APPLICATIONS OF MONTE CARLO MODEL

The present thesis has been focussed on the execution of Monte Carlo model for analysing the conceptual limitations in PPG and to explore PPG principle for applications beyond the measurement of arterial oxygen saturation measurement. The MC model also is explored in some other applications in this work, which might not directly or accurately related to PPG descriptions, however, contribute to the basic understanding of interaction of light with perfused bed of tissue and different sensor geometries. Here, the optical properties of muscle and fully oxygenated blood, which are already introduced in previous chapters, have been used for the simulation.

Differential Pathlength Factor in monolayer muscle, blood and brain like tissue:

Detail discussion on a multilayer volume of human forearm has been presented in Chapter 9. Apart from that study, the Monte Carlo model has been explored to investigate the DPF for a single layer of brain, blood and muscle like tissues. In all cases, DPF values are greater than 1, validating the definition of DPF. The DPF value of a single layer of tissue might not be adequate for an experimental setup as there are always other tissue layers which contribute in the light-tissue interaction for a typical non-invasive diagnosis modality. However, the study on the individual layer might give an insight to

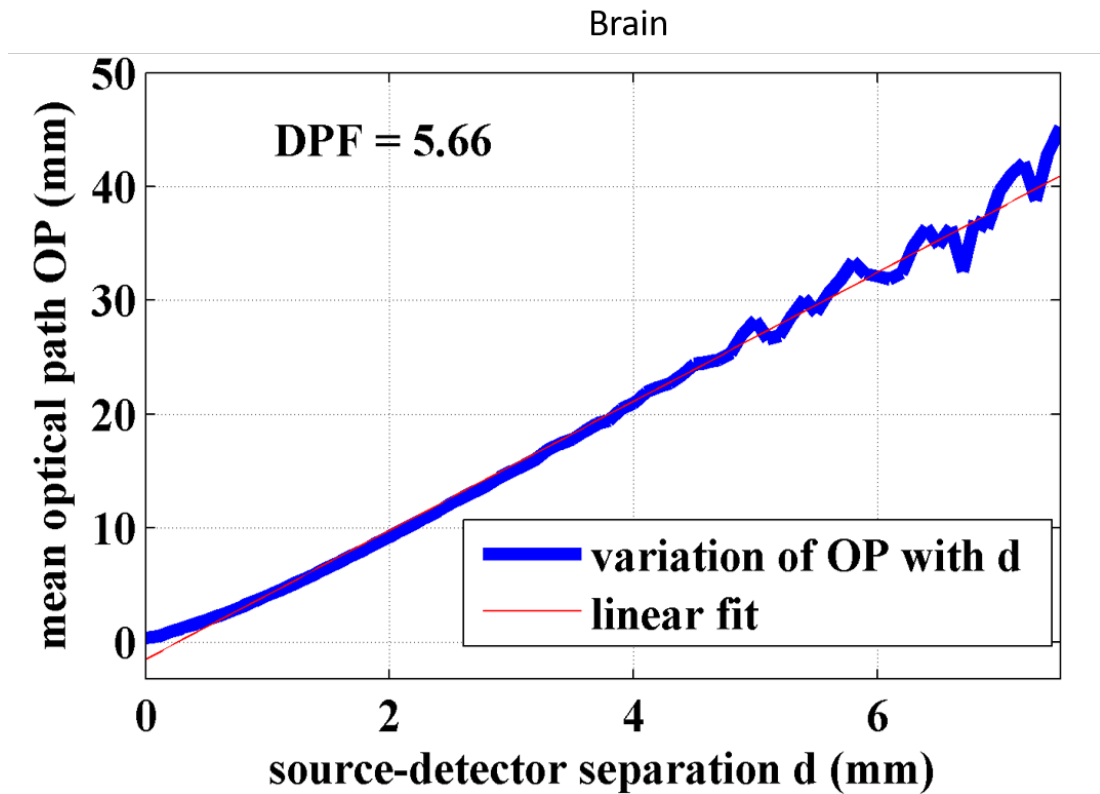


Figure A.1: Distribution of optical path as a function of source-detector separation through brain like tissue at 810 nm wavelength. The average DPF is shown as the slope of the graph.

the contribution of the specific tissue region. Figure A.1 represents the mean optical path plotted against source-detector separation at a near-infrared wavelength 810 nm. Figure A.2 represents the mean optical path plotted against the source-detector separation at red (660 nm) and infrared (940 nm) wavelengths. In both cases, DPF is calculated as the slope of the optical paths and source-detector separations. A more specific approach of the finding the DPF is to calculate this for a specific source-detector separation as stated in Chapter 9, whereas the slope gives average outlook. Nature of DPF in different tissues show distinct features, which also vary with wavelengths and source-detector separations. This relates to the Modified Beer-Lambert law described in the theory section of the thesis (Eq. 3.34).

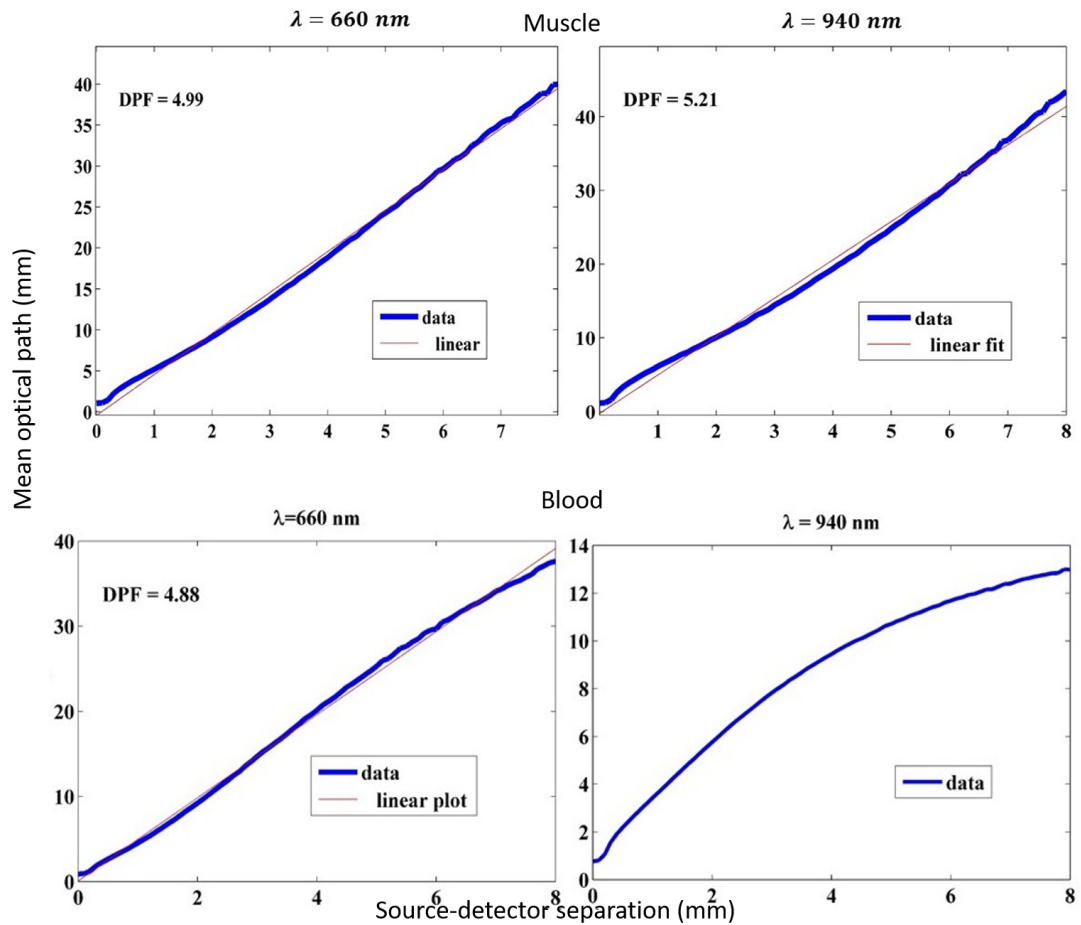


Figure A.2: Distribution of optical path as a function of source-detector separation through blood and muscle like tissues at 660 nm and 940 nm wavelength, as noted. The average DPF is shown as the slope of the graph.

Heterogeneous model with blood and muscle:

In usual pulse oximeter set-up, signals are collected using a sensor with a very small source-detector separation with which light can penetrate till the dermal and subdermal layers (in reflectance mode) and unlikely to reach a large artery site. However, if the source-detector separation is higher, it is likely to penetrate deeper and interact with the usual tissue-structure of a cylindrical blood vessel surrounded by muscle tissue. Such studies can be used for very important applications if modified necessarily. In Figure A.3, light propagation from the source to detector placed 4 mm apart through a muscle slab containing a cylinder of blood of radii 2 mm (a) and 4 mm(b) are shown in a 3D Cartesian geometry (view in xz plane). The projection in yz plane is presented for two cases in (c) and (d) respectively. The cylinder is considered to be at a depth of 1 mm from

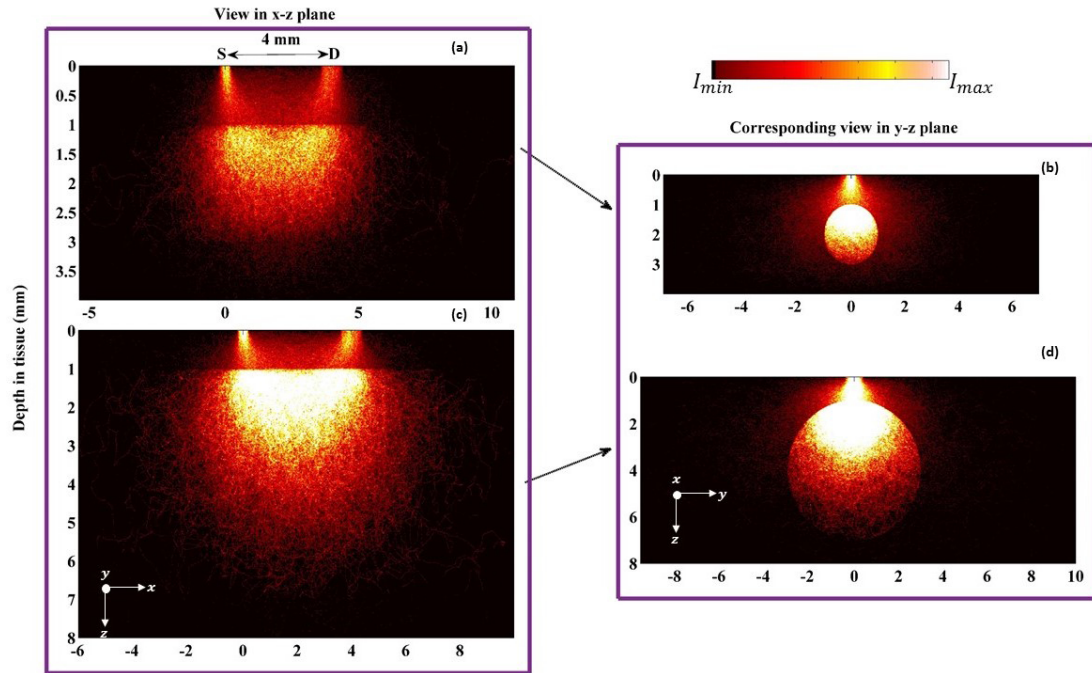


Figure A.3: Light propagation from the source to detector placed 4 mm apart through a muscle slab containing a cylinder of blood of radii 2 mm (a) and 4 mm (b) are shown in a 3D Cartesian geometry (view in xz plane). The projection in yz plane is presented for two cases in (c) and (d) respectively. The cylinder is considered to be at a depth of 1 mm from the top surface of muscle. Colourbar shows the distribution of scattering events (I) between the minimum and maximum values.

the top surface of muscle. The circular shape of the scatter plot in (c) and (d) establish the cylindrical modelling. Higher scattering is seen in the tissue with higher diameter of blood vessel.

Multiple detector:

There are studies with multiple detectors in the PPG-based measurement systems. A monolayer muscle tissue is explored to investigate the relative changes in the penetration depth and the detected intensity (i.e., reflectance) of the signal in different detectors. A nominal number of photons 10^3 are detected in each detector. The total intensity of light decreases from the source to the detector at further distances. Similar study is also performed on the monolayer blood tissue. The comparative results of the penetrated depth and detected reflectance of blood and muscle at different source-detector separations are shown in Fig. A.5. The similar experimentation is carried out with a muscle tissue slab

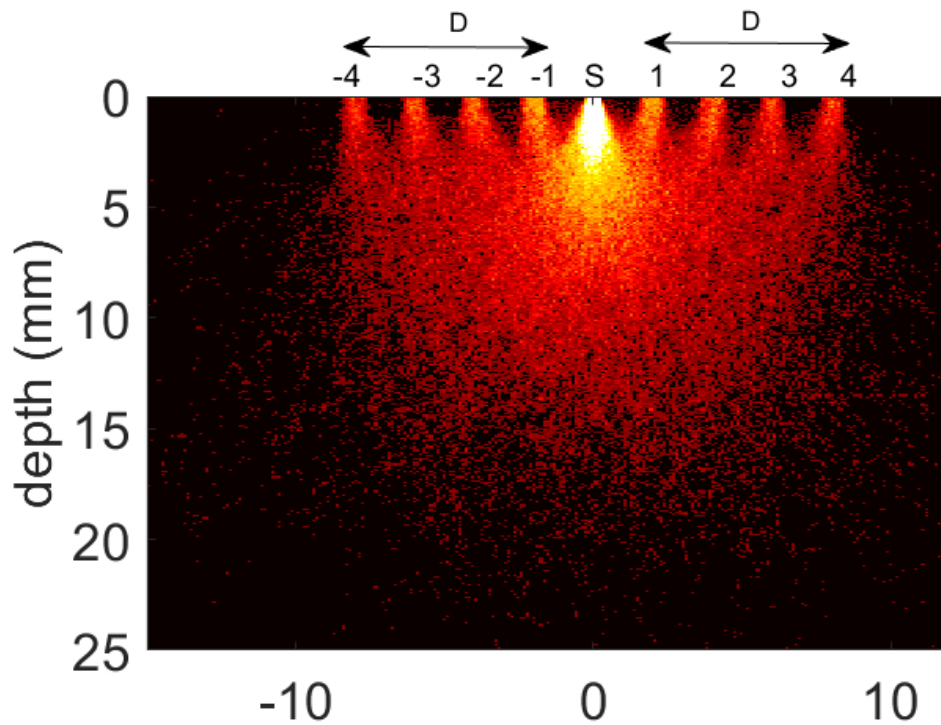


Figure A.4: Propagation of light through blood tissue having detectors at two opposite sides of the source (S). The detector positions along the positive and negative sides of the source are indicated by the serial numbers 1,2,3,4 and -1,-2,-3,-4 respectively. The same number of photons (10^3) are detected in each detector.

containing a cylindrical blood vessel. The scatter plot and the mean depth of penetration of the detected photon clusters at various distances are plotted in Figure A.6. Investigation is performed with blood vessel of radii 1 mm and 3 mm (the plot shown in (a) is for radius 1 mm).

From the above simulations, it is clear that absolute values of penetration depth increase with increasing source-detector separation. However, in plot, the negative values of x denotes the detector to be placed in the opposite direction and hence, the depth is seen to be decreasing. the same explanation goes with mean reflectance, which basically increases with increasing source detector separations (taken the absolute values). In the layer of muscle with blood cylinder, the absolute penetration depth is higher in bigger diameter of the vessel.

All these observations are likely to contribute with potential knowledge on the feasibility of the model to explore the effect of the sensor of optical path and depth, however a fool-proof study would need further problem-oriented investigations.

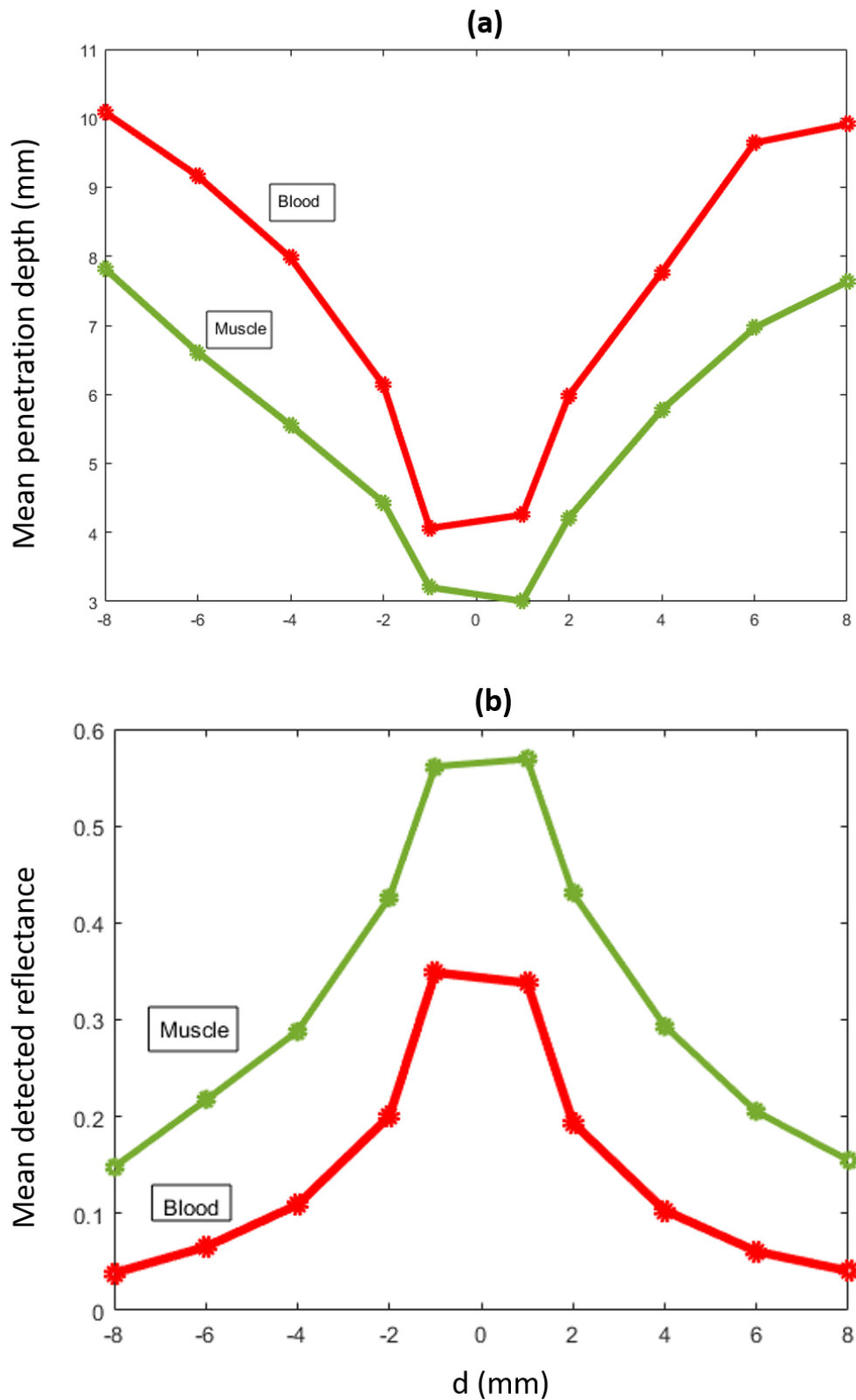


Figure A.5: The mean penetrated depth (a) and the detected reflectance (b) of the photon clusters received at the detectors placed at different distances in monolayer tissue models of blood and muscle are shown.

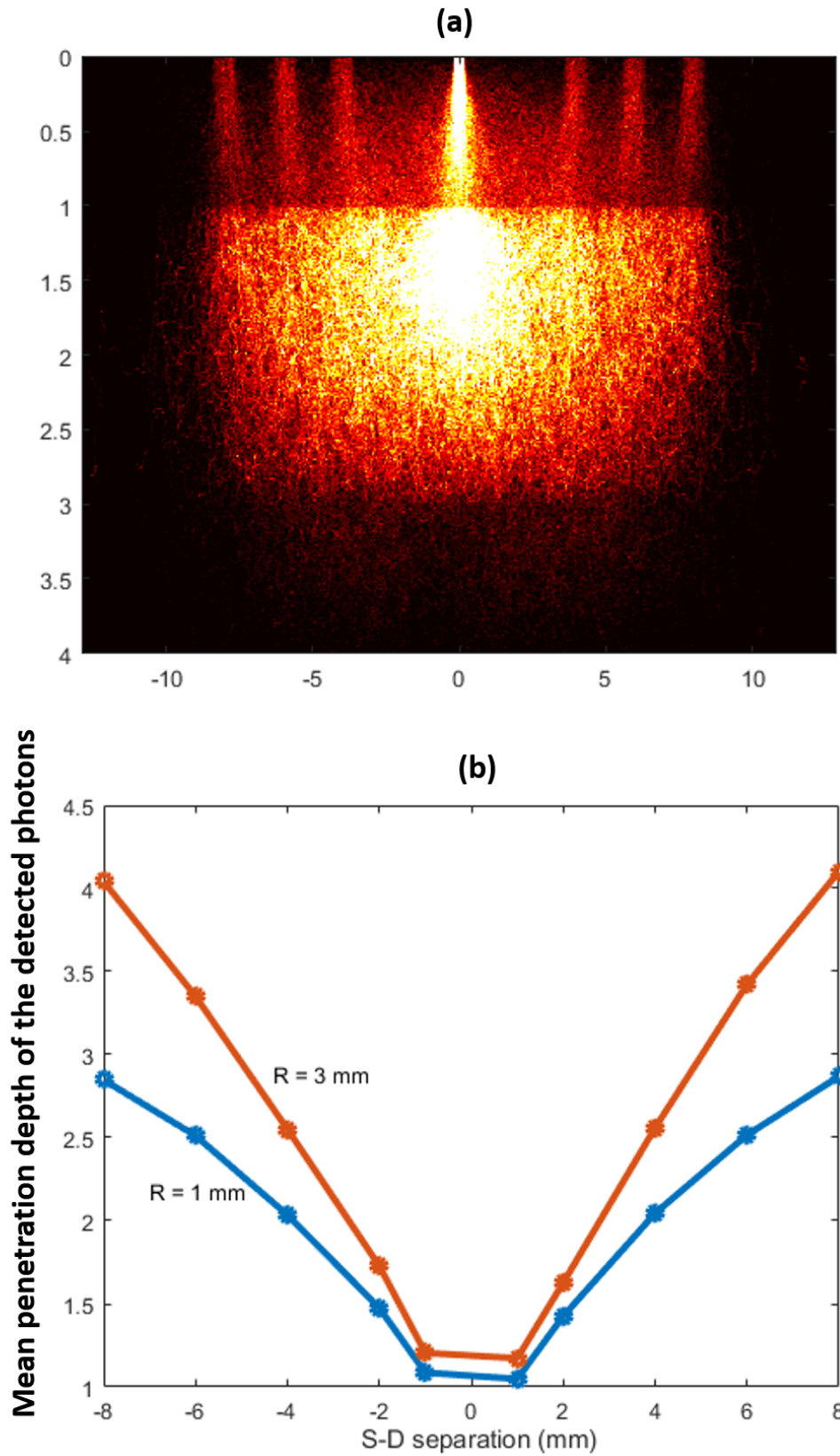


Figure A.6: The distribution of scatter (a) and the mean penetrated depth (b) of the photon clusters received at the detectors placed at different distances on the top of the muscle tissue slab containing a cylindrical blood vessel are shown. The detector distances are same as the monolayer model.

COMPUTATIONAL PROGRAM

As stated previously, the code for simulation has been written in MATLAB platform. The basic code is the same, however, is has been amended every time depending on the application. Here, as an example, the basic code for a multilayer transmittance pulse oximetry model is presented. Although this is written in a single thread code, often in practice the code was run by multi-threading in order to simulate a large number of photons in small time.

```

clc;clear;
N_phot=10e8;
lambda=660;
s=4;
Sat=0.9;
mua_bl=7.84*10^7*(lambda^-3.255);
mua_mel=(6.6*10^10)*(lambda^(-3.33));
Sat_A=Sat;
Sat_V=Sat_A-0.1;
fibrad2=1;
entry=0;
detect=0;
discard=0;
ni=1.4; %internal refractive index of tissue
nt=1; %external refractive index of air
radl=1; %Gaussian beam radius
Rsp=((ni-nt)/(ni+nt))^2;
k=0; %number of position of photon
j=0; %total positions of detected photons
.....
mua_W=0.0036; %660nm;
% % mua_W=0.0560; %880nm;
% % mua_W=0.2674; %940nm;
mua_HHb=1.64; %660 nm
mua_Hbo=0.15; %660 nm
% % mua_HHb=0.43; %940 nm
% % mua_Hbo=0.65; %940 nm
% % mua_HHb=0.44; %880nm
% % mua_Hbo=0.56; %880nm
mua_A=Sat_A*mua_Hbo+(1-Sat_A)*mua_HHb;
mua_V=Sat_V*mua_Hbo+(1-Sat_V)*mua_HHb;
musl_skin=2.562; %660nm
% % musl_skin=1.681; %880nm
% % musl_skin=1.568; %940nm
g_skin=0.9;
musl_fat=1.24; %660 nm
% % musl_fat=1.09; %880nm
% % musl_fat=1.085; %940nm
g_fat=0.8;
musl_musc=0.861; %660nm
% % musl_musc=0.635; %880nm
% % musl_musc=0.581; %940nm
g_musc=0.9;
.....
vW=0.05;
mua_sc=mua_W*vW+(1-vW)*mua_bl;%stratum croneum
.....
.....
vW=0.2;
vmel=0.1; %skin melanin volume fraction
mua_epi=vmel*mua_mel++mua_W*vW+(1-vmel-vW)*mua_bl; %upper epidermis
abs. coeff.

```

```

.....
....
vW=0.5;
v=0.04;
vA=v/2;
vV=v/2;
mua_papder=mua_A*vA+mua_V*vV+mua_W*vW+(1-(vA+vV+vW))*mua_bl;
%papillary dermis abs. coeff.
.....
....
vW=0.6;
v=0.3;
vA=v/2;
vV=v/2;
mua_upblder=mua_A*vA+mua_V*vV+mua_W*vW+(1-(vA+vV+vW))*mua_bl; %upper
blood net dermis abs. coeff.
.....
....
vW=0.7;
v=0.04;
vA=v/2;
vV=v/2;
mua_retder=mua_A*vA+mua_V*vV+mua_W*vW+(1-(vA+vV+vW))*mua_bl;
%reticular dermis abs. coeff.
.....
....
v=0.1;
vA=v/2;
vV=v/2;
mua_dpbllder=mua_A*vA+mua_V*vV+mua_W*vW+(1-(vA+vV+vW))*mua_bl; %deep
blood net plexus abs. coeff.
.....
v=0.05;
vA=v/2;
vV=v/2;
mua_fat=mua_A*vA+mua_V*vV+mua_W*vW+(1-(vA+vV+vW))*mua_bl; %subdermis
abs. coeff.
.....
vW=0.6;
v=0.35;
vA=v/2;
vV=v/2;
mua_musc=mua_A*vA+mua_V*vV+mua_W*vW+(1-(vA+vV+vW))*mua_bl; %muscle
abs. coeff.
.....finger model: total thicknes 1 cm.....
t1=0.02;
t2=t1+0.25;
t3=t2+0.1;
t4=t3+0.08;
t5=t4+0.2;
t6=t5+0.3;
t7=t6+0.5;

```

```

t8=t7+7.1; %muscle
t9=t8+0.5;
t10=t9+0.3;
t11=t10+0.2;
t12=t11+0.08;
t13=t12+0.1;
t14=t13+0.25;
t15=t14+0.02;
% .....arm model: total thicknes 4 cm .....
% % t1=0.02;
% % t2=t1+0.1;
% % t3=t2+0.2;
% % t4=t3+0.1;
% % t5=t4+1.23;
% % t6=t5+0.12;
% % t7=t6+3.23;
% % t8=t7+30; %muscle
% % t9=t8+3.23;
% % t10=t9+0.12;
% % t11=t10+1.23;
% % t12=t11+0.1;
% % t13=t12+0.2;
% % t14=t13+0.1;
% % t15=t14+0.02;
.....
while detect<N_phot
alpha=2*pi*rand; %cylindirical co-ord
angle
r_source=rad1*sqrt(-log(rand));
x_source=r_source*cos(alpha);
y_source=r_source*sin(alpha);
w=1-Rsp;
W1=0;
W2=0;
W3=0;
W4=0;
W5=0;
W6=0;
W7=0;
W8=0;
W9=0;
W10=0;
W11=0;
W12=0;
W13=0;
W14=0;
W15=0;
OP1=0;
OP2=0;
OP3=0;
OP4=0;
OP5=0;

```

```

OP6=0;
OP7=0;
OP8=0;
OP9=0;
OP10=0;
OP11=0;
OP12=0;
OP13=0;
OP14=0;
OP15=0;
x=x_source; %Gaussian distribution
y=y_source;
z=0;
ux=0;
uy=0;
uz=1;
n_ent=1;
entry=entry+1; %total entered photon
k=k+1;
X(k)=x;Y(k)=y;Z(k)=z;
L=0; %total pathlength of a single photon
mu_a=mua_epi;
g=g_skin;
mu_s=mus1_skin/(1-g);
while n_ent==1
theta=acos(abs(uz));
l=-log(rand)/(mu_a+mu_s);
L=L+l;
x2=x+(l*ux);
y2=y+(l*uy);
z2=z+(l*uz);
k=k+1;
if (w<=10^-4)%Roulet
    if(rand<=1/10)
        w=10*w;
    else
        n_ent=0;
        discard=discard+1;
        k=0;
        clear X Y Z;
    end
%.....Transmittance.....
elseif (z2>=t15)%exit below
    x3=((t15-z)*ux/uz)+x;
    y3=((t15-z)*uy/uz)+y;
%    s=sqrt((x3)^2+(y3)^2); %for MOP
    if ((x3^2+y3^2)<=fibrad2^2)
        detect=detect+1;
        disp(detect)
        OP(detect)=L;
        W(detect)=w;
%    S(detect)=s; %for MOP

```

```

        N_Scat(detect)=k;
        WA1(detect)=W1;
        WA2(detect)=W2;
        WA3(detect)=W3;
        WA4(detect)=W4;
        WA5(detect)=W5;
        WA6(detect)=W6;
        WA7(detect)=W7;
        WA8(detect)=W8;
        WA9(detect)=W9;
        WA15(detect)=W15;
        WA14(detect)=W14;
        WA13(detect)=W13;
        WA12(detect)=W12;
        WA11(detect)=W11;
        WA10(detect)=W10;
        n_ent=0;
        w=0;
        k=k+1;
        X(k)=x3; Y(k)=y3; Z(k)=t15;
        X1(j+1:j+k)=X(:);
        Y1(j+1:j+k)=Y(:);
        Z1(j+1:j+k)=Z(:);
        j=j+k;
        k=0;
        clear X Y Z;
elseif (abs(uz)==1||theta>asin(nt/ni)) %OI/TIR
    uz=-uz;
    z2=-z2;
    X(k)=x2; Y(k)=y2; Z(k)=z2;
else
    theta_t=asin(ni*sin(theta));
    a=theta-theta_t;
    b=theta+theta_t;
    aa=sin(a)/sin(b);
    bb=tan(a)/tan(b);
    r_fres=(aa^2+bb^2)*0.5;
    if(rand>r_fres) %photon exits tissue
        discard=discard+1;
        k=0;
        n_ent=0;
        w=0;
        clear X Y Z;
    else %photon reflects back in tissue
        uz=-uz;
        z2=-z2;%internal reflection
        x=x2;
        y=y2;
        z=z2;
        X(k)=x2;
        Y(k)=y2;
        Z(k)=z2;

```

```

        end
    end
elseif (z2<0)%exit above
    if (abs(uz)==1||theta>asin(nt/ni)) %OI/TIR
        uz=-uz;
        z2=-z2;
        X(k)=x2;Y(k)=y2;Z(k)=z2;
    else
        theta_t=asin(ni*sin(theta));
        a=theta-theta_t;
        b=theta+theta_t;
        aa=sin(a)/sin(b);
        bb=tan(a)/tan(b);
        r_fres=(aa^2+bb^2)*0.5;
        if(rand>r_fres) %photon exits tissue
            discard=discard+1;
            k=0;
            n_ent=0;
            w=0;
            clear X Y Z;
        else %photon reflects back in tissue
            uz=-uz;
            z2=-z2;%internal reflection
            x=x2;
            y=y2;
            z=z2;
            X(k)=x2;Y(k)=y2;Z(k)=z2;
        end
    end
end

.....
...

elseif((z2>=0)&&(t1>z2))% stratum croneum
    mu_a=mua_sc;
    g=g_skin;
    mu_s=mus1_skin/(1-g);
    [ux,uy,uz]=scattering_prahl(ux,uy,uz,g);
    x=x2;
    y=y2;
    z=z2;
    X(k)=x2;
    Y(k)=y2;
    Z(k)=z2;
    dw=w*mu_a/(mu_a+mu_s);
    W1=W1+dw;
    w=w-dw;
    OP1=OP1+1;
elseif ((z2>=t1)&&(t2>z2))%epidermis
    mu_a=mua_epi;
    g=g_skin;
    mu_s=mus1_skin/(1-g);

```

```

[ux, uy, uz]=scattering_prahl(ux, uy, uz, g);
x=x2;
y=y2;
z=z2;
X(k)=x2;
Y(k)=y2;
Z(k)=z2;
dw=w*mu_a/(mu_a+mu_s);
W2=W2+dw;
w=w-dw;
OP2=OP2+1;
elseif ((z2>=t2)&&(t3>z2))%papillary dermis
mu_a=mua_papder;
g=g_skin;
mu_s=mus1_skin/(1-g);
[ux, uy, uz]=scattering_prahl(ux, uy, uz, g);
x=x2;
y=y2;
z=z2;
X(k)=x2; Y(k)=y2; Z(k)=z2;
dw=w*mu_a/(mu_a+mu_s);
W3=W3+dw;
w=w-dw;
OP3=OP3+1;
elseif ((z2>=t3)&&(t4>z2))%upper blood net dermis
mu_a=mua_upblder;
g=g_skin;
mu_s=mus1_skin/(1-g);
[ux, uy, uz]=scattering_prahl(ux, uy, uz, g);
x=x2;
y=y2;
z=z2;
X(k)=x2;
Y(k)=y2;
Z(k)=z2;
dw=w*mu_a/(mu_a+mu_s);
W4=W4+dw;
w=w-dw;
OP4=OP4+1;
elseif ((z2>=t4)&&(t5>z2))%reticular dermis
mu_a=mua_retder;
g=g_skin;
mu_s=mus1_skin/(1-g);
[ux, uy, uz]=scattering_prahl(ux, uy, uz, g);
x=x2;
y=y2;
z=z2;
X(k)=x2;
Y(k)=y2;
Z(k)=z2;
dw=w*mu_a/(mu_a+mu_s);
W5=W5+dw;

```

```

w=w-dw;
OP5=OP5+1;
elseif ((z2>=t5)&&(t6>z2))%deep blood bet dermis
mu_a=mua_dpbllder;
g=g_skin;
mu_s=mus1_skin/(1-g);
[ux,uy,uz]=scattering_prahl(ux,uy,uz,g);
x=x2;
y=y2;
z=z2;
X(k)=x2;
Y(k)=y2;
Z(k)=z2;
dw=w*mu_a/(mu_a+mu_s);
W6=W6+dw;
w=w-dw;
OP6=OP6+1;
elseif ((z2>=t6)&&(t7>z2))%fat
mu_a=mua_fat;
g=g_fat;
mu_s=mus1_fat/(1-g);
[ux,uy,uz]=scattering_prahl(ux,uy,uz,g);
x=x2;
y=y2;
z=z2;
X(k)=x2;
Y(k)=y2;
Z(k)=z2;
dw=w*mu_a/(mu_a+mu_s);
W7=W7+dw;
w=w-dw;
OP7=OP7+1;
elseif ((z2>=t7)&&(t8>z2))%muscle
mu_a=mua_musc;
g=g_musc;
mu_s=mus1_musc/(1-g);
[ux,uy,uz]=scattering_prahl(ux,uy,uz,g);
x=x2;
y=y2;
z=z2;
X(k)=x2;
Y(k)=y2;
Z(k)=z2;
dw=w*mu_a/(mu_a+mu_s);
W8=W8+dw;
w=w-dw;
OP8=OP8+1;
elseif ((z2>=t8)&&(t9>z2))%fat
mu_a=mua_fat;
g=g_fat;
mu_s=mus1_fat/(1-g);
[ux,uy,uz]=scattering_prahl(ux,uy,uz,g);

```

```

X(k)=x2;Y(k)=y2;Z(k)=z2;
x=x2;
y=y2;
z=z2;
dw=w*mu_a/(mu_a+mu_s);
W9=W9+dw;
w=w-dw;
OP9=OP9+1;
elseif ((z2>=t9)&&(t10>z2))%deep blood net
mu_a=mua_dpbllder;
g=g_skin;
mu_s=mus1_skin/(1-g);
[ux,uy,uz]=scattering_prahl(ux,uy,uz,g);
X(k)=x2;Y(k)=y2;Z(k)=z2;
x=x2;
y=y2;
z=z2;
dw=w*mu_a/(mu_a+mu_s);
W10=W10+dw;
w=w-dw;
OP10=OP10+1;
elseif ((z2>=t10)&&(t11>z2))%reticular dermis
mu_a=mua_retder;
g=g_skin;
mu_s=mus1_skin/(1-g);
[ux,uy,uz]=scattering_prahl(ux,uy,uz,g);
X(k)=x2;Y(k)=y2;Z(k)=z2;
x=x2;
y=y2;
z=z2;
dw=w*mu_a/(mu_a+mu_s);
W11=W11+dw;
w=w-dw;
OP11=OP11+1;
elseif ((z2>=t11)&&(t12>z2))%upper blood net
mu_a=mua_upbllder;
g=g_skin;
mu_s=mus1_skin/(1-g);
[ux,uy,uz]=scattering_prahl(ux,uy,uz,g);
X(k)=x2;Y(k)=y2;Z(k)=z2;
x=x2;
y=y2;
z=z2;
dw=w*mu_a/(mu_a+mu_s);
W12=W12+dw;
w=w-dw;
OP12=OP12+1;
elseif ((z2>=t12)&&(t13>z2))%papillary dermis
mu_a=mua_papder;
g=g_skin;
mu_s=mus1_skin/(1-g);
[ux,uy,uz]=scattering_prahl(ux,uy,uz,g);

```

```

X(k)=x2;Y(k)=y2;Z(k)=z2;
x=x2;
y=y2;
z=z2;
dw=w*mu_a/(mu_a+mu_s);
W13=W13+dw;
w=w-dw;
OP13=OP13+1;
elseif ((z2>=t13)&&(t14>z2))%epidermis
    mu_a=mua_epi;
    g=g_skin;
    mu_s=mus1_skin/(1-g);
    [ux,uy,uz]=scattering_prahl(ux,uy,uz,g);
X(k)=x2;Y(k)=y2;Z(k)=z2;
x=x2;
y=y2;
z=z2;
dw=w*mu_a/(mu_a+mu_s);
W14=W14+dw;
w=w-dw;
OP14=OP14+1;
else
    mu_a=mua_sc;%strat croneum
    g=g_skin;
    mu_s=mus1_skin/(1-g);
    [ux,uy,uz]=scattering_prahl(ux,uy,uz,g);
X(k)=x2;Y(k)=y2;Z(k)=z2;
x=x2;
y=y2;
z=z2;
dw=w*mu_a/(mu_a+mu_s);
W15=W15+dw;
w=w-dw;
OP15=OP15+1;
end
end
end
save(['transdia_',num2str(lambda),'_',num2str(Sat_A),'_',num2str(n),'.
mat']);
% end

```

BIBLIOGRAPHY

- Abay, T. and Kyriacou, P. [2018], 'Photoplethysmography for blood volumes and oxygenation changes during intermittent vascular occlusions', *Journal of Clinical Monitoring and Computing* **32**(3), 447–455.
- Abay, T. Y. [2016], Reflectance Photoplethysmography for Non-invasive Monitoring of Tissue Perfusion, PhD dissertation, City, University of London, UK.
- Abay, T. Y. and Kyriacou, P. A. [2015], 'Reflectance photoplethysmography as noninvasive monitoring of tissue blood perfusion', *IEEE Transactions on Biomedical Engineering* **62**(9), 2187–2195.
- Alberts, B. [2017], *Molecular Biology of the Cell*, Garland science.
- Alian, A. A. and Shelley, K. H. [2014], Photoplethysmography: Analysis of the pulse oximeter waveform, in 'Monitoring Technologies in Acute Care Environments', Springer, pp. 165–178.
- Allen, J. [2007], 'Photoplethysmography and its application in clinical physiological measurement', *Physiological Measurement* **28**(3), R1–R39.
- Allen, J. and Murray, A. [2002], 'Age-related changes in peripheral pulse timing characteristics at the ears, fingers and toes', *Journal of Human Hypertension* **16**(10), 711.
- Arfken, G. B. and Weber, H. J. [1999], 'Mathematical methods for physicists'.
- Baheti, D. K. and Laheri, V. [2014], *Understanding Anesthetic Equipment & Procedures: A Practical Approach*, JP Medical Ltd.

- Barnes, R. W., Clayton, J. M., Bone, G. E., Slaymaker, E. E. and Reinertson, J. [1977], 'Supraorbital photoplethysmography. simple, accurate screening for carotid occlusive disease', *Journal of Surgical Research* **22**(4), 319–327.
- Bashkatov, A., Genina, E., Kozintseva, M., Kochubei, V., Gorodkov, S. Y. and Tuchin, V. [2016], 'Optical properties of peritoneal biological tissues in the spectral range of 350–2500 nm', *Optics and Spectroscopy* **120**(1), 1–8.
- Beer, A. [1852], 'Bestimmung der absorption des rothen lichts in farbigen flüssigkeiten', *Annalen der Physik* **162**, 78–88.
- Boas, D. A., Gaudette, T., Strangman, G., Cheng, X., Marota, J. J. and Mandeville, J. B. [2001], 'The accuracy of near infrared spectroscopy and imaging during focal changes in cerebral hemodynamics', *Neuroimage* **13**(1), 76–90.
- Bohren, C. F. and Huffman, D. R. [2008], *Absorption and Scattering of Light by Small Particles*, John Wiley & Sons.
- Bonner, R., Nossal, R., Havlin, S. and Weiss, G. [1987], 'Model for photon migration in turbid biological media', *Journal of the Optical Society of America A* **4**(3), 423–432.
- Born, M. and Wolf, E. [2013], *Principles of Optics: Electromagnetic Theory of Propagation, Interference and Diffraction of Light*, Elsevier.
- Bosschaart, N., Edelman, G. J., Aalders, M. C., van Leeuwen, T. G. and Faber, D. J. [2014], 'A literature review and novel theoretical approach on the optical properties of whole blood', *Lasers in Medical Science* **29**(2), 453–479.
- Bouguer, P. [1729], *Essai d'optique sur la gradation de la lumière*, Chez Claude Jombert, ruë S. Jacques, au coin de la ruë des Mathurins, à l'Image Notre-Dame.
- Budidha, K. [2016], In vivo Investigations of Photoplethysmograms and Arterial Oxygen Saturation from the Auditory Canal in Conditions of Compromised Peripheral Pperfusion, PhD dissertation, City, University of London, UK.
- Budidha, K. and Kyriacou, P. [2018], 'In vivo investigation of ear canal Pulse Oximetry during hypothermia', *Journal of Clinical Monitoring and Computing* **32**(1), 97–107.

- Budidha, K., Rybynok, V. and Kyriacou, P. A. [2018], 'Design and development of a modular, multichannel photoplethysmography system', *IEEE Transactions on Instrumentation and Measurement* .
- Calabro, K. W. and Bigio, I. J. [2014], 'Influence of the phase function in generalized diffuse reflectance models: review of current formalisms and novel observations', *Journal of biomedical optics* **19**(7), 075005.
- Case, K. M. and Zweifel, P. F. [1967], *Linear transport theory*, Addison-Wesley.
- Cashwell, E. D. and Everett, C. J. [1959], *A practical manual on the Monte Carlo method for random walk problems*, Pergamon.
- Chan, E. D., Chan, M. M. and Chan, M. M. [2013], 'Pulse Oximetry: understanding its basic principles facilitates appreciation of its limitations', *Respiratory Medicine* **107**(6), 789–799.
- Chandrasekhar, S. [2013], *Radiative Transfer*, Courier Corporation.
- Chen, B., Stamnes, K. and Stamnes, J. J. [2001], 'Validity of the diffusion approximation in bio-optical imaging', *Applied Optics* **40**(34), 6356–6366.
- Chen, Z., Yang, X., Teo, J. T. and Ng, S. H. [2013], Noninvasive monitoring of blood pressure using optical ballistocardiography and photoplethysmograph approaches, in 'Engineering in Medicine and Biology Society (EMBC), 35th Annual International Conference', IEEE, pp. 2425–2428.
- Colledge, N., Walker, B. and Ralston, S. [2010], *Davidson's principles & Practice of Medicine, 21st edition*, Churchill Livingstone.
- Collins, D. G. and Wells, M. B. [1965], Monte Carlo codes for study of light transport in the atmosphere, volume 2: utilization instructions, Technical report, Radiation Research Associates.
- Criée, C., Sorichter, S., Smith, H., Kardos, P., Merget, R., Heise, D., Berdel, D., Köhler, D., Magnussen, H., Marek, W., Mitfessel, H., Rasche, K., Rolke, M., Worth, H. and

- Jörres, R. A. [2011], 'Body plethysmography—its principles and clinical use', *Respiratory medicine* **105**(7), 959–971.
- De Mul, F. F., Blaauw, J., Aarnoudse, J. G., Smit, A. J. and Rakhorst, G. [2007], 'Diffusion model for iontophoresis measured by laser-doppler perfusion flowmetry, applied to normal and preeclamptic pregnancies', *Journal of Biomedical Optics* **12**(1), 014032.
- Delpy, D. and Cope, M. [1997], 'Quantification in tissue near-infrared spectroscopy', *Philosophical Transactions of the Royal Society of London B: Biological Sciences* **352**(1354), 649–659.
- Delpy, D. T., Cope, M., van der Zee, P., Arridge, S., Wray, S. and Wyatt, J. [1988], 'Estimation of optical pathlength through tissue from direct time of flight measurement', *Physics in Medicine and Biology* **33**(12), 1433.
- DeMeulenaere, S. [2007], 'Pulse oximetry: uses and limitations', *The Journal for Nurse Practitioners* **3**(5), 312–317.
- Doronin, A. [2014], The unified Monte Carlo model of photon migration in scattering tissue-like media for the needs of Biomedical Optics, PhD dissertation, University of Otago, New Zealand.
URL: <http://hdl.handle.net/10523/4651>
- Doronin, A., Fine, I. and Meglinski, I. [2011], 'Assessment of the calibration curve for transmittance pulse-oximetry', *Laser Physics* **21**(11), 1972–1977.
- Doronin, A. and Meglinski, I. [2011], 'Online object oriented Monte Carlo computational tool for the needs of biomedical optics', *Biomedical Optics Express* **2**(9), 2461–2469.
- Duncan, A., Meek, J. H., Clemence, M., Elwell, C. E., Tyszczyk, L., Cope, M. and Delpy, D. [1995], 'Optical pathlength measurements on adult head, calf and forearm and the head of the new infant using phase resolved optical spectroscopy', *Physics in Medicine & Biology* **40**(2), 295.
- Durduran, T., Yodh, A., Chance, B. and Boas, D. [1997], 'Does the photon-diffusion coefficient depend on absorption?', *Journal of the Optical Society of America A* **14**(12), 3358–3365.

- Durian, D. and Rudnick, J. [1997], 'Photon migration at short times and distances and in cases of strong absorption', *Journal of the Optical Society of America A* **14**(1), 235–245.
- Elert, G. [2014], Volume of blood in a human, in 'The Physics Factbook', <https://hypertextbook.com/facts/1998/LanNaLee.shtml>.
- Engel, M. S. and Kochilas, L. K. [2016], 'Pulse oximetry screening: a review of diagnosing critical congenital heart disease in newborns', *Medical devices (Auckland, NZ)* **9**, 199.
- Epstein, C. D. and Haghenbeck, K. T. [2014], 'Bedside assessment of tissue oxygen saturation monitoring in critically ill adults: an integrative review of the literature', *Critical Care Research and Practice* **2014**.
- Essenpreis, M., Elwell, C., Cope, M., Van der Zee, P., Arridge, S. and Delpy, D. [1993], 'Spectral dependence of temporal point spread functions in human tissues', *Applied Optics* **32**(4), 418–425.
- Evans, C. L., Potma, E. O., Puoris' haag, M., Côté, D., Lin, C. P. and Xie, X. S. [2005], 'Chemical imaging of tissue in vivo with video-rate coherent anti-Stokes Raman scattering microscopy', *Proceedings of the National Academy of Sciences of the United States of America* **102**(46), 16807–16812.
- Fanconi, S. [1989], 'Pulse Oximetry for hypoxemia: a warning to users and manufacturers', *Intensive Care Medicine* **15**(8), 540–542.
- Fine, I. and Weinreb, A. [1995], 'Multiple scattering effect in transmission Pulse Oximetry', *Medical and Pulse Oximetryng and Computing* **33**(5), 709–712.
- Gandjbakhche, A. H. and Weiss, G. H. [1995], 'V: Random walk and diffusion-like models of photon migration in turbid media', *Progress in Optics* **34**, 333–402.
- Ganesan, A. R. and Hecht, E. [2008], *Optics*, Pearson Education.
- Gate, L. [1972], 'Light scattering in microporous materials using a photon diffusion model', *Journal of Physics D: Applied Physics* **5**(4), 837.
- Giovanelli, R. [1955], 'Reflection by semi-infinite diffusers', *Optica Acta: International Journal of Optics* **2**(4), 153–162.

- Goldsmith, L. A. [1991], *Biochemistry and Physiology of the Skin*, Oxford University Press, UK.
- Hale, G. M. and Querry, M. R. [1973], 'Optical constants of water in the 200-nm to 200- μ m wavelength region', *Applied Optics* **12**(3), 555–563.
- Heney, L. G. and Greenstein, J. L. [1941], 'Diffuse radiation in the galaxy', *The Astrophysical Journal* **93**, 70–83.
- Hertzman, A. B. [1937], 'Photoelectric plethysmography of the fingers and toes in man', *Proceedings of the Society for Experimental Biology and Medicine* **37**(3), 529–534.
- Hickey, M. and Kyriacou, P. [2007], 'Optimal spacing between transmitting and receiving optical fibres in reflectance Pulse Oximetry', *Journal of Physics: Conference Series* **85**(1), 012030.
- Hickey, M., Samuels, N., Randive, N., Langford, R. M. and Kyriacou, P. A. [2010], 'Measurement of splanchnic photoplethysmographic signals using a new reflectance fiber optic sensor', *Journal of Biomedical Optics* **15**(2), 027012.
- Hiraoka, M., Firbank, M., Essenpreis, M., Cope, M., Arridge, S., Van Der Zee, P. and Delpy, D. [1993], 'A Monte Carlo investigation of optical pathlength in inhomogeneous tissue and its application to near-infrared spectroscopy', *Physics in Medicine and Biology* **38**(12), 1859.
- Hulst, H. C. v. d. [1957], *Light scattering by small particles*, Courier Corporation.
- Ishimaru, A. [1978], *Wave Propagation and Scattering in Random Media, vol. 2*, Academic Press New York.
- Jacques, S. [1998], Skin optics summary, in 'Oregon Medical Laser Center News', <https://omlc.org/news/jan98/skinoptics.html>.
- Jacques, S. L. [2011], *Optical-Thermal Response of Laser-Irradiated Tissue*, Springer Netherlands.
- Jacques, S. L. [2013], 'Optical properties of biological tissues: a review', *Physics in Medicine & Biology* **58**(11), R37.

- Jacques, S. L. and McAuliffe, D. J. [1991], 'The melanosome: threshold temperature for explosive vaporization and internal absorption coefficient during pulsed laser irradiation', *Photochemistry and Photobiology* **53**(6), 769–775.
- Jacques, S. and Prahl, S. A. [2007], 'Introduction to biomedical optics', *Oregon Graduate Institute*, [http://omlc.ogi.edu/classroom/ece532/\(Feb 2001\)](http://omlc.ogi.edu/classroom/ece532/(Feb%2001)) .
- Jue, T. and Masuda, K. [2013], *Application of Near Infrared Spectroscopy in Biomedicine*, Springer.
- Kalos, M. H. and Whitlock, P. A. [2008], *Monte Carlo methods*, John Wiley & Sons.
- Kamshilin, A. A., Mamontov, O. V., Koval, V. T., Zayats, G. A. and Romashko, R. V. [2015], 'Influence of a skin status on the light interaction with dermis', *Biomedical Optics Express* **6**(11), 4326–4334.
- Kohl, M., Nolte, C., Heekeren, H. R., Horst, S., Scholz, U., Obrig, H. and Villringer, A. [1998], 'Determination of the wavelength dependence of the differential pathlength factor from near-infrared pulse signals', *Physics in Medicine & Biology* **43**(6), 1771.
- Kubelka, P. [1948], 'New contributions to the optics of intensely light-scattering materials. part I', *Journal of the Optical Society of America* **38**(5), 448–457.
- Kubelka, P. [1954], 'New contributions to the optics of intensely light-scattering materials. part II: Nonhomogeneous layers', *Journal of the Optical Society of America* **44**(4), 330–335.
- Kyriacou, P. A. [2013], 'Direct Pulse Oximetry within the esophagus, on the surface of abdominal viscera, and on free flaps', *Anesthesia & Analgesia* **117**(4), 824–833.
- Kyriacou, P. A., Powell, S., Langford, R. M. and Jones, D. P. [2002], 'Esophageal Pulse Oximetry utilizing reflectance photoplethysmography', *IEEE Transactions on Biomedical Engineering* **49**(11), 1360–1368.
- Kyriacou, P., Moye, A., Choi, D., Langford, R. and Jones, D. [2001], 'Investigation of the human oesophagus as a new monitoring site for blood oxygen saturation', *Physiological Measurement* **22**(1), 223.

- Ladakis, C., Myrianthefs, P., Karabinis, A., Karatzas, G., Dosios, T., Fildissis, G., Gogas, J. and Baltopoulos, G. [2001], 'Central venous and mixed venous oxygen saturation in critically ill patients', *Respiration* **68**(3), 279–285.
- Lambert, J. H. [1892], *Lamberts Photometrie:(Photometria, sive De mensura et gradibus luminis, colorum et umbrae)(1760)*, W. Engelmann.
- Lapeyre, B., Pardoux, E. and Sentis, R. [2003], *Introduction to Monte-Carlo methods for transport and diffusion equations*, Vol. 6, Oxford University Press on Demand.
- Laufer, J., Simpson, R., Kohl, M., Essenpreis, M. and Cope, M. [1998], 'Effect of temperature on the optical properties of ex vivo human dermis and subdermis', *Physics in Medicine & Biology* **43**(9), 2479.
- Lee, A., Yau, C., Giles, M. B., Doucet, A. and Holmes, C. C. [2010], 'On the utility of graphics cards to perform massively parallel simulation of advanced Monte Carlo methods', *Journal of Computational and Graphical Statistics* **19**(4), 769–789.
- Li, J. and Harrington, J. A. [1998], *Biomedical Optics and lasers: Diagnostics and treatment*, Vol. 3548, SPIE - The International Society for Optical Engineering.
- Lima, A. P., Beelen, P. and Bakker, J. [2002], 'Use of a peripheral perfusion index derived from the Pulse Oximetry signal as a noninvasive indicator of perfusion', *Critical Care Medicine* **30**(6), 1210–1213.
- Lux, I. and Koblinger, L. [1991], *Monte Carlo Particle Transport Methods: Neutron and Photon Calculations*, CRC Press, USA.
- Mannheimer, P. D. [2007], 'The light–tissue interaction of Pulse Oximetry', *Anesthesia & Analgesia* **105**(6), S10–S17.
- Mannheimer, P. D., Cascini, J., Fein, M. E. and Nierlich, S. L. [1997], 'Wavelength selection for low-saturation Pulse Oximetry', *IEEE transactions on Biomedical Engineering* **44**(3), 148–158.

- Mannheimer, P. D., O'neil, M. P. and Konecny, E. [2004], 'The influence of larger subcutaneous blood vessels on Pulse Oximetry', *Journal of Clinical Monitoring and Computing* **18**(3), 179–188.
- Marble, D. R., Burns, D. H. and Cheung, P. W. [1994], 'Diffusion-based model of Pulse Oximetry: in vitro and in vivo comparisons', *Applied Optics* **33**(7), 1279–1285.
- Marble, D. R. and Cheung, P. W. [1988], Mathematical model of transmission Pulse Oximetry, in 'Engineering in Medicine and Biology Society, Proceedings of the Annual International Conference', IEEE, pp. 542–543.
- Marchuk, G. I., Mikhailov, G. A., Nazareliev, M., Darbinjan, R. A., Kargin, B. A. and Elepov, B. S. [2013], *The Monte Carlo methods in atmospheric optics*, Vol. 12, Springer.
- Marcinkevics, Z., Kusnere, S., Aivars, J. I., Rubins, U. and Zehtabi, A. H. [2009], 'The shape and dimensions of photoplethysmographic pulse waves: a measurement repeatability study', *Acta Universitatis Latviensis Biology* **753**, 99–106.
- Matcher, S., Cope, M. and Delpy, D. [1994], 'Use of the water absorption spectrum to quantify tissue chromophore concentration changes in near-infrared spectroscopy', *Physics in Medicine & Biology* **39**(1), 177.
- Meglinski, I. and Matcher, S. [2003], 'Computer simulation of the skin reflectance spectra', *Computer methods and programs in biomedicine* **70**(2), 179–186.
- Meglinski, I. V. and Matcher, S. J. [2002], 'Quantitative assessment of skin layers absorption and skin reflectance spectra simulation in the visible and near-infrared spectral regions', *Physiological Measurement* **23**(4), 741.
- Meglinsky, I. and Matcher, S. [2001], 'Modelling the sampling volume for skin blood oxygenation measurements', *Medical and Pulse Oximetryng and Computing* **39**(1), 44–50.
- Mendelson, Y. and Kent, J. C. [1989], 'Variations in optical absorption spectra of adult and fetal haemoglobins and its effect on Pulse Oximetry', *IEEE Transactions on Biomedical Engineering* **36**(8), 844–848.

- Metropolis, N. [1987], 'The beginning of the Monte Carlo method', *Los Alamos Science, Special issue dedicated to S. Ulam* **15**, 125–130.
- Metropolis, N. and Ulam, S. [1949], 'The Monte Carlo method', *Journal of the American Statistical Association* **44**(247), 335–341.
- Middleton, P. M., Tang, C. H., Chan, G. S., Bishop, S., Savkin, A. V. and Lovell, N. H. [2011], 'Peripheral photoplethysmography variability analysis of sepsis patients', *Medical and Pulse Oximetryng and Computing* **49**(3), 337–347.
- Mitra, K. and Kumar, S. [1999], 'Development and comparison of models for light-pulse transport through scattering–absorbing media', *Applied Optics* **38**(1), 188–196.
- Morley, A., Davenport, J. J., Hickey, M. and Phillips, J. P. [2017], 'Development and optimization of a miniaturized fiber-optic photoplethysmographic sensor', *Optical Engineering* **56**(11), 117111.
- Moyle, J. T. [2002], *Pulse Oximetry*, BMJ books, UK.
- Mudry, K. M., Plonsey, R. and Bronzino, J. D. [2003], *Biomedical Imaging*, CRC Press, USA.
- Murkin, J. and Arango, M. [2009], 'Near-infrared spectroscopy as an index of brain and tissue oxygenation', *British Journal of Anaesthesia* **103**(suppl_1), i3–i13.
- Netter, F. H. [2017], *Atlas of Human Anatomy E-Book*, Elsevier Health Sciences.
- Nic, M., Hovorka, L., Jirat, J., Kosata, B. and Znamenacek, J. [2005], *IUPAC Compendium of Chemical Terminology-The Gold Book*, International Union of Pure and Applied Chemistry.
- Nicolai, B. M., Beullens, K., Bobelyn, E., Peirs, A., Saeys, W., Theron, K. I. and Lammertyn, J. [2007], 'Nondestructive measurement of fruit and vegetable quality by means of nir spectroscopy: A review', *Postharvest Biology and Technology* **46**(2), 99–118.
- Niederreiter, H. [1992], *Random number generation and quasi-Monte Carlo methods*, Vol. 63, Society for Industrial and Applied Mathematics, Philadelphia, USA.

- Nilsson, L., Goscinski, T., Kalman, S., Lindberg, L.-G. and Johansson, A. [2007], 'Combined photoplethysmographic monitoring of respiration rate and pulse: a comparison between different measurement sites in spontaneously breathing subjects', *Acta Anaesthesiologica Scandinavica* **51**(9), 1250–1257.
- Nitzan, M., Babchenko, A., Khanokh, B. and Taitelbaum, H. [2000], 'Measurement of oxygen saturation in venous blood by dynamic near ir spectroscopy', *Journal of Biomedical Optics* **5**(2), 155–163.
- Nitzan, M., Noach, S., Tobal, E., Adar, Y., Miller, Y., Shalom, E. and Engelberg, S. [2014], 'Calibration - free Pulse Oximetry based on two wavelengths in the infrared - a preliminary study', *Sensors* **14**(4), 7420–7434.
- Nitzan, M. and Taitelbaum, H. [2008], 'The measurement of oxygen saturation in arterial and venous blood', *IEEE Instrumentation & Measurement Magazine* **11**(3).
- Njoun, H. and Kyriacou, P. A. [2017], 'Photoplethysmography for the assessment of haemorheology', *Scientific Reports* **7**(1), 1406.
- Oak, S.-S. and Aroul, P. [2015], 'How to design peripheral oxygen saturation (S_pO_2) and optical heart rate monitoring (OHRM) systems using the AFE4403', *Texas Instruments Incorporated, SLAA655-March* .
- OpenStax [2013], *NIRS*, Rice University, USA.
- Patel, Z., Thaha, M. A. and Kyriacou, P. A. [2017], Development of an intraluminal intestinal photoplethysmography sensor, in 'Engineering in Medicine and Biology Society (EMBC), 39th Annual International Conference', IEEE, pp. 1840–1843.
- Patel, Z., Thaha, M. A. and Kyriacou, P. A. [2018], 'The effects of optical sensor-tissue separation in endocavitary photoplethysmography', *Physiological measurement* .
- Patterson, M. S., Chance, B. and Wilson, B. C. [1989], 'Time resolved reflectance and transmittance for the noninvasive measurement of tissue optical properties', *Applied Optics* **28**(12), 2331–2336.

- Patterson, M. S., Wilson, B. C. and Wyman, D. R. [1991], 'The propagation of optical radiation in tissue: I. models of radiation transport and their application', *Lasers in Medical Science* **6**(2), 155–168.
- Patwardhan, S. V., Dhawan, A. P. and Relue, P. A. [2005], 'Monte Carlo simulation of light-tissue interaction: three-dimensional simulation for trans-illumination-based imaging of skin lesions', *IEEE transactions on Biomedical Engineering* **52**(7), 1227–1236.
- Pellicer, A. and del Carmen Bravo, M. [2011], 'Near-infrared spectroscopy: a methodology-focused review', **16**(1), 42–49.
- Periyasamy, V. and Pramanik, M. [2014], 'Monte Carlo simulation of light transport in turbid medium with embedded object - spherical, cylindrical, ellipsoidal, or cuboidal objects embedded within multilayered tissues', *Journal of Biomedical Optics* **19**(4), 045003.
- Phillips, J., Langford, R., Kyriacou, P. and Jones, D. [2006], 'Optical fibre catheter photoplethysmograph', *Measurement and Control* **39**(3), 84–87.
- Phillips, J. P., Kyriacou, P. A. and Jones, D. P. [2010], Calculation of photon path changes due to scatter in Monte Carlo simulations, in 'Engineering in Medicine and Biology Society (EMBC), Annual International Conference of the IEEE', IEEE, pp. 4959–4962.
- Phillips, J. P., Langford, R. M., Chang, S. H., Kyriacou, P. A. and Jones, D. P. [2011], 'Photoplethysmographic measurements from the esophagus using a new fiber-optic reflectance sensor', *Journal of Biomedical Optics* **16**(7), 077005–077005.
- Pomraning, G. C. [1973], *The Equations of Radiation Hydrodynamics*, Courier Corporation.
- Prahl, S. [1988], Light Transport in Tissue, PhD dissertation, University of Texas at Austin, USA.
URL: <https://omlc.org/prahl/pubs/pdf/prahl88.pdf>
- Prahl, S. A. [1995], The Adding-Doubling Method, in 'Optical-thermal response of laser-irradiated tissue', Springer, pp. 101–129.
- Prasad, P. N. [2004], *Introduction to Biophotonics*, John Wiley & Sons.

- Preis, T., Virnau, P., Paul, W. and Schneider, J. J. [2009], 'GPU accelerated Monte Carlo simulation of the 2D and 3D Ising model', *Journal of Computational Physics* **228**(12), 4468–4477.
- Preston, W. and Kelly, C. [2016], *Respiratory nursing at a glance*, John Wiley & Sons.
- Ramaley, J. [1969], 'Buffon's noodle problem', *The American Mathematical Monthly* **76**(8), 916–918.
- Rees, P., Chilvers, C. and Clark, T. [1980], 'Evaluation of methods used to estimate inhaled dose of carbon monoxide.', *Thorax* **35**(1), 47–51.
- Reif, R., A'Amar, O. and Bigio, I. J. [2007], 'Analytical model of light reflectance for extraction of the optical properties in small volumes of turbid media', *Applied Optics* **46**(29), 7317–7328.
- Reisner, A., Shaltis, P. A., McCombie, D. and Asada, H. H. [2008], 'Utility of the photoplethysmogram in circulatory monitoring', *The Journal of the American Society of Anesthesiologists* **108**(5), 950–958.
- Renkin, E. M., Michel, C. C. and Geiger, S. R. [1984], *Microcirculation*, American Physiological Society.
- Reuss, J. L. [2005], 'Multilayer modeling of reflectance Pulse Oximetry', *IEEE transactions on Biomedical Engineering* **52**(2), 153–159.
- Reuss, J. L. and Siker, D. [2004], 'The pulse in reflectance Pulse Oximetry: modeling and experimental studies', *Journal of Clinical Monitoring and Computing* **18**(4), 289–299.
- Rice, B. W., Cable, M. D. and Nelson, M. B. [2001], 'In vivo imaging of light-emitting probes', *Journal of Biomedical Optics* **6**(4), 432–440.
- Righini, G. C., Tajani, A. and Cutolo, A. [2009], *An Introduction to Optoelectronic Sensors*, Vol. 7, World Scientific.
- Saidi, I. S. [1992], Transcutaneous Optical Measurement of Hyperbilirubinemia in Neonates, PhD thesis, Rice University, USA.

- Sakaguchi, K., Tachibana, T., Furukawa, S., Katsura, T., Yamazaki, K., Kawaguchi, H., Maki, A. and Okada, E. [2007], 'Experimental prediction of the wavelength-dependent path-length factor for optical intrinsic signal analysis', *Applied Optics* **46**(14), 2769–2777.
- Salasche, S. J. and Bernstein, G. [1988], *Surgical Anatomy of the Skin*, Appleton & Lange.
- Scanlon, V. C. and Sanders, T. [2014], *Essentials of NIRS*, FA Davis.
- Scheeren, T., Schober, P. and Schwarte, L. [2012], 'Monitoring tissue oxygenation by near infrared spectroscopy (NIRS): background and current applications', *Journal of Clinical Monitoring and Computing* **26**(4), 279–287.
- Schmitt, J. M. [1991], 'Simple photon diffusion analysis of the effects of multiple scattering on Pulse Oximetry', *IEEE Transactions on Biomedical Engineering* **38**(12), 1194–1203.
- Severinghaus, J. W. [1993], 'History and recent developments in Pulse Oximetry', *Scandinavian Journal of Clinical and Laboratory Investigation* **53**(sup214), 105–111.
- Severinghaus, J. W., Naifeh, K. H. and Koh, S. O. [1989], 'Errors in 14 pulse oximeters during profound hypoxia', *Journal of Clinical Monitoring* **5**(2), 72–81.
- Shafique, M. and Kyriacou, P. [2012], 'Photoplethysmographic signals and blood oxygen saturation values during artificial hypothermia in healthy volunteers', *Physiological Measurement* **33**(12), 2065.
- Shen, X. and van Wijk, R. [2006], *Biophotonics: Optical Science and Engineering for the 21st Century*, Springer Science & Business Media.
- Sherebrin, M. and Sherebrin, R. [1990], 'Frequency analysis of the peripheral pulse wave detected in the finger with a photoplethysmograph', *IEEE Transactions on Biomedical Engineering* **37**(3), 313–317.
- Silva, S. M. L., Castilla, M. L. D. and Martín, J. P. S. [2003], 'Near-infrared transmittance Pulse Oximetry with laser diodes', *Journal of Biomedical Optics* **8**(3), 525–534.

- Simpson, C. R., Kohl, M., Essenpreis, M. and Cope, M. [1998], 'Near-infrared optical properties of ex vivo human skin and subcutaneous tissues measured using the Monte Carlo inversion technique', *Physics in Medicine & Biology* **43**(9), 2465.
- Splinter, R. and Hooper, B. A. [2006], *An Introduction to Biomedical Optics*, Taylor & Francis.
- Steinke, J. and Shepherd, A. [1988], 'Diffusion model of the optical absorbance of whole blood', *Journal of the Optical Society of America A* **5**(6), 813–822.
- Stern, R. M. [1974], 'Ear lobe photoplethysmography', *Psychophysiology* **11**(1), 73–75.
- Strangman, G., Franceschini, M. A. and Boas, D. A. [2003], 'Factors affecting the accuracy of near-infrared spectroscopy concentration calculations for focal changes in oxygenation parameters', *Neuroimage* **18**(4), 865–879.
- Tamura, T., Maeda, Y., Sekine, M. and Yoshida, M. [2014], 'Wearable Photoplethysmographic Sensors - Past and Present', *Electronics* **3**(2), 282–302.
- Tortora, G. J. and Derrickson, B. H. [2008], *Principles of Anatomy and Physiology*, John Wiley & Sons.
- Träger, F. [2012], *Springer handbook of lasers and optics*, Springer Science & Business Media.
- Tuchin, V. [2007], *Tissue Optics: Light Scattering Methods and Instruments for Medical Diagnosis*, Vol. 13, SPIE press Bellingham.
- Tuchin, V. V. [1993], Light interaction with biological tissues: overview, in 'OE/LASE'93: Optics, Electro-Optics, & Laser Applications in Science & Engineering', International Society for Optics and Photonics, pp. 234–272.
- Tuchin, V. V. [1997], 'Light Scattering Study of Tissues', *Physics-Uspekhi* **40**(5), 495–515.
- Tuchin, V. V. [2002], *Handbook of Optical Biomedical Diagnostics*, SPIE Press, Washington, USA.

- Tuchin, V. V., Bashkatov, A. N., Genina, E. A., Kochubey, V. I., Lychagov, V. V., Portnov, S. A., Trunina, N. A., Miller, D. R., Cho, S., Oh, H., Shim, B., Kim, M., Oh, J., Eum, H., Ku, Y., Kim, D. and Yang, Y. [2011], Finger tissue model and blood perfused skin tissue phantom, in 'Proceedings of SPIE', Vol. 7898, p. 78980Z.
- Uludağ, K., Steinbrink, J., Villringer, A. and Obrig, H. [2004], 'Separability and cross talk: optimizing dual wavelength combinations for near-infrared spectroscopy of the adult head', *Neuroimage* **22**(2), 583–589.
- Umeyama, S. and Yamada, T. [2009], 'New method of estimating wavelength-dependent optical path length ratios for oxy- and deoxyhemoglobin measurement using near-infrared spectroscopy', *Journal of Biomedical Optics* **14**(5), 054038.
- Van der Zee, P. [1992], Measurement and Modelling of the Optical Properties of Human Tissue in the Near Infrared, PhD thesis, University of London, UK.
- Van der Zee, P., Cope, M., Arridge, S., Essenpreis, M., Potter, L., Edwards, A., Wyatt, J., McCormick, D., Roth, S., Reynolds, E. and Delpy, D. [1992], 'Experimentally measured optical pathlengths for the adult head, calf and forearm and the head of the newborn infant as a function of inter optode spacing', *Advances in Experimental Medicine and Biology* **316**, 143–153.
- Vigneshvar, S., Sudhakumari, C., Senthilkumaran, B. and Prakash, H. [2016], 'Recent advances in biosensor technology for potential applications—an overview', *Frontiers in Bioengineering and Biotechnology* **4**, 11.
- Volgyesi, G., Kolesar, R. and Lerman, J. [1990], 'An in vitro model for evaluating the accuracy of pulse oximeters.', *Canadian Journal of Anaesthesia* **37**(4 Pt 2), S67.
- Wang, L. and Jacques, S. L. [1992], Monte Carlo modeling of light transport in multi-layered tissues in standard C, Technical report, The University of Texas, MD Anderson Cancer Center, Houston, <http://coilab.caltech.edu/mcr5/Mcman.pdf>.
- Wang, L., Jacques, S. L. and Zheng, L. [1995], 'MCML - Monte Carlo modeling of light transport in multi-layered tissues', *Computer Methods and Programs in Biomedicine* **47**(2), 131–146.

- Wang, R. K. and Tuchin, V. V. [2013], *Advanced Biophotonics: Tissue Optical Sectioning*, CRC Press, USA.
- Webster, J. G. [1997], *Design of Pulse Oximeters*, CRC Press, USA.
- Williams, P. L., Warwick, R., Dyson, M., Bannister, L. H. *et al.* [1989], *Gray's Anatomy*, Vol. 378, Churchill livingstone Edinburgh.
- Wilson, B. and Adam, G. [1983], 'A Monte Carlo model for the absorption and flux distributions of light in tissue', *Medical Physics* **10**(6), 824–830.
- Wilson, B. J., Cowan, H. J., Lord, J. A., Zuege, D. J. and Zygun, D. A. [2010], 'The accuracy of pulse oximetry in emergency department patients with severe sepsis and septic shock: a retrospective cohort study', *BMC emergency medicine* **10**(1), 9.
- Wing, G. M. [1962], *An Introduction to Transport Theory*, John Wiley and Sons.
- Witt, A. N. [1977], 'Multiple scattering in reflection nebulae. ii. uniform plane-parallel nebulae with foreground stars', *The Astrophysical Journal Supplement Series* **35**, 7–19.
- Wukitsch, M. W., Petterson, M. T., Tobler, D. R. and Pologe, J. A. [1988], 'Pulse Oximetry: analysis of theory, technology, and practice', *Journal of Clinical Monitoring* **4**(4), 290–301.
- Yaroslavsky, A., Schulze, P., Yaroslavsky, I., Schober, R., Ulrich, F. and Schwarzmaier, H. [2002], 'Optical properties of selected native and coagulated human brain tissues in vitro in the visible and near infrared spectral range', *Physics in Medicine & Biology* **47**(12), 2059.
- Yoo, K., Liu, F. and Alfano, R. [1990], 'When does the diffusion approximation fail to describe photon transport in random media?', *Physical Review Letters* **64**(22), 2647.
- Yun, S. H. and Kwok, S. J. [2017], 'Light in diagnosis, therapy and surgery', *Nature Biomedical Engineering* **1**(1), 0008.
- Zhu, C. and Liu, Q. [2013], 'Review of Monte Carlo modeling of light transport in tissues', *Journal of Biomedical Optics* **18**(5), 050902–050902.

Zijlstra, W. G., Buursma, A. and van Assendelft, O. W. [2000], *Visible and Near Infrared Absorption Spectra of Human and Animal Haemoglobin: Determination and Application*, VSP Publishing, UK.